

DYNAMICAL MECHANISMS FOR THE  
TELECONNECTION BETWEEN ENSO AND  
NAO IN LATE WINTER

YING LI

A DISSERTATION  
PRESENTED TO THE FACULTY  
OF PRINCETON UNIVERSITY  
IN CANDIDACY FOR THE DEGREE  
OF DOCTOR OF PHILOSOPHY

RECOMMENDED FOR ACCEPTANCE  
BY THE PROGRAM IN  
ATMOSPHERIC AND OCEANIC SCIENCES  
ADVISER: NGAR-CHEUNG LAU

NOVEMBER 2011

© Copyright by Ying Li, 2012.

All Rights Reserved

# Abstract

The dynamical mechanisms for the late-winter teleconnection between El Niño-Southern Oscillation (ENSO) and the North Atlantic Oscillation (NAO) are examined using output from two global climate models and various reanalysis datasets.

During El Niño winters, the intensified transient disturbances along the equatorward shifted North Pacific storm track extend their influences farther downstream, thereby leading to eastward extension of eddy vorticity forcing to the North Atlantic region. Such eddy forcing induces negative geopotential height tendencies along the southern lobe of the NAO, thus favoring more occurrences of negative NAO events. It is further demonstrated that these transient eddy effects can be reproduced in atmospheric GCM integrations subjected to ENSO-related SST anomalies in the tropical Pacific region.

Analysis of the persistent anomalous circulation episodes in the North Pacific-North America-North Atlantic sector further demonstrate the contributions of downstream eddy development to the ENSO/NAO teleconnection. These episodes are characterized by a strengthened Pacific subtropical jet stream and an equatorward-shifted Pacific storm track. The wave packets that populate the storm tracks travel eastward through downstream development. The pursuant barotropic forcing of the embedded synoptic-scale eddies is conducive to the formation of the negative phase of the NAO. The more frequent and higher persistence of those episodes during El Niño winters contribute to the prevalence of negative NAO conditions.

A higher frequency of weak (strong) stratospheric vortex events for El Niño (La Niña) condition is generated in a climate model with a more realistic upper atmosphere. During El Niño events, the enhanced tropospheric stationary wave-1 driving contributes to the increased frequency of stratospheric weak vortex events. The easterly wind anomalies induced by Eliassen-Palm (EP)-flux convergence over the polar cap propagate downward to the lower stratosphere/upper troposphere. Anomalous

westerly in the subtropics cannot be explained by the stratospheric planetary-wave-mean-flow interaction. Rather, it is driven by the upper tropospheric eddy momentum flux convergence, which in turn results from strong poleward wave refraction. This upper-tropospheric westerly anomaly is linked to the lower-troposphere via the eddy-driven tropospheric overturning circulation, and the resulting SLP anomaly response resembles the negative NAO in the North Atlantic region.

## Acknowledgements

First and foremost, I offer my sincerest gratitude to my advisor, Dr. Ngar-Cheung (Gabriel) Lau. Throughout the past five years, Gabriel has given me the best advising one can ever dream of on all aspects of my research and life. From the frequent and detailed discussion in the early stage to the high-level and big-picture advising while encouraging me to work increasingly independent towards the end of my Ph.D. study journey, and from accompanying me to enter GFDL on my first day to helping me improve my writing and presentation skills and advising and assisting in my post-doc finding, Gabriel has mentored me to grow step by step from a curious yet naïve fresh Ph.D. student to a fledged scientist want to be. With his superb knowledge and great enthusiasm, Gabriel has taught me a rigorous yet innovative way of conducting scientific research. This will be my greatest fortune for my future career.

I gratefully thank Dr. Isaac Held for serving as my committee member and dissertation reader. His encouragement and insightful comments are deeply appreciated. I would also like to thank the rest of my committee members: Drs. Thomas Delworth and Geoffrey Vallis for providing a wealth of expertise and helpful suggestions that have shaped the quality of my work. Thanks also go to Dr. David Thompson (CSU) for serving on my reading committee and providing constructive comments on my research.

I am indebted to many scientists at GFDL and the entire AOS faculty for generously sharing their wisdom: Drs. Andrew Wittenberg, Gabriel Vecchi, Shaoqing Zhang, Rong Zhang, Rym Msadek, Isidoro Orlanski and many others. In particular, I appreciate greatly the helpful discussion with Andrew Wittenberg at various stages of my dissertation. Many thanks to Mary Jo Nath for providing her technical expertise and helping me with implementation of the AM2.1 experiments.

I gratefully acknowledge my friends and fellow AOS students, who have made my life at Princeton enjoyable. Especially, I am grateful to Sarah Kang, Gang Chen, Yi

Huang, Fuyu Li, Yuanyuan Fang, Ian Lloyd, Yves Plancherel, Daniele Bianchi, Erica Staehling, Andrew Ballinger, Amanda O'Rourke and Ilissa Ocko for their assistance in one way or another.

Last but not least, I would like to thank my beloved family: to my dearest husband Bin Qin for his unconditional love and support and encouragement, to our adorable son Zachary for the joys he has brought, and to my parents Kaiping Li and Guojuan Gong, to whom this dissertation is dedicated.

This research was supported by Cooperative Institute of Climate Sciences (CICS) at Princeton University.

# Contents

Abstract . . . . .	iii
Acknowledgements . . . . .	v
List of Tables . . . . .	xii
List of Figures . . . . .	xiii
List of Notations and Acronyms . . . . .	xviii
<b>1 Introduction</b>	<b>1</b>
1.1 Motivation . . . . .	1
1.2 Various pathways for ENSO influences on the circulation in the North Atlantic-European sector . . . . .	5
1.2.1 Tropospheric pathway – role of transient eddies . . . . .	5
1.2.2 Stratospheric pathway – role of vertical propagation of planet- ary waves . . . . .	6
1.3 Outline . . . . .	8
<b>2 Seasonal Averaged Characteristics of the Transient-Eddy Forcing during ENSO Winters and Their Implications on the Phase of NAO</b>	<b>10</b>
2.1 Introduction . . . . .	10
2.2 Data and methodology . . . . .	11
2.2.1 Model description . . . . .	11
2.2.2 Observational datasets . . . . .	12

2.2.3	Analysis tools . . . . .	13
2.3	Simulation of ENSO and NAO variability . . . . .	14
2.3.1	ENSO variability and its impacts on SLP over the North Pacific and North Atlantic . . . . .	14
2.3.2	NAO variability and ENSO impact on the frequency of occur- rence of its different phases . . . . .	17
2.3.3	Observed and simulated surface climate response to ENSO and NAO in late winter . . . . .	18
2.4	Eddy-mean flow interaction in observed and simulated El Niño and La Niña events . . . . .	20
2.4.1	Composites of mean flow and transient eddy intensity . . . . .	20
2.4.2	Composites of $\mathbf{E}$ vectors and geopotential height tendencies .	21
2.4.3	ENSO response after removal of NAO signal . . . . .	24
2.4.4	Storm track variations over North America and its relationship to both ENSO and NAO . . . . .	25
2.5	Circulation patterns and SST environment associated with various combinations of ENSO and NAO phases . . . . .	26
2.5.1	Mean flow and transient eddy intensity in the ‘strong’ and ‘weak’ combinations . . . . .	27
2.5.2	Centers of warming in the tropical Pacific in the ‘strong’ and ‘weak’ combinations . . . . .	28
2.6	Summary and discussion . . . . .	30
<b>3</b>	<b>Contributions of Downstream Eddy Development to the ENSO- NAO Teleconnection</b>	<b>54</b>
3.1	Introduction . . . . .	54
3.2	Data and analysis procedures . . . . .	56
3.2.1	Model description . . . . .	56

3.2.2	Observational datasets . . . . .	56
3.2.3	Analysis tool . . . . .	57
3.2.4	Identification of persistent events . . . . .	59
3.3	Relationships between EOF1 and ENSO, NAO and the seasonal cycle	60
3.3.1	The dependence of the persistent events on the phase of ENSO	60
3.3.2	NAO phase during the persistent circulation anomalies . . . . .	62
3.3.3	Seasonal dependence of frequency of occurrence of persistent EOF1± days . . . . .	62
3.4	Eddy-mean flow interactions during persistent EOF1+ and EOF1– events . . . . .	63
3.4.1	Composites of persistent EOF1+ events . . . . .	64
3.4.2	Composites of persistent EOF1– events . . . . .	65
3.5	Linkage between Pacific and Atlantic variability through downstream development . . . . .	66
3.5.1	One-point lagged regression patterns based on persistent EOF1+ events . . . . .	66
3.5.2	One-point lagged regression patterns based on persistent storm track events . . . . .	70
3.5.3	Time lag of SLP signals in the Atlantic relative to those in the Pacific . . . . .	72
3.6	Case study of the 2009/2010 season . . . . .	74
3.7	Summary and discussion . . . . .	76
<b>4</b>	<b>Results from Atmospheric GCM Simulations</b>	<b>95</b>
4.1	Introduction . . . . .	95
4.2	Experimental design . . . . .	96
4.3	Seasonal averaged characteristics . . . . .	97
4.3.1	Surface climate response to ELNO and LANA . . . . .	97

4.3.2	Eddy-mean flow interaction in AGCM results . . . . .	98
4.4	Statistics of persistent episodes in AGCM . . . . .	99
4.4.1	Selection of persistent flow pattern and storm path pattern . .	99
4.4.2	The dependence of the persistent events on the AGCM experiments . . . . .	100
4.5	Summary and discussion . . . . .	102
<b>5</b>	<b>Influences of ENSO on Stratospheric Variability and Downward Penetration of the Stratospheric Perturbations to Lower Troposphere</b>	<b>110</b>
5.1	Introduction . . . . .	110
5.2	Description of model experiment, observational datasets and diagnostic tools . . . . .	112
5.2.1	Model . . . . .	112
5.2.2	Observational datasets . . . . .	113
5.2.3	Diagnostic tool . . . . .	113
5.3	Simulation of ENSO, NAO, and stratospheric variability . . . . .	116
5.3.1	Phase locking of ENSO to the seasonal cycle . . . . .	116
5.3.2	ENSO/NAO relationship . . . . .	117
5.3.3	Seasonality of stratospheric mean state and its variability . . .	118
5.3.4	Characteristics of troposphere and stratosphere stationary waves	118
5.4	Relationships between ENSO and stratospheric vortex anomalies, and their seasonal dependence . . . . .	120
5.4.1	Identification of anomalous stratospheric polar vortex months	120
5.4.2	The dependence of the stratospheric vortex anomalies on the phase of ENSO . . . . .	121
5.4.3	Seasonal dependence of frequency of occurrence of weak/strong vortex months . . . . .	122

5.5	The individual and combined effects of ENSO and vortex anomalies on the stratospheric stationary waves . . . . .	122
5.5.1	Stationary wave response during ENSO winters . . . . .	122
5.5.2	Stationary wave precursors one month before the weak/strong vortex-only events . . . . .	123
5.5.3	Combinations of the ENSO responses and strong/weak vortex precursors . . . . .	124
5.6	Relationship between wave propagation and zonal-mean meridional circulation . . . . .	129
5.6.1	EP-flux patterns . . . . .	129
5.6.2	zonal-mean meridional overturning circulation . . . . .	133
5.7	Responses of the zonal-mean zonal wind and SLP . . . . .	135
5.7.1	Zonal-mean zonal wind . . . . .	135
5.7.2	Response of surface annular mode anomalies . . . . .	137
5.8	Summary . . . . .	138
<b>6</b>	<b>Conclusions</b>	<b>159</b>
6.1	Summary . . . . .	159
6.2	Future Work . . . . .	163
<b>A</b>	<b>Partial Correlation Coefficient</b>	<b>166</b>
<b>Bibliography</b>		<b>167</b>

# List of Tables

2.1	List of observed El Niño and La Niña events selected using the DJF-mean Niño-3 index . . . . .	35
2.2	Temporal correlation coefficients among indices for the DJF-mean Niño-3, the late winter NAO, and the late winter storm path index . .	36
3.1	Summary statistics for the two types of persistent events . . . . .	79
4.1	As in Table 3.1, but for summary statistics for the four types of persistent events based on three AGCM experiments . . . . .	105
5.1	The number of weak and strong vortex events for El Niño, La Niña and ENSO-Neutral winters . . . . .	142
5.2	Vertical component of EP fluxes at 100 hPa averaged over 45°–75°N for zonal wavenumber-1 and -2 . . . . .	142

# List of Figures

2.1	Spatial patterns of the leading EOF of DJF-mean SSTAs over the tropical Pacific . . . . .	37
2.2	Composite monthly evolution of the Niño-3 SSTAs . . . . .	38
2.3	Distributions of the regression coefficients of DJFM-mean SLP versus the standardized DJF-mean Niño-3 index . . . . .	39
2.4	(a,b) Time-longitude and (c,d) time-latitude variations of the regression coefficients of SLP anomalies versus standardized DJF-mean Niño-3 index . . . . .	40
2.5	The spatial pattern of the leading EOF of seasonal mean SLP over the NA sector . . . . .	41
2.6	(a) Density histogram and (b) PDFs of the seasonal mean NAO indices	42
2.7	Horizontal distributions of (a–d) El Niño minus La Niña composites and (e–h) NAO– minus NAO+ composites. . . . .	43
2.8	As in Fig. 2.7, but for El Niño (a–d) and La Niña (e–f) composites .	44
2.9	Horizontal distributions of El Niño and La Niña composites of the 250-hPa geopotential height and rms of the 2–10 d bandpass-filtered 500-hPa geopotential height . . . . .	45
2.10	As in Fig. 2.9, but for 250-hPa extended Eliassen-Palm <b>E</b> vectors and eddy-induced height tendencies . . . . .	46
2.11	As in Fig. 2.9e–h, but for 850-hPa meridional eddy heat flux . . . . .	47

2.12 spatial pattern of the (a,c) first and (b) second EOF of the seasonal mean normalized rms of filtered 500-hPa height field over the North American sector . . . . .	48
2.13 Scatterplot of normalized DJF-mean Niño-3 index vs normalized FM-mean NAO index for the 2000-yr CM2.1 dataset . . . . .	49
2.14 Composites of 250-hPa geopotential height and rms of the bandpass filtered 500-hPa geopotential height . . . . .	50
2.15 ENSO+/NAO– minus ENSO+/NAO+ composites of SST and precipitation . . . . .	51
2.16 Horizontal distributions of El Niño and La Niña composites of geopotential height anomaly at 10 hPa, 50 hPa and 500 hPa . . . . .	52
2.17 Time-height evolution of El Niño and La Niña anomaly for the polar cap geopotential height and zonal mean zonal wind at 60°N . . . . .	53
 3.1 Spatial patterns of the leading EOF of 8-d low-pass filtered 250-hPa height for the 121-d winter period over the region 20°–70°N, 120°E–0°–15°E . . . . .	80
3.2 Number of positive and negative EOF1 days for each (a) El Niño and (b) La Niña winter season . . . . .	81
3.3 Time series of the composites of the EOF1 index . . . . .	82
3.4 PDFs of the normalized daily NAO indices . . . . .	83
3.5 Distribution of frequency of occurrence of number of days belonging to persistent EOF1± events for each calendar month of the winter season	84
3.6 Horizontal distribution of composites of the (a) and (b) 8-d low-pass filtered 250-hPa geopotential height and 250-hPa envelope function, (c) and (d) extended <b>E</b> vectors and eddy-induced height tendencies, (e) and (f) 8-d low-pass filtered sea-level pressure . . . . .	85
3.7 Same as in Fig. 3.6, but for results based on persistent EOF1– events	86

3.8	One-point lagged regression maps of unfiltered 250-hPa meridional velocity $v$ anomalies during the persistent EOF1+ events . . . . .	87
3.9	Same as in Fig. 3.8, but for results based on ‘all-winter’ days . . . . .	88
3.10	Longitude-time diagrams of one-point lagged regression coefficients of 250-hPa unfiltered meridional velocity at 35°N . . . . .	89
3.11	As in Fig. 3.8, but for the persistent SPI± . . . . .	90
3.12	Average of time lag $\Delta T$ (in days) of the peak SLP at individual grid points relative to the peak day of the EOF1 index over all persistent EOF1+ event . . . . .	91
3.13	The time series of NAO index for the 2009/2010 winter . . . . .	92
3.14	Longitude-time sections of (a) 250-hPa unfiltered anomalous $v$ averaged over 30°–45°N and (b) 250-hPa anomalous envelope function ( $Z_e$ ) . . . . .	93
3.15	Latitude-time sections of anomalous 250-hPa (a) 8-d low-pass filtered $Z$ and envelope function $Z_e$ (b) 8-d low-pass filtered $Z$ and eddy induced height tendency . . . . .	94
4.1	Same as in right panels of Fig. 2.8, but for results based on responses in ELNO and LANA experiments . . . . .	106
4.2	Pattern correlations between the ensemble mean and the 30 individual ensemble members . . . . .	107
4.3	Same as in Fig. 2.9, but for results based on responses in ELNO and LANA experiments . . . . .	108
4.4	Same as in Fig. 3.3, but for the results based on the persistent Z250± episodes in three AGCM runs . . . . .	109
4.5	Boxplots showing distribution of mean duration for persistent Z250± in three AGCM runs . . . . .	109
5.1	Composite monthly evolution of the Niño-3 SSTAs . . . . .	143

5.2	Time-latitude variations of the regression coefficients of SLP anomalies versus standardized DJF-mean Niño-3 index . . . . .	144
5.3	Monthly evolution of zonal-mean zonal wind climatology and its standard deviation . . . . .	145
5.4	Climatological (NDJFM-mean) all-wavenumber, zonal wavenumber-1 and wavenumber-2 of geopotential height fields at 10 hPa and 300 hPa	146
5.5	Frequency distribution of the monthly vortex strength indices for the selected El Niño winters . . . . .	147
5.6	Frequency distribution of weak and strong vortex events per year in given month . . . . .	147
5.7	Composite longitude–height cross sections of wave-1 and -2 components of geopotential height, as averaged between 45° and 75°N, for climatology and composite ENSO events . . . . .	148
5.8	As in Fig. 5.7, but for weak/strong vortex-only events . . . . .	149
5.9	As in Fig. 5.8, but for the four types of combination . . . . .	150
5.10	Horizontal distributions of the composites all-wave, wave-1 and -2 of geopotential height fields at 10 hPa and 300 hPa during the lag of –1 month of the two ‘strong combinations’ . . . . .	151
5.11	As in Fig. 5.10, but for the two ‘weak combinations’ . . . . .	152
5.12	Composites of latitude–height cross sections of EP flux and its divergence for all-wave, wave-1 and -2 . . . . .	153
5.13	Composites of latitudinal profile of meridional component of anomalous EP flux at 300 hPa for ENSO, and vortex-only events . . . . .	154
5.14	Composites of latitude–height cross sections of anomalous residual zonal-mean circulation during lags of 0 and +1 month . . . . .	155
5.15	Composites of anomalous mean meridional mass streamfunction averaged from the lag of 0 to +1 month . . . . .	156

5.16 Composites of latitude–height cross sections of anomalous zonal-mean zonal wind from lag of $-1$ month to $+2$ month . . . . .	157
5.17 Horizontal distributions of composites of SLP anomalies averaged from lag of $0$ to $2$ month . . . . .	158

# List of Notations and Acronyms

## Notations

### Chapter 2

( )'	2–10 d bandpass-filtered quantities .....	13
$\overline{()}$	time averaging over an individual winter month .....	13

### Chapter 3

( )'	2–8 d band-pass filtered quantities .....	57
$\overline{()}$	smoothing with 8-d low-pass filter .....	57

### Chapter 5

( )*	zonal deviations of the quantities .....	114
[ ]	zonal mean of the quantities .....	114
( )'	deviations of the monthly mean, submonthly eddies .....	141
$\overline{()}$	time averaging over an individual winter month .....	141

## Acronyms

AGCM	atmospheric general circulation model
AL	Aleutian Low
AM2	atmospheric component of CM2.1
AM3	atmospheric component of CM3
AO	Arctic Oscillation
ECMWF	European Center for Medium-Range Weather Forecasts
CM2.1	coupled climate model CM2.1 at GFDL
CM3	coupled climate model CM3 at GFDL
CTRL	Control experiment with AM2.1
E	Extended Eliassen-Palm vector
ELNO	El Niño experiment with AM2.1

ENSO	El Niño-Southern Oscillation
EOF	Empirical Orthogonal Function
EP	Eliassen-Palm
ERSST V3	extended reconstructed SST version 3
GCM	general circulation model
GFDL	Geophysical Fluid Dynamics Laboratory
GPCP	Global Precipitation Climatology Project
IL	Icelandic Low
LANA	La Niña experiment with AM2.1
MOM	Modular Ocean Model
NA	North Atlantic
NAE	North Atlantic-European
NAM	Northern Annular Mode
NAO	North Atlantic Oscillation
NH	Northern Hemisphere
NP	North Pacific
NCAR	The National Center for Atmospheric Research
NCEP	National Centers for Environmental Prediction
PDF	probability density function
PNA	Pacific/North American
QBO	Quasi-Biennial Oscillation
rms	root mean square
SAT	surface air temperature
SLP	sea level pressure
SPI	storm path index
SST	sea surface temperature
SSTA	sea surface temperature anomaly

SSW Stratospheric Sudden Warming  
TEM Transformed Eulerian-Mean  
20thC dataset a recently released atmospheric reanalysis for the 1891–2008 period  
 $\partial Z/\partial t$  eddy vorticity flux induced geopotential height tendency

# Chapter 1

## Introduction

### 1.1 Motivation

The term ‘teleconnection’ suggests that circulation anomalies and the associated temperature and precipitation anomalies in one location are related to those in remote regions. Seasonal predictions based on such relationships are of great utility and economic value. The best known examples are the global teleconnections related to the strong sea surface temperature (SST) variability associated with the El Niño-Southern Oscillation (ENSO) phenomenon in the tropical Pacific.

ENSO, as the dominant pattern of interannual climate variability, has strong influences on the atmospheric circulation around the globe (e.g., [Bjerknes 1969](#); [Horel and Wallace 1981](#); [Trenberth et al. 1998](#)). Particular attention has been devoted to the relationships between ENSO and various meteorological anomalies associated with the Pacific/North American (PNA) teleconnection pattern ([Wallace and Gutzler 1981](#)). However, some studies have pointed out that the ENSO-related circulation pattern is distinct from the internally generated PNA pattern (e.g., [Straus and Shukla 2002](#); [Nigam 2003](#)).

North Atlantic Oscillation (NAO) is another prominent mode of interannual variability in the Northern Hemisphere (NH) extratropics (Branston and Livezey 1987; Hurrell 1995; Hurrell and van Loon 1997). It is characterized by opposing changes in the sea level pressure (SLP) centers near the Azores in the subtropical North Atlantic (NA) and Iceland. It may be viewed as the Atlantic component of a larger hemispheric mode referred to as North Annular Mode (NAM)/Arctic oscillation (AO) (e.g., Thompson and Wallace 1998, 2000). Variations in amplitude and polarity of the NAO exert a strong influence on fluctuations in the storm track, temperature and precipitation from the NA to Eurasia (e.g., Walker and Bliss 1932; van Loon and Rogers 1978; Thompson and Wallace 2001).

While the responses of the climate over the North Pacific (NP) and North America to ENSO are well known (see Trenberth et al. 1998 for a review), the effects of ENSO on North Atlantic-European (NAE) region are less certain (Greatbatch et al. 2004; Toniazzo and Scaife 2006; Brönnimann 2007). The existence of a weak but significant ENSO response over NAE has been suggested in both observational studies and numerical experiments.

In some earlier studies, it was indicated that the association between ENSO and NAO is weak and difficult to detect in short observational records (Rogers 1984; Fraedrich 1994). More recent works based on observational data (Fraedrich and Müller 1992; Dong et al. 2000; Moron and Gouirand 2003; Pozo-Vázquez et al. 2001, 2005; Brönnimann et al. 2004, 2007) and numerical experimentation (Merkel and Latif 2002; Gouirand et al. 2007; Ineson and Scaife 2009) indicate that ENSO can extend its influence to the remote NAE sector, with responses in early winter being different from those in late winter. Some authors note a non-stationary ENSO response over Europe (Greatbatch et al. 2004), whereas Brönnimann et al. (2007) find a consistent and stationary relationship between ENSO and the late-winter climate in Europe using reconstructed SLP data for the past 300 years. Nonlinearity in the response of SLP

over the NA to the strength of El Niño (Toniazzo and Scaife 2006; Bell et al. 2009) and to the polarity of ENSO phase (Pozo-Vázquez et al. 2001, 2005; Gouirand and Moron 2003) have also been noted. Despite the considerable level of inter-event variability (e.g., Hamilton 1988; Gouirand and Moron 2003; Mathieu et al. 2004; Larkin and Harrison 2005; Gouirand et al. 2007), a majority of observational and modeling studies shows that the following features are prevalent in the late winters of El Niño events: high SLP anomaly from Iceland to Scandinavia, low SLP anomaly from the east coast of the U.S. to the Black Sea, as well as cold and dry conditions over northern Europe, and warm and wet conditions over parts of the Mediterranean (Fraedrich and Müller 1992; Fraedrich 1994; Merkel and Latif 2002; Moron and Gouirand 2003; Gouirand et al. 2007).

Although ENSO influences on the climate over the remote NAE region have been noted in many recent studies, large variability of the atmospheric responses over that site during individual ENSO events (Hamilton 1988; Kumar and Hoerling 1997; Toniazzo and Scaife 2006) makes it difficult to identify statistically significant signals on the basis of limited observational records. Questions remain regarding the dynamical mechanisms for the teleconnection between ENSO and NAO. This thesis takes advantage of multicentury-long, pre-industrial control simulations of two global climate models developed at Geophysical Fluid Dynamics Laboratory (GFDL), i.e., CM2.1 and CM3. The possible pathways in the troposphere and stratosphere are examined utilizing the CM2.1 and CM3 simulations, respectively. This work aims to answer the following specific questions:

- 1) Is there any statistically significant relationship between ENSO and NAO? What is the seasonal dependence of this relationship?
- 2) How do changes of the ENSO forcing affect the behavior of transient synoptic eddies over the NA sector via the tropospheric pathway? What are the implications of this relationship for the phase of NAO?

- 3) What is the SST environment in the equatorial Pacific that favors the eastward extension of transient eddy activity?
- 4) Does the enhanced stratospheric resolution in the model contribute to a stronger ENSO/NAO relationship?
- 5) Many previous studies have found stronger upward propagation of the wavenumber-1 component of the planetary waves from troposphere under El Niño winters than under La Niña winters. What is the role of the wavenumber-2 component during El Niño and La Niña winters? What are the implications of these effects for the dynamical linkage between ENSO and stratospheric variability?
- 6) How do the stratospheric perturbations penetrate downward to the troposphere during the two opposing phases of ENSO? What is the role of the ENSO forcing on the eddy-induced tropospheric overturning circulation?

Focusing on the model runs with pre-industrial climate forcing allows us to study the natural model variability. Understanding the possible link between the natural variability of ENSO and NAO has important implications for seasonal prediction in the NAE region. Since the negative correlation between ENSO and NAO indices is projected to strengthen in the future ([Müller and Roeckner 2006](#)), results from our present study on ENSO/NAO relationship can be ultimately applied to the understanding and assessment of future climate change.

## 1.2 Various pathways for ENSO influences on the circulation in the North Atlantic-European sector

The main objective of this thesis is to identify possible pathways linking ENSO and NAO. In this section, we present a brief review of the existing literature, and propose two hypotheses of the tropospheric and stratospheric pathways.

### 1.2.1 Tropospheric pathway – role of transient eddies

An equatorward shift and eastward extension of the Pacific storm track during El Niño have been noted in previous studies (e.g., Held et al. 1989; Trenberth and Hurrell 1994; Hoerling and Ting 1994; Straus and Shukla 1997; Chang 1998; Zhang and Held 1999; Seager et al. 2003; Lau et al. 2005; Orlanski 2005). Changes in the midlatitude storm tracks during El Niño events alter the vorticity flux by transient synoptic eddies, thereby modulating the amplitude and structure of the extratropical planetary-scale wave trains initiated by tropical sea surface temperature anomalies (SSTAs) (Kok and Opsteegh 1985; Held et al. 1989; Hoerling and Ting 1994; Kushnir et al. 2002; Orlanski 2005, among others). To our knowledge, the prior studies have not devoted much attention to the effects of transient eddies on the flow pattern downstream of the PNA sector.

A few other studies has noted the influences of upstream seeding of transient disturbances from the eastern Pacific on the NAO. Franzke et al. (2004) point out that the initial latitudinal position of the Pacific storm track is essential for determining the NAO phase. Rivière and Orlanski (2007) also emphasize that waves originating from the eastern Pacific and breaking cyclonically or anticyclonically over the Atlantic play an important role in determining the phase of NAO. This upstream influence

from the eastern Pacific suggests a role of the transient eddies in linking the flow patterns over the NP and NA. In addition, strong linkage between the Pacific and Atlantic storm tracks has been identified by [James and Burkhardt \(2006\)](#).

The term ‘downstream development’ is often used to describe the successive appearance of troughs and ridges downstream from an existing trough or ridge. This behavior is particularly noticeable in the wave packets that populate the storm tracks, and is associated with the dispersive character of baroclinic eddies embedded therein. There are numerous modeling and observational studies on downstream development and wave packets (e.g., [Simmons and Hoskins 1979](#); [Chang 1993](#); [Lee and Held 1993](#)). The climatological aspects of these features are well documented (e.g., [Chang and Yu 1999](#); [Chang 1999](#)).

Given the evidence of the meridional shift and eastward extension of the Pacific storm track during ENSO events, and the possible eddy propagation from NP to NA, it is anticipated that a linkage exists between ENSO and the NAO due to the downstream eddy development and the ensuing transient eddy forcing of the low-frequency circulation anomaly in the NA sector.

### **1.2.2 Stratospheric pathway – role of vertical propagation of planetary waves**

ENSO has been found to influence the extratropical circulation in the stratosphere in both observations and model studies. Early observational works (e.g., [van Loon and Labitzke 1987](#); [Hamilton 1993](#)) have provided evidence for El Niño events to produce a weakened stratospheric polar vortex through an intensification of the Aleutian high in lower stratosphere. On the other hand, the polar vortex during La Niña events is anomalously strong. However, the connection between ENSO and the zonal-mean circulation of the extratropical stratosphere is somewhat inconclusive due to the difficulty of isolating ENSO effects in observations from other sources of natural variabil-

ity, such as the quasi-biennial oscillation (QBO) effects (e.g., [Hamilton 1993](#); [Baldwin and O’Sullivan 1995](#)).

Recent studies based on reanalysis data have found statistically significant warming in the polar stratosphere during El Niño winters (e.g., [García-Herrera et al. 2006](#); [Camp and Tung 2007](#); [Garfinkel and Hartmann 2008](#)). Using different GCMs extending into the middle atmosphere, the distinct emergence of a stratospheric response to El Niño events and enhanced tropospheric driving of stationary wave-1 have been demonstrated ([Sassi et al. 2004](#); [Taguchi and Hartmann 2006](#); [Manzini et al. 2006](#); [Ineson and Scaife 2009](#)). The effects of La Niña on the stratospheric polar vortex are less certain. Although the signal is weak, a stronger than normal polar vortex has been reported during La Niña winters ([Limpasuvan et al. 2005](#); [Manzini et al. 2006](#); [García-Herrera et al. 2006](#)).

The anomalous stratospheric polar vortex can in turn affect the late winter climate in the NAE region through downward propagation of the pertinent atmospheric signals (e.g., [Baldwin and Dunkerton 2001](#); [Sassi et al. 2004](#); [García-Herrera et al. 2006](#); [Manzini et al. 2006](#)). Different processes have also been proposed to explain the dynamical mechanisms by which the stratosphere might affect the troposphere. One is the downward control mechanism by the meridional circulation (e.g., [Haynes et al. 1991](#); [Thompson et al. 2006](#)) and the equivalent inversion of the stratospheric potential vorticity ([Hartley et al. 1998](#); [Black 2002](#); [Ambasum and Hoskins 2002](#)). A second mechanism is through the downward planetary wave reflection in the stratosphere ([Perlitz and Harnik 2003, 2004](#)). A third mechanism involves the impact of the stratospheric circulation on the index of refraction of vertically propagating waves (e.g., [Chen and Robinson 1992](#); [Hartmann et al. 2000](#); [Shindell et al. 2001](#)). Additionally, the modulation of tropospheric synoptic eddies can feedback on the downward influence from the lower stratosphere ([Kushner and Polvani 2004](#); [Song and Robinson 2004](#); [Chen and Held 2007](#)).

Given the evidence on the influence of ENSO on the stratosphere polar vortex, and the possible downward influence of the polar vortex on the phase of NAO, it is anticipated that ENSO can remotely affect the NAE climate through stratospheric dynamics. The possible link between ENSO and the NAE climate via the stratospheric pathway has been noted recently (Brönnimann et al. 2004; Bell et al. 2009; Cagnazzo and Manzini 2009; Ineson and Scaife 2009). However, most of those previous studies focus on the linkage between the warm phase of ENSO and the weakening of the stratospheric polar vortex, and the subsequent negative NAM signature near the surface. In this work, we extend the scope of the previous studies by investigating the tropospheric stationary wave forcing from the two opposing phases of ENSO, and considering both the strong and weak stratospheric vortex events in the analysis.

### 1.3 Outline

Chapter 2 reports on our study of the effect of ENSO on the seasonally averaged behavior of transient eddies in both the Pacific and Atlantic sectors, and the impact of the accompanying eddy forcings on the phase of NAO. The primary data base for this part of the study is the output from a 2000-yr integration of a coupled GCM (CM2.1), as well as two independent reanalysis datasets used for validating the model results. It is found that the pattern of eddy forcing due to the transient disturbances leads to a downstream displacement of the low-frequency circulation anomaly. This part of the work will appear in Li and Lau (2012a).

While the work in chapter 2 improves our understanding of ENSO forcing of eddy-mean flow interaction in both NP and NA sectors, it does not offer a detailed description of the eddy processes involved in such interaction. To address this issue, chapter 3 further documents the role of downstream eddy development in the ENSO-NAO teleconnection by using daily values from the reanalysis and CM2.1 datasets.

Particular attention is devoted to the persistent circulation episodes in the North Pacific-North American-North Atlantic sector. Evidence is shown that there is more coherent wave packet propagation across North America into the Atlantic in the course of these persistent episodes. The barotropic forcing of the synoptic-scale eddies embedded in the wave packets over the NA leads to the formation of the more slowly-varying flow pattern over NA. This part of the work will appear in [Li and Lau \(2012b\)](#).

To further demonstrate the impacts of the tropical Pacific SST forcing on the atmospheric variability in the NA sector, chapter 4 examines the results from AGCM experiments, and compares these findings with those obtained from the fully coupled model simulation in chapter 2 and chapter 3. Experiments are conducted using the atmospheric component of CM2.1 (AM2.1), with ENSO-related anomalous SST prescribed only in the tropical Pacific. It is shown that ENSO-related SSTAs in the tropical Pacific play a significant role in modulating eddy-mean flow interactions over the NA sector. Part of the work in this chapter will appear in [Li and Lau \(2012a\)](#).

A new version of the global coupled climate model (CM3) with increased vertical resolution and extent in the model stratosphere is analyzed in Chapter 5, to examine the ENSO teleconnection through the stratospheric pathway. The individual effects of ENSO and stratospheric polar vortex anomalies on the stationary wave modulation are studied. It is found that ENSO plays an important role in modulating the frequency occurrence of the stratospheric polar vortex anomalies via its impact on the amplitudes of the stationary wave-1 and wave-2, especially in late winter. The Eliassen-Palm flux, meridional overturning circulation, zonal-mean flow patterns during warm/cold ENSO episodes in combination with strong/weak stratospheric vortices are also examined. The work presented in this chapter will be summarized in a manuscript to be submitted to *Journal of Climate*.

Finally, a summary of this dissertation and recommendations for future work are provided in chapter 6.

# **Chapter 2**

## **Seasonal Averaged Characteristics of the Transient-Eddy Forcing during ENSO Winters and Their Implications on the Phase of NAO**

### **2.1 Introduction**

As mentioned in chapter 1, the meridional shift and eastward extension of the Pacific storm track during ENSO events have been noted in previous studies (e.g., Hoerling and Ting 1994; Straus and Shukla 1997; Chang 1998; Zhang and Held 1999; Seager et al. 2003; Lau et al. 2005; Orlanski 2005). In this chapter, we extend the scope of previous works by investigating the nature of transient eddy forcing farther downstream of the PNA sector towards the NAE region during ENSO events.

Our intention here is not to provide explicit evidence on the propagation of individual eddies from NP to NA, which will be discussed in chapter 3; we hope rather to improve our understanding of ENSO forcing of eddy-mean flow interaction in both

the NP and NA sectors. One can then better appreciate the importance of ENSO-related transient eddy feedbacks over NA. Moreover, the coupled GCM integration being analyzed has a duration of 2000 yr output. This extended experiment allows for adequate sampling of various features of interest, so that their mutual relationships can be established with a higher degree of confidence.

The GCM as well as the observational datasets used for validating the model results are described in section 2.2. Simulated and observed aspects of the impacts of ENSO and the NAO on the atmospheric variability in the NA sector are presented, and the significant linkage between the two modes is documented in section 2.3. The characteristics of the simulated and observed synoptic eddies, their interaction with the monthly mean flow, and the vorticity forcing in terms of eddy-induced geopotential height tendencies are shown and discussed in section 2.4 for the warm and cold phases of the ENSO anomalies. The flow patterns and SST environment associated with various combinations of ENSO and NAO phases are examined in section 2.5. Summary and discussion are given in section 2.6.

## 2.2 Data and methodology

### 2.2.1 Model description

The model data analyzed in this study is generated by a 2000-yr long integration of CM2.1 global coupled climate model developed at GFDL (Delworth et al. 2006; Wittenberg 2009), with radiative forcing being fixed at the pre-industrial (1860) level throughout the experiment. The resolution of the atmospheric component of CM2.1 (hereafter referred to as AM2.1) is  $2^\circ$  latitude  $\times$   $2.5^\circ$  longitude. The 24 vertical levels are structured in a hybrid coordinate, with 5 levels in the stratosphere and a model top at about 3 hPa. The physics packages employed in AM2.1 are described by the GFDL Global Atmospheric Model Development Team (2004). The dynamical core of this

model uses the finite volume method coded by [Lin \(2004\)](#). The oceanic component of CM2.1 builds on the fourth generation of the Modular Ocean Model (MOM4), as described in [Griffies et al. \(2004\)](#). The resolution is  $1^\circ$  latitude  $\times$   $1^\circ$  longitude, with meridional grid spacing decreasing to  $1/3^\circ$  towards the equator. There are altogether 50 vertical levels, with 22 levels being located in the top 220 m ([Gnanadesikan et al. 2006](#)). The atmosphere, ocean, land and sea ice exchange fluxes once every 2 h, and fluxes are conserved within machine precision. The model has been run without any flux adjustments for over 2000 years and exhibits no appreciable climate drifts in the quantities examined in this chapter.

### 2.2.2 Observational datasets

The observational data used to compare with model findings include:

- Monthly precipitation data from the Global Precipitation Climatology Project (GPCP) version 2 ([Adler et al. 2003](#)). This is a product that merges satellite microwave and infrared data with rain gauge observations and covers the 1979–2009 period.
- Surface air temperature (SAT), SLP, geopotential height and upper level wind (1948–present) from National Centers for Environmental Prediction/National Center for Atmospheric Research (NCEP/NCAR) reanalysis ([Kalnay et al. 1996](#)).
- A recently released atmospheric reanalysis for the 1891–2008 period, hereafter referred to as the 20thC dataset ([Compo et al. 2006](#)). This dataset is based primarily on the assimilation of surface pressure observations before the radiosonde era, and has been demonstrated to yield an adequate depiction of the large-scale tropospheric circulation features ([Whitaker et al. 2004; Compo et al. 2006](#)).

- Monthly mean SST from the NOAA extended reconstructed SST version 3 dataset (ERSST V3, see [Smith et al. 2008; Xue et al. 2003](#)).

### 2.2.3 Analysis tools

Storm track characteristics are depicted using eddy variance and covariance statistics. Following [Lau \(1988\)](#), a 2–10 d bandpass Lanczos filter ([Duchon 1979](#)) with 41 weights is applied to the daily 500-hPa geopotential height data  $Z$  at each gridpoint, and then the root-mean-square (rms) of the filtered height  $(\overline{Z'^2})^{1/2}$  is computed. Here the prime represents the bandpass-filtered quantities and overbar denotes time averaging over an individual winter month.

Extended Eliassen-Palm vectors (hereafter referred to as  $\mathbf{E}$ ) are used to illustrate the properties of transient eddies and local interactions between transient eddies and the time-mean flow ([Hoskins et al. 1983](#)). The horizontal components of  $\mathbf{E}$  used in this study are given by [Trenberth \(1986\)](#):

$$\frac{1}{2}(\overline{v'^2} - \overline{u'^2})\mathbf{i} - \overline{u'v'}\mathbf{j}.$$

Here  $u, v$  are the zonal and meridional wind components, respectively. The  $\mathbf{E}$  vectors point approximately in the direction of the wave energy propagation relative to the local time-mean flow. The divergence and curl of  $\mathbf{E}$  indicate eddy-induced acceleration of the local mean zonal and meridional wind, respectively.

The barotropic feedback of the transient eddies on the quasi-stationary flow is illustrated by the eddy-induced geopotential height tendency associated with horizontal convergence of eddy vorticity flux at the 250-hPa level as given by [Lau and Holopainen \(1984\)](#):

$$\left( \frac{\partial Z_{250}}{\partial t} \right)_{edd} = \frac{f}{g} \nabla^{-2} [-\nabla \cdot (\overline{\mathbf{V}' \zeta'})]. \quad (2.1)$$

Here  $Z_{250}$  is the geopotential height at 250 hPa,  $\mathbf{V}$  the horizontal wind vector,  $\zeta$  the relative vorticity,  $f$  the Coriolis parameter and  $g$  the acceleration due to gravity.

## 2.3 Simulation of ENSO and NAO variability

### 2.3.1 ENSO variability and its impacts on SLP over the North Pacific and North Atlantic

An empirical orthogonal function (EOF) analysis of December–February (DJF) mean SSTs over the tropical Pacific region is performed. The observed and simulated spatial patterns resulting from this EOF analysis are presented in Fig. 2.1. The observed (Fig. 2.1a) and simulated (Fig. 2.1b) patterns explain 64.5 and 67.7% of the total variance, respectively. The data value shown in these panels depict the local amplitudes of SSTAs corresponding to one standard deviation ( $\sigma$ ) of the temporal coefficients of the EOF. It is evident that the amplitude of SST variations in the model is higher than that in the observations, and the simulated SSTA extends too far westward to the equatorial Western Pacific. We shall henceforth present the results based on the Niño-3 index (SSTAs averaged over 5°S–5°N, 150°–90°W; see boxed area in Fig. 2.1). Analyses based on alternative indices [such as Niño-3.4 (5°S–5°N, 170°–120°W) and the temporal coefficients of the leading EOF of SST field] yield similar results.

A warm (cold) ENSO event is identified when the DJF-mean Niño-3 index is more than  $1\sigma$  above (below) the time mean. This criterion yields 10 warm and 9 cold events based on NOAA ERSST V3 dataset for the 1948–2010 period, and 19 warm and 20 cold events based on the same dataset for the 1891–2008 period. Table 2.1 lists the selected cases. Analogous analysis of the CM2.1 data yields 252 warm events and 215 cold events.

To investigate the phase locking of ENSO variability with the seasonal cycle, Fig. 2.2 shows the composite month-to-month evolution of the Niño-3 SSTAs during El Niño and La Niña events for both observations and the CM2.1 simulation. For El Niño events, the observed anomaly peaks near Dec(0), while the corresponding model result shows large positive anomalies over a broad period, with a primary peak in Feb(1) that corresponds to the mature phase, and a secondary peak in Aug(0) resulting from the semiannual phase locking of the model ENSO (see discussion in [Wittenberg et al. 2006](#)). The delayed occurrence of the mature phase in the CM2.1 simulation relative to observations is also evident in La Niña events.

The anomalous surface circulation associated with ENSO during the extended boreal winter season of December–March (DJFM) is illustrated by the patterns of regression coefficients of SLP versus standardized Niño-3 SSTAs (Fig. 2.3). In the observed pattern (Fig. 2.3a), a deepened Aleutian low is seen over the NP, and a weak anomalous low pressure over central-western Atlantic near 35°N is discernible. In the CM2.1 simulation (Fig. 2.3b), the westward displacement of the anomaly over the NP relative to observations is likely related to the excessive westward spread of the simulated SST forcing in the tropical Pacific (Fig. 2.1) and the associated precipitation changes ([Wittenberg et al. 2006](#)). The simulated anomalous low over the NA extends farther eastward to eastern Europe. Caution may be needed when comparing the model and observational results over the western NA because the simulated anomalous low over the NP extends too far into the western NA.

To illustrate the seasonality of the SLP signal accompanying ENSO, the time evolution of the regression coefficients of SLP anomalies versus Niño-3 index over both the NP and NA sectors are shown in Fig. 2.4. For the NP sector (Figs. 2.4a,b), zonal variations are presented for averages over the latitudes between 35° and 55°N; for the NA sector (Figs. 2.4c,d), meridional variations are shown for averages over the longitudes between 70° and 20°W.

The observed negative anomaly in the NP region (Fig. 2.4a) is captured by CM2.1 (Fig. 2.4b), except that the simulated feature is more persistent in time, and maintains a stronger presence through March and April. The simulated anomaly position is also displaced westward by  $15^{\circ}$  of longitude.

Over the NA sector, the observed response in November and December (Fig. 2.4c) is characterized by a low pressure anomaly to the north and a weak high pressure anomaly to the south. This configuration is reversed in the January–April period, and the pressure pattern corresponds to the negative phase of NAO. Because the SLP pattern over the NA in December is almost opposite to that in January–March, averaging the pressure signals over the entire season (DJFM), as was done in computing Fig. 2.3a, leads to much weaker responses than the anomalies for individual months. The above seasonal dependence of the ENSO relationship with SLP over the NA sector is in agreement with [Moron and Gouirand \(2003\)](#), who analyze a longer record of observational data (1873–1996). The negative NAO signal in response to El Niño during late winter is captured by the model (Fig. 2.4d). However, positive pressure anomaly in the high latitudes in the model atmosphere emerges in February, about one month later than the observations. In addition, the simulated positive anomaly peaks in April, about two months after the negative anomaly attains maximum amplitudes.

In view of the occurrence of the strongest observed NAO signals in January–February (JF), and the strongest simulated signals in February–March (FM), we shall hereafter define ‘late winter’ as the JF period for the observations, and the FM period for the model. This slight difference in the definition of the later winter season for observed and model data is further motivated by the 1-month delay of the tropical Pacific SST forcing in CM2.1 relative to the observations, as illustrated in Fig. 2.2.

### 2.3.2 NAO variability and ENSO impact on the frequency of occurrence of its different phases

We next examine the NAO pattern in the observed and model atmospheres. The NAO pattern is defined as the leading EOF of the late winter (JF for observations and FM for the simulation) SLP field within the region of 20°–70°N, 80°W–20°E, and is displayed in Fig. 2.5. Both the observed (Fig. 2.5a) and simulated (Fig. 2.5b) data exhibit a dipole-like pattern with centers of action at 40° and 65°N. The normalized temporal coefficients of the leading EOF of the SLP field serve as the NAO index. Outstanding NAO events correspond to those seasons with indices exceeding  $1\sigma$  from normal.

Fig. 2.6a shows density histograms of the normalized JF-mean NAO indices for the selected El Niño (red columns) and La Niña (blue columns) events during the period 1891–2008 (see Table 2.1). The NAO indices in this period are obtained using the 20thC dataset. This figure illustrates strong negative NAO indices (less than  $-1.0$ ) are more frequent during El Niño years than during La Niña years. Conversely, strong positive NAO indices (greater than  $1.0$ ) are more frequent during La Niña years than El Niño years. The average values of NAO index during the observed 19 El Niño winters and 20 La Niña winters are  $-0.35$  and  $+0.51$ , respectively. The difference between these composite values is statistically significant ( $p$  value = 0.008) using a  $t$  test.

The probability density functions (PDFs) of the normalized FM-mean NAO indices during El Niño winters (red curve) and La Niña winters (blue curve) in the CM2.1 simulation are compared in Fig. 2.6b. A pronounced shift in the distribution towards negative and positive NAO values are apparent for the El Niño and La Niña years, respectively, in agreement with observational results. The two distributions are statistically different ( $p$  value < 0.01) using a Kolmogorov-Smirnov test (Smirnov 1948). Statistically different composite values of the normalized NAO index are also

found based on the simulated 252 El Niño winters and 215 La Niña winters ( $-0.40$  vs  $+0.33$ ,  $p$  value  $< 0.01$ ). It is noteworthy that the difference between the composite NAO indices for El Niño and La Niña episodes exceeds  $0.7\sigma$  in both observations and model. This difference may be sufficiently large to be of practical use in seasonal forecasting. It should also be noted that the magnitude of the composite NAO indices associated with El Niño winters is slightly stronger than that associated with La Niña winters in the CM2.1 simulation. This results is opposite to the results based on 20thC dataset, and previous observational studies (Pozo-Vázquez et al. 2001, 2005).

### 2.3.3 Observed and simulated surface climate response to ENSO and NAO in late winter

The link between ENSO and NAO is further explored by examining the surface climate signals in the NAE sector associated with these two phenomena. The top four panels of Fig. 2.7 show the difference between the El Niño and La Niña composites of late-winter SLP, SAT and precipitation, for both observations and model. These ENSO responses may be compared with the corresponding patterns based on differences between outstanding positive and negative NAO events, as shown in the bottom four panels.

The distribution of observed SLP for late winter (JF, see Fig. 2.7a) associated with ENSO shows a more distinct dipole-like pattern than the corresponding chart for the DJFM season (Fig. 2.3a). This dipolar pattern resembles the SLP pattern corresponding to the negative NAO phase (Fig. 2.7e). This dipolar feature is discernible in the corresponding SLP pattern in CM2.1 (Fig. 2.7b), although the simulated negative center over the extratropical NA is displaced westward relative to its observed counterpart. The amplitude of the dipolar anomaly is reduced in the simulation, as previously noted in Figs. 2.4c,d. The relatively weaker amplitude of SLP anomaly is possibly due to the very limited vertical resolution in the model stratosphere, so

that El Niño teleconnection through stratospheric pathway (e.g., [Bell et al. 2009](#)) is not well captured by the CM2.1 simulation. In addition, the relatively low horizontal resolution could also contribute to this weaker SLP response to ENSO in the NAE region ([Merkel and Latif 2002](#)).

The ENSO-related responses of the SLP over NA depend linearly on the strength of both the warm and cold SSTAs in the tropical Pacific (Fig. 2.8). Thus the non-linear response to the amplitude of the El Niño anomaly over the eastern NA, as noted by [Toniazzo and Scaife \(2006\)](#) on the basis of reanalysis data, is not evident in the CM2.1 simulation.

Over NA, the dipolar SLP response to ENSO is associated with a quadruple pattern of SAT anomalies in both observations and model (Figs. 2.7a,b), with warming over eastern Canada/Greenland and southwestern Asia/Northern Africa, and cooling over southeastern U.S. and northern Europe. These temperature signals bear a considerable resemblance to the negative NAO features as shown in Figs. 2.7e,f, and also compare well with those in previous observational studies (e.g., [Hurrell 1996](#)).

The model also reproduces the main features of the ENSO-related precipitation anomalies (Figs. 2.7c,d). Note in particular the wet band extending eastward from the California coast to southern Europe, as well as the dry conditions over northern Europe. This pattern of precipitation change resembles that associated with the NAO pattern (see Figs. 2.7g,h). The discrepancy between the observed and simulated precipitation signals over the west coast of Canada (Figs. 2.7c,d) is related to the prevalence of anomalous southerly (easterly) surface flow in that region, as inferred from the SLP patterns based on observational (model) data (Figs. 2.7a,b).

The above comparisons demonstrate a strong relationship between the surface climate anomalies accompanying ENSO and NAO, and the ability of CM2.1 in capturing this relationship. These findings lend credence to the model as a useful tool for investigating the mechanism for the teleconnection between ENSO and NAO.

## 2.4 Eddy-mean flow interaction in observed and simulated El Niño and La Niña events

### 2.4.1 Composites of mean flow and transient eddy intensity

Fig. 2.9 shows the composites of 250-hPa height and rms of bandpass-filtered 500-hPa height for El Niño (left panels) and La Niña (right panels), as computed using the NCEP/NCAR reanalysis (first row), 20thC reanalysis (second row) and CM2.1 output (third and fourth rows). The results for ‘pure’ El Niño years in the last row will be discussed later in this section. The composite pattern for 250-mb geopotential height (contours) during El Niño is characterized by a familiar wave train ([Horel and Wallace 1981](#)) over the Pacific-North American sector, with negative anomaly over the southeastern U.S. extending farther eastward to the NA. As inferred geostrophically from the height field, the NP jet stream is strengthened in the subtropics and weakened in the extratropics during the El Niño events. The corresponding rms of filtered 500-hPa height (shading in Fig. 2.9) is positively correlated with the strength of the westerly flow, i.e., eddy activity over the NP is enhanced at 30°N and suppressed at 50°N. Furthermore, the enhanced storm track activity extends across the NA, with an axis that is oriented from southwest to northeast. This feature is consistent with the poleward deflection of the storm trajectory at the jet exit ([Hoskins et al. 1983; Orlanski 1998](#)). Such eastward extension of the storm tracks beyond the site of strengthening of the time-mean flow has been well documented in many observational and model investigations (e.g., [Chang 1998; Seager et al. 2003; Lau et al. 2005; Seager et al. 2010a](#)). These studies note that the ENSO-induced enhancement of the vertical and horizontal wind shears in the vicinity of the jet stream could favor the development of transient disturbances, which propagate eastward and alter the pattern of eddy momentum fluxes farther downstream. The latent heat release

within the precipitation zone along the NA storm track may also contribute to the maintenance of the eddy activity in that region ([Hoskins and Valdes 1990](#)).

Due to asymmetries in the tropical diabatic forcing in the two opposing phases of ENSO ([Hoerling et al. 1997](#)), both the observed and simulated wave trains in the La Niña events are displaced westward (right panels of Fig. 2.9) relative to their counterpart in the El Niño events (left panels of Fig. 2.9). The shading patterns in the right panels of Fig. 2.9 indicate that the NP storm track is shifted poleward in La Niña events.

#### 2.4.2 Composites of **E** vectors and geopotential height tendencies

Fig. 2.10 shows the anomalous **E** vectors and  $\partial Z/\partial t$  (see definition in section 2.2.3) in the same layout as Fig. 2.9. The patterns of **E** in the El Niño composites show a continuous stream of eastward directed **E** arrows along the enhanced storm track axis near 35°N, extending from the central NP to the NA sector in both observations and model (left panels of Fig. 2.10). These **E** patterns indicate enhanced eastward group propagation of the transient eddies relative to the mean flow.

At the eastern end of the Pacific storm track, there is a strong divergence of the **E** vectors for El Niño composites, with northeastward-directed arrows north of the storm track, and southeastward arrows farther south. This pattern implies that the eddy momentum transport leads to acceleration of the westerly mean flow along the storm track (e.g., [Trenberth 1986](#)). The eddies therefore reinforce the subtropical westerly anomalies located south of the climatological jet, and maintain the deepened Aleutian low associated with El Niño.

Farther downstream over the western and central Atlantic, the anomalous **E** vectors are mostly directed poleward. This pattern is associated with divergence of **E** and zonal wind acceleration along 30°N, and convergence of **E** and zonal wind de-

celeration along  $50^{\circ}\text{N}$ . The cyclonic curvature of  $\mathbf{E}$  in midlatitude NA is indicative of northward wind acceleration (e.g., Trenberth 1986). The above configuration of zonal and meridional wind changes is conducive to negative height tendencies in the temperate zone of the NA.

The composite  $\partial Z/\partial t$  during El Niño winters (shading in left panels of Fig. 2.10) shows negative  $\partial Z/\partial t$  to the north of the equatorward shifted storm track, with one center located southeast of the Aleutian Islands, and another prominent feature extending from the east coast of North America to the midlatitude NA. The negative  $\partial Z/\partial t$  pattern over the NA are in accord with the above-mentioned divergence and curl of  $\mathbf{E}$  over that region. Comparison between the spatial pattern of  $Z$  (left panels of Fig. 2.9) and that of  $\partial Z/\partial t$  (left panels of Fig. 2.10) reveals that the transient eddies act to maintain the upper tropospheric negative height anomalies over the Aleutians and the southeastern North America. This finding is consistent with previous studies highlighting positive feedback between transient eddy vorticity flux and the extratropical atmospheric response to tropical SSTAs (Held et al. 1989; Branstator 1995; Kushnir et al. 2002; Orlanski 2005). The amplitude of these negative  $\partial Z/\partial t$  anomalies over the NP is lower in the CM2.1 simulation than in observations. The weaker eddy forcing in the model atmosphere may be related to the relatively low horizontal resolution of CM2.1.

Most interestingly, substantial eddy vorticity forcing is discernible over the NA region, with spatial extent and amplitude being larger than that over the NP region. This coherent eastward extension of eddy forcing from the NP sector has not yet been emphasized previously in the literature.

The pattern of simulated meridional eddy heat flux  $\overline{v'T'}$  at 850 hPa (Fig. 2.11) during El Niño winters is characterized by a prominent maximum along the enhanced storm track axis near  $35^{\circ}\text{N}$ , and extending from the central NP to the NA. This pattern indicates strong heat flux convergence poleward of the storm track axis, and

is associated with positive geopotential height tendency in the upper troposphere and negative tendency near the surface (Lau and Nath 1991). Although baroclinic effects of eddy heat flux tend to offset the barotropic effects of the eddy vorticity flux in the upper troposphere, the latter is stronger than the former by 50–80% (Lau and Nath 1991). Thus, the net eddy-induced  $\partial Z/\partial t$  at 250-hPa level can still be as large as 6–10 m per day over the midlatitude NA. The characteristic time scale of the eddy forcing, as estimated from the ratio of the amplitudes of the height anomaly (left panels of Fig. 2.9) to those of the  $\partial Z/\partial t$  (left panels of Fig. 2.10), is about 6 to 10 days over the western Atlantic. In the lower troposphere, due to the cooperation between the forcing associated with heat and vorticity fluxes (Lau and Holopainen 1984; Lau and Nath 1991), the eddy forcing could be even more efficient in producing the negative SLP tendencies at 30–50°N over NA.

Inspection of the La Niña composites in the right panels of Fig. 2.10 indicates that the eastward-directed  $\mathbf{E}$  vectors along the poleward shifted storm tracks, as simulated by CM2.1 (Fig. 2.10f), is not evident in the observations. However, there still exist some common features between observations and model. For example, westward-directed and convergent  $\mathbf{E}$  vectors are found along the belt of suppressed synoptic variability over the NP near 30°N, where zonal wind deceleration occurs. Moreover, the anticyclonic curvature of  $\mathbf{E}$  (and implied southward acceleration) over the central NP and North America is consistent with the local  $\partial Z/\partial t$  pattern. The positive center of  $\partial Z/\partial t$  over the central Pacific is displaced to the west of its El Niño counterpart, indicating that the transient feedback contributes to the maintenance of the asymmetric height response (cf. left and right panels of Fig. 2.9). This zone of positive  $\partial Z/\partial t$  also extends eastward to the western Atlantic, and is coincident with the positive height anomaly in that region during La Niña winters.

### 2.4.3 ENSO response after removal of NAO signal

In order to exclude the contribution of NAO-related eddy forcing from the model composites displayed in Figs. 2.9–2.10, the composites are also constructed using an alternate set of ‘pure’ ENSO years. Pure El Niño (La Niña) correspond to those episodes with DJF-mean Niño-3 index greater (less) than  $+1.0\sigma$  ( $-1.0\sigma$ ), but with only weak values of the FM-mean NAO index (i.e., between  $-0.2\sigma$  and  $+0.2\sigma$ ). There are 42 and 36 winters in the CM2.1 simulation satisfying the criteria for pure El Niño and pure La Niña, respectively. The results are displayed in the last row of Figs. 2.9–2.10.

Since the simulated geopotential height anomalies based on all El Niño and La Niña events are weak over the eastern Atlantic (see contours in Figs. 2.9e,f), it is thus not surprising that the changes of the geopotential height anomalies is not very dramatic, except for the slightly reduced amplitude over the western Atlantic (see contours in Figs. 2.9g,h). This negative geopotential height anomaly over the western NA maintains the southward shifted storm track over that site and locations farther east (see shading in Figs. 2.9g,h). Thus although the eddy-induced height tendency shows less penetration into the eastern NA, its amplitude over the western NA is still substantial and comparable to those in Figs. 2.10e,f. This result confirms that ENSO influences over the western NA are substantial even after the removal of the NAO-related contributions. Hence, we conclude that ENSO can influence the storm track and transient eddy forcing over the western NA region irrespective of the strength of NAO.

#### 2.4.4 Storm track variations over North America and its relationship to both ENSO and NAO

The spatial distributions of storm track intensity (shading in Fig. 2.9) show distinct meridional shifts in the zone of maximum transient eddy activity over southern U.S./Gulf of Mexico and the Pacific Northwest during ENSO events. These findings are consistent with the recent results of Seager et al. (2010a), who show that waves propagate along a more southern path towards southwestern North America during El Niño, while they take a more northward route towards the Pacific Northwest during La Niña. To depict such interannual variations of the site of eddy activity over the North American sector, we perform an EOF analysis of the rms of filtered 500-hPa height field over the region 15°–60°N, 130°–70°W (see boxed area in Fig. 2.9) in late winter season for both observations and model.

The first or second EOF mode based on all three datasets examined here (Fig. 2.12) is dominated by a center over northwestern North America, and another center of the opposite polarity over southern U.S. and Gulf of Mexico. The patterns in Fig. 2.12 compare well with the El Niño composites of rms amplitudes over North America (shading in the left panels of Fig. 2.9).

The temporal coefficients of the EOF patterns presented in Fig. 2.12 represent the variations in the strength and location of the storm path over North America. We shall henceforth refer to this time series as the ‘storm path index’ (SPI). The temporal correlation coefficients among the SPI, ENSO and NAO indices are displayed in Table 2.2. It is evident that the correlation coefficients between SPI and both ENSO and NAO indices (see bottom two rows of Table 2.2) are not only highly significant ( $p$  value  $< 0.05$ ) for each dataset, but also much higher than the linear correlation between ENSO and NAO indices (see top row of Table 2.2). This finding signifies that the storm-track anomaly over North America plays a crucial role in the linkage between ENSO and NAO. In view of the three-way relationship between

SPI, ENSO and NAO, the partial correlation coefficient (e.g., Spiegel 1988, see the Appendix A for details) between ENSO and NAO is computed using CM2.1 data, with the contribution from SPI being removed from both ENSO and NAO. This procedure yields a partial correlation coefficient of 0.06, which is noticeably smaller than the corresponding value (i.e.,  $-0.2$ , with a  $p$  value  $< 0.01$ , see upper right entry of Table 2.2) as obtained without removal of SPI contribution. This partial correlation analysis suggests that ENSO would have almost no impact on NAO if the storm-track variability over North America were removed.

## 2.5 Circulation patterns and SST environment associated with various combinations of ENSO and NAO phases

The covariability of ENSO and NAO events can be summarized by the scatter graph shown in Fig. 2.13, in which the data for each winter season in the 2000-yr simulation are indicated by a dot, with abscissa and ordinate corresponding to the normalized FM-mean NAO index and DJF-mean Niño-3 index, respectively. Despite the weak (but nonetheless statistically significant) overall correlation of  $-0.20$  between the ENSO and NAO indices, we have presented ample evidence in the previous sections on the preferred occurrence of negative NAO events during El Niño, and positive NAO events during La Niña. It is hence of interest to study in more detail the circulation characteristics in those winter seasons with strong positive indices in ENSO and strong negative indices in NAO (see red dots in top-left quadrant of Fig. 2.13; hereafter labeled as ENSO+/NAO-), as well as strong negative indices in ENSO and strong positive indices in NAO (ENSO-/NAO+; see red dots in bottom-right quadrant). The threshold for identifying strong indices is  $1\sigma$  from normal. These

two subgroups of winters conform to the ENSO/NAO relationship documented in the previous sections, and are referred as the ‘strong combinations’. It is also of interest to contrast the behavior in these ‘strong combinations’ against that in the winters with strong positive ENSO and NAO (ENSO+/NAO+; blue dots in top-right quadrant of Fig. 2.13), or with strong negative NAO and ENSO (ENSO-/NAO-; blue dots in bottom-left quadrant). The latter two subgroups do not conform to the ENSO/NAO relationship noted earlier, and are referred as the ‘weak combinations’. In accord with the PDF distributions in Fig. 2.6b, the number of winters in the ‘weak combinations’ is considerably fewer than that in the ‘strong combinations’ (see population counts shown at the four corners of Fig. 2.13). For example, in late winter it is 2–3 times more likely to have a strong negative NAO during El Niño events than a strong positive NAO. Similarly, a strong positive NAO is 2–3 times more likely to occur than a strong negative NAO during La Niña events.

Our main goal in this section is to contrast the spatial patterns of the circulation and storm track activity occurring in each of the four combinations described above, and to study the possible factors contributing to the differences among the composites based on these categories. The limited observational record precludes a parallel analysis of the events occurring in the real climate system.

### 2.5.1 Mean flow and transient eddy intensity in the ‘strong’ and ‘weak’ combinations

Fig. 2.14 presents composite geopotential height anomalies and rms of filtered 500-hPa height fields, as constructed based on the four types of combinations among the ENSO and NAO indices. As expected from the definition of the ENSO+/NAO- and ENSO-/NAO+ categories, the 250-hPa height anomaly patterns for the ‘strong combinations’ (Figs. 2.14a,d) exhibit a distinct zonally symmetric character, with out-of-phase variations between anomalies at 40°N and those in the Arctic zone. As

compared to the composites based on the ENSO index (Figs. 2.9e,f), the features in Figs. 2.14a,d are extended much more eastward to the eastern Atlantic and Europe. The patterns in Figs. 2.14a,d are also similar to the height anomaly pattern during and after the mature phase of the seesaw between Aleutian and Icelandic lows, as presented by Honda et al. (2001, see their Figs. 6e–g). The rms of filtered 500-hPa for the ‘strong combinations’ also exhibit elongated positive anomalies along 35°N in ENSO+/NAO– (Fig. 2.14a) and 60°N in ENSO-/NAO+ (Fig. 2.14d). The zonally extended nature of the rms patterns in these panels suggests a possible linkage between the Pacific and Atlantic storm tracks in those winters.

In contrast, the height patterns in the ‘weak combinations’ (Figs. 2.14b,c) are characterized by a much stronger degree of zonal asymmetry. The associated storm track activities appear to be organized on a smaller regional scale, i.e., over the NP and NA basins separately. It is also noticeable that the height anomaly center over the NP in the ‘strong combinations’ is stronger as compared to the corresponding ‘weak combinations’.

The relatively larger number of ‘strong combinations’ events suggests a preference for the circulation anomalies to be more zonally symmetric during ENSO events. Seager et al. (2003) have also noted that ENSO forcing exerts a significant impact on the zonally symmetric extratropical circulation in winter and spring.

## 2.5.2 Centers of warming in the tropical Pacific in the ‘strong’ and ‘weak’ combinations

The question that may be raised, then, is how could the transient disturbances maintain their intensity near the decay region at the eastern end of the Pacific storm track during the winters with ‘strong combinations’. Fig. 2.15 shows the (ENSO+/NAO–) minus (ENSO+/NAO+) composites of FMA-mean SST and precipitation in CM2.1.

April is included in the composite in view of the fact that the tropical Atlantic exhibits a delayed warming relative to that in the Pacific.

In ENSO+/NAO– winters, the warm SSTA in the eastern equatorial Pacific is significantly stronger than that in ENSO+/NAO+ winters (Fig. 2.15a). The precipitation (and the accompanying condensational heating) in ENSO+/NAO– winters is also relatively stronger over the central and eastern Pacific (Fig. 2.15b). Thus the baroclinicity near the surface and the lower troposphere are expected to strengthen over the central and eastern Pacific in ENSO+/NAO– winters. Similar increased baroclinicity in the mideastern Pacific has been noted in [Orlanski \(2005\)](#) for El Niño winters. He argues that the reduced amplitude of the eastern Pacific ridge in El Niño winters is associated with the generation or regeneration of baroclinic waves in the mideastern Pacific, which tend to break cyclonically and produce a trough tendency. Our study indicates that the enhanced subtropical baroclinicity over the central and eastern tropical Pacific could be a possible explanation for the eastward penetration of the NP storm track to the southern U.S. in ENSO+/NAO– winters.

The east-west dipolar pattern of the SSTAs in Fig. 2.15a resembles the second EOF pattern of the tropical Pacific SST (not shown). The averaged value of the normalized temporal coefficients of this second EOF are 1.21 and 0.65 for the ENSO+/NAO– and ENSO+/NAO+ subgroups, respectively. The significant difference between these two composite values of the EOF coefficients ( $p$  value = 0.02) suggests that the El Niño events in ENSO+/NAO– winters are characterized by enhanced SST warming in the eastern equatorial Pacific, whereas ENSO+/NAO+ winters are associated with warming in the central Pacific.

Fig. 2.15b shows stronger positive precipitation anomalies near 30°N over the NA in ENSO+/NAO– than that in ENSO+/NAO+. The enhanced latent heat release in this site could lead to stronger growth of the disturbances along the equatorward shifted storm track in the ENSO+/NAO– cases. [Hoskins and Valdes \(1990\)](#) have also

noted the importance of diabatic heating in maintaining the low-level baroclinicity, which in turn supports the development of transient eddies.

## 2.6 Summary and discussion

The mechanisms contributing to the tropospheric teleconnection between ENSO and NAO are examined based on a multi-century integration with a coupled GCM. The model captures well the observed features of both ENSO and NAO responses at the surface in late winter. The relationship between ENSO and NAO has a distinct seasonal dependence in both observations and model. Negative NAO phase occurs more frequently in late winter during El Niño events, and positive NAO phase in La Niña events. The model output exhibits a 1-month delay in the emergence of the NAO signals. This discrepancy may be related to the postponement of the ENSO mature phase in the simulation.

We investigated the mechanism of this ENSO/NAO relationship by examining the role of transient eddy forcing over the NAE region. The negative 250-hPa height anomaly over the NP is part of a stationary Rossby wave-train forced by SST changes in the tropical Pacific during El Niño events. The strengthened zonal flows on the equatorward flank of this height anomaly enhance the development of synoptic-scale disturbances. In those El Niño events with strong SST warming in the equatorial Pacific, the storm-track disturbances remain active over the eastern portion of the subtropical NP due to the strengthened meridional SST gradient over that site. As these transient fluctuations reach the Atlantic storm-track region, they induce negative  $\partial Z/\partial t$  over the region corresponding to the southern lobe of NAO. Many of the model results are verified by two independent reanalysis datasets.

The characteristic patterns of storm track variability over North America associated with ENSO are themselves the principal modes of storm-track variability in

both NCEP/NCAR reanalysis and CM2.1. The corresponding principal component is significantly correlated with both ENSO and NAO indices in each dataset. This result suggests the role of the storm-track anomaly over the North America in the linkage between ENSO and NAO.

The following processes may contribute to the seasonal dependence of the ENSO/NAO relationship documented in this study:

- Aleutian low and Icelandic low seesaw

The time evolution of the regression coefficients of SLP anomalies versus ENSO (Fig. 2.4) is consistent with the formation of the SLP seesaw between Aleutian Low (AL) and Icelandic Low (IL), as described by [Honda et al. \(2001\)](#). In particular, their results show that the out-of-phase relationship between the intensity of AL and IL during the late winter (February to mid-March) is preceded by weak in-phase association during early and middle winter (November–December). This seesaw is initiated by the amplification of the AL anomalies due to wave-activity accumulation in early and middle winter. Then the propagation of a Rossby wave train across North America leads to the formation of stationary anomalies in the vicinity of IL. [Honda et al. \(2001\)](#) focused on the role of Rossby wave propagation in the formation of the northern lobe of the NAO. Our study emphasizes the contribution of transient eddy forcing to the circulation changes along the southern lobe of the NAO.

- Delay in tropical atmospheric response to ENSO

[Kumar and Hoerling \(2003\)](#) propose that the lagged atmospheric response to tropical Pacific SSTAs can be attributed to the seasonality of the total SST field in the tropical eastern Pacific. When SSTAs associated with El Niño cycle are superimposed on the seasonal cycle of climatological SST, the total SST reaches a maximum in early spring, 1–3 months later than the peak of SSTAs. These

authors argued that it is the total, rather than anomalous, SST that forces the tropical convective rainfall in the eastern Pacific, which in turn generates the extratropical wave train.

- Influence of extratropical SSTAs over NA

It has been demonstrated that fluctuations in surface heat fluxes and Ekman transport driven by atmospheric variability are important contributors to extratropical SST variability (e.g., [Lau and Nath 2001](#); [Alexander et al. 2002](#); [Alexander and Scott 2002, 2008](#)). The nature of atmospheric response to extratropical SSTAs is not yet fully understood, largely due to the high-level internal variability of the midlatitude atmosphere, which tends to obscure any direct effect of the underlying SSTAs. Although the atmospheric response to midlatitude SST forcing is weak, it is not negligible. Hence extratropical air–sea feedbacks may play a role in the characteristics of the local atmospheric variability, especially during the transition seasons when the atmospheric internal variability is reduced (see review by [Kushnir et al. 2002](#), and references therein). As shown in Fig. 2.15a, a tripolar pattern of NA SSTAs (e.g., [Deser and Blackmon 1993](#); [Kushnir 1994](#)) is discernible in the ENSO+/NAO– minus ENSO+/NAO+ composites for the FMA(1) period, with a cold anomaly centered at 30°N being straddled by warm anomalies to the north and south. The air–sea coupling associated with this characteristic SST pattern may exert considerable influences on the prevalent atmospheric circulation patterns over the NA. More study is needed to clarify the processes linking the tripolar SST pattern to NAO variability.

- Stratosphere–troposphere coupling

It has been noted that strong El Niño events are associated with weakening of the stratospheric polar vortex ([Labitzke and van Loon 1999](#); [Taguchi and Hart-](#)

mann 2006), which in turn can affect the late winter climate in NAE through downward propagation (e.g., Baldwin and Dunkerton 2001; Sassi et al. 2004; García-Herrera et al. 2006; Manzini et al. 2006). Due to the low vertical resolution of the model stratosphere in CM2.1 (see section 2.2.1), the El Niño effect on the simulated extratropical stratosphere is very weak. The geopotential height anomaly associated with El Niño events at 50 hPa (Fig. 2.16) is about 3–4 times weaker than that of the corresponding signal based on observations and other simulations with an adequate representation of upper atmosphere (see Fig. 3 in Cagnazzo and Manzini 2009). In the CM2.1 simulation, weak easterly anomaly (less than  $-1 \text{ m s}^{-1}$ ) in the zonal mean zonal wind at  $60^\circ\text{N}$  appears almost simultaneously at all pressure levels in March and April (Fig. 2.16). This pattern is quite different from those in observations and other GCM simulations (see Fig. 4 in Manzini et al. 2006 and Fig. 4 in Ineson and Scaife 2009), with easterly anomalies (on the order of  $-10 \text{ m s}^{-1}$ ) propagating downward from the upper stratosphere in early winter to the lower stratosphere and troposphere in late winter. The feeble stratosphere signals in the CM2.1 experiment might partially explain the reduced north-south SLP gradient across the NA, and also the 2-month delay in the occurrence of the positive anomalies in the northern lobe of the NAO pattern relative to the negative anomalies in the southern lobe (see Fig. 2.4d).

It would be worthwhile to explore the importance of stratospheric processes in the ENSO/NAO relationship using a GCM with a more realistic upper atmosphere. Recently, a new GFDL climate model (CM3) has been developed, with altogether 48 vertical levels and a model top at 0.01 hPa (Donner et al. 2011). The correlation between the ENSO and NAO indices based on output from this model is noticeably stronger than that inferred from the CM2.1 simulation. Diagnosis of the stratosphere-

troposphere coupling accompanying ENSO events in this new model will be presented in chapter 5.

Finally, it should be borne in mind that this study focuses on the seasonally averaged characteristics of the transient eddy forcing associated with the ENSO cycle. The zonally extended pattern of the rms of bandpass filtered geopotential height (see shading in Fig. 2.9) from NP to NA is suggestive of strengthened linkages between the Pacific and Atlantic storm tracks during ENSO events. However, such seasonal statistics by themselves don't provide explicit evidence on the propagation of individual eddies from NP to NA. Moreover, the NAO variability is related to the behavior of large-scale persistent and recurrent flow patterns, also known as weather regimes (e.g., Vautard 1990; Cassou et al. 2004, 2005; Straus et al. 2007), with typical time scales on the order of only 10 days (Feldstein 2000). The seasonal results shown in this chapter hence represent averages over several episodes of shorter durations. It is hence of interest to examine the nature of, and the dynamical processes associated with, these individual episodes in greater detail. In chapter 3, we shall analyze the daily data in the 2000-yr simulation of CM2.1, so as to illustrate the detailed spatio-temporal evolution of various meteorological phenomena associated with persistent anomalous circulation episodes in the North Pacific-North American-North Atlantic sector. Evidence will be shown on the downstream development of the wave packet in the course of these persistent episodes. The effects of the subsequent barotropic forcing due to synoptic-scale eddies embedded in the wave packets on the formation of the more slowly-varying flow pattern over NA will also be examined.

Table 2.1: List of observed El Niño and La Niña events selected using the DJF-mean Niño-3 index. The year of initiation of the selected ENSO event is designated as year(0); the following year is referred as year(1). The listed year correspond to year(1). Years used for the composites in the NCEP/NCAR reanalysis dataset are underlined.

El Niño events									
1897	1900	1903	1912	1919	1926	1931	1941	<u>1958</u>	<u>1966</u>
<u>1973</u>	1977	<u>1983</u>	<u>1987</u>	<u>1992</u>	1995	<u>1998</u>	<u>2003</u>	<u>2007</u>	<u>2010*</u>
La Niña events									
1893	1894	1909	1910	1911	1917	1918	1923	1925	1934
1943	<u>1950</u>	<u>1956</u>	<u>1968</u>	<u>1971</u>	<u>1974</u>	<u>1976</u>	<u>1989</u>	<u>2000</u>	<u>2008</u>

\*Recent El Niño event not covered by the 20thC reanalysis dataset.

Table 2.2: Temporal correlation coefficients among indices for the DJF-mean Niño-3, the late winter NAO, and the late winter storm path index, as computed using the NCEP/NCAR reanalysis, 20thC reanalysis and CM2.1 simulation. The storm path index (SPI) is defined as the temporal coefficients of the EOF patterns presented in Fig. 2.12, See text in section 2.4.4 for details. Values exceeding the 95% significance level are given in bold. The  $p$  values as estimated by applying a two-tailed Student's  $t$  test are given in parentheses. Degrees of freedom is estimated following that outlined in footnote 1 of [Lau and Nath \(2004\)](#). Specifically, the spectra for the simulated and observed ENSO indices [Fig. 19 of [Wittenberg et al. 2006](#)] suggest that typical period of an ENSO “cycle” in both simulated and observed system is approximately 4 yr. Given that there are 2 degrees of freedom in each ENSO, we assume that 2 yr of data are required to yield 1 degree of freedom.

	NCEP/NCAR	20thC	CM2.1
Niño-3 vs NAO ( $p$ value)	-0.15 (0.4)	-0.19 (0.14)	<b>-0.20</b> (< 0.01)
SPI vs Niño-3 ( $p$ value)	<b>0.61</b> (< 0.01)	<b>0.53</b> (< 0.01)	<b>0.54</b> (< 0.01)
SPI vs NAO ( $p$ value)	<b>-0.38</b> (< 0.01)	<b>-0.27</b> (0.04)	<b>-0.46</b> (< 0.01)

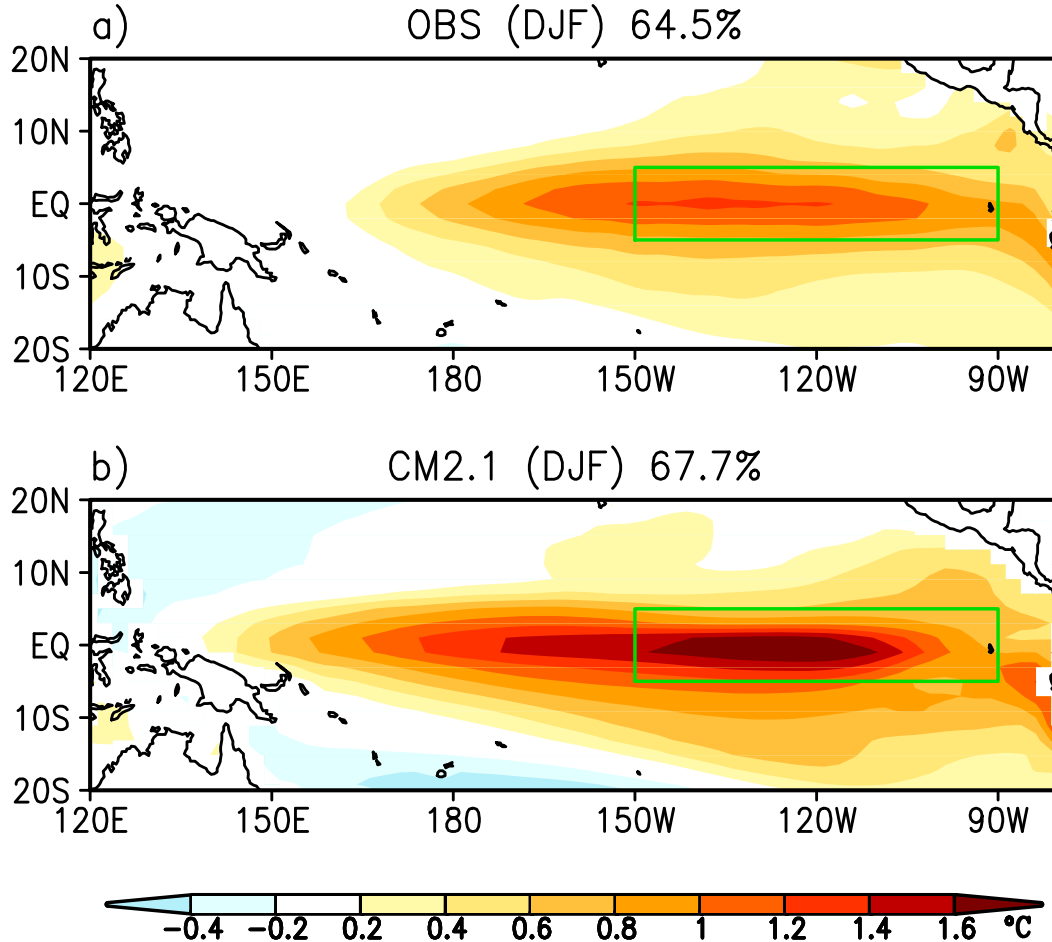


Figure 2.1: Spatial patterns of the leading empirical orthogonal function (EOF) of DJF-mean sea surface temperature anomalies (SSTAs) over the tropical Pacific based on the (a) NOAA ERSST V3 dataset for the 1948–2010 period and (b) CM2.1 simulation. The patterns show the regression coefficients of DJF-mean SST versus the standardized temporal coefficients of the EOF. Units:  $^{\circ}\text{C}$ . These observed and simulated EOF modes account for 64.5 and 67.7% of the total variance, respectively. The rectangular outline depicts the Niño-3 region ( $5^{\circ}\text{S}$ – $5^{\circ}\text{N}$ ,  $150^{\circ}$ – $90^{\circ}\text{W}$ ). The observed and simulated standard deviations of Niño-3 SST are  $0.97^{\circ}\text{C}$  and  $1.22^{\circ}\text{C}$ , respectively.

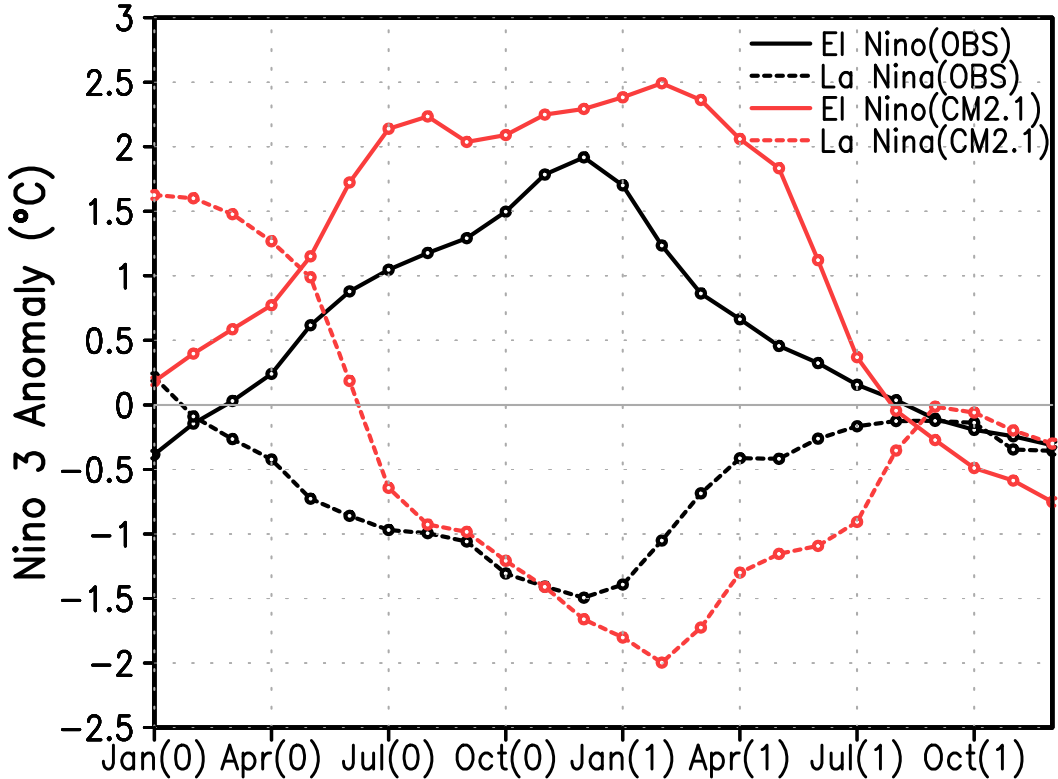


Figure 2.2: Composite monthly evolution of the Niño-3 SSTAs for El Niño (black solid curve) and La Niña (black dashed curve) events in observations, and El Niño (red solid curve) and La Niña (red dashed curve) events in the CM2.1 simulation. The abscissa represents a 24-month period from January of year(0) to December of year(1). A specific month in this period is identified by a label consisting of the first three letters of that month, followed by the year indicator (0 or 1) in parentheses. For instance, Dec(0) refers to the month of December in year(0).

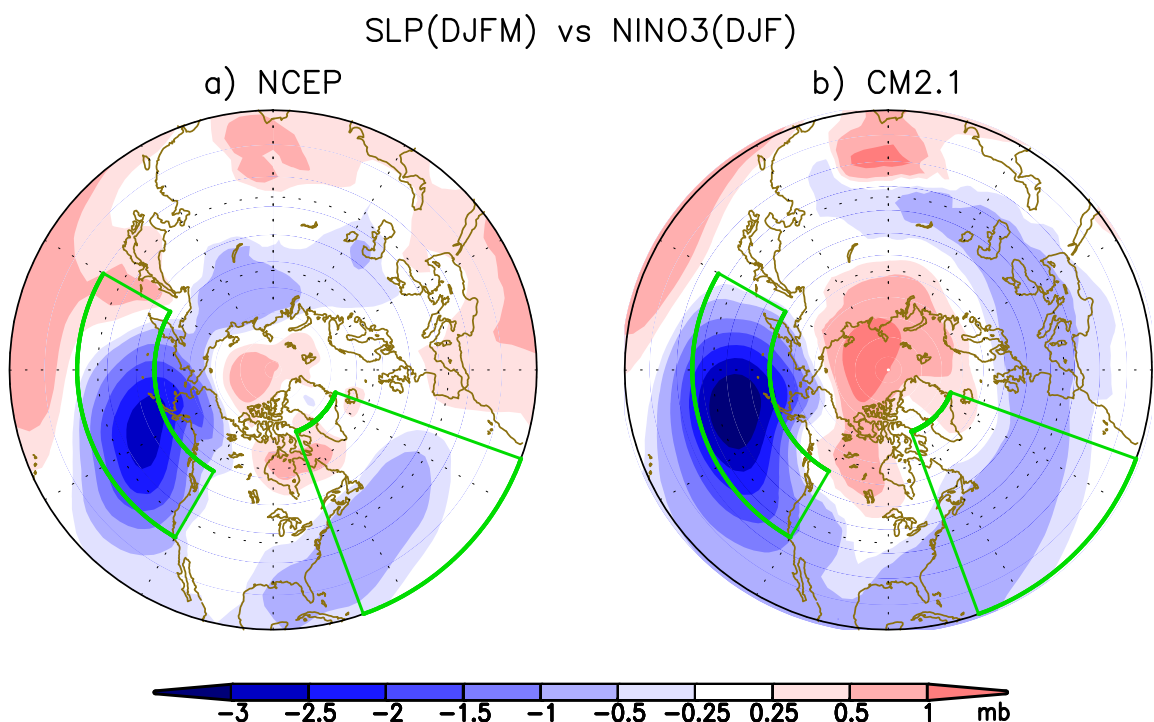


Figure 2.3: Distributions of the regression coefficients of DJFM-mean SLP versus the standardized DJF-mean Niño-3 index based on the (a) NCEP/NCAR reanalysis and (b) CM2.1 simulation. Units: mb. Latitude and longitude ranges used for computing the zonal and meridional averages over the North Pacific (NP) and North Atlantic (NA) sectors (see Fig. 2.4) are indicated by green borders.

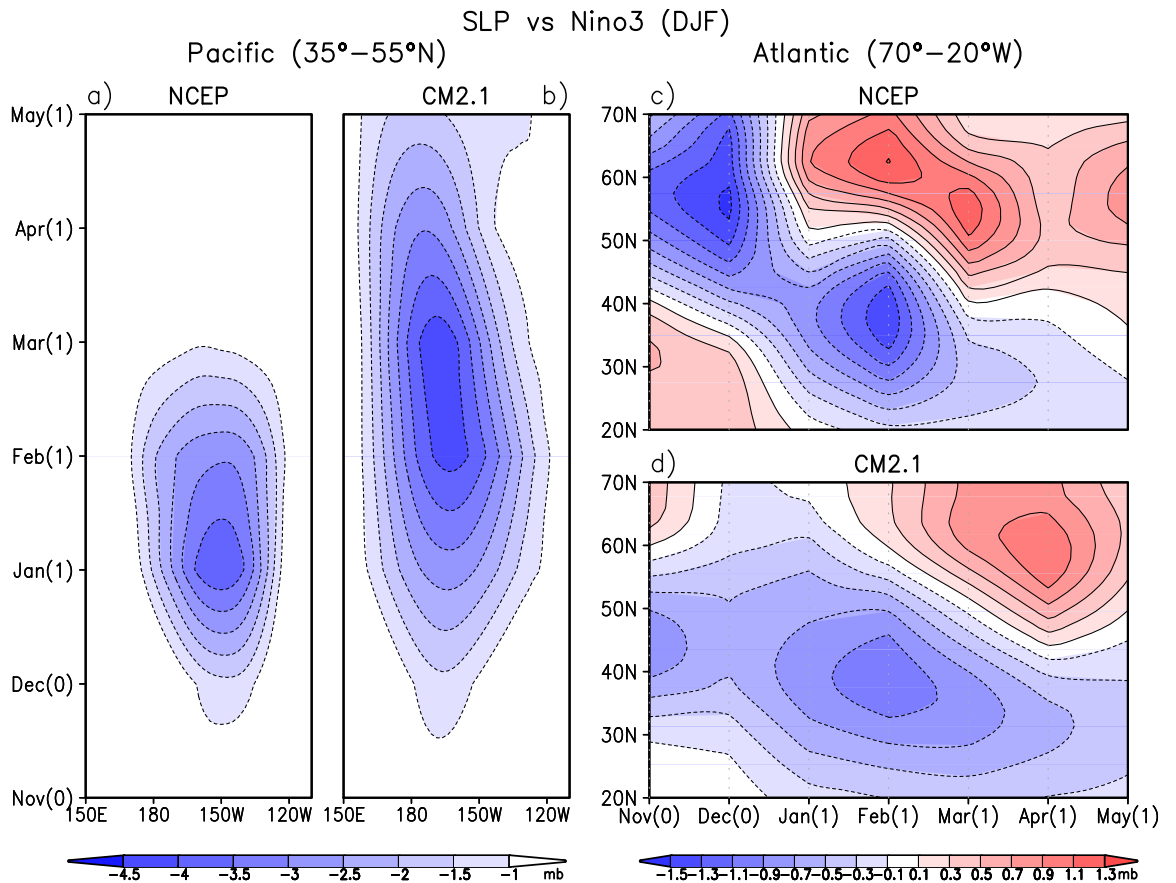


Figure 2.4: (a,b) Time-longitude and (c,d) time-latitude variations of the regression coefficients of SLP anomalies versus standardized DJF-mean Niño-3 index, as computed using the (a,c) NCEP/NCAR reanalysis and (b,d) CM2.1 simulation. SLP anomalies are averaged meridionally over  $35^{\circ}$ – $55^{\circ}$ N zone in the NP sector (a,b) and zonally over  $70^{\circ}$ – $20^{\circ}$ W zone in the NA sector (c,d), see green outlines in Fig. 2.3. Contour interval are 0.5 mb for (a)–(b) and 0.2 mb for (c)–(d).

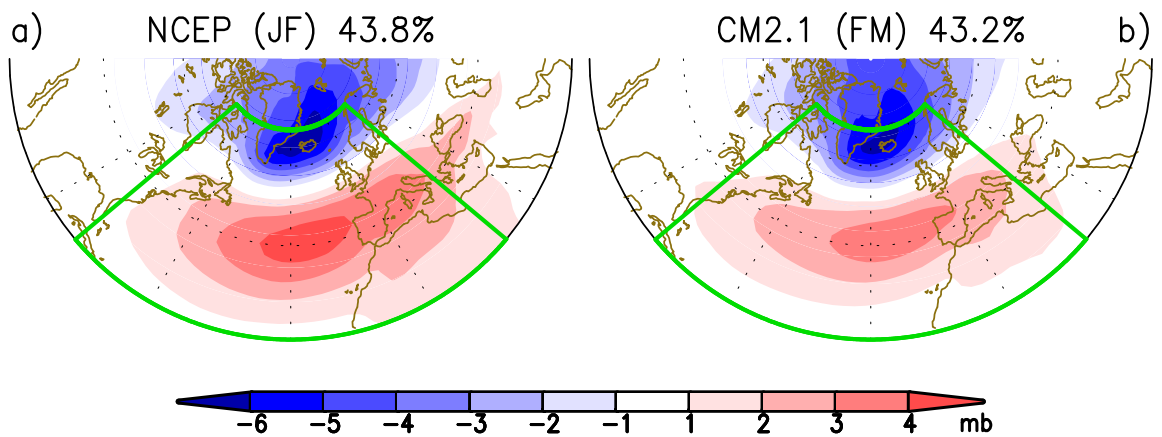


Figure 2.5: The spatial pattern of the leading EOF of seasonal mean SLP over the NA sector ( $20^{\circ}$ – $70^{\circ}$ N,  $80^{\circ}$ W– $20^{\circ}$ E, see green border), based on the (a) NCEP/NCAR reanalysis for the JF-mean season and (b) CM2.1 simulation for the FM-mean season. The patterns show the regression coefficients of seasonal mean SLP versus the standardized temporal coefficients of the EOF. Units: mb. The observed and simulated EOF modes account for 43.8 and 43.2% of the total variance, respectively.

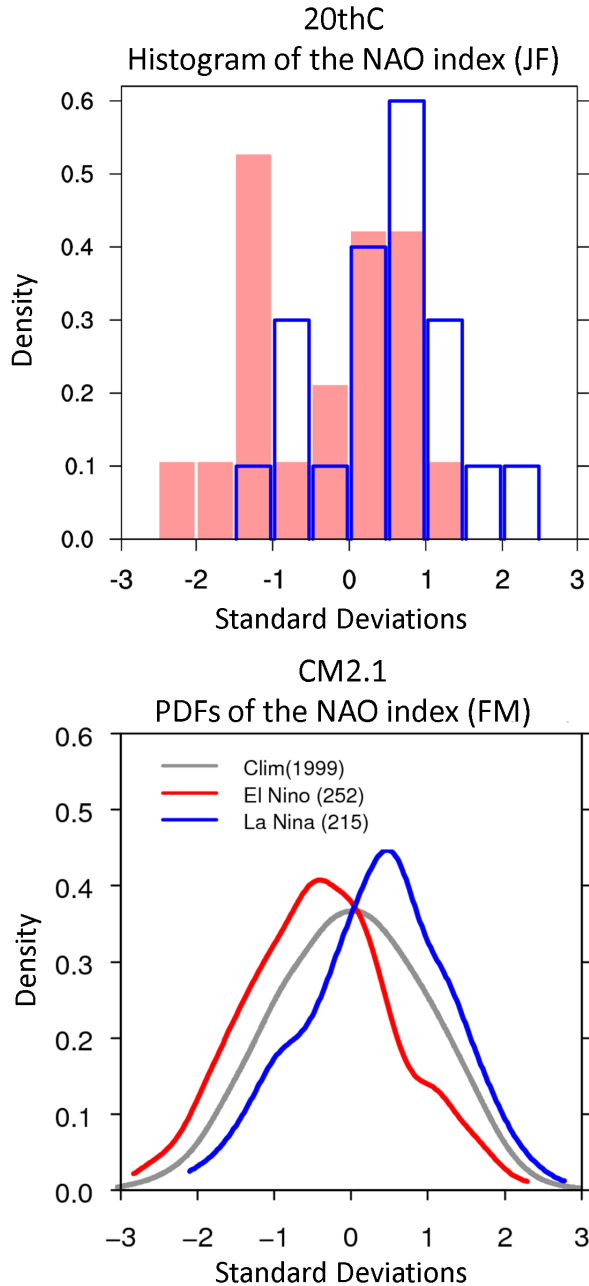


Figure 2.6: (a) Density histogram of the normalized JF-mean NAO indices for the selected El Niño winters (red-filled columns) and La Niña winters (blue unfilled columns) listed in Table 2.1 for the 1891–2008 period, as constructed based on the 20thC reanalysis. (b) Probability density functions (PDFs) of the normalized FM-mean NAO indices for the selected El Niño winters (red curve), La Niña winters (blue curve) and all winters (gray curve) in the CM2.1 simulation. The PDFs are obtained by a kernel density estimation.

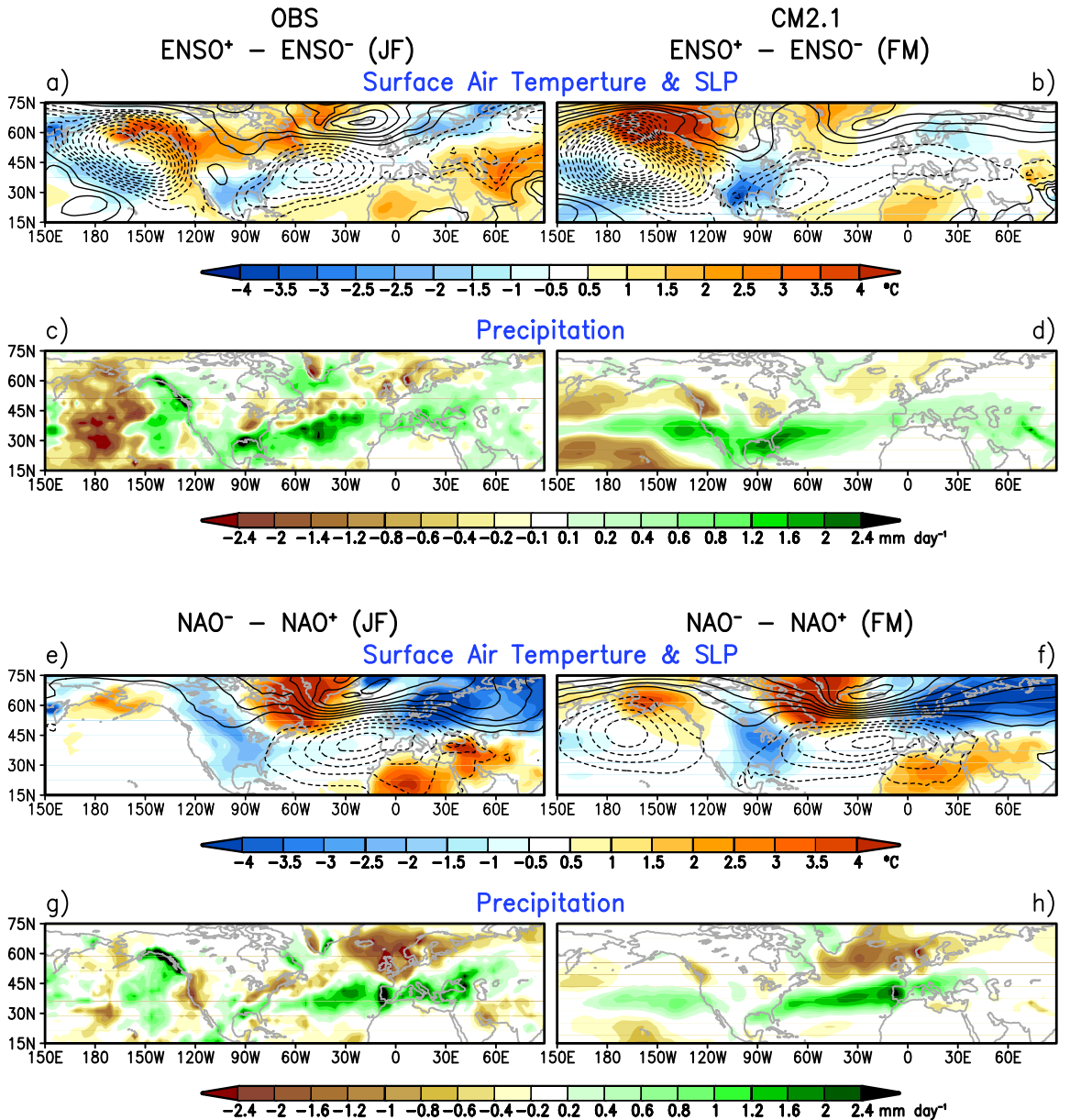


Figure 2.7: Horizontal distributions of (a–d) El Niño minus La Niña composites and (e–h) NAO<sup>−</sup> minus NAO<sup>+</sup> composites. The displayed fields are (first and third rows) surface air temperature (SAT; shading) and SLP [contours; intervals in panels (a),(b) and (e),(f) are 1 and 2 mb, respectively], and (second and fourth rows) precipitation. Observations for the JF(1) period are shown in the left panels. CM2.1 data for the FM(1) period are shown in the right panels. The observational results use the NCEP/NCAR reanalysis for SLP and SAT fields, and the GPCP dataset for precipitation. Observed (simulated) NAO $\pm$  events are defined when the normalized JF(FM)-mean NAO indices exceed one standard deviation from normal.

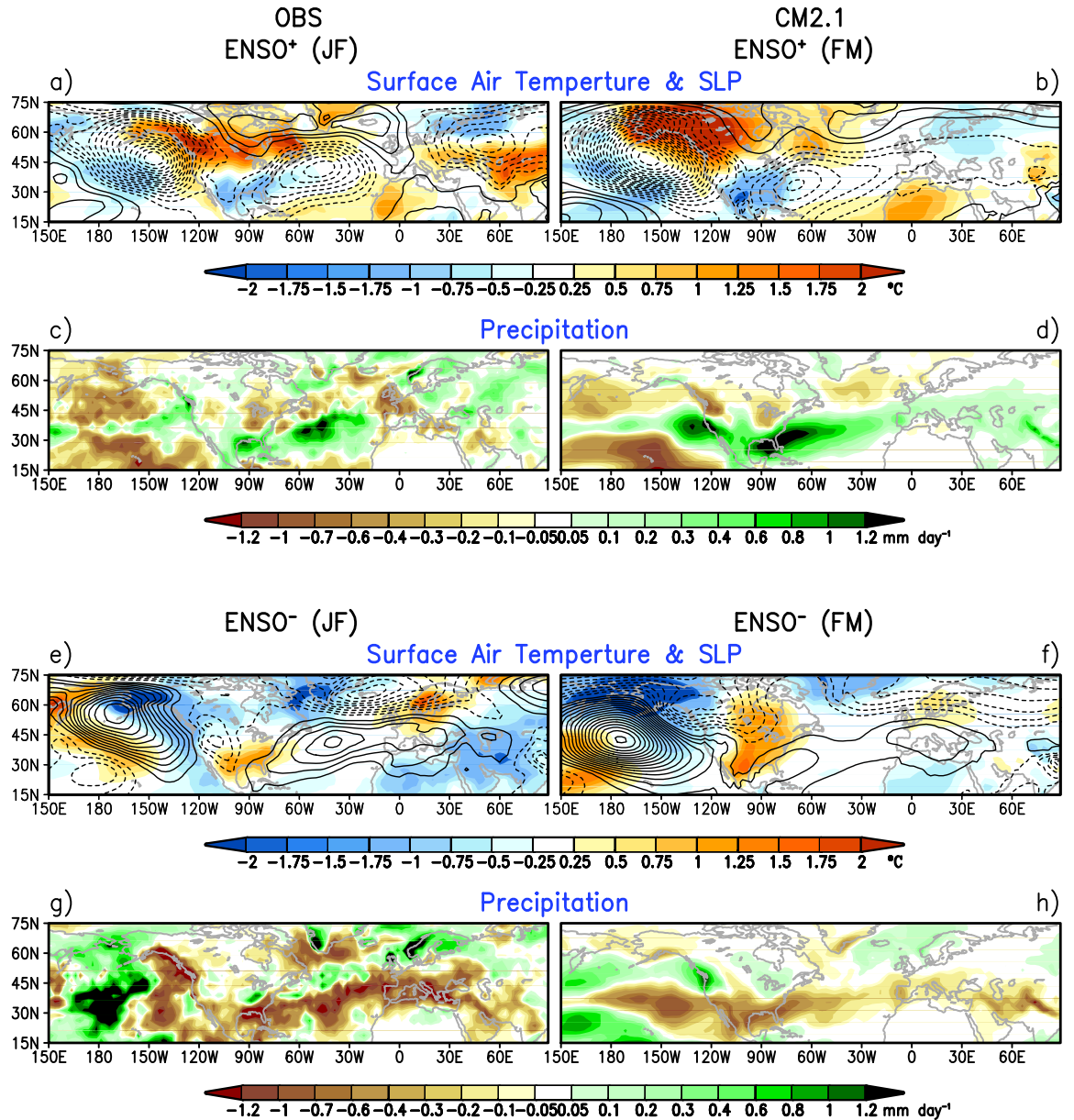


Figure 2.8: As in Fig. 2.7, but for El Niño (a–d) and La Niña (e–f) composites. Contour intervals: 0.5 mb.

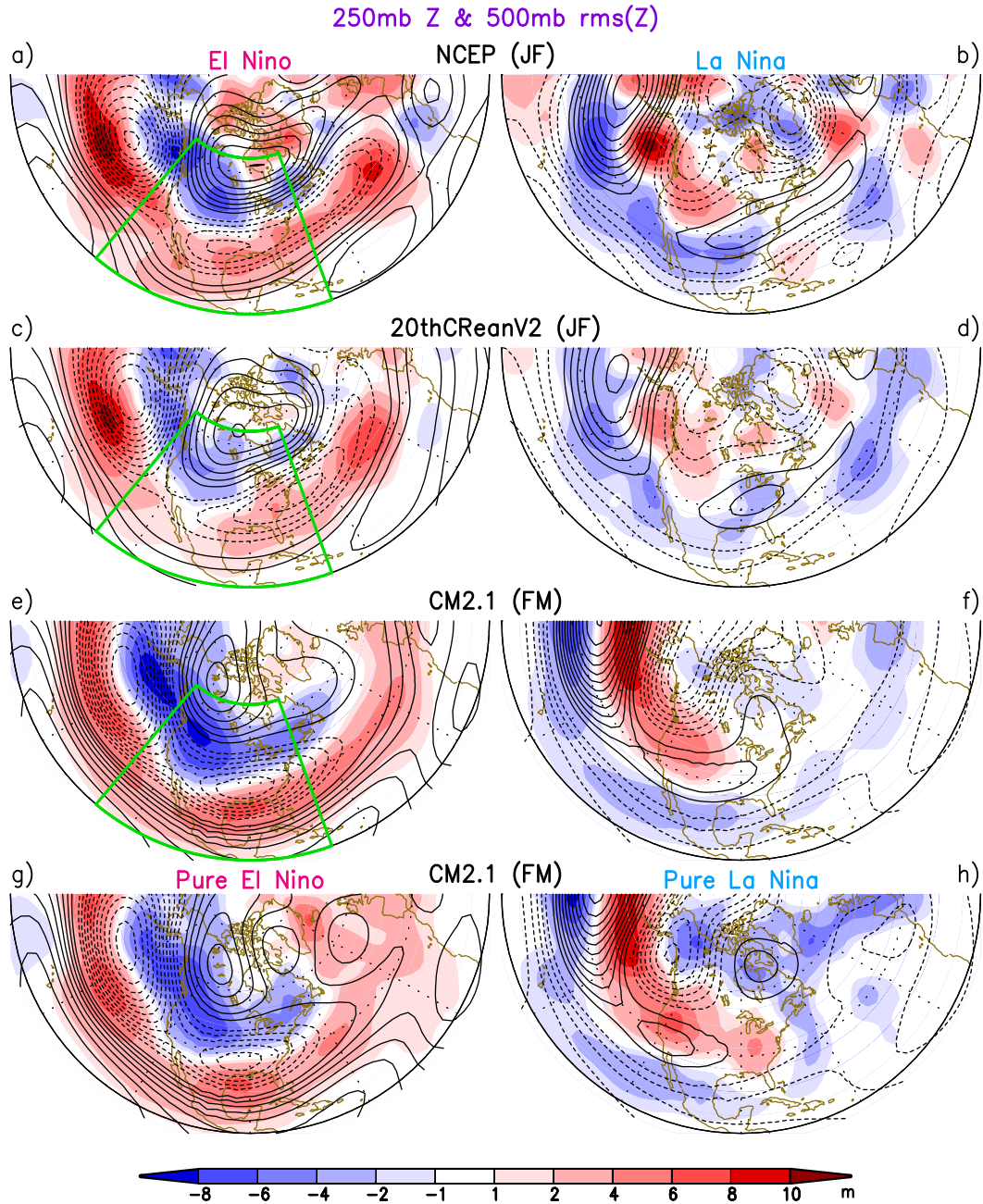


Figure 2.9: Horizontal distributions of El Niño (left panels) and La Niña (right panels) composites of the 250-hPa geopotential height (contours, interval: 10 m) and rms of the 2–10 d bandpass-filtered 500-hPa geopotential height (shading, see scale bar at bottom). Results are shown for the NCEP/NCAR reanalysis (first row) and 20thC reanalysis (second row) for the JF(1) period, and for the CM2.1 simulation for the FM(1) period (third row). Results in the fourth row show composites over pure El Niño (La Niña) events, which correspond to those episodes with DJF-mean Niño-3 index greater (less) than  $+1.0\sigma$  ( $-1.0\sigma$ ), but with only weak values of the FM-mean NAO index (i.e., between  $-0.2\sigma$  and  $+0.2\sigma$ ). The outermost latitude circle represents 15°N. Regions for the EOF of filtered 500-mb height are indicated by green borders in (a), (c) and (e).

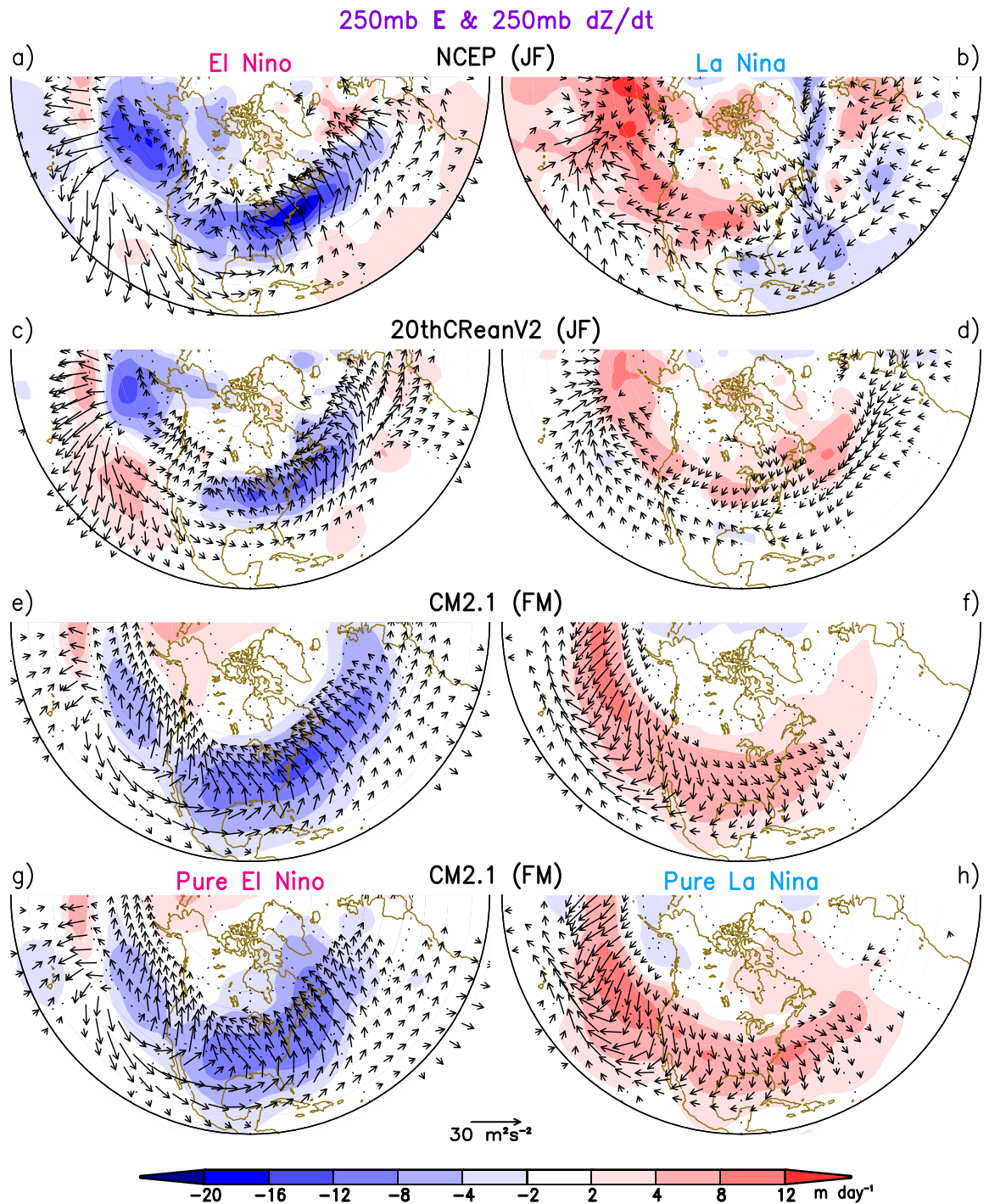


Figure 2.10: As in Fig. 2.9, but for 250-hPa extended Eliassen-Palm **E** vectors (arrows, see scale at bottom) and eddy-induced height tendencies (shading, see scale bar at bottom). **E** vectors with magnitude smaller than  $3 \text{ m}^2 \text{s}^{-2}$  are not plotted.

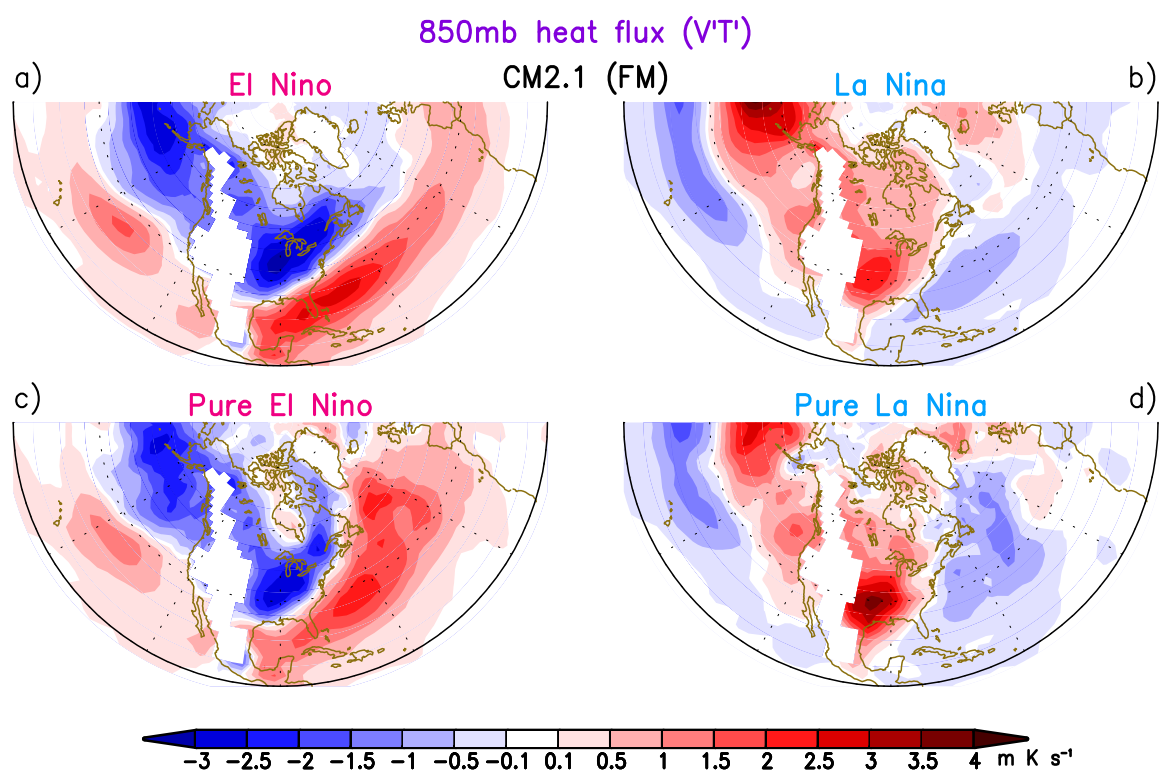


Figure 2.11: As in Fig. 2.9e-h, but for 850-hPa meridional eddy heat flux (shadings, see scale bar at bottom).

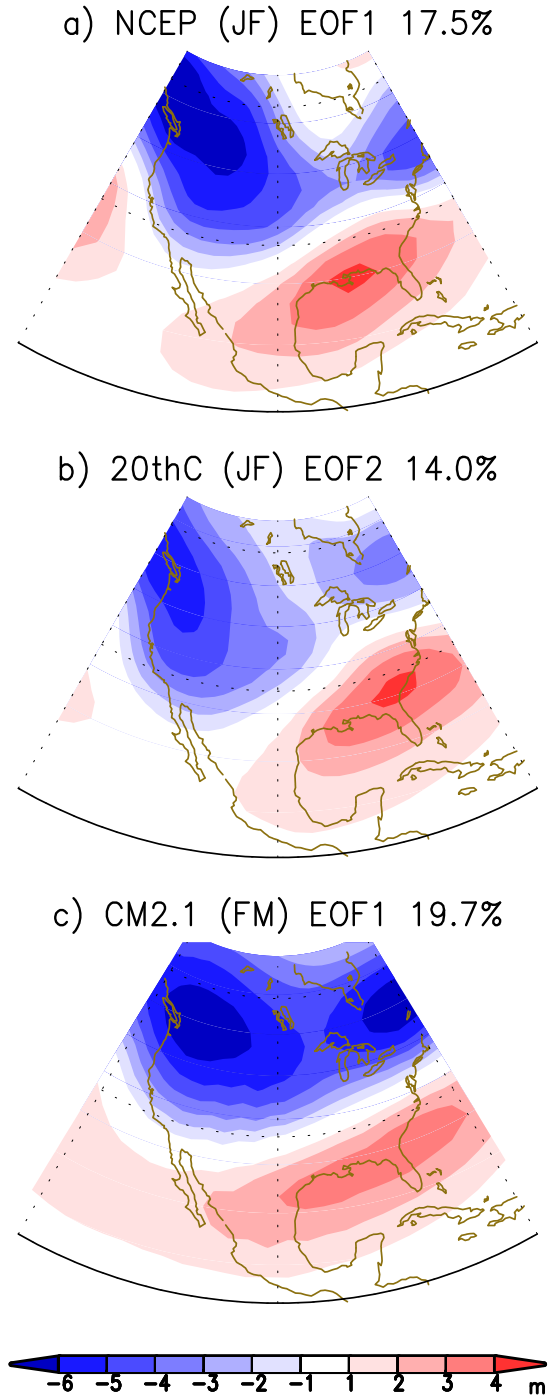


Figure 2.12: The spatial pattern of the (a,c) first and (b) second EOF of the seasonal mean normalized rms of filtered 500-hPa height field over the North American sector ( $15^{\circ}$ – $60^{\circ}$ N,  $130^{\circ}$ – $70^{\circ}$ W) based on the (a) NCEP/NCAR reanalysis for the JF-mean season, (b) 20thC reanalysis for the JF-mean season and (c) CM2.1 simulation for FM-mean season. The patterns show the regression coefficients of seasonal mean rms filtered 500-hPa height versus the standardized temporal coefficients of the EOF. Units: m. The fraction of variance explained by each EOF mode is given on the top of each panel.

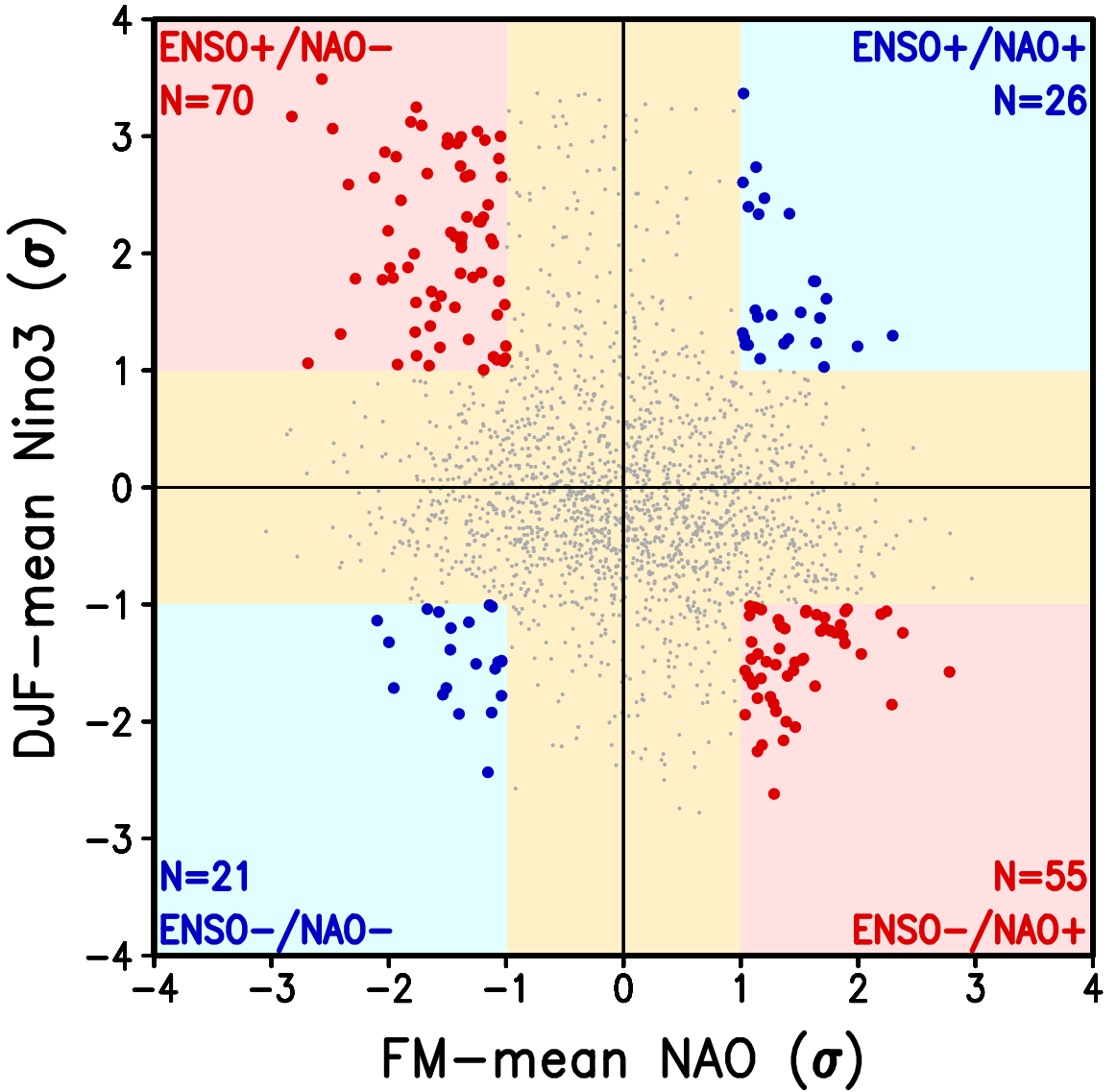


Figure 2.13: Scatterplot of normalized DJF-mean Niño-3 index vs normalized FM-mean NAO index for the 2000-yr CM2.1 dataset. The abscissa (ordinate) of each dot in this diagram represents the amplitude and sign of the NAO (Niño-3) index for an individual winter season. Both weak ENSO and NAO winters (i.e., all winters in the yellow region) are displaced with small gray dots. Red and blue dots indicate the four subgroups with strong Niño-3 and NAO indices. Red dots represent the cases of ‘strong combination’, and blue dots are the cases of ‘weak combination’. These four subgroups of cases are selected for constructing composites in Fig. 2.14. The number of events for each subgroup is shown at the four corners.

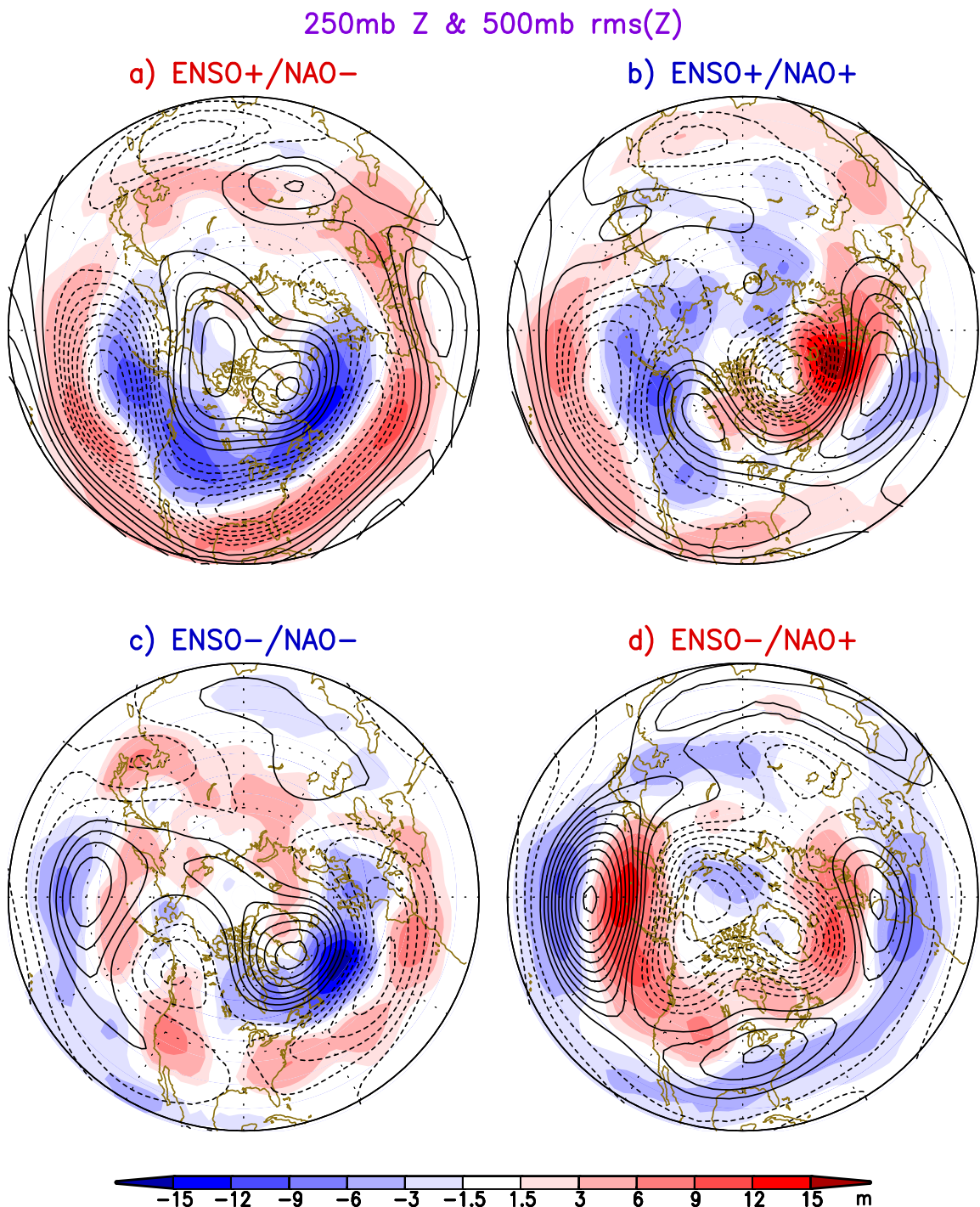


Figure 2.14: Composites of 250-hPa geopotential height (contours, interval: 15 m) and rms of the bandpass filtered 500-hPa geopotential height (shading, see scale bar at bottom) for the FM(1) period. Composites are shown for the subgroups of (a) ENSO+/NAO-, (b) ENSO+/NAO+, (c) ENSO-/NAO- and (d) ENSO-/NAO+ in the CM2.1 simulation. The outermost latitude circle represents 20°N.

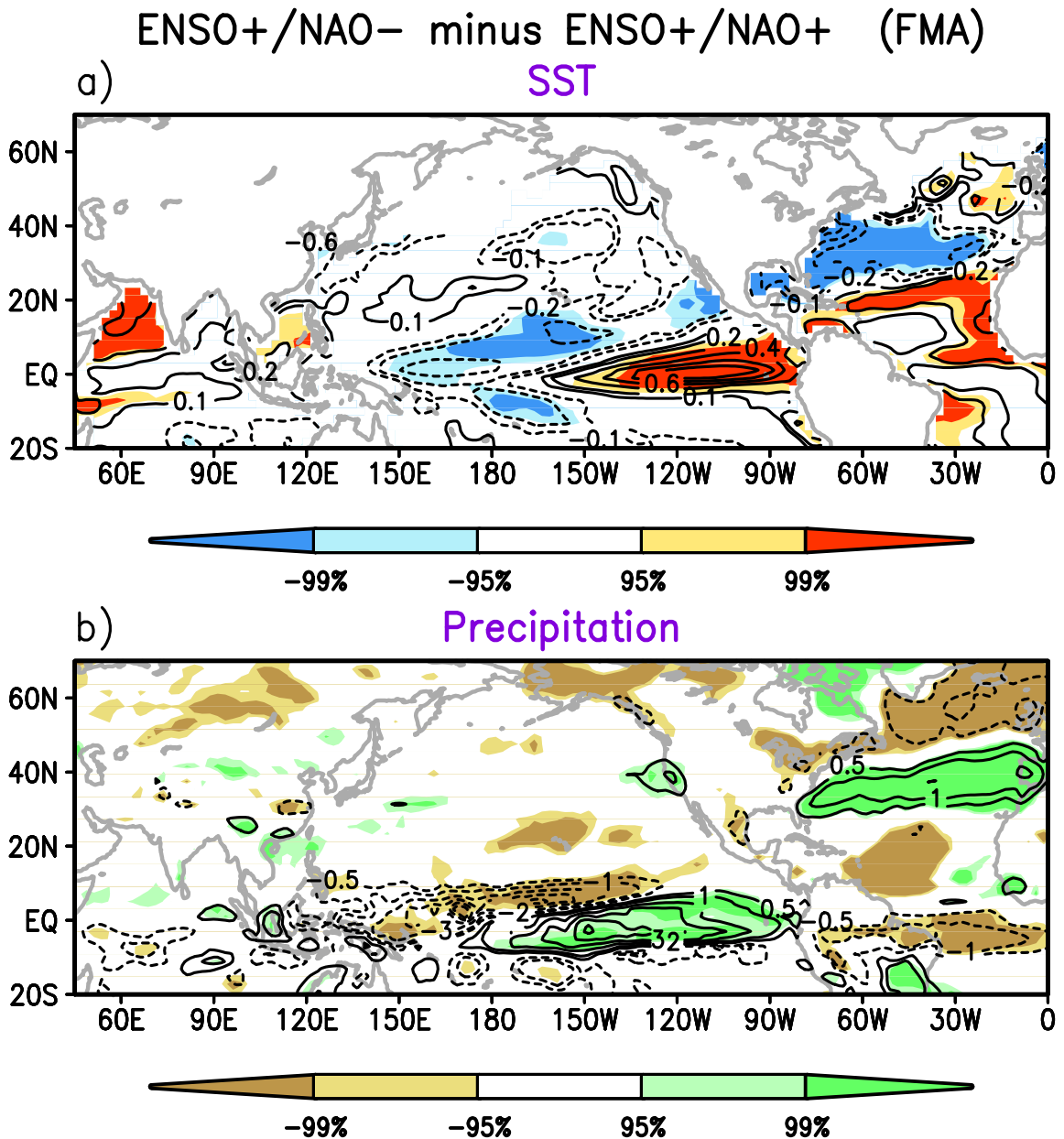


Figure 2.15: The (ENSO $+$ /NAO $-$ ) minus (ENSO $+$ /NAO $+$ ) composites of (a) SST (units:  $^{\circ}\text{C}$ ) and (b) precipitation (units:  $\text{mm day}^{-1}$ ) for the FMA(1) period, as computed using the CM2.1 simulation. SST in (a) is contoured at  $\pm 0.1$ ,  $\pm 0.2$ ,  $\pm 0.4$ ,  $\pm 0.6$ ,  $\pm 0.8$ ,  $\pm 1.0$ . Precipitation in (b) is contoured at  $\pm 0.5$ ,  $\pm 1.0$ ,  $\pm 2.0$ ,  $\pm 3.0$ ,  $\pm 4.0$ . Shadings indicate the regions of 95% and 99% confidence levels by using a two-tailed Student's  $t$  test.

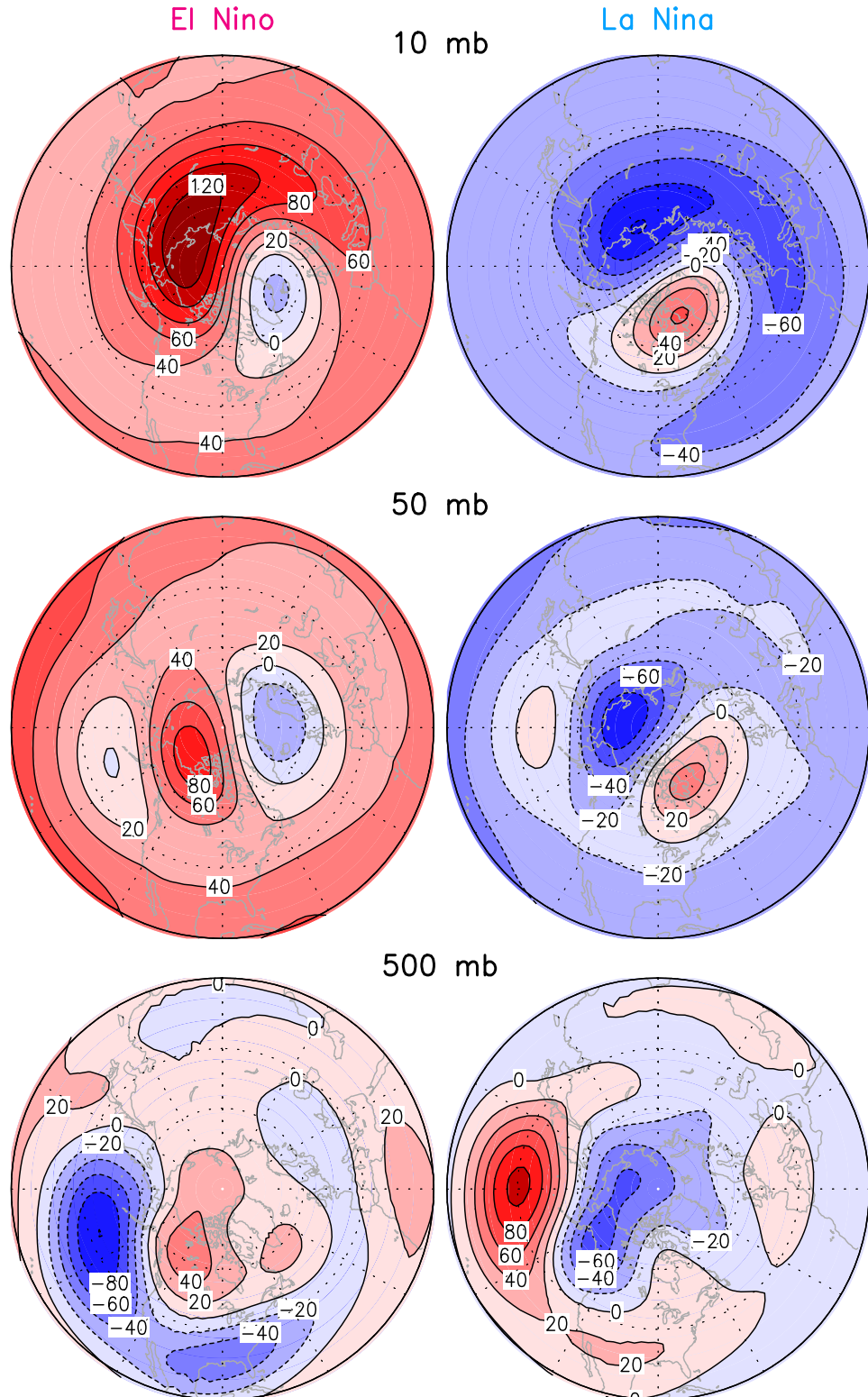


Figure 2.16: Horizontal distributions of El Niño (top panels) and La Niña (bottom panels) composites of geopotential height anomaly at 10 hPa (left panels), 50 hPa (middle panels) and 500 hPa (right panels).

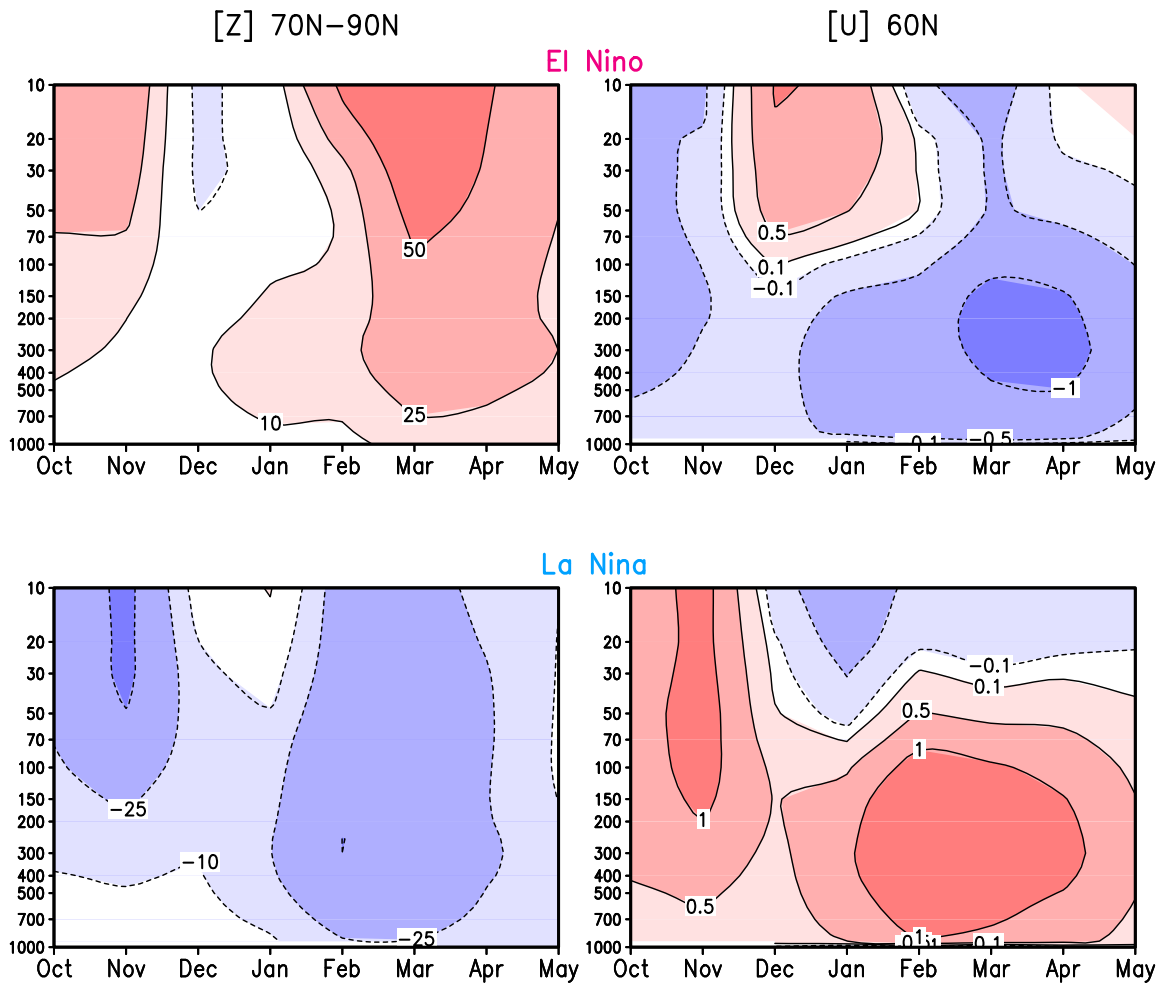


Figure 2.17: Time-height evolution of El Niño (top panels) and La Niña (bottom panels) anomaly for the area-weighted ( $70^{\circ}$ - $90^{\circ}$ N) zonal mean polar cap geopotential height (left panels) and zonal mean zonal wind at  $60^{\circ}$ N (right panels) for CM2.1.

# Chapter 3

## Contributions of Downstream Eddy Development to the ENSO-NAO Teleconnection

### 3.1 Introduction

In chapter 2, the dynamical mechanism for the late winter teleconnection between ENSO and NAO is examined using mostly composites of seasonal means. By analyzing the output from a 2000-yr long coupled atmosphere-ocean GCM, and by performing parallel analysis of observational data, we have explicitly shown the potential role of high-frequency transient eddies in the linkage between ENSO and NAO.

Many observational studies have shown that a substantial fraction of low-frequency variability is related to the behavior of large-scale persistent and recurrent flow patterns. Some investigations have referred to these features as weather regimes (e.g., Vautard 1990). Notable examples of such phenomena include blocking events and episodes with strong zonal flows (e.g., Dole and Gordon 1983). The characteristic time scales of persistent anomalies over NP, NA, and Siberia are estimated to be on

the order of 10–15 days (Dole 1986; Feldstein 2000). Since the analysis performed in chapter 2 is mostly based on averages over two entire calendar months in late winter, the results presented in that chapter may be viewed as the crude average over several life cycles of such anomalous episodes. In those instances when episodes of both polarities occur within a given 2-month period, or when the episodes are interspersed with extended periods with weak anomalies, the previous computations based on 2-month averages might not yield optimal information on the processes associated with episodes of a given sign. In this chapter, an attempt is made to sharpen the analysis approach in chapter 2 by focusing only on those periods when the episodes of interest attain sufficiently large amplitudes.

Our primary interest in this chapter is to illustrate the downstream development of the wave packets in the course of identified persistent episodes. While the seasonal statistics, as shown in chapter 2, suggest a strengthened linkage between NP and NA storm tracks during ENSO winters, the results in this chapter provide additional evidence in support of ENSO impact on the downstream development of the wave packets from the Pacific towards the eastern Atlantic, and subsequent feedback onto the mean flow.

The 2009/2010 winter is noted for the storminess over the North America. El Niño and strong negative NAO conditions also prevailed in this period. We are hence motivated to perform a case study on the role of transient disturbances in the linkage between ENSO and NAO in this particular winter season, and to examine the implications of this relationship on the surface weather over North America.

The basic datasets, analysis tools, and procedure for the selection of persistent events are described in section 3.2. Section 3.3 documents the relationships between the frequency of occurrence of persistent events, ENSO, NAO and their seasonal dependence. The characteristics of the eddy intensity, eddy propagation, and eddy-induced geopotential height tendencies during both phases of the persistent events

are discussed in section 3.4. Section 3.5 shows the downstream development of the wave packets in the course of the selected persistent events. Results on surface cyclone development, downstream evolution of wave packets and eddy forcing over NA, all for the outstanding winter season of 2009/2010, are presented in section 3.6. Discussion and conclusions are given in section 3.7.

## 3.2 Data and analysis procedures

### 3.2.1 Model description

The model data analyzed in this study are generated by a 2000-yr long, pre-industrial control simulation using a global coupled climate model at the Geophysical Fluid Dynamics Laboratory (GFDL) (CM2.1; see [Delworth et al. 2006](#); [Gnanadesikan et al. 2006](#); [Griffies et al. 2004](#)). Readers are referred to chapter 2 for more detailed descriptions of this model simulation. As shown in chapter 2, this model captures many salient features of the observed behavior of both ENSO and NAO, as well as their impacts on the surface climate in late winter.

### 3.2.2 Observational datasets

The observed data used in this study are based on daily averaged fields (1948–present) from National Centers for Environmental Prediction/National Center for Atmospheric Research (NCEP/NCAR) reanalysis ([Kalnay et al. 1996](#)). Six-hourly circulation fields in the 2009/2010 winter season are used in the case study presented in section 3.6. DJF-mean Niño-3 index (SSTAs averaged over 5°S–5°N, 150°–90°W) based on the NOAA extended reconstructed SST version 3 dataset (ERSST V3, see [Smith et al. 2008](#); [Xue et al. 2003](#)), is used to describe ENSO variability in the 1948–2010 period.

The geopotential height and sea level pressure (SLP) fields are multiplied by the factor [ $\sin 45^\circ \text{N} / \sin(\text{latitude})$ ] to obtain streamfunction-like anomalies, which are bet-

ter indicators of the associated wind and vorticity anomalies (Dole and Gordon 1983; Nakamura and Wallace 1990).

### 3.2.3 Analysis tool

A Lanczos 2–8 d band-pass filter with 41 weights (Duchon 1979) is used to retain high-frequency variability associated with baroclinic waves. Another 8-d low-pass filter is employed to capture the low-frequency circulation anomalies, which may be regarded as the background state for the high-frequency eddies. Nakamura et al. (2002) and Nakamura and Shimpo (2004) have used the same cutoff period of 8-d to separate the fluctuations in the two frequency bands. This cutoff period is slightly shorter than that used in chapter 2 (10-d), in order to reduce the impact of the low-pass filtering on the selection of persistent events (see section 3.2.4).

As in chapter 2, the characteristics of transient eddies are illustrated by using an index of storm track activity, extended Eliassen-Palm vectors (hereafter referred to as E) and the barotropic component of eddy forcing. The main distinction between the analysis approach in chapter 2 and the present study is that the previous investigation is based on monthly or seasonal averages of these diagnostic quantities, whereas the current work makes use of the same quantities defined on individual days.

A measure of the level of eddy activity on each day is given by the ‘envelope function’ ( $Z_e$ ) as defined by Nakamura and Wallace (1990):

$$\sqrt{2 \times \overline{Z'^2}} [\sin 45^\circ \text{N} / \sin(\text{latitude})].$$

Here the prime denotes the 2–8 d band-pass filtered geopotential height, and overbar the smoothing with 8-d low-pass filter.

The horizontal components of  $\mathbf{E}$  for each day are given by [Trenberth \(1986\)](#):

$$\frac{1}{2}(\overline{v'^2} - \overline{u'^2})\mathbf{i} - \overline{u'v'}\mathbf{j}.$$

Here  $u, v$  are the zonal and meridional wind components, respectively. Primes and overbars have the same meanings as in the definition of the envelope function above.

The daily fields of the lowpass-filtered tendency of the 250-hPa geopotential height, as induced by the convergence of transient eddy vorticity flux, are computed as ([Nakamura et al. 1997](#)):

$$\left( \frac{\partial Z_{250}}{\partial t} \right)_{eddy} = \frac{f_0}{g} \nabla^{-2} [-\nabla \cdot (\overline{\mathbf{V}'\zeta'})]. \quad (3.1)$$

Here  $Z_{250}$  is the geopotential height at 250 hPa,  $\mathbf{V}$  the horizontal wind,  $\zeta$  the relative vorticity,  $f_0$  the Coriolis parameter at 45°N and  $g$  the acceleration due to gravity. Since  $f_0$  is fixed to the value for 45°N, Eq. (3.1) yields a streamfunction tendency, which can be compared with the streamfunction-like height anomalies.

[Trenberth \(1981\)](#) shows that the power spectrum of  $v$  is dominated by high-frequency fluctuations. Unfiltered meridional wind velocity  $v$  is thus used to illustrate the spatial pattern and downstream propagation of the synoptic waves.

Following [Nakamura and Wallace \(1990\)](#), the daily anomaly of a given variable at each grid point is defined as its departure from the local value of the climatological-mean annual cycle. The annual cycle is obtained from the sum of the annual mean and first three harmonics of the 365-day climatological time series. The anomalous time series computed in this way contain both intraseasonal and interannual fluctuations.

The period of investigation consists of 62 winter seasons from 1948/1949 to 2009/1010 based on the NCEP/NCAR reanalysis, and 1999 winter seasons based on the CM2.1 simulation. Winter is defined as the 121-day period starting from 1 December.

### 3.2.4 Identification of persistent events

Most of the previous studies examine eddy-mean flow interactions over the NP and NA basins separately (e.g., Wallace et al. 1988). However, as noted in chapter 2, circulation anomalies appear to be more zonally symmetric during ENSO events. In addition, strong linkage between the Pacific and Atlantic storm tracks has been identified by James and Burkhardt (2006), thus suggesting that it might be misleading to treat the two storm tracks as distinct, independent circulation systems. Therefore, an empirical orthogonal function (EOF) analysis of low-frequency geopotential height fields at 250 hPa over a broad region encompassing both the NP and NA sectors ( $20^{\circ}$ – $70^{\circ}$ N,  $120^{\circ}$ E– $0^{\circ}$ – $15^{\circ}$ E) is performed to identify the dominant large scale flow pattern.

The observed (Fig. 3.1a) and simulated (Fig. 3.1b) first EOF pattern (EOF1) explain 12.3 and 11.7% of the total variance, respectively. Both the observed and simulated EOF1 modes are dominated by a wave-like pattern over the NP and North America (Wallace and Gutzler 1981), with centers of action near Hawaii and western North America of one sign, and over the NP and southeastern U.S. of the opposite sign. A similar leading EOF pattern of the low-pass filtered 500-hPa height for the 90-day winter period over the Northern Hemisphere (NH) is documented by Cheng and Wallace (1993).

The daily expansion coefficients associated with EOF1 (hereafter referred as the EOF1 index) are normalized by the standard deviations of the entire time series. A EOF1 $\pm$  day is defined as any day in which the EOF1 index exceeds  $\pm 1.0$ . A persistent EOF1 $\pm$  episode is considered to occur when the daily standardized EOF1 index exceeds  $\pm 1.0$  for at least 10 consecutive days. Once a persistent episode is determined, an onset (decay) day is defined corresponding to the first (last) day of that episode. The duration criteria of 10 days is typically used in previous studies (Dole and Gordon 1983; Higgins and Schubert 1996, 1997). We choose threshold amplitude value of 1.0 so that the typical event is sufficiently strong, and that an adequate

population of events is captured for statistical analysis. Following Nakamura and Wallace (1990) and Feldstein (1998), if the decay of a persistent anomaly is followed by the onset of another anomaly pattern with the same polarity within 10 days, these two periods are merged and treated as one episode. There is a total of 39 EOF1+ and 39 EOF1– episodes based on NCEP/NCAR reanalysis data for the 1948–2010 period, and 992 EOF1+ and 1188 EOF1– episodes based on the 2000-yr CM2.1 simulation (see Table 3.1).

### 3.3 Relationships between EOF1 and ENSO, NAO and the seasonal cycle

#### 3.3.1 The dependence of the persistent events on the phase of ENSO

The wave-like pattern associated with EOF1+ (Fig. 3.1) could result from internal variability of the atmosphere or from external forcing, such as that related to ENSO. Similarity between this pattern and that associated with El Niño (left panels of Fig. 2.9 in chapter 2) indicates that ENSO-related tropical forcing may influence the frequency of occurrence of the EOF1 mode. These qualitative impressions can be illustrated by showing the total number of EOF1+ and EOF1– days (see definition in section 3.2.4) for each DJFM season during warm and cold ENSO events.

Fig. 3.2a shows the observed total number of EOF1+ days (see red shaded bars) and EOF1– days (blue bars) in each warm ENSO event. Analogous statistics for cold ENSO events are given in Fig. 3.2b. A warm (cold) ENSO is identified when the DJF-mean Niño-3 index is more than  $0.5\sigma$  above (below) the time mean. A more relaxed Niño-3 amplitude is used to include weak ENSO winters. In a majority of warm ENSO events, the number of EOF1+ days is larger than the number of EOF1–

days. The number of EOF1+ days in most of the warm ENSO winters is above the average number of EOF1+ days for all winters in the 1948–2009 period (i.e., 19.7 d; see red solid line in Fig. 3.2a). In contrast, the number of EOF1– days is below the average number of EOF1– days (i.e., 19.9 d; see blue dashed line in Fig. 3.2a). The opposite situation holds in the cold ENSO events (see Fig. 3.2b).

The persistence characteristics of the EOF1 $\pm$  events can be illustrated by compositing the temporal evolution of EOF1 indices relative to the onset day, as shown for model data in Fig. 3.3. This procedure has been performed separately over the persistent episodes during El Niño winters only, La Niña winters only and all winters. The simulated El Niño and La Niña winters are identical to those examined in chapter 2. For the persistent EOF1+ events (Fig. 3.3a), the EOF1 index during El Niño winters (red curve) stays above  $1\sigma$  longer than the EOF1 index during La Niña winters (blue curve). The opposite situation holds in the persistent EOF1– events (Fig. 3.3b).

The dependence of the characteristics of the persistent EOF1 events on the phase of ENSO is further delineated by computing the averaged number, frequency and duration of the EOF1 $\pm$  events, as well as averaged number of EOF1 $\pm$  days separately for all winters, El Niño winters only, and La Niña winters only, based on both observations and model simulation. These statistics are displayed in Table 3.1. The average number of both EOF1+ and EOF1– days for all winters is approximately 20 for both observations and simulation (see also Fig. 3.2). The number of EOF1+ days in El Niño winters is significantly larger than the all-winter average, and is statistically significantly larger than the corresponding counts in La Niña winters by a factor of about 3 (7) for observations (model data). Moreover, the average duration of persistent EOF1+ events in El Niño winters is almost twice as long as that in La Niña winters for both observations and simulation (see also Fig. 3.3a). Conversely, EOF1– events are more frequent and longer-lasting in La Niña events.

### 3.3.2 NAO phase during the persistent circulation anomalies

To examine the phase of NAO during the persistent EOF1 $\pm$  events, the average value and probability density functions (PDFs) of the normalized daily NAO index during persistent EOF1 $\pm$  events are calculated and compared in this subsection. The daily NAO index is constructed by projecting the daily low-pass filtered SLP field onto the spatial pattern of the leading EOF of the SLP field over the NA region in the DJFM-mean winter season (similar to Fig. 2.5, but for the DJFM-mean season).

The observed values of normalized daily NAO index, as computed based on the average over 682 (746) days within the duration of persistent EOF1+ (EOF1-) events, are  $-0.39 (+0.41)$ . The difference between these composite values is statistically significant on the basis of a *t*-test (*p*-value  $< 0.01$ ). Statistically different composite values of the normalized NAO index are also found based on the CM2.1 simulation (i.e.,  $-0.33$  vs  $+0.34$ , *p*-value  $< 0.01$ ).

The PDFs of the daily NAO index during the persistent EOF1+ and EOF1- events are compared for the NCEP/NCAR reanalysis (Fig. 3.4a) and CM2.1 simulation (Fig. 3.4b). Pronounced shifts in the distribution toward negative and positive NAO values are apparent for the persistent EOF1+ and EOF1- events, respectively, for both observations and simulation. The two distributions are statistically different (*p*-value  $< 0.01$ ) using a Kolmogorov-Smirnov test (Smirnov 1948), for both NCEP/NCAR and CM2.1 datasets.

### 3.3.3 Seasonal dependence of frequency of occurrence of persistent EOF1 $\pm$ days

To explore the variation of the frequency of persistent events within the winter season, frequencies of days belonging to persistent EOF1 $\pm$  events are calculated for each winter month and the results are shown in Fig. 3.5. For instance, the light blue bar

in Fig. 3.5a shows the ratio of the number of days belonging to the persistent EOF1+ event in December to the total number of days in December. Results based on the NCEP/NCAR reanalysis and CM2.1 simulation are shown on the left and right side of each panel, respectively. Fig. 3.5a indicates that the frequency of the persistent days belonging to EOF1+ events are notably higher in January and February for the NCEP/NCAR reanalysis, and in January, February and March for the CM2.1 simulation. This seasonal dependence of the EOF1+ statistics is consistent with the seasonal timing of strong eddy-mean flow interaction related to the linkage between ENSO and NAO, as noted in chapter 2. The approximate 1-month lag between the distributions based on observational and model data in Fig. 3.5a may partially be attributed to the delay of the ENSO mature phase in the simulation (see Fig. 2.2).

For the persistent EOF1– events (Fig. 3.5b), higher frequencies are found in December, January and February for the NCEP/NCAR reanalysis, and in January, February and March for the CM2.1 simulation. Although the late winter peak noted for the EOF1+ events is less evident in the EOF1– events, the 1-month delay in the model distribution relative to the observed distribution is still discernible for the EOF1– events.

### 3.4 Eddy-mean flow interactions during persistent EOF1+ and EOF1– events

We shall henceforth focus on the behavior of the synoptic-scale eddies and their interactions with the background flow during the persistent EOF1 $\pm$  events. For each persistent episode selected using the procedure in section section 3.2.4, simple time means are taken of the anomalous fields (see definition in section 3.2.3) over the duration of that episode. Composites are then obtained by averaging over the means for all episodes.

### 3.4.1 Composites of persistent EOF1+ events

Fig. 3.6 shows the composites of 250-hPa low-pass filtered geopotential height  $Z$  and envelope function  $Z_e$  (top panels), extended  $\mathbf{E}$  vectors and eddy induced height tendency ( $\partial Z / \partial t$ , middle panels), and low-pass filtered SLP (bottom panels) averaged over all selected EOF1+ events. The observational and model results are shown in the left and right panels of Fig. 3.6, respectively. The observed composite pattern for 250-hPa low-frequency  $Z$  (contours in Fig. 3.6a) is characterized by a wave train (Wallace and Gutzler 1981) over the PNA sector. The anomalous height pattern over the NP sector is indicative of a strengthened Pacific subtropical jet stream, which is in turn associated with enhanced eddy activity along the Pacific storm track near 35°N (see shading in Fig. 3.6a).

At the eastern end of the Pacific storm track, strong divergence of the  $\mathbf{E}$  vectors is discernible in both observations and simulation, with northward-directed arrows north of the storm track, and southeastward arrows farther south. This configuration implies that the eddy momentum convergence leads to acceleration of the westerly mean flow (e.g., Trenberth 1986), reinforcement of the subtropical westerly anomalies at this location, as well as strengthening of storm track activities farther east over the southern U.S./Gulf of Mexico. Farther downstream over the western and central Atlantic, the anomalous  $\mathbf{E}$  vectors are mostly divergent (leading to zonal flow acceleration) near 30°N, and convergent (zonal flow deceleration) near 50°N. The cyclonic curvature of  $\mathbf{E}$  in midlatitude NA is indicative of northward wind acceleration (e.g., Trenberth 1986). The above configuration of zonal and meridional wind changes is consistent with negative height tendency  $\partial Z / \partial t$  in the temperate zone of NA (see shadings in Figs. 3.6c,d). This negative center is displaced eastward of the height anomaly (see contours in Figs. 3.6a,b) by 20° of longitude in observations, and 40° in simulation. Such coherent eastward extension of negative height tendencies over the Atlantic sector has been emphasized in chapter 2.

At the surface, the observed pattern displays a distinct dipole-like pattern, with low pressure anomaly over the central-western Atlantic near 35°N, and a high pressure anomaly to the south of Iceland (Fig. 3.6e). This dipolar pattern resembles the SLP pattern corresponding to the negative NAO phase. The characteristic SLP pattern, with a prominent cyclonic anomaly over NP and an anticyclonic anomaly south of Iceland, is similar to the SLP seasaw pattern between Aleutian Low (AL) and Icelandic Low (IL) in its peak period, as described by [Honda et al. \(2001\)](#).

Both the dipolar and seesaw features are discernible in the corresponding SLP pattern in the CM2.1 simulation (Fig. 3.6f), although the amplitude of the dipolar anomaly is reduced in the simulation. This relatively weaker amplitude of SLP anomaly has been noted in chapter 2 for the ENSO composites of seasonal means (see Figs. 2.4c,d), and is possibly due to both the relatively low horizontal resolution in the model atmosphere, and the very limited vertical resolution in the model stratosphere.

### 3.4.2 Composites of persistent EOF1– events

The polarity of the low frequency anomalies in  $Z$  at 250 hPa and in SLP during observed persistent EOF1– events (Figs. 3.7a and 3.7e) is opposite to that for EOF1+ events. The positive anomaly center to the south of Alaska is typical of the classic blocking situation over NP (e.g., [Dole and Gordon 1983; Renwick and Wallace 1996](#)). This blocking pattern is accompanied by notable diversions in the Pacific storm track and background westerlies. As indicated by  $Z_e$  (shading in Fig. 3.7a), the Pacific storm track is more active than its climatological mean to the north of the anomalous high and in the subtropics, whereas suppressed activity prevails in the zone situated between these two active sites. The relative quiescent belt along 35°N is characterized by strong convergence of the  $\mathbf{E}$  vectors (Fig. 3.7c), which implies zonal wind deceleration. Negative (positive) height anomalies over the northwestern (southeastern) quadrant of the North America (contours in Fig. 3.7a) are indicative of strengthened

northeasterly flow over much of the interior of this continent. The slightly enhanced eddy activity over eastern Canada, together with the diminished activity over the southeastern U.S. (shading in Fig. 3.7a) are indicative of the northward shift of the Atlantic storm track. On the southern flank of the Atlantic storm track, anticyclonic curvature of  $\mathbf{E}$  and positive  $\partial Z/\partial t$  pattern extends eastward from the northeastern U.S. to the western Atlantic along 45°N (Fig. 3.7c).

The principal features of the simulated patterns in the right panels of Fig. 3.6 and Fig. 3.7 are in overall agreement with their observational counterparts. Hence the observed inferences on eddy-mean flow interactions are also applicable to the much larger samples of persistent events generated by the CM2.1 simulation.

The strength and preferred location of  $\partial Z/\partial t$  over NA, as shown in Figs. 3.6–3.7 for persistent episodes, bear some similarities to the corresponding charts shown for the ENSO composites of seasonal means (Figs. 2.9 and 2.10 in chapter 2). The comparability of these two sets of results indicate that eddy forcing during the persistent episodes plays an important role in determining the phase and amplitude of the seasonal averaged features. These findings also suggest that, during the persistent episodes, transient eddies can efficiently induce cyclonic or anticyclonic tendencies over NA.

## 3.5 Linkage between Pacific and Atlantic variability through downstream development

### 3.5.1 One-point lagged regression patterns based on persistent EOF1+ events

One-point lag-correlation maps have been widely used to study the horizontal structure and time variation of waves and wave packets (e.g., Blackmon et al. 1984a,b;

Wallace et al. 1988). Since we are more interested in the relative amplitude of wave disturbances in different geographical regions, we shall devote our attention to the spatial patterns of lagged regression coefficients, following Lim and Wallace (1991) and Chang (1993). The lagged regression coefficient  $b(\lambda, \phi, \tau)$  at a particular longitude  $\lambda$ , and latitude  $\phi$  at lag time  $\tau$  is calculated as

$$b(\lambda, \phi, \tau) = \frac{\overline{\langle v'(\lambda_0, \phi_0, t)v'(\lambda, \phi, t + \tau) \rangle}}{\sigma[v'(\lambda_0, \phi_0, t)]}, \quad (3.2)$$

where  $\lambda_0$  and  $\phi_0$  are the longitude and latitude, respectively, for the time series at the reference grid point,  $v'(\lambda, \phi, t)$  is the deviation of the unfiltered 250-hPa meridional velocity from its corresponding time mean at that grid point,  $v'(\lambda, \phi, t) = v(\lambda, \phi, t) - \overline{v(\lambda, \phi, t)}$ ,  $\sigma^2[v'(\lambda_0, \phi_0, t)] = \langle \overline{(v'(\lambda_0, \phi_0, t))^2} \rangle$ , the overbar indicates a temporal average from the onset day to the decay day of individual persistent episode, the angle bracket denotes the ensemble average over all persistent episodes,  $\tau$  is the number of days by which the time series  $v'(\lambda, \phi)$  lags the reference time series  $v'(\lambda_0, \phi_0)$ .

It should be pointed out that the above-mentioned previous studies using this one-point lagged correlation or regression technique are based on the average over ‘all-winter’ days. However, due to the large meridional variation of the trajectories for both individual eddies and the entire wave packets, the signal of interest is often diluted in such climatological lagged correlation or regression maps. In order to highlight the features related to eddy development, we limit the sample populations to those episodes with persistent flow pattern or storm path pattern. A similar approach has been taken by Hakim (2003), who uses ensemble averaging of cases that share common ray paths as an indication of wave packet evolution, and conclude that Pacific wave packets often serve as ‘seeding’ for the Atlantic storm track.

Left panels of Fig. 3.8 show the one-point lag-regression maps of unfiltered 250-hPa meridional velocity anomalies for lags of  $-1, 0, +1, +2, +3$  and  $+4$  d, as computed

using observational data. The reference point is located at (35°N, 180°), i.e., along the axis of the Pacific storm track (see green dot in Fig. 3.6a). On day 0 (Fig. 3.8b), the zonally oriented wavetrain extends from east Asia all the way across the Pacific. The consecutive positive and negative centers are separated by approximately 30° longitude, thus implying a wavelength of about 6000 km. As estimated from the time-lagged regressions from day  $-1$  to day  $+3$ , the individual centers travel eastward by about 40° in 4 d, thus yielding a phase speed ( $c_p$ ) of about  $13 \text{ m s}^{-1}$ , and a period of about 6 d.

Comparison between the regression pattern on day  $-1$  and that on day  $+1$  reveals that relatively higher wave amplitudes are observed on the upstream side of the reference center on day  $-1$ , and on the downstream side on day  $+1$ . These asymmetries of the regression patterns with respect to the reference point and to the time lag clearly indicate the evolution of an eastward propagating wave packet, with successive growth (decay) of troughs and ridges downstream (upstream) of the reference site. On day  $+1$ , the leading edge of the packet, labeled with ' $d_1$ ' in Fig. 3.8c, is situated over the central portion of the North America continent. This center experiences substantial growth on days  $+2$ , and two new centers (' $d_2$ ' and ' $d_3$ ') are seen to emerge still farther downstream (Fig. 3.8d). The wave packet over NA preserves its coherence on days  $+3$  and  $+4$  (Figs. 3.8e,f).

The right panels of Fig. 3.8 show the corresponding patterns obtained from the CM2.1 simulation. The simulated results are in general agreement with the observational results with regards to the wavelength and period. The coherent wave packet over NA emerges on day  $+4$  (Fig. 3.8l), with a 1-d delay relative to observations (Fig. 3.8e).

We have also examined similar one-point lagged regression maps but based on the average over ‘all-winter’ days for both the NCEP/NCAR reanalysis dataset and CM2.1 simulation (Fig. 3.9). On day  $+2$ , the corresponding amplitude of the dis-

turbance ‘ $d_1$ ’ in such ‘all-winter’ statistics (see Fig. 3.9d) is only about 50% of the value shown in Fig. 3.8d, and no signal is discernible in locations farther east of ‘ $d_1$ ’. On days +3 and +4, the observed wave packets based on ‘all-winter’ data are less coherent than the patterns in Figs. 3.8e,f, with no discernible signal over NA. These findings compare well with previous observational results (Chang 1993, see their Fig. 5; Chang and Yu 1999, see their Fig. 2). Similarly, the coherent wave packet propagating across the NA is not apparent in the lagged regression patterns based on CM2.1 data for ‘all-winter’ days (Figs. 3.9j-l). Such comparisons illustrate that the successive eddy downstream development from NP to the NA is particularly strong during the persistent EOF1+ episodes.

To objectively analyze the propagation characteristics of the wave packets seen in Fig. 3.8, longitude-time diagrams of the lagged regression coefficients at 35°N is plotted in Figs. 3.10a and 3.10b, for persistent EOF1+ events in the observed and modeled atmosphere, respectively. The corresponding distributions based on ‘all-winter’ days are displayed in Figs. 3.10c,d. Following Fraedrich and Lutz (1987), the  $c_p$  of the individual eddies embedded in the wave packet is determined by the slope of the axis of the maximum positive regression coefficients crossing the base point (blue line), i.e., dividing the distance between the positive extrema (blue crosses) on days –1 and +1 by 2 days. The group velocity ( $c_g$ ) is given by the slope of the axis (red line) connecting the first negative center upstream of the base point at day –1 and the one downstream of the base point at day +1 (red crosses). The estimated values of  $c_p$  and  $c_g$  are displayed at the lower right corner of each panel. The  $c_g$  is about 3.5–5 times larger than the  $c_p$ . These results are in accord with the characteristics of downstream development associated with wave packets, as described by Lee and Held (1993).

Comparing the  $c_p$  and  $c_g$  during the persistent EOF1+ events to those during the ‘all-winter’ days reveals that during persistent EOF1+ events, both the  $c_p$  and  $c_g$  are

larger. Such behavior may be explained by the strengthened Pacific subtropical jet stream associated with the persistent EOF1+ events, since agreement between the  $c_p$  ( $c_g$ ) and lower (upper) level winds has been shown in several observational and modeling studies (e.g., Blackmon et al. 1984b; Simmons and Hoskins 1979; Lee and Held 1993)

The preferred downstream development of the wave packet can also be inferred from the asymmetry in the longitudinal extent of the disturbances with respect to the base point. Specifically, it is seen from Fig. 3.10b that the disturbances extend for about one wavelength upstream of the base point, but for about two wavelengths downstream of the base point. This upstream-downstream asymmetry is more distinct in the CM2.1 simulation (Fig. 3.10b) than in observations (Fig. 3.10a), partially due to the limited sample size in the latter dataset. The patterns observed from ‘all-winter’ data (Figs. 3.10c,d) exhibit a much stronger degree of symmetry relative to the base point. The amplitude of the eddies downstream of the base point in the latter patterns is almost comparable to that in the upstream sector.

### 3.5.2 One-point lagged regression patterns based on persistent storm track events

The interannual variations of the latitudinal position of the zone of maximum transient eddy activities over North America, and their relationship to both ENSO and NAO has been illustrated in chapter 2. However, it is not feasible to infer from seasonal statistics presented in chapter 2 the behavior of individual eddies as they propagate from NP to NA. The recent study of Seager et al. (2010b) shows that the transient waves propagate along a more southern path towards southwestern North America during El Niño, and a more northern route towards the Pacific Northwest during La Niña. However, these authors do not investigate the propagation of those waves farther eastward to the NA sector. We have highlighted these two preferred paths of

eddy propagation during the persistent EOF1+ and EOF1– events in Figs. 3.6a,b and Figs. 3.7a,b. It is hence of interest to study the downstream eddy development from NP towards NA during those periods of persistent eddy activity along these two preferred paths. In view of the important role of storm track activities over southern U.S./Gulf of Mexico and northwestern North America in linking the circulation anomalies over NP and NA, a daily storm path index (SPI) is defined by taking the normalized difference between  $Z_e$  averaged over these two regions (i.e.,  $100^\circ\text{--}70^\circ\text{W}$ ,  $20^\circ\text{--}35^\circ\text{N}$  and  $130^\circ\text{--}100^\circ\text{W}$ ,  $35^\circ\text{--}50^\circ\text{N}$ ; see boxed areas in Fig. 3.6a). Persistent SPI $\pm$  events are selected using the same methodology as described in section 3.2.4 (using amplitude and duration thresholds of  $\pm 1\sigma$  and 10 days, respectively). This procedure yields 13 SPI+ and 19 SPI– cases based on the 62-yr NCEP/NCAR reanalysis data, and 509 SPI+ and 487 SPI– cases based on the 2000-yr CM2.1 simulation. As for the persistent EOF1+(–) events, more frequent and long-lived SPI+(–) episodes are observed and simulated during El Niño (La Niña) winters.

Using the same reference point as in Fig. 3.8, a one-point lagged regression analysis is carried out over the duration of persistent SPI $\pm$  events. Since the number of observational cases is too small to generate statistically significant patterns, only the model results are shown in Fig. 3.11 for SPI+ (left panels) and SPI– (right panels) events. During the persistent SPI+ events, a coherent wave packet is evident and extends all the way to the eastern Atlantic on day +2 and day +3. The evolution of the leading edge of the packet during the persistent SPI+ events bears a strong resemblance to that in the persistent EOF1+ events, although the amplitudes based on the SPI+ events are almost twice as large as those for the EOF1+ events (e.g., compare ‘ $d_2$ ’ in Fig. 3.8j and Fig. 3.11d, ‘ $d_3$ ’ in Fig. 3.8l and Fig. 3.11f).

In contrast, the downstream development of the wave packet is considerably weaker during the persistent SPI– events. Almost no wave activity is discernible over the Atlantic basin from day +1 to day +3 (Figs. 3.11h–j). In addition, the ed-

dies are tilted in the southwest-to-northeast direction (Figs. 3.11g–i) as they approach the west coast of North America, thus indicating northward eddy momentum flux. This characteristic is consistent with the northward shift of the jet and associated storm track activity.

The strong packet evolution during the persistent SPI+ events indicates the importance of the persistent transient eddy activities over southern U.S./Gulf of Mexico in the downstream development of the wave packet over NA. During the SPI+ episodes, the strong and steady eddy forcing of the synoptic eddies contributes to the formation of the negative phase of NAO. Since El Niño-related tropical forcing could enhance transient eddy activity over southern U.S./Gulf of Mexico (see Fig. 2.9), the results presented in this section hence provide additional evidence in support of the ENSO impact on the downstream development of the wave packets from the Pacific towards the eastern Atlantic.

A possible contributor to the strong downstream eddy development during the persistent SPI+ events could be the enhanced eddy kinetic energy over southern U.S./Gulf of Mexico, since large positive anomalous  $Z_e$  is seen in this region during those episodes (see Figs. 3.6a,b).

### 3.5.3 Time lag of SLP signals in the Atlantic relative to those in the Pacific

The typical time sequence of the appearance of SLP signals at various sites during persistent EOF1+ events is established using the following procedure. For each persistent EOF1+ event, the date of the occurrence of the maximum in the EOF1 index (defined in section 3.2.4), denoted as  $T_1$ , is determined. For each grid point in the domain of interest, the date (within the event being examined) on which the local SLP anomaly attain peak amplitude, denoted as  $T_2$ , is also identified.  $\Delta T = T_2 - T_1$  is hence a measure of the time elapsed between the peak phase of the EOF1+ episode

and that of the SLP anomaly at a particular grid point. The typical time lag is then determined by averaging the values of  $\Delta T$  over all available persistent episodes. The geographical distribution of the resulting quantity is displayed in Fig. 3.12 using shading. Superposed on this pattern is the composite of the SLP anomaly averaged over the duration of individual persistent EOF1+ episodes (contours, same as Figs. 3.6e,f).

Over the NP sector, increasing time lags are seen to spread from near 150°W in both westward and eastward directions. The westward spreading indicates westward phase retrogression (Kushnir 1987; Branstator 1987; Lau and Nath 1999). The  $c_p$  of the westward traveling feature, as inferred from the patterns in Fig. 3.12, is approximately 10°–15° of longitude per day, and is in agreement with the estimates reported by the studies cited above.

Over the NA sector, the peak phase of SLP centers typically lag that in the NP sector by 1 d (2 d) in the observed (model) pattern. These time lags are consistent with those inferred from the one-point lagged regression maps in Fig. 3.8, and also with those inferred from the estimated  $c_g$  in Fig. 3.10. The time lag over NA, as deduced from model data, is larger than that based on observations by almost 1 d. This is consistent with our earlier finding that it takes about one day longer for the wave packets to travel downstream towards NA in the simulation as compared with observations (see Fig. 3.8).

Similarly, the time lag  $\Delta T$  based on geopotential height at 250 hPa is also examined. As in Fig. 3.12, the signals in the NA also lags by 1 d (2 d) relative to those in NP in the observed and (model) pattern, except that the signals at upper level peak one day earlier than the corresponding signals at the surface (not shown).

### 3.6 Case study of the 2009/2010 season

The 2009/2010 winter season is characterized by a series of severe winter storms across the U.S. and Europe, which resulted in anomalously heavy seasonal snowfall over the central and eastern U.S. and northwestern Europe (Seager et al. 2010a). This season also coincides with a moderate El Niño and a persistent negative phase of the NAO. As shown in Fig. 3.13, the NAO index is mostly negative from December through March. The combination of El Niño and a negative NAO accentuates the atmospheric anomalies associated with these individual phenomena. In particular, the geopotential height anomaly exhibits a strong zonal symmetric pattern, with out-of-phase variations between anomalies at 40°N and those in the Arctic zone (see Fig. 2.14a for ENSO+/NAO– winters; Fig. 1a in Cattiaux et al. 2010 for 2009/2010 winter season). The storm track is shifted southward in both Pacific and Atlantic basins (see Fig. 2.14a). This strengthened linkage between the Pacific and Atlantic storm tracks is indicative of the propagation of transient disturbances all the way from NP to NA, with enhanced cyclone development over the North America.

Fig. 3.14a shows the longitude-time distribution of 250-hPa unfiltered anomalous  $v$  for the December 2009 – March 2010 period based on the NCEP/NCAR reanalysis data. Averages are taken over the 30°–45°N band. In most normal winters, the climatological ridge near 140°W tends to ‘block’ the propagation of the eddies to the east (Orlanski 1998). However, the ridge in the 2009/2010 winter (not shown) is much weaker than normal, so that many wave packets in the Pacific storm track can propagate across the continental U.S. towards NA. Chang (1993) and Chang et al. (2002) have similarly documented the coherent propagation of the wave packets for winter 1983/1984 and 1980/1981, respectively.

In order to delineate the relationships between the upper level circulation and developments near the surface, cyclone trajectories are superimposed in Fig. 3.14a using black dots. These paths of surface weather disturbances are obtained by track-

ing the center of maximum 1000-hPa geostrophic relative vorticity,  $\zeta_g$ , on a  $2.5^\circ \times 2.5^\circ$  latitude-longitude grid every 6 h during the lifetime of each identified winter storm. Tracking the minima in SLP yields similar trajectories. The abscissa and ordinate of each black dot correspond to the longitude and date of occurrence of the  $\zeta_g$  maxima, respectively. As seen in Fig. 3.14a, almost all surface cyclones are collocated with positive wind anomalies at 250 hPa. This relationship indicates that the upper-level low/trough is typically situated to the west of the surface low/trough. Since upper-level divergence and lower-level convergence prevail in the air column downwind of the upper-level trough (e.g., Holton 2004), this vertical structure provides a favorable environment for surface cyclogenesis (Petterssen and Smebye 1971).

The daily evolution in the amplitude of the envelope function  $Z_e$  at 250 hPa in this winter is shown in the time-longitude diagram in Fig. 3.14b. The latitude of the storm-track axis is determined for each calendar day by tracking the peak value of  $Z_e$  value along each meridian. Values of  $Z_e$  are averaged over a  $10^\circ$  latitude interval centered on the storm track axis on each meridian. This procedure hence takes into account the meridional displacement of the storm-track axis. In Fig. 3.14b, we can identify several cases with the band of large  $Z_e$  extending across the Pacific and North America into the Atlantic. These zonally elongated signals are indicative of the downstream development of the wave packet during persistent SPI+ events as suggested in section 3.5.2.

We proceed to examine the role of eddy vorticity forcing in the evolution of the circulation over NA during the 2009/2010 winter. The time-latitude sections of the following quantities are shown in Fig. 3.15: 250-hPa low-pass filtered geopotential height anomalies  $Z$  (contours) and the envelope function  $Z_e$  (shading) in the upper panel, and 250-hPa  $Z$  (contours) and eddy-induced height tendencies  $\partial Z / \partial t$  (shading) the lower panel. All values are based on longitudinal averages over the NA sector (i.e.,  $70^\circ\text{--}20^\circ\text{W}$ ). The strong negative  $Z$  anomalies at  $40^\circ\text{N}$  and positive anomalies

near  $65^{\circ}\text{N}$  (contours in Fig. 3.15a) depict the prominent negative NAO phase in this winter season. The negative  $Z$  anomalies in middle latitudes are accompanied by strengthened eastward flows on their southern flank, and weakened eastward flows on their northern flank. Such zonal wind variations in turn modulate the intensity of transient disturbances (as inferred from the pattern of  $Z_e$ ), with positive and negative anomalies of  $Z_e$  occurring to the south and north of the midlatitude  $Z$  anomalies, respectively. The changes in the eddy induced height tendencies ( $\partial Z / \partial t$ ), are in phase with the local  $Z$  anomalies. This result confirms the strong feedbacks of eddy forcing on the ambient background flow in this particular winter.

### 3.7 Summary and discussion

The study of chapter 2 is extended to examine the role of transient eddies in the ENSO/NAO relationship during submonthly anomalous episodes. Our results indicate that ENSO events exert a strong influence on the frequency and duration of such episodes. Specifically, El Niño winters tend to favor persistent episodes with strengthened Pacific subtropical jet stream, equatorward shifted Pacific storm track, enhanced cyclone activities along the southeastern Gulf of Mexico/southeastern U.S., and a negative phase of the NAO. La Niña winters are accompanied by more frequent occurrence of poleward shifted jet stream and storm track over the Pacific, and a positive NAO phase.

Lagged regression analysis reveals strong downstream development of wave packets during the observed and simulated persistent episodes. The leading edge of the packet travels from North America to the western Atlantic in 1–2 d. In such development, synoptic-scale transient eddies induce negative  $\partial Z / \partial t$  over the region corresponding to the southern lobe of the NAO. The more frequent occurrence and longer duration of those episodes during El Niño winters are accompanied by stronger and more steady

transient eddy forcings, as well as farther eastward penetration of the wave packets to the NA sector. These effects contribute to the higher incidence of negative NAO-like anomalies in El Niño winters. These results, as inferred from weather episodes with submonthly time scales, offer a more detailed perspective of eddy processes responsible for the ENSO/NAO relationships examined in chapter 2 using seasonal averages.

There are two possible explanations for the downstream extension of wave packets along the southern route across southern U.S./Gulf of Mexico associated during El Niño winters. First, stronger eastward phase propagation of baroclinic eddies and eastward propagation of the entire wave packets are facilitated by the strengthened Pacific subtropical jet stream during the persistent EOF1+ episodes. Second, the positive anomalies of  $Z_e$  near the Gulf of Mexico may contribute to increased eddy kinetic energy in this region during persistent SPI+ episodes (see Figs. 3.6a,b). Since these two conditions often occur simultaneously, they may together contribute to the enhanced downstream extension of the wave packets.

It should also be pointed out that the downstream development of wave packets from the northern route through northwestern North America is less evident than that from the southern route. This is probably due to the equatorward refraction of the midlatitude waves with a dominant southwest-northeast tilt (See Fig. 3.11j; e.g., James 1994; Orlanski 2003).

Most of the findings based on multi-year datasets are confirmed by a case study of the 2009/2010 winter season, in which a strong negative NAO phase coincides with a moderate El Niño. It is shown that a majority of the severe winter storms over the U.S. in that season are associated with coherent upper level wave packets originating from NP and propagating across North America. Within this winter, there are many synoptic episodes in which a surface cyclone develops to the east of an upper-level trough embedded in a wave packet. These results indicate that surface

cyclone development often occurs at the approach of an upper-level trough at the leading edge of the wave packet.

A number of studies consider the NAO as the remnant of upstream wave breaking (e.g., Benedict et al. 2004; Franzke et al. 2004; Rivière and Orlanski 2007; Strong and Magnusdottir 2008a,b). These studies point out that anticyclonic and cyclonic wave breaking of the synoptic eddies could lead to the formation of the positive and negative phase of the NAO, respectively. In particular, Rivière and Orlanski (2007) note that the anticyclonic and cyclonic breaking over NA of synoptic-scale waves originating from the eastern Pacific is crucial for determining the NAO phase. Anticyclonic and cyclonic wave breaking, as in the LC1 and LC2 idealized baroclinic wave life cycles (e.g., see Thorncroft et al. 1993), is characterized by northeast-southwest (NE-SW) and southeast-northwest (SE-NW) tilt of the trough/ridge axes, respectively. In this study, the SE-NW (NE-SW) orientations of the synoptic-scale eddies near the eastern Pacific during the persistent SPI+(SPI-) (Fig. 3.11) episodes also supports the above notion that the phase of the NAO is influenced by the transient waves originating from the eastern Pacific.

Table 3.1: Summary statistics for the two types of persistent events (EOF1+ and EOF1-) based on observations and the CM2.1 simulation. If the statistics for El Niño and La Niña winters (see second and third column of each grouping in the table) are significantly different at 95% confidence based on a standard  $t$ -test, the values are shown in bold type.

Type	Dataset	No. of event			No. of events per DJFM season			Avg. No. of days per DJFM season			Avg. duration (days)		
		All	EN	LN	All	EN	LN	All	EN	LN	All	EN	LN
EOF1+	OBS	41	9	2	0.6	<b>0.9</b>	<b>0.2</b>	19.7	<b>32.1</b>	<b>10.6</b>	17.5	24.0	13.5
	CM2.1	992	352	21	0.5	<b>1.4</b>	<b>0.1</b>	19.8	<b>47.3</b>	<b>6.6</b>	18.7	<b>23.9</b>	<b>11.7</b>
EOF1-	OBS	39	2	10	0.6	<b>0.2</b>	<b>1.1</b>	19.9	<b>5.7</b>	<b>35.8</b>	19.1	11.5	20.3
	CM2.1	1188	18	242	0.6	<b>0.1</b>	<b>1.1</b>	19.7	<b>3.6</b>	<b>33.5</b>	18.4	<b>12.3</b>	<b>20.3</b>

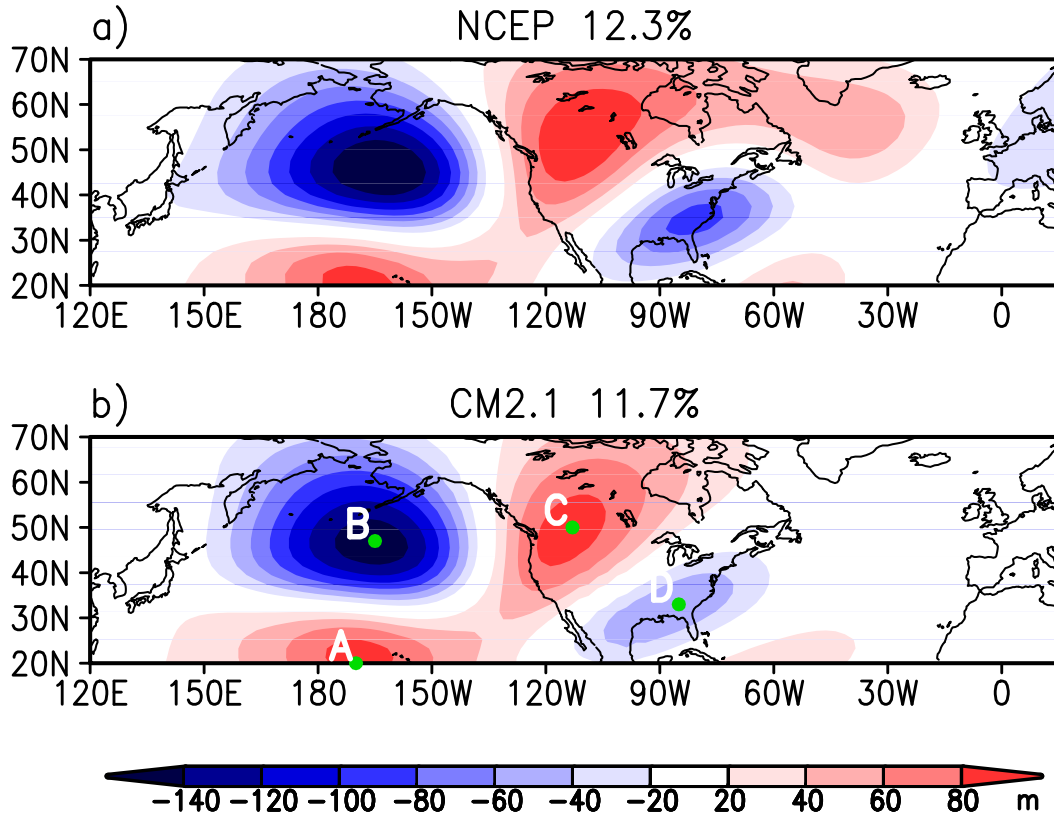


Figure 3.1: Spatial patterns of the leading empirical orthogonal function (EOF1) of 8-d low-pass filtered 250-hPa height for the 121-d winter period (starting from 1 December) over the region  $20^{\circ}$ – $70^{\circ}$ N,  $120^{\circ}$ E– $15^{\circ}$ W based on the (a) NCEP/NCAR reanalysis and (b) CM2.1 simulation. The patterns show the regression coefficients of low-pass filtered 250-hPa height versus the standardized temporal coefficients of EOF1. Units: m. The observed and simulated EOF1 modes account for 12.3% and 11.7% of the total variance, respectively. The four green dots A, B, C and D in (b) correspond to the four points used for computing the pattern index in section 4.4.1.

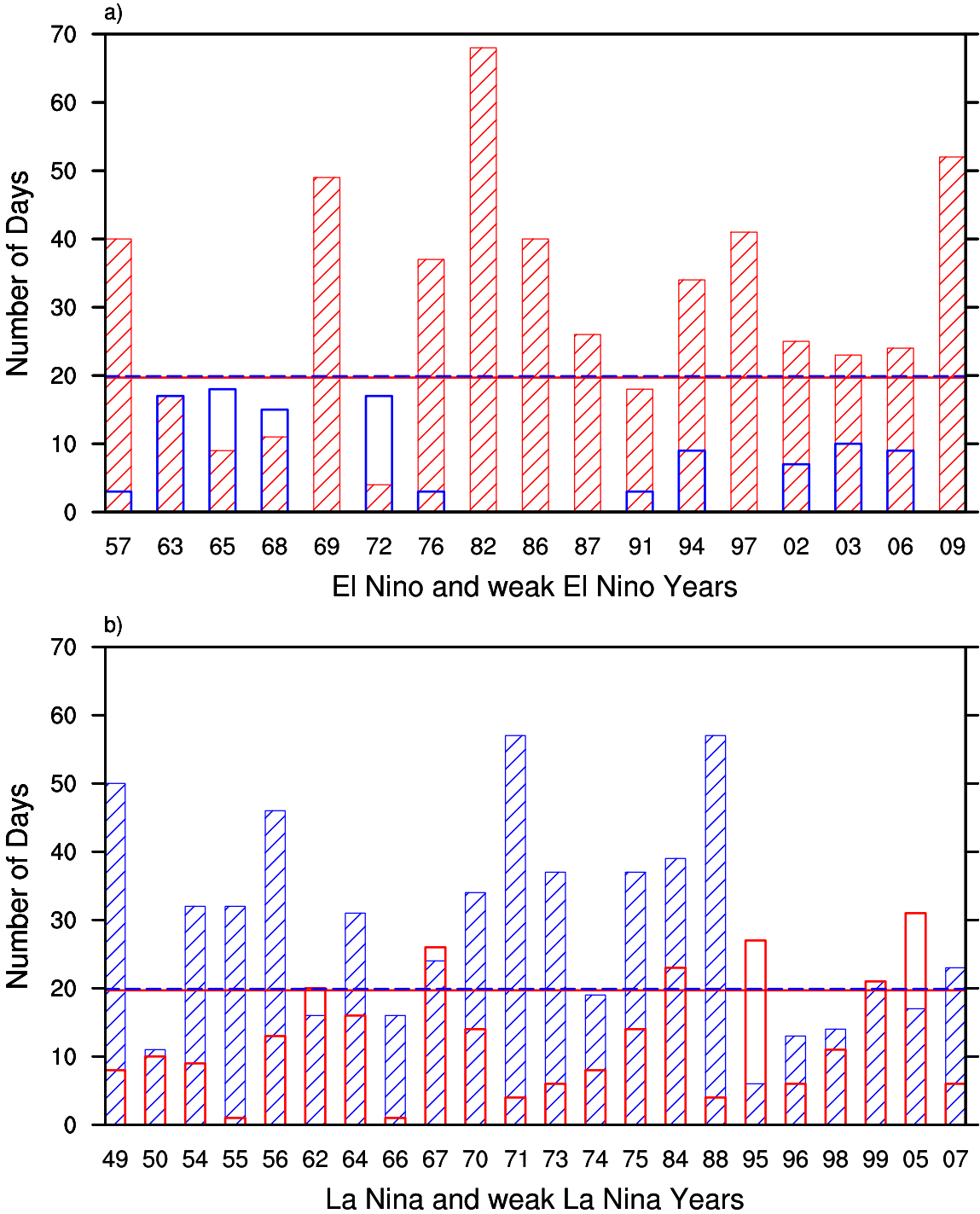


Figure 3.2: Number of positive (red bars) and negative (blue bars) EOF1 days for each (a) El Niño and (b) La Niña winter season based on the NCEP/NCAR reanalysis. A positive (negative) EOF1 day is defined as any day in which EOF1 index (temporal coefficient of the leading EOF as shown in Fig. 3.1a) exceeds  $\pm 1.0\sigma$ . A El Niño (La Niña) winter is identified when the DJF-mean Niño-3 index exceeds  $\pm 0.5\sigma$ . The average number of EOF1+ and EOF1- days for all winters are shown as the red and blue lines, respectively, in each panel.

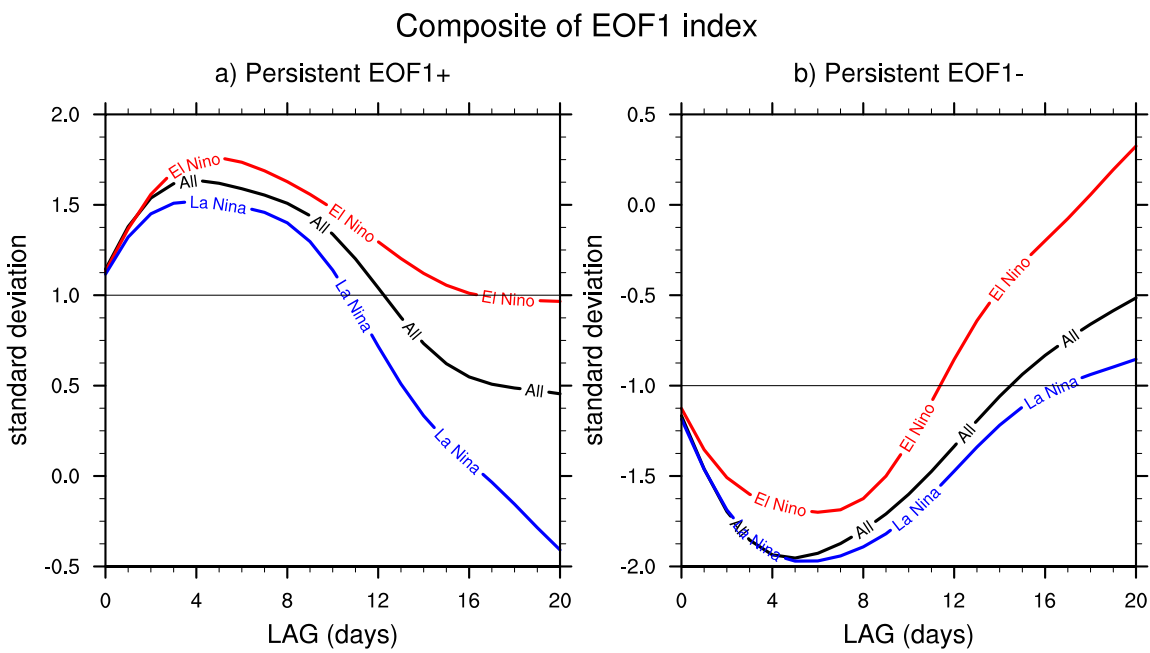


Figure 3.3: Time series of the composites of the EOF1 index based on the CM2.1 simulation. Composites are computed at various lags relative to the onset day of each persistent EOF1 event, and are based on the persistent EOF1+ (left panels) and EOF1- (right panels) episodes during El Niño winters only (red curve), La Niña winters only (blue curve), and all winters (black curve).

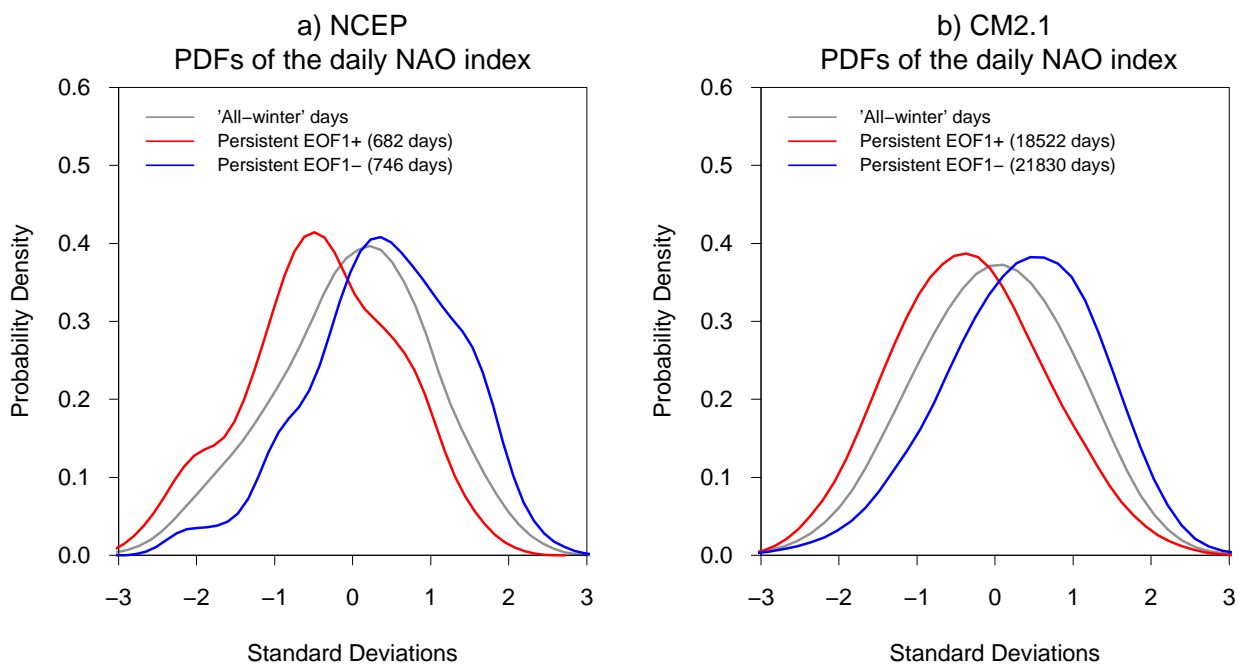


Figure 3.4: Probability density function (PDF) of the normalized daily NAO indices for days within the persistent EOF1+ events (red curve), persistent EOF1- events (blue curve) and ‘all-winter’ days (gray curve). Results based on the NCEP/NCAR reanalysis and and CM2.1 simulation are shown in the left and right panel, respectively.

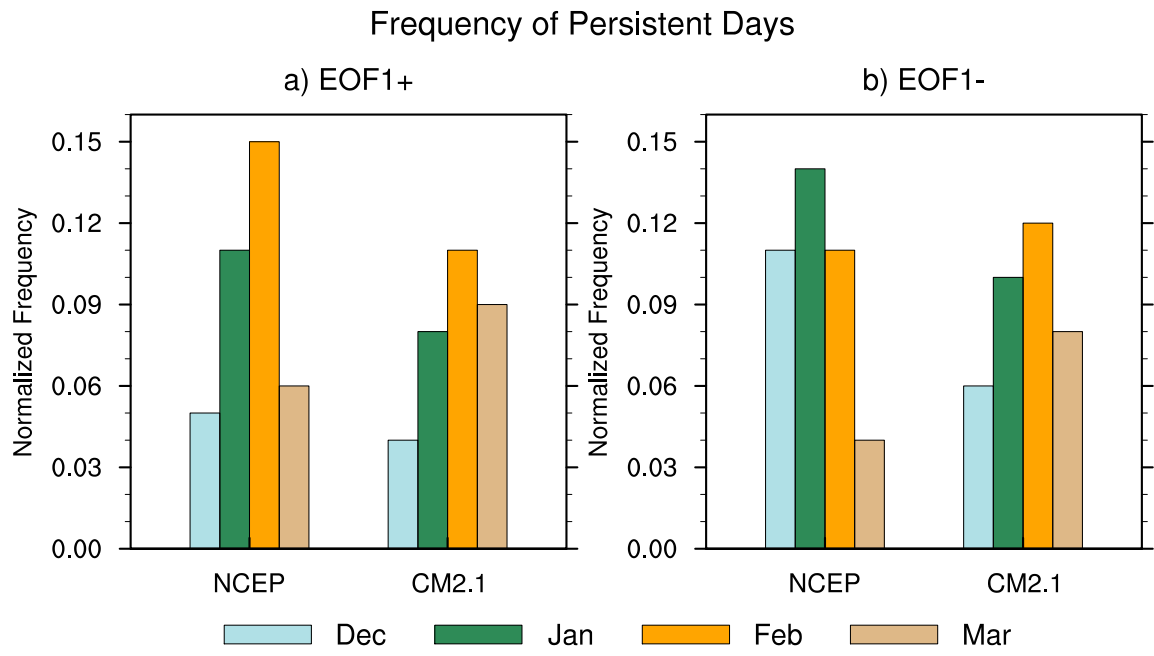


Figure 3.5: Distribution of frequency of occurrence of number of days belonging to persistent (a) EOF1+ and (b) EOF1– events for each calendar month of the winter season. The bars are normalized by dividing by the total number of days in that month. Results based on the NCEP/NCAR reanalysis and CM2.1 simulation are shown in the left and right side of each panel.

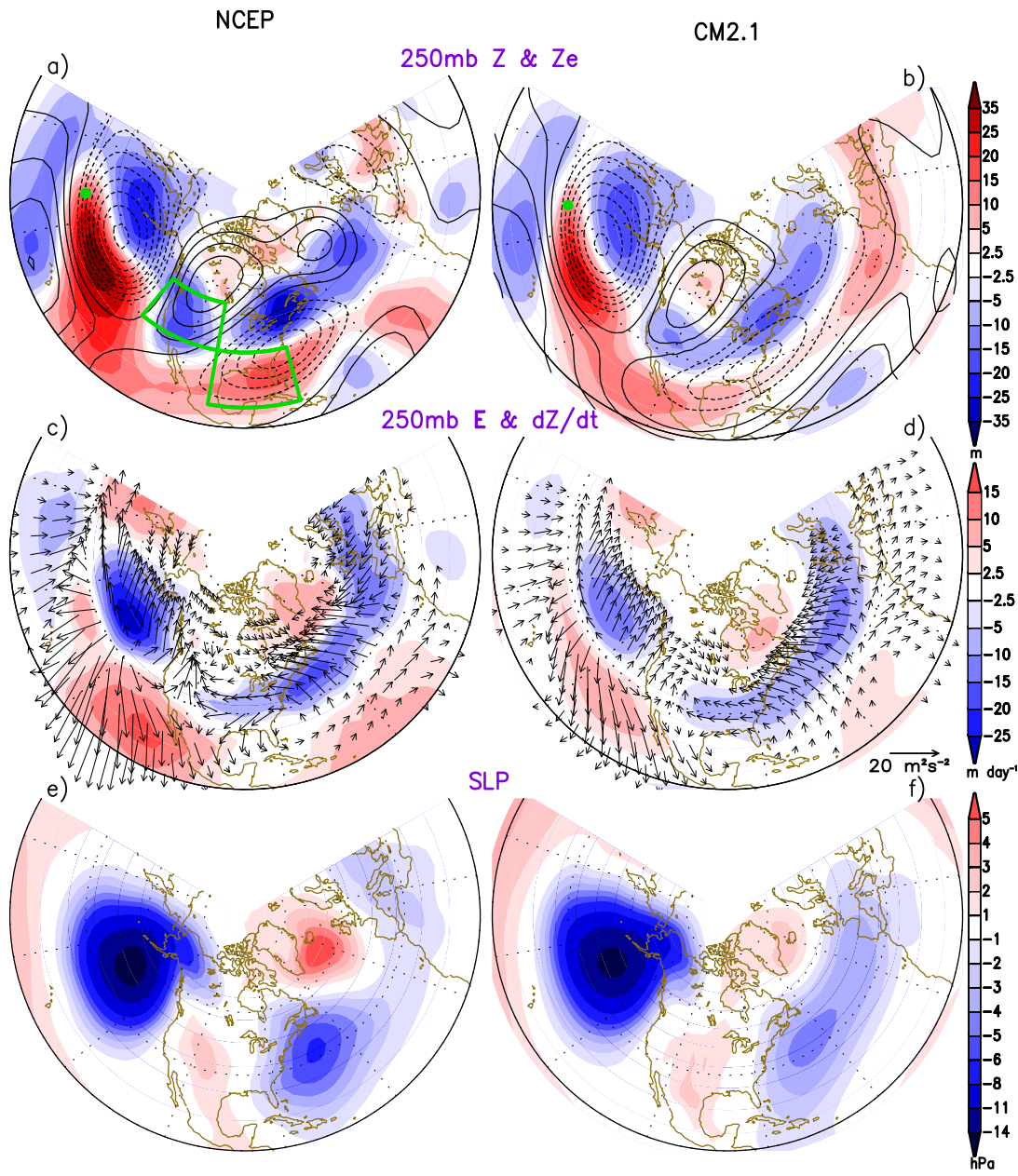


Figure 3.6: Horizontal distribution of composites of the (a) and (b) 8-d low-pass filtered 250-hPa geopotential height (contours, interval: 30 m; dashed contours indicate negative values) and 250-hPa envelope function (shading, see scale bar at right), (c) and (d) extended  $\mathbf{E}$  vectors (arrows, see scale at right) and eddy-induced height tendencies (shading, see scale bar at right), (e) and (f) 8-d low-pass filtered sea-level pressure (shading, see scale at right). The composites are averaged over the duration of all persistent EOF1+ events. Results based on the NCEP/NCAR reanalysis and CM2.1 simulation are shown in the left and right panels, respectively. The outermost latitude circle represents 15°N. Green dot in (a, b) denotes the location of the reference point for the one-point lagged regression analysis in Section 3.5. The green boxes in (a) depict the boundaries of regions used for computing the storm path index (SPI) in Section 3.5.2.

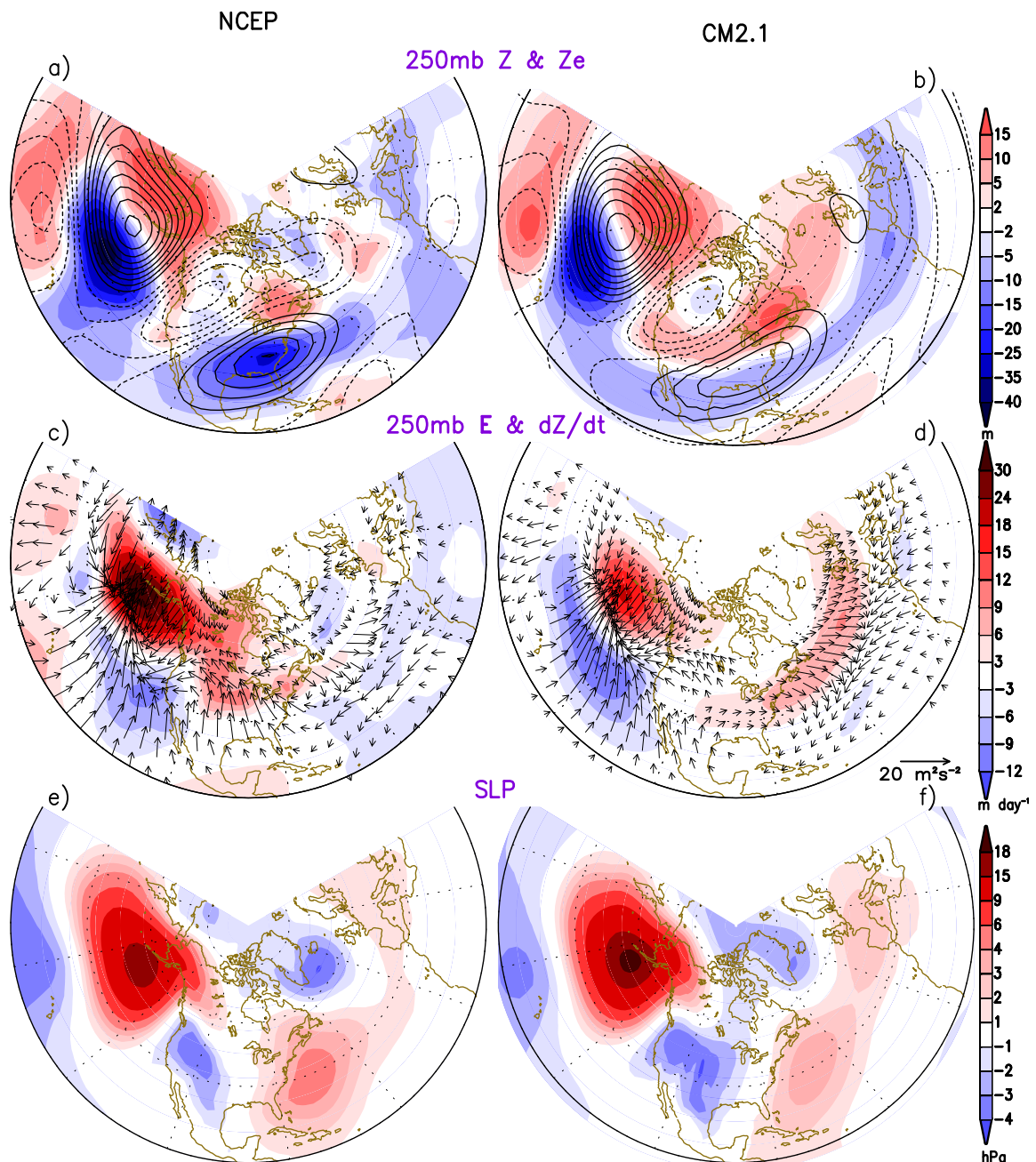


Figure 3.7: Same as in Fig. 3.6, but for results based on persistent EOF1 – events.

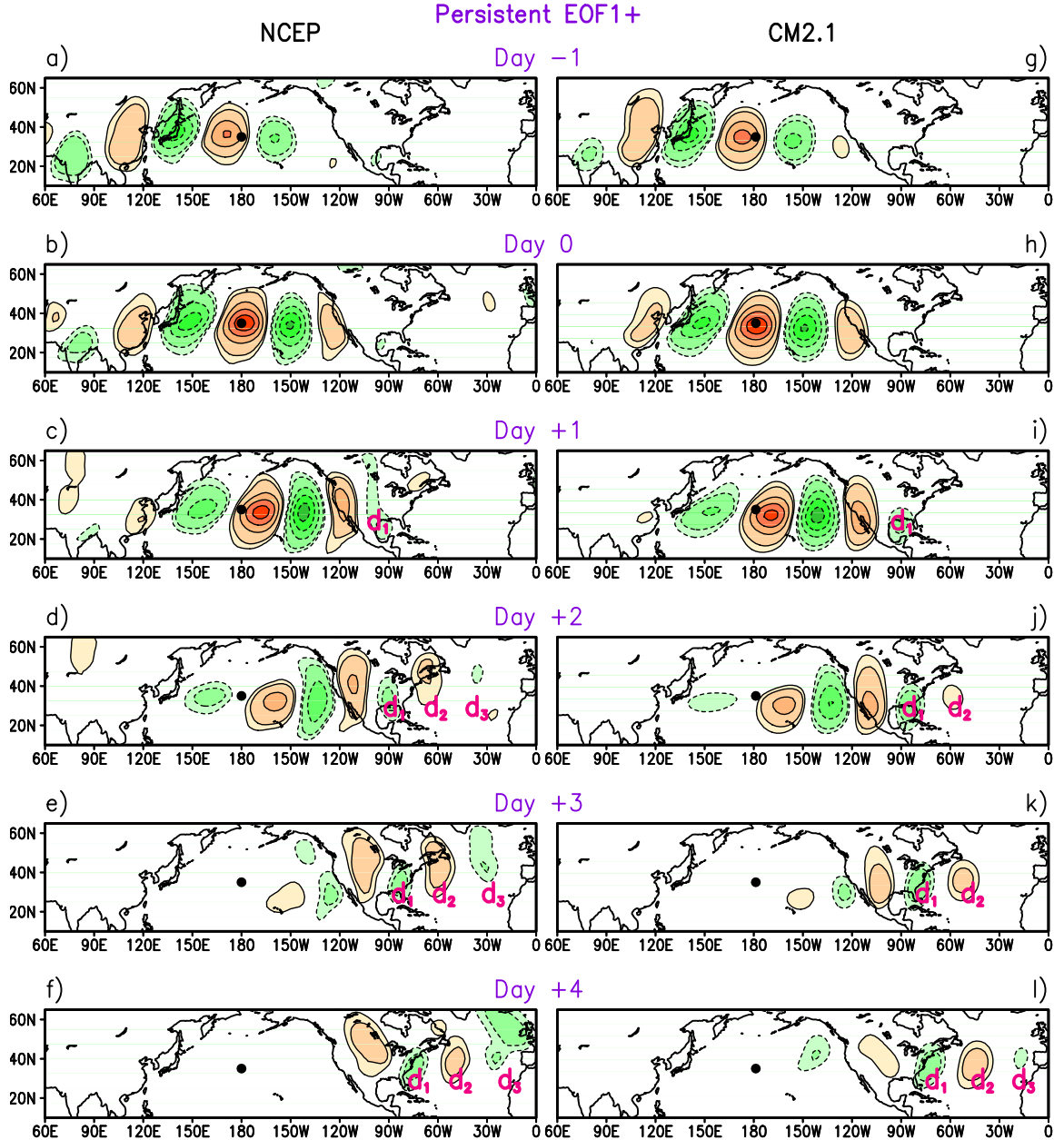


Figure 3.8: One-point lagged regression maps of unfiltered 250-hPa meridional velocity  $v$  anomalies during the persistent EOF1+ events. The reference time series is 250-hPa unfiltered  $v$  on day 0 at  $(35^\circ\text{N}, 180^\circ)$ , as indicated by the black dot in each panel and the green dot in Figs. 3.6a,b. Maps for lags of  $-1$ ,  $0$ ,  $+1$ ,  $+2$ ,  $+3$  and  $+4$  days are shown. The regression coefficients are contoured at  $\pm 2$ ,  $\pm 3$ ,  $\pm 6$ ,  $\pm 9$ ,  $\pm 12 \text{ m s}^{-1}$ . Dashed contours indicate negative values.

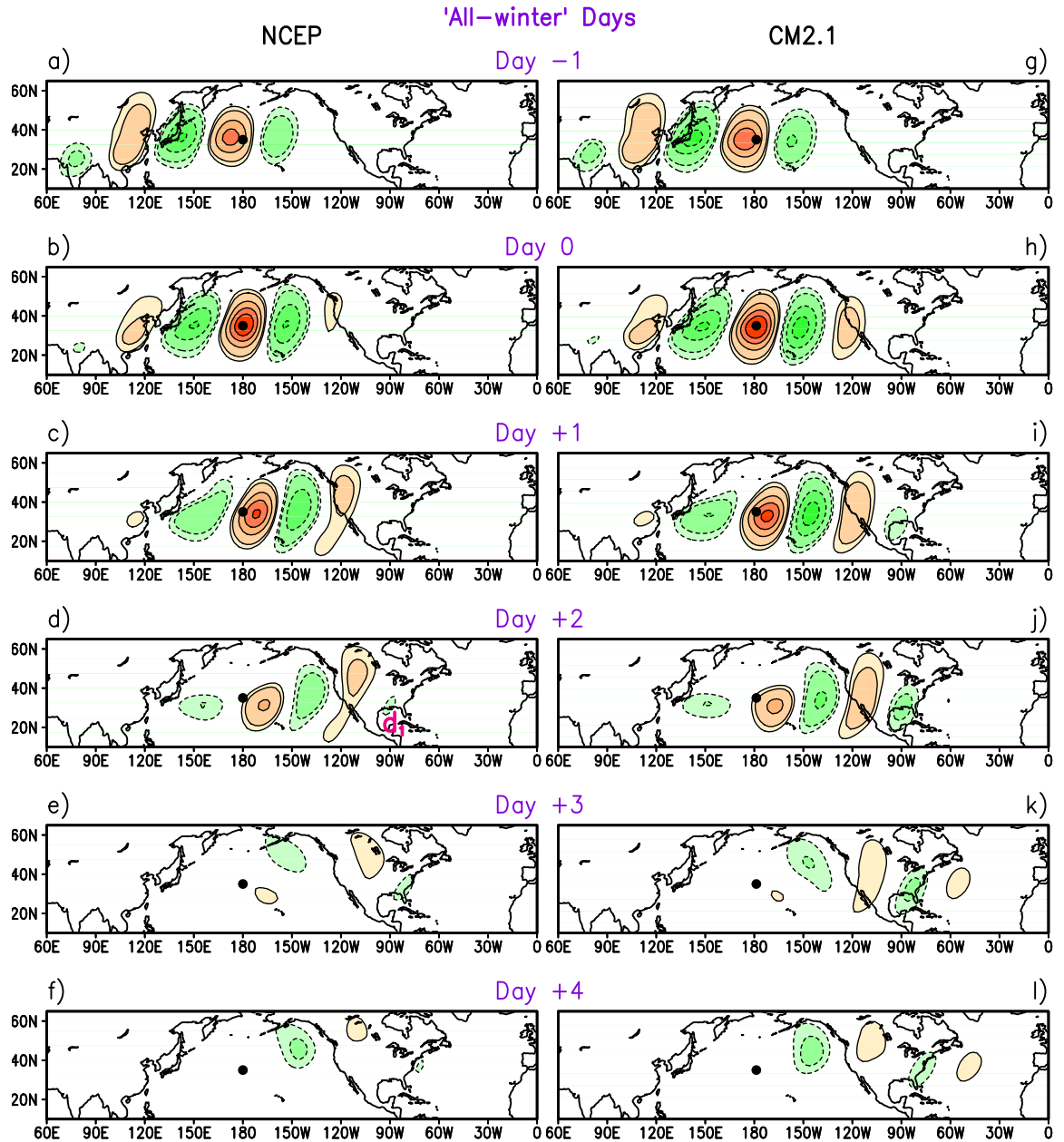


Figure 3.9: Same as in Fig. 3.8, but for results based on 'all-winter' days.

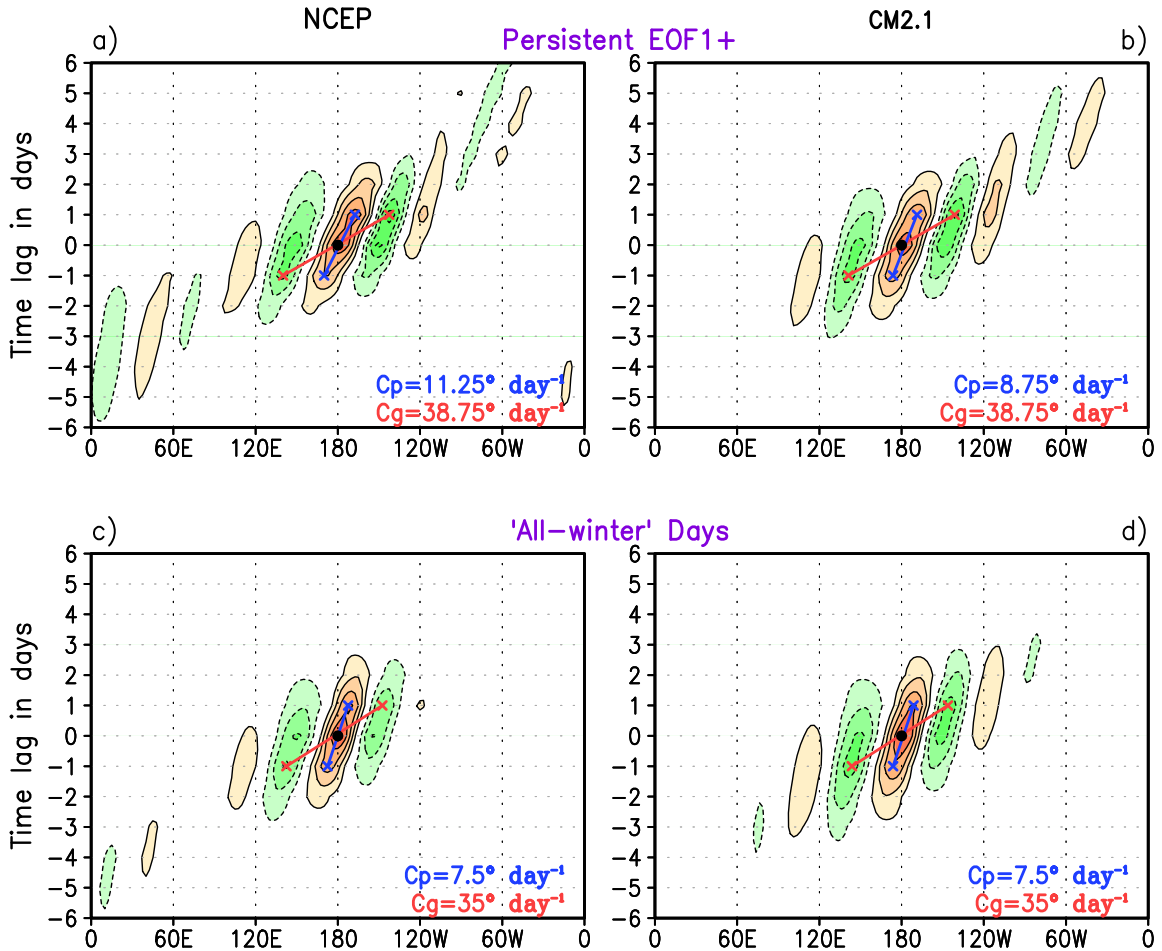


Figure 3.10: Longitude-time diagrams of one-point lagged regression coefficients of 250-hPa unfiltered meridional velocity at 35°N for (a) and (b) persistent EOF1+ events, and for (c) and (d) ‘all-winter’ days. The base point is indicated with a black filled dot. The phase speed ( $c_p$ ) and group velocity ( $c_g$ ) are determined by the slopes of blue and red lines, respectively. Specifically, the  $c_p$  of the individual eddies embedded in the wave packet is determined by the slope of the axis of the maximum positive regression coefficients crossing the base point (blue line), i.e., by dividing the distance between the positive extrema (blue crosses) on days  $-1$  and  $+1$  by 2 days. The  $c_g$  is given by the slope of the axis (red line) connecting the first negative center upstream of the base point on day  $-1$  and the one downstream of the base point on day  $+1$  (red crosses). Their values are presented at the lower right of each panel. Results based on the NCEP/NCAR reanalysis and CM2.1 simulation are presented in left and right panels, respectively. Contour interval: 3 m s<sup>-1</sup>. Dashed contours indicate negative values.

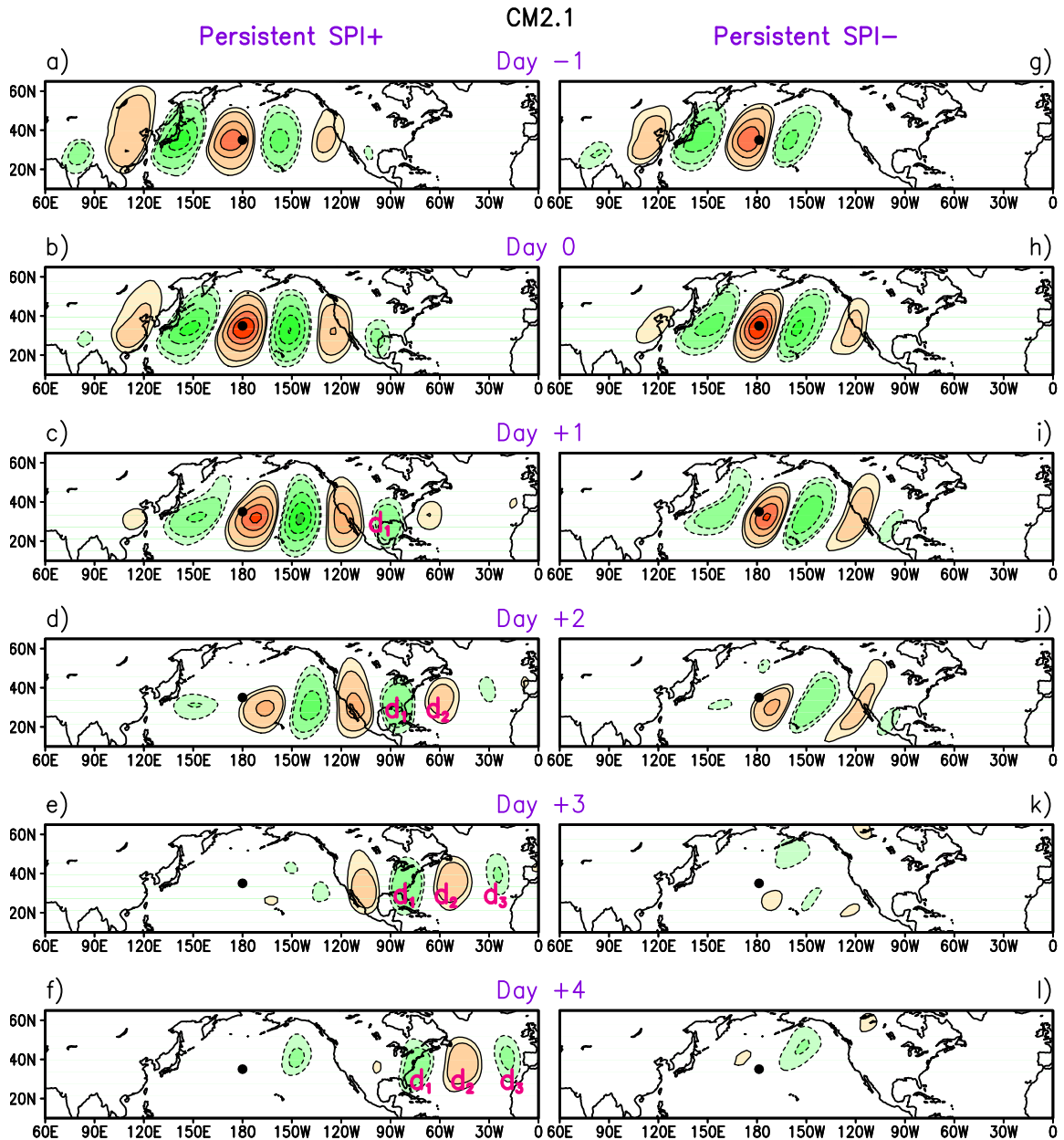


Figure 3.11: As in Fig. 3.8, but for the persistent SPI+ (left panels) and SPI- (right panels) episodes based on the CM2.1 simulation.

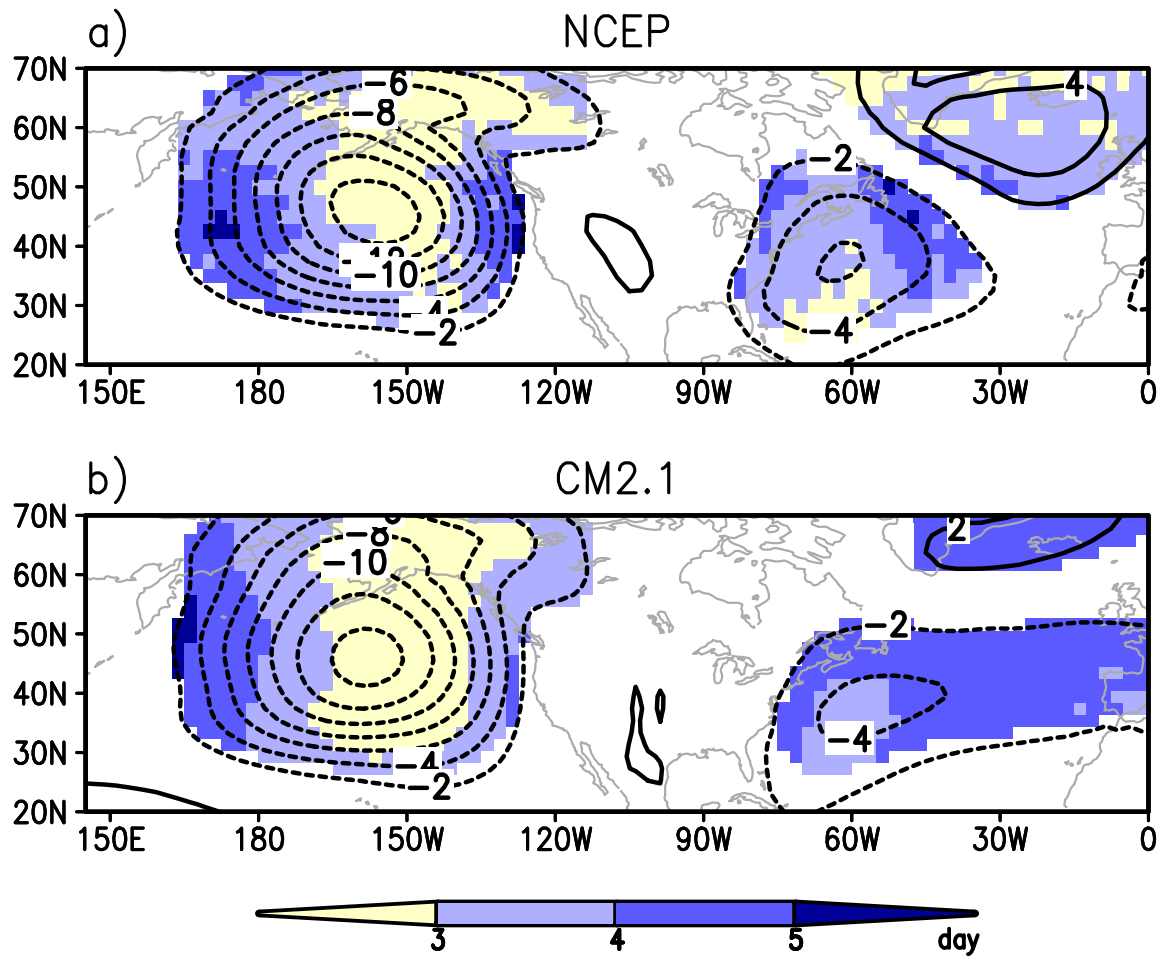


Figure 3.12: The shading shows the average of time lag  $\Delta T$  (in days) of the peak SLP at individual grid points relative to the peak day of the EOF1 index over all persistent EOF1+ event for the NCEP/NCAR reanalysis (top) and the CM2.1 simulation (bottom). See text for further details of the computation procedure. The contours show the average of low-frequency SLP anomaly over the duration of all EOF+ episodes (interval: 2 mb). No color shading is used in grid boxes that have relative small amplitude of the corresponding circulation anomaly.

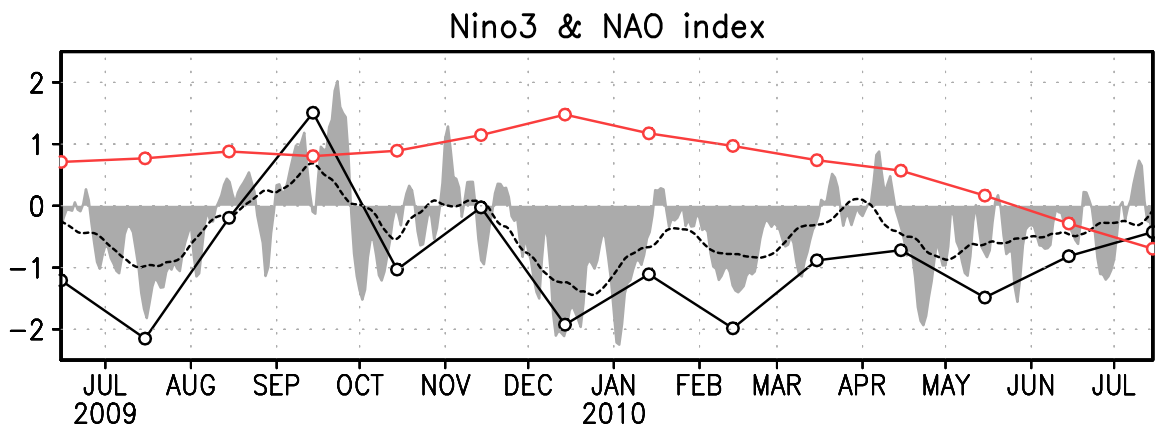


Figure 3.13: The time series of daily NAO index (shading), 30-d running mean (dashed line), monthly mean NAO index (solid line) and monthly ENSO index of Niño-3 (red line) for the 2009/2010 winter. (The daily and monthly NAO indices are obtained online from <ftp://ftp.cpc.ncep.noaa.gov/cwlinks/norm.daily.nao.index.b500101.current.ascii>, and <http://www.cpc.ncep.noaa.gov/products/precip/CWlink/pna/norm.nao.monthly.b5001> respectively.)

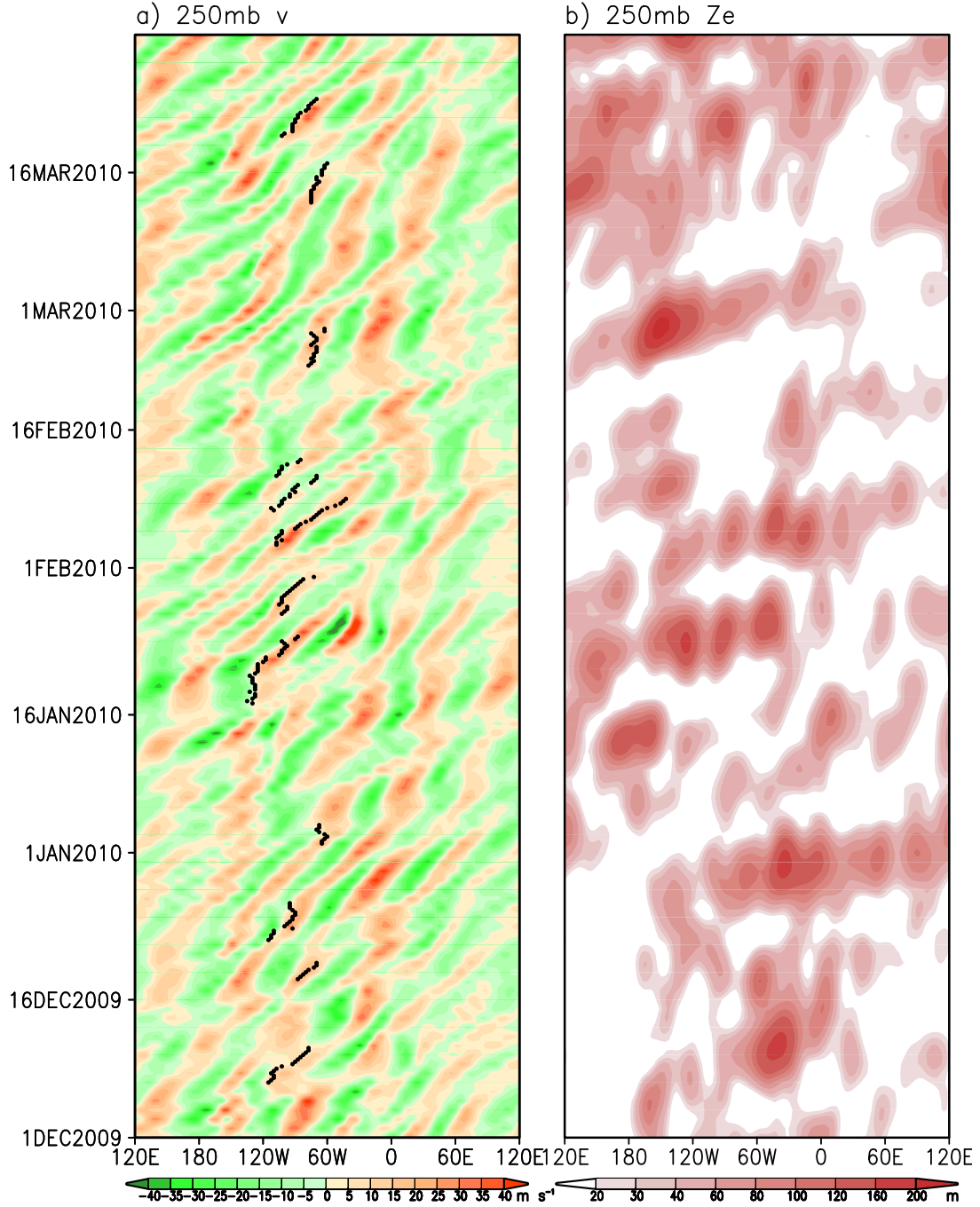


Figure 3.14: Longitude-time (Hovmöller) sections of (a) 250-hPa unfiltered anomalous  $v$  averaged over  $30^{\circ}$ – $45^{\circ}$ N and (b) 250-hPa anomalous envelope function ( $Z_e$ ). The amplitude in (b) at each meridian is obtained by averaging over a  $10^{\circ}$  latitude interval centered on the storm-track axis in  $Z_e$  and then applying Gaussian spatial smoothing with width of  $60^{\circ}$  (one wavelength) along the longitude axis. Each black dot in (a) denotes the time and longitude position of occurrence of the maxima of the 1000-hPa geostrophic relative vorticity every 6 h during the lifetime of each winter storm. The identified winter storms are obtained from [http://www.hpc.ncep.noaa.gov/winter\\_storm\\_summaries/winter\\_storm\\_summaries.shtml](http://www.hpc.ncep.noaa.gov/winter_storm_summaries/winter_storm_summaries.shtml). See text for more details.

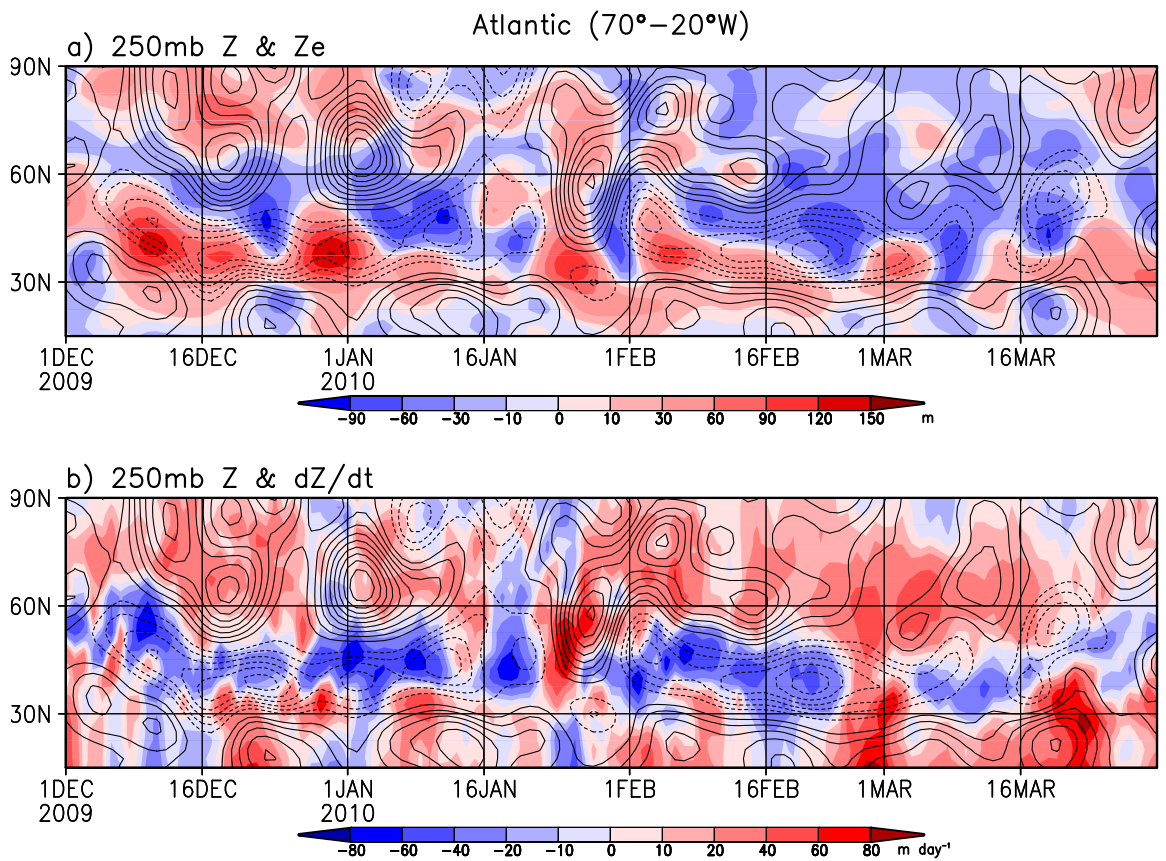


Figure 3.15: Latitude-time sections of anomalous 250-hPa (a) 8-d low-pass filtered  $Z$  (contour interval: 50 m; dashed contours indicate negative values) and envelope function  $Z_e$  (shading, see scale bar at bottom), (b) 8-d low-pass filtered  $Z$  (contours) and eddy induced height tendency (shading, see scale bar at bottom). All data are averaged over the  $70^{\circ}$ – $20^{\circ}$ W zone.

# Chapter 4

## Results from Atmospheric GCM Simulations

### 4.1 Introduction

In chapters 2 and 3, evidence from both observations and the coupled model simulations are presented showing that NAO-like response over the Atlantic sector to the ENSO-related SST forcing in the tropical Pacific can be attributed to:

- 1) the downstream displacement of the pattern of the eddy induced height tendency relative to the pattern of geopotential height; and
- 2) the downstream development of the wave packet associated with the Pacific storm track toward the Atlantic storm track.

The main purpose of this chapter is to further demonstrate the impacts of the tropical Pacific SST forcing on the atmospheric variability in the NA sector. To do so, ensemble atmospheric GCM (AGCM) integrations, with anomalous SST prescribed only in the tropical Pacific, are designed and tested for their ability to reproduce some of the results described in chapters 2 and 3.

The structure of this chapter is as follows. In section 4.2, the experimental design and SST forcing are described. In section 4.3, the seasonal averaged characteristics of surface climate response and eddy-mean flow interaction are analyzed, along with the degree of agreement among the individual ensemble members. In section 4.4, daily values from the AGCM output are used, and the frequency and duration of the persistent episodes selected from the AGCM experiments are documented. Conclusions are drawn, and implications of the AGCM results are discussed in section 4.5.

## 4.2 Experimental design

The model employed in this chapter is AM2.1, the atmospheric component of CM2.1. Readers are referred to chapter 2 for more detailed description of the model. Three experiments with AM2.1 are carried out:

- a 30-yr control experiment (CTRL) in which the 2000-yr averaged climatological seasonal cycle of the SST field generated in the CM2.1 simulation is imposed at the lower boundary at all ocean gridpoints
- an El Niño experiment (ELNO)
- a La Niña experiment (LANA)

The latter two experiments differ from the CTRL experiment only in the prescription procedure of the SST field in the tropical Pacific. Monthly-averaged composite El Niño (La Niña) anomalies are obtained from composites of El Niño (La Niña) events identified in the 2000-yr simulation with CM2.1. The composite monthly SSTAs in the tropical Pacific ( $15^{\circ}\text{S}$  to  $15^{\circ}\text{N}$ ,  $135^{\circ}\text{E}$  to the American coasts) from Mar(0) to Nov(1) is then added to the climatological mean seasonal cycle. All anomalies outside of the tropical Pacific are masked out. A 30-member ensemble of the 21-month [Mar(0) to Nov(1)] integrations is performed separately for the composite El Niño forcing and La

Niña forcing scenario. Within each ensemble, the individual members are initiated from independent conditions as extracted from various years in the 30-yr-long CTRL experiment. The design of these experiments is very similar to that used in [Lau and Nath \(2009\)](#), to which the readers are referred for further details. In the following analysis, the anomalous response of AM2.1 to composite SST forcing prescribed in tropical Pacific region is obtained by subtracting the 30-yr average of the CTRL run from the 30-member ensemble mean of the ELNO or LANA experiment.

## 4.3 Seasonal averaged characteristics

### 4.3.1 Surface climate response to ELNO and LANA

Fig. 4.1 shows the ELNO (left panels) and LANA (right panesl) responses of the FM average of the SLP, SAT, and precipitation. The ELNO response exhibits a dipolar pattern in SLP over NA, with positive anomalies over the Iceland and negative anomalies extending from southern U.S. to southern Europe across the Atlantic subtropics. This dipolar SLP response is associated with a quadruple pattern of SAT anomalies over NA. The precipitation response to ELNO (Fig. 4.1c) clearly shows the anomalous wet conditions extending eastward from the California coast to southern Europe, and anomalously dry conditions over northern Europe. These structures of the anomalies are broadly consistent with the composites El Niño events simulated by CM2.1 (Figs. 2.8b,d).

The LANA response appears approximately opposite to the ELNO response but there are differences in the position of the extrema. Over the western NA, the SLP response to ELNO is stronger than the response to LANA, whereas in the eastern NA the response to LANA is stronger. This feature is also consistent with the ENSO composite results from the CM2.1 simulation (Figs. 2.8f,h).

The qualitative comparison between the ensemble mean of the AGCM simulation and the coupled model simulations indicate that the former does resemble the latter. Now, we move on to examine the extent of agreement among the individual ensemble members. To address this question, we compare the FM-mean SLP anomalies from each ensemble member of the ELNO and LANA experiments with the ensemble mean of the ELNO and LANA experiments, respectively, using a spatial correlation statistic. The statistic is computed as the correlation of area-weighted anomalies at all grid points in the NA domain covering  $20^{\circ}\text{--}70^{\circ}\text{N}$ ,  $80^{\circ}\text{W}\text{--}20^{\circ}\text{E}$  (same region as the EOF analysis of SLP performed in Fig. 2.5). Correlations for each individual ensemble members are shown in Fig. 4.2. In the case of ELNO experiment (Fig. 4.2a), 25 out of 30 of the ensemble members are positively correlated with the ensemble mean. For the LANA experiment (Fig. 4.2b), only 1 ensemble member is negatively correlated with the ensemble mean, and the spread of correlations within the ensemble is small. Hence, the differences between individual ensemble members are relatively small. These results indicate that there is a relatively high degree of reproducibility of the forced response.

### 4.3.2 Eddy-mean flow interaction in AGCM results

Fig. 4.3 shows the FM-mean ELNO (left) and LANA (right) responses in 250-hPa geopotential height (contours), rms of filtered 500-hPa height (shading in panels a,b),  $\mathbf{E}$  (arrows) and  $\partial Z/\partial t$  (shading in panels c,d). The ELNO and LANA experiments reproduce the teleconnection pattern associated with El Niño and La Niña events based on CM2.1 (Figs. 2.9e,f) remarkably well. Most strikingly, the 250-hPa height response in the ELNO experiment (Fig. 4.3a) is characterized by a negative NAO pattern with below-normal heights extending eastward from the southeastern U.S. to NA, and above-normal heights extending from western Canada to southern Greenland. The polarities of these anomaly centers are reversed in the LANA experiment

(Fig. 4.3b). These results indicate that much of the 250-hPa height changes on inter-annual time scale may be attributed to the tropical Pacific SST forcing alone.

Patterns of the storm track,  $\mathbf{E}$  and  $\partial Z/\partial t$  also bear a considerable resemblance to those in Figs. 2.9e,f and Figs. 2.10e,f. These results are consistent with the model study of Seager et al. (2010a), who demonstrate that changes in eddy propagation in the PNA sector during ENSO events can be generated by tropical Pacific SST forcing alone. Our results further indicate that the changes in transient eddy forcing over the NA sector are also linked to the ENSO-related SSTAs in the tropical Pacific.

## 4.4 Statistics of persistent episodes in AGCM

To further demonstrate the impact of the tropical Pacific SST forcing on the frequency and duration of the persistent EOF $\pm$  and SPI $\pm$  events, we proceed to use the AGCM output and restrict analysis to the daily data within the 121-day winter period starting from 1 December. Thus the AGCM datasets used here consists of:

- 121 days  $\times$  29 yr based on CTRL experiment
- 121 days  $\times$  30 members based on ELNO experiment
- 121 days  $\times$  30 members based on the LANA experiment

The 250-hPa low-pass filtered geopotential height and envelope function ( $Z_e$ ) are calculated as deduced in Section 3.2.3.

### 4.4.1 Selection of persistent flow pattern and storm path pattern

On the basis of the EOF1 pattern presented in Fig. 3.1b, we derive daily low frequency flow indices for CTRL, ELNO and LANA separately. The index is defined based on

four centers of action:

$$Z250 = \frac{Z'_A}{\sigma_A} + \frac{Z'_C}{\sigma_C} - \frac{Z'_B}{\sigma_B} - \frac{Z'_D}{\sigma_D}. \quad (4.1)$$

Here A, B, C and D are four grid points shown in Fig. 3.1b.  $Z'$  is the deviation of the 8-day low-pass filtered 250-hPa height from its corresponding climatology annual cycle at those grid points. The daily anomalies at individual grid point are normalized by the local temporal standard deviation  $\sigma$ , where  $\sigma^2 = \langle \overline{Z'^2} \rangle$ . The overbar indicates a temporal average over the 121-day period for an individual ensemble member, the angle bracket denotes the 30-member ensemble mean for the ELNO and LANA experiments, and 29-yr averages for the CTRL experiment. The same climatological annual cycle, defined as the mean plus the first three harmonics of the 29-yr mean annual cycle from the CTRL experiment, is used for the three experiments. Thus the difference between the ELNO (LANA) and CTRL experiment is taken as the response to the prescribed SST forcing in the tropical Pacific region.

Analogous envelope function indices (Z250EF) are defined as the normalized difference of  $Z_e$  averaged over the region between  $100^\circ$ – $70^\circ$ W,  $20^\circ$ – $35^\circ$ N and  $130^\circ$ – $100^\circ$ W,  $35^\circ$ – $50^\circ$ N (same regions where the SPI index was defined in Section 3.5.2). Then the same selection criteria, introduced in section 3.2.4, are applied to the Z250 and Z250EF indices for the CTRL, ELNO and LANA separately, to define the persistent events in each of the three experiments.

#### 4.4.2 The dependence of the persistent events on the AGCM experiments

The same statistics of the selected persistent  $Z250\pm$  and  $Z250EF\pm$  events for the three experiments are displayed in Table 4.1. The average number of both  $Z250+$  and  $Z250-$  events in the CTRL experiment is approximately 40. The number of  $Z250+$  events in the ELNO experiment is larger than that in the LANA experiment

(49 vs. 5). Also, the number of Z250+ days in the ELNO experiment is significantly larger than the corresponding accounts in the LANA experiment by a factor of 3–4. The average duration of persistent Z250+ in the CTRL experiment is 19.4 d, which is comparable to the average duration of the persistent EOF1+ events based on all winter seasons in the CM2.1 simulation (18.7 d; see Table 3.1). However, the average duration increases substantially in the ELNO experiment (55.1 d), and is more than three times longer than that in the LANA experiment (see also Fig. 4.4a). Conversely, Z250– events are more frequent and longer-lasting in LANA experiment. As for the persistent Z250EF $\pm$  events, although the difference between ELNO and LANA is not as distinct as for the persistent Z250 $\pm$  events, similar conclusion also holds. Larger number of events and days for Z250EF+(−) are simulated in the ELNO (LANA) experiment.

The persistence characteristics of the Z250 $\pm$  events are further illustrated by compositing the temporal evolution of Z250 indices relative to the onset day, as shown in Fig. 4.4. This procedure has been performed separately over the persistent events during the ELNO, LANA, and CTRL experiments. Since the number of Z250EF $\pm$  cases is too small to generate statistically significant results, only the results for the persistent Z250 $\pm$  events are shown. For the persistent Z250+ events (Fig. 4.4a), the Z250 index in the ELNO experiment (red curve) stays above 1.0 beyond 20 days after the onset day. This persistence time scale is longer than that of the Z250 index during both CTRL and LANA runs. The opposite situation holds in the persistent Z250– events (Fig. 4.4b).

The distribution of the duration for all persistent Z250+(−) events found in the ELNO (LANA) and CTRL experiments is shown with a boxplot in Fig. 4.5a(b). The box of each plot shows the interquartile range. The central line of the box shows the median. The whiskers of the box show the minimum and maximum points in the distribution that are not outliers. Outliers are marked with an “x” and are defined as

any points that are greater than 3/2 times the interquartile range from the ends of the box. The mean value is plotted with a filled circle. Fig. 4.5a shows that persistent Z250+ events in the ELNO experiment have significantly longer duration as well as greater interquartile range than the events in the CTRL experiment. Opposite conclusion for persistent Z250– events can be deduced from Fig. 4.5b.

As shown in Section 3.5.1, the downstream development is more effective during the persistent flow pattern or storm path pattern. The increases in both the frequency and duration of the persistent Z250+(−) and Z250EF+(−) events in the ELNO (LANA) experiment indicate that the wave packets continuously propagate into the NA from the upstream NP. The barotropic forcing of the synoptic-scale eddies embedded in these wave packets over the NA leads to the formation of the more slowly-varying flow pattern that is associated with the NAO− (NAO+) phenomenon in the ELNO (LANA) experiment.

## 4.5 Summary and discussion

The evidence presented in this chapter indicates that the seasonal averaged surface climate in late winter during ENSO winters can be reproduced in the ensemble integrations of AGCM forced by monthly varying ENSO-related SST condition in the tropical Pacific region alone (Fig. 4.1). The small differences between individual ensemble members (Fig. 4.2) also indicate that there is a relatively high degree of reproducibility for the forced response. The reproduction of the transient eddy effects in the ELNO and LANA experiments (Fig. 4.3) further provides evidence that ENSO-related SSTAs in the tropical Pacific play a significant role in modulating eddy-mean flow interactions over the NA sector.

The frequency and duration dependence of the submonthly persistent episodes on the El Niño/La Niña forcing (Fig. 4.4 and 4.5; Table 4.1) are consistent with those

statistics of the persistent episodes in the two opposing phases of the ENSO cycle. Presuming that the downstream extension of the wave packets from the NP towards NA is notably stronger during the persistent episodes, the more frequent and longer-lasting persistent equatorward (poleward) shifted jet stream and storm path episodes contribute to the stronger and more steady transient eddy forcing, which in turn is conducive to the formation of the flow pattern that resembles the negative (positive) phase of the NAO in the ELNO (LANA) experiments.

It is noteworthy that although the patterns of the height anomalies in the ELNO and LANA runs (Figs. 4.3a,b) resemble those in the El Nino and La Nina composites based on output from the fully coupled simulation (Figs. 2.9e,f), the amplitudes in the former are generally higher than those in the latter. These results could be due to the absence of oceanic negative feedback on surface heat flux forcing in the midlatitude in the AGCM simulation ([Lau and Nath 1996](#)). Moreover, since there is no two-way air-sea coupling in both the tropical Indian and Atlantic Oceans in the AGCM simulation, the difference between AM2.1 and CM2.1 results could also be attributed to the remote SST forcing originating from these ocean basins, which could amplify or reduce the midlatitude atmospheric response (e.g., [Alexander et al. 2002](#); [Annamalai et al. 2007](#)). As noted in [Annamalai et al. \(2007\)](#), height anomalies forced by Indian Ocean SSTAs are opposite to those forced by tropical Pacific SSTAs over the PNA region. In the hybrid coupled models like the Tropical Ocean and Global Atmosphere-Mixed Layer (TOGA-ML) model described by [Lau and Nath \(1996\)](#), where the tropical SST variability is specified but the midlatitude atmosphere is coupled with a slab ocean mixed-layer model, the extratropical positive oceanic feedback on the atmosphere could reinforce atmospheric anomalies that have driven them. Further investigation of these issues, and especially the relative importance of the different factors involved, would require additional simulations with coupling

being confined to extratropical and tropical ocean basins, either separately or in combination with each other. Such investigation is beyond the scope of this study.

Table 4.1: As in Table 3.1, but for summary statistics for the four types of persistent events based on three AGCM experiments, CTRL (CN), ELNO (EN) and LANA (LN).

Type	No. of event			No. of events per DJFM season			Avg. No. of days per DJFM season			Avg. duration (days)		
	CN	EN	LN	CN	EN	LN	CN	EN	LN	CN	EN	LN
Z250+	40	49	5	1.4	<b>1.6</b>	<b>0.2</b>	63.2	<b>104.7</b>	<b>29.1</b>	19.4	<b>55.1</b>	<b>16.8</b>
Z250-	41	4	56	1.4	<b>0.1</b>	<b>1.9</b>	57.7	<b>16.3</b>	<b>91.9</b>	20.1	<b>12.2</b>	<b>32.6</b>
Z250EF+	11	24	12	0.4	<b>0.8</b>	<b>0.4</b>	59.8	<b>87.2</b>	<b>56.3</b>	14.6	<b>15.5</b>	<b>18.9</b>
Z250EF-	8	4	9	0.3	<b>0.1</b>	<b>0.3</b>	61.1	<b>33.6</b>	<b>64.6</b>	14.8	12.2	11.6

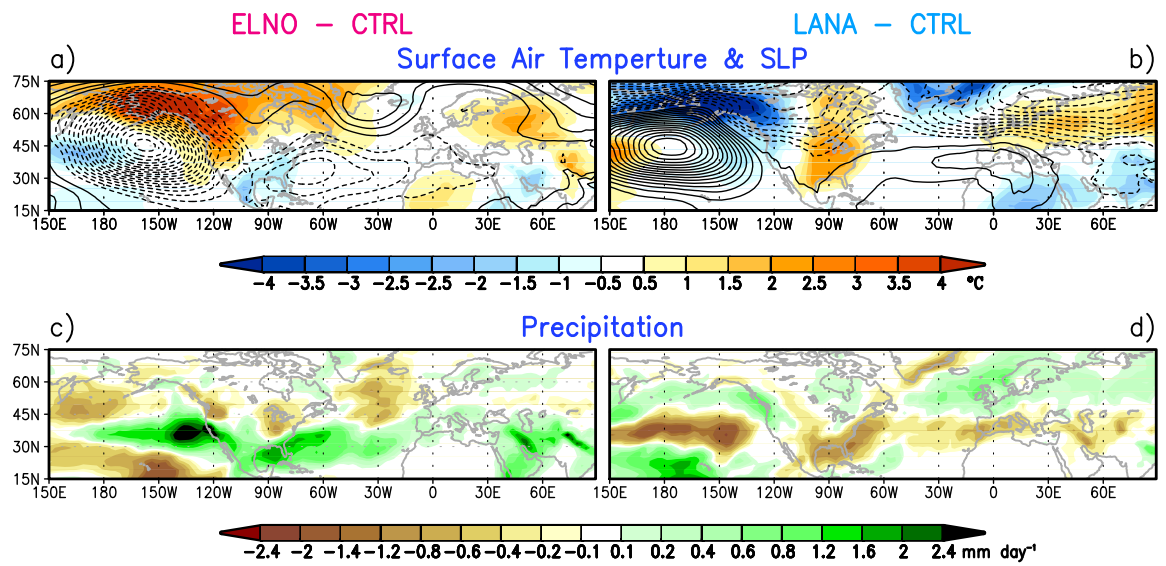


Figure 4.1: Same as in right panels of Fig. 2.8, but for results based on responses in ELNO (left panel) and LANA (right panel) experiments. Contour interval is 1 mb. Results are obtained by subtracting the data for the CTRL experiments from the output of the ELNO or LANA experiments.

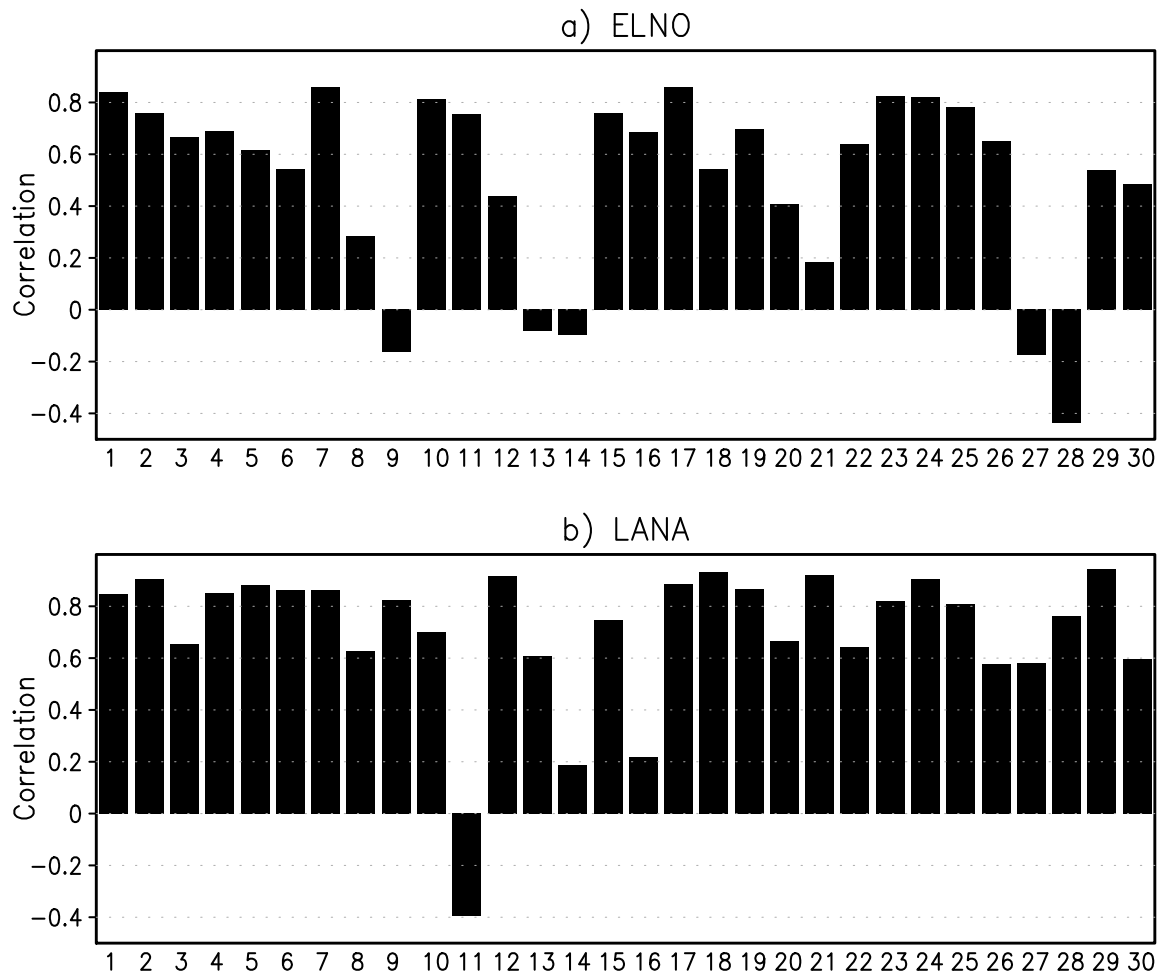


Figure 4.2: Pattern correlations between the ensemble mean and the 30 individual ensemble members, as computed in the NA region ( $20^{\circ}$ – $70^{\circ}$ N,  $80^{\circ}$ W– $20^{\circ}$ E) for the FM-mean SLP anomalies for (a) ELNO, (b) LANA experiment.

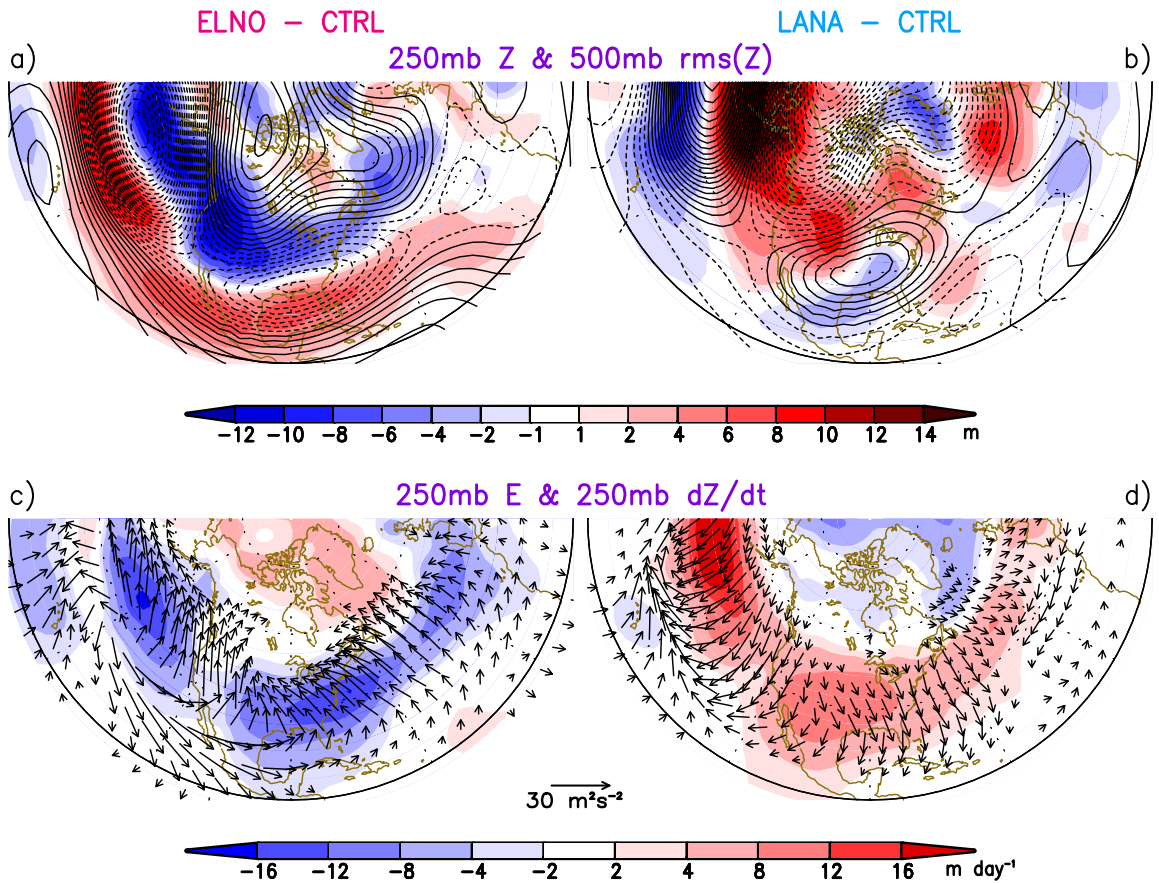


Figure 4.3: (a,b) Same as in Fig. 2.9e,f, (c,d) same as in Fig 2.10e,f, but for results based on responses in ELNO (left panels) and LANA (right panels) experiments. Results are obtained by subtracting the data for the CTRL experiments from the output of the ELNO or LANA experiments.

### Composite of Z250 index

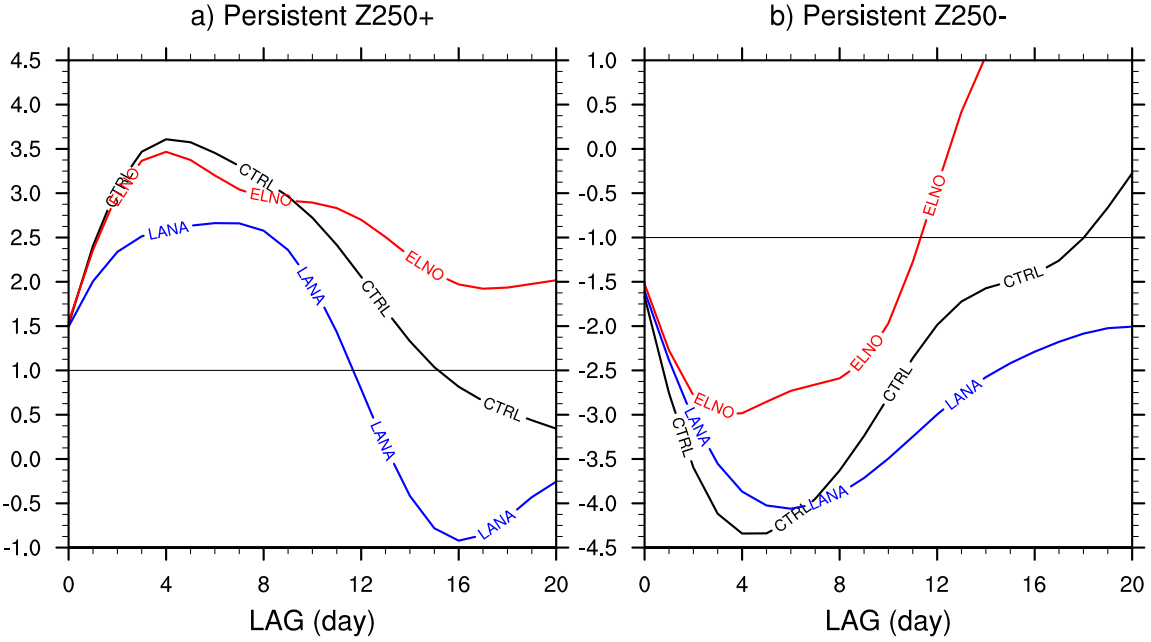


Figure 4.4: Same as in Fig. 3.3, but for the results based on the a) persistent Z250+ and b) Z250– episodes in ELNO (red curve), LANA (blue curve) and CTRL(black curve) run.

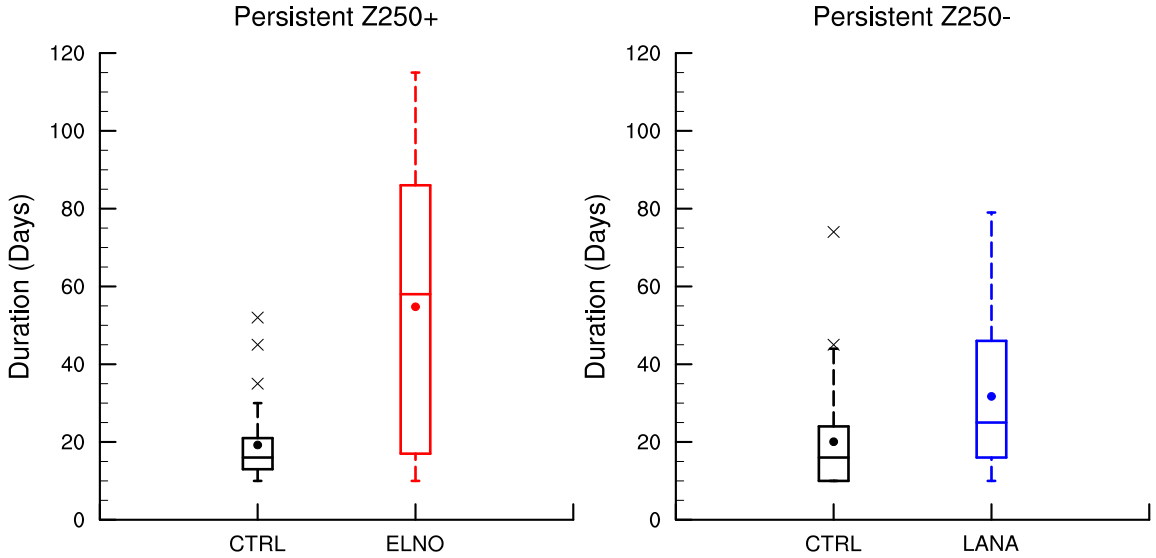


Figure 4.5: Boxplots showing distribution of mean duration for a) persistent Z250+ and b) Z250– (right) in CTRL, ELNO, LANA experiments. The box of each plot shows the interquartile range. The central line of the box shows the median. The whiskers of the box show the minimum and maximum points in the distribution that are not outliers. Outliers are marked by “x”. The mean is shown by a dot. Outliers are defined as any points that are greater than 3/2 times the interquartile range from the ends of the box.

# **Chapter 5**

## **Influences of ENSO on Stratospheric Variability and Downward Penetration of the Stratospheric Perturbations to Lower Troposphere**

### **5.1 Introduction**

The late winter teleconnection between ENSO and NAO via the tropospheric pathway due to the role of transient eddies has been investigated in previous chapters. As indicated in chapter 2, due to the low vertical resolution of the model stratosphere in CM2.1, the El Niño effect on the simulated extratropical stratosphere is very weak. The ENSO/NAO relationship identified in the CM2.1 simulation is primarily due to the tropospheric pathway. In this chapter, we use another 800-yr integration of the general circulation model with a more realistic upper atmosphere (CM3; see

[Donner et al. 2011](#)), and compare the ENSO/NAO relationship as simulated in this model with that in CM2.1. Such comparison provides insights into the impact of the stratospheric processes on the ENSO/NAO relationship. Furthermore, this extended GCM integration allows for adequate sampling to reveal the independent effects of ENSO and the variability in the stratospheric polar vortex. Such analysis is not feasible with the limited observational record.

In a GCM simulation forced with perpetual January El Niño or La Niña SST conditions in the Pacific, [Taguchi and Hartmann \(2006\)](#) have shown that wave-1 Stratospheric Sudden Warmings (SSW) are twice as likely to occur in El Niño winters than in La Niña winters, while wave-2 events occur more frequently in the La Niña condition. However, [Butler and Polvani \(2011\)](#) recently examine the frequency of the SSWs during ENSO winters based on 53 years of reanalysis data, and find that SSWs occur with equal probability during El Niño and La Niña winters. It seems likely that the small sample size of the observational data and the small number of the SSWs may contribute to the contradictory results in the literature, since the statistical relationship between SSWs and ENSO is more ambiguous than that between the seasonal-mean state of the stratosphere and ENSO. Thus, rather than focus on the small number of SSWs, we search for links between ENSO and variability of stratospheric polar vortex in general. The long duration of the CM3 integration also ensures us to evaluate the statistical relationship between ENSO and stratospheric variability with a high degree of confidence.

The remainder of this chapter is organized as follows. The basic datasets and analysis tools are described in section 5.2. Section 5.3 documents the aspects of the seasonality of ENSO and ENSO/NAO relationship in observations and two coupled model simulations. The characteristics of the stratospheric mean state, variability, and stationary waves are also shown in this section. In section 5.4, the procedure for the selection of the stratospheric weak/strong vortex events, the relationships

between the frequency of occurrence of strong/weak vortex events and ENSO, and the seasonal dependence of these relationships are presented. The modulations of the stationary wave due to ENSO and anomalous vortex events, both separately and in combination with each other, are presented in section 5.5. The wave propagation in terms of EP flux, and its relationship with the meridional circulation are analyzed in section 5.6. The zonal-mean zonal wind and surface pressure responses are shown in section 5.7. Summaries are given in section 5.8.

## 5.2 Description of model experiment, observational datasets and diagnostic tools

### 5.2.1 Model

The numerical model used in this study is the new Geophysical Fluid Dynamics Laboratory (GFDL) global coupled climate model CM3. The horizontal resolution of the atmospheric component of CM3 (hereafter referred to as AM3) is  $2^\circ$  latitude  $\times$   $2.5^\circ$  longitude. The dynamical core of AM3 uses new finite-volume core formulated on cube-sphere grid (Putman and Lin 2007), instead of the original latitude-longitude grid used in AM2 (Lin 2004). This new method greatly improves the computational efficiency and simulation quality in the polar region. The number of vertical layers has been increased to 48 from 24 layers in AM2, with the model top at 0.01 hPa (Donner et al. 2011). The increased vertical resolution and extent in the model stratosphere in AM3 help reasonably simulate the stratospheric chemical and dynamical processes. The dynamical core, physical parametrization, and basic simulation characteristics of the AM3 are described by Donner et al. (2011). The ocean component of CM3 uses the MOM4p1 code (Griffies 2009), whereas the ocean component of CM2.1 is based on the MOM4.0 code (Griffies et al. 2004). The physical parameterizations and

grid resolution of the CM3 ocean component are the same as that used in CM2.1, as detailed in Griffies et al. (2005) and Gnanadesikan et al. (2006). As in chapter 2, we choose to focus on the pre-industrial (1860) control simulation of CM3. Using such control integrations allows us to eliminate the influence of externally forced climate variability on the stratosphere and troposphere, such as that due to volcanoes, aerosols or trends in greenhouse gas forcing. Our model analysis is focused on the 800-yr output of this control run.

It should be noted that the vertical resolution in CM3 is still not sufficiently fine to simulate the quasi-biennial oscillation (QBO) (Giorgetta et al. 2006). Thus, the possible influence of QBO on the interannual variability of the northern winter stratospheric flow (Holton and Tan 1980, 1982) is not considered in the present study.

### 5.2.2 Observational datasets

The observed data used in this study are based on monthly and daily mean fields (September 1957 to August 2002) from the European Center for Medium-Range Weather Forecasts (ECMWF) Re-Analysis (ERA-40; see Uppala et al. 2005). This dataset has a horizontal resolution of  $2.5^\circ \times 2.5^\circ$  and extends from 1000 to 1 hPa with 23 vertical pressure levels.

DJF-mean Niño-3 index (SSTAs averaged over  $5^\circ\text{S}$ – $5^\circ\text{N}$ ,  $150^\circ\text{--}90^\circ\text{W}$ ), based on the NOAA extended reconstructed SST version 3 dataset (ERSST V3, see Smith et al. 2008; Xue et al. 2003), is used to describe ENSO variability in the 1948–2010 period.

### 5.2.3 Diagnostic tool

The close relationship between the wave and mean flow changes is most clearly expressed by the Transformed Eulerian-Mean (TEM) equations (Andrews et al. 1987; Edmon et al. 1980; Dunkerton et al. 1981; Vallis 2006). In the absence of diabatic

heating and frictional damping, the QG approximation of the zonal-mean zonal momentum and thermodynamic equations in spherical and log-pressure coordinates can be written as

$$\frac{\partial[u]}{\partial t} - f[\tilde{v}] = \frac{1}{\rho_0 a \cos \phi} \nabla \cdot \mathbf{F} \equiv D_F, \quad (5.1)$$

$$\frac{\partial[\theta]}{\partial t} + [\tilde{w}][\theta]_z = 0. \quad (5.2)$$

Here, square bracket denotes the zonal mean.  $\rho_0$  is air density which varies approximately with height as  $\rho_s \exp(-z/H)$  where  $\rho_s$  is a constant and  $H$  is standard constant scale height (7 km),  $a$  is the radius of Earth,  $\phi$  is latitude,  $f = 2\Omega \sin \phi$  is the Coriolis parameter,  $z = -H \ln(p/1000)$  is pressure altitude,  $u$  and  $v$  are the zonal and meridional velocity components.  $\theta$  denotes potential temperature, and its partial derivative with respect to  $z$  is written as  $\theta_z$ .

In Eq. (5.1),  $\mathbf{F} = (F_\phi, F_z)$  is the Eliassen-Palm (EP) vector in the  $(\phi, z)$  plane, given by

$$F_\phi = -\rho_0 a \cos \phi [v^* u^*], \quad (5.3)$$

$$F_z = f \rho_0 a \cos \phi \frac{[v^* \theta^*]}{[\theta]_z}, \quad (5.4)$$

with its divergence given by:

$$\nabla \cdot \mathbf{F} = \frac{1}{a \cos \phi} \frac{\partial}{\partial \phi} (F_\phi \cos \phi) + \frac{\partial}{\partial z} (F_z). \quad (5.5)$$

Here asterisk denotes the deviation from the zonal mean. The term on the right hand side of Eq. (5.1),  $D_F$ , is the zonal force per unit mass, which represents the zonal-mean zonal flow acceleration due to the wave activity. The factor  $(\rho_0 a \cos \phi)^{-1}$  in  $D_F$  arises due to the fact that the true EP flux divergence  $\nabla \cdot \mathbf{F}$  relates to angular momentum changes rather than directly to changes in zonal-mean zonal flow. By

expanding the daily  $u$ ,  $v$  and  $\theta$  fields into their Fourier harmonics, the EP flux and its divergence for zonal wave 1 and 2 are calculated.

The associated “residual” zonal-mean circulation ( $\tilde{[v]}$ ,  $\tilde{[w]}$ ) is defined by

$$\tilde{[v]} \equiv [v] - \frac{1}{\rho_0} \frac{\partial}{\partial z} \left( \rho_0 \frac{[v^* \theta^*]}{[\theta]_z} \right), \quad (5.6)$$

$$\tilde{[w]} \equiv [w] + \frac{1}{a \cos \phi} \frac{\partial}{\partial \phi} \left( \frac{[v^* \theta^*]}{[\theta]_z} \cos \phi \right). \quad (5.7)$$

The quantities  $\tilde{[v]}$  and  $\tilde{[w]}$  are linked by a continuity equation

$$\frac{1}{a \cos \phi} \frac{\partial}{\partial \phi} (\tilde{[v]} \cos \phi) + \frac{1}{\rho_0} \frac{\partial}{\partial z} (\rho_0 \tilde{[w]}) = 0. \quad (5.8)$$

In comparison with TEM, the conventional zonal Eulerian-mean momentum and thermodynamic equations presented in spherical and log-pressure coordinates are:

$$\frac{\partial [u]}{\partial t} - f[v] = -\frac{1}{a \cos^2 \phi} \frac{\partial}{\partial \phi} ([v^* u^*] \cos^2 \phi) \equiv D_M, \quad (5.9)$$

$$\frac{\partial [\theta]}{\partial t} + [w][\theta]_z = -\frac{1}{a \cos \phi} \frac{\partial}{\partial \phi} ([v^* \theta^*] \cos \phi). \quad (5.10)$$

The term on the right hand side of Eq. (5.9),  $D_M$ , is the eddy momentum flux convergence. This is also the component of  $D_F$  due to the meridional derivative of  $F_\phi$  (cf. first term in Eq. 5.5).

The zonal-mean meridional circulation, which is composed of  $[v]$  and  $[w]$ , can be described by a mass streamfunction, which is defined by calculating the northward mass flux above a particular level  $p$ .

$$\Psi_M = \frac{2\pi a \cos \phi}{g} \int_0^p [v] dp \quad (5.11)$$

For calculations involving the EP flux, the daily  $u$ ,  $v$  and  $\theta$  are used to compute the daily fields of EP flux. Monthly mean EP flux is then computed from the monthly

average of the daily EP flux. In this way, contributions of both stationary and transient waves are included. The climatological annual cycle is computed by long-term averaging of each calendar month, and the annual cycle is then removed from the monthly EP flux to produce the monthly EP flux anomalies.

According to the convention described in [Dunkerton et al. \(1981\)](#), the respective values of  $F_\phi$  and  $F_z$  are multiplied by factors proportional to the distances occupied on the diagram by one radian of latitude, and one meter of pressure-altitude [ $-H \ln(p/1000)$ ], so that  $\mathbf{F}$  determines the directions and relative magnitudes of the arrow uniquely in the diagram. In addition, the EP flux vectors are scaled by the inverse of the air density at the given level so that some indication of wave propagation in the stratosphere is possible.

## 5.3 Simulation of ENSO, NAO, and stratospheric variability

### 5.3.1 Phase locking of ENSO to the seasonal cycle

As in chapter 2, a warm (cold) ENSO event is identified when the DJF-mean Niño-3 index is more than one standard deviation ( $\sigma$ ) above (below) the time mean. This criterion yields 125 warm and 133 cold events based on the CM3 simulation. The selected ENSO events in both observations and CM2.1 simulation are the same as in chapter 2. Fig. 5.1 shows the composite month-to-month evolution of the Niño-3 SSTAs during El Niño and La Niña events for the observations and two coupled model simulations. The observed El Niño and La Niña events show the tendency of the event to reach the peak amplitude toward the end of the year near Dec(0) (see black curves in Fig. 5.1). However, it is apparent that both models have a preference for peak Niño-3 SSTAs in late winter near Feb(1). It should also be noted that the

amplitude of the El Niño events is much smaller than CM2.1, and comparable to the observations.

### 5.3.2 ENSO/NAO relationship

To illustrate the seasonality of the anomalous surface circulation over the NA sector associated with ENSO, the time evolution of the regression coefficients of SLP anomalies versus Niño-3 index is shown in Fig. 5.2. The plots are presented in the latitude-time cross sections averaged over the longitudes between  $70^{\circ}$  and  $20^{\circ}$ W. During the Jan(1)–Apr(1) period, the observed pressure pattern (Fig. 5.2a) is characterized by a low pressure anomaly to the south, and a high pressure anomaly to the north, corresponding to the negative phase of NAO. This SLP configuration is captured by both of the model simulations (Figs. 5.2b,c), except that the positive anomaly peaks two months after the negative anomaly attains maximum amplitude, as noted in chapter 2. The amplitude of dipolar anomaly in the CM3 simulation is about 20% larger than that in the CM2.1 simulation. The relatively stronger amplitude of SLP anomaly in the CM3 simulation is actually more comparable to the observations. In addition, the linear correlation between Niño-3 and JFMA-mean NAO indices is also strengthened in the CM3 simulation ( $-0.23$  in the CM2.1 simulation and  $-0.30$  in the CM3 simulation). These results indicate that ENSO teleconnection through the stratospheric pathway, as facilitated by the enhanced vertical resolution in the model, is a possible factor contributing to the stronger NAO-like SLP response to ENSO in the NA region.

### 5.3.3 Seasonality of stratospheric mean state and its variability

The monthly mean zonal-mean zonal wind at 10 hPa as a function of latitude and time for both the ERA-40 reanalysis and CM3 simulation is shown in Figs. 5.3a and 5.3b, respectively. The winter season stratospheric westerlies at polar latitudes are captured by the model, except that the jets in the model are 30% stronger than in observations. This westerly bias has been noted in [Donner et al. \(2011\)](#), and may result from the “cold pole” problem prevalent in many stratosphere resolving GCMs ([Pawson et al. 2000](#)). In addition, the simulated zonal-mean zonal wind peaks in January and February, about one month later than the observations.

Figs. 5.3c,d show the seasonal cycle of the standard deviation of the monthly mean zonal-mean zonal wind at 10 hPa. The observations show large interannual variability of the stratospheric polar jet in January and February. This large interannual stratospheric variability at the polar latitudes during the winter season reflects the weakening of the stratospheric polar vortex by planetary-scale Rossby waves in winter (e.g., [Matsuno 1971](#)), and strengthening by thermal relaxation toward radiative equilibrium ([Holton and Mass 1976](#)). The simulated maximum variance is delayed towards February and March.

### 5.3.4 Characteristics of troposphere and stratosphere stationary waves

The observed NH wintertime climatological (NDJFM-mean) stationary wave field (the time-averaged geopotential height with the zonal mean removed,  $\overline{Z}^* = \overline{Z} - [\overline{Z}]$ ), along with its first two zonal harmonic wave components, on representative tropospheric and stratospheric levels, 300 hPa and 10 hPa, are shown in Fig. 5.4. The upper tropospheric stationary wave is characterized by troughs and ridges over the western

and eastern oceans, respectively (Fig. 5.4d). This feature indicates that the orography and diabatic heating in the NH are important in the maintenance of the tropospheric stationary wave (e.g., Lau 1979; Held et al. 2002). The stratospheric stationary wave pattern (Fig. 5.4a) is dominated by zonal wavenumber-1 dipolar structure (Fig. 5.4b), with relatively small amplitude of wavenumber-2 component (Fig. 5.4c). This wave-1 structure features a stationary cyclone over the Eurasian continent and an anticyclone over the Aleutian Islands, indicating the climatological Arctic vortex is shifted toward the Eurasian continent.

The phases of both the stationary wave-1 and -2 at 10 hPa are rotated westward with respect to those at 300 hPa. This pronounced westward tilt of the geopotential height perturbations with height is the characteristic of vertically propagating waves from mid- and high-latitude troposphere. The observed large scale stationary wave structure in the stratosphere can be understood in terms of the Charney-Drain theory (Charney and Drazin 1961) that describes the filtering of the higher-wavenumber waves propagating into the stratosphere (e.g., Andrews et al. 1987).

The wintertime climatological stationary wave derived from the model simulation (Figs. 5.4g–l) appears remarkably similar to that of the observations in both the structure and amplitude. The local extrema at both 300 hPa and 10 hPa are captured by the model simulation. The predominant wave-1 structure is simulated in the model stratosphere. The simulated zonal wave-1 and -2 structures are also nearly identical to the corresponding observed pattern. The main difference is the reduced wave-1 amplitude growth with height in the model simulation, as compared with observations (compare Figs. 5.4b,e and h,k). Possibly, this is because of insufficient upward propagation of the planetary waves, which may have resulted from deficiencies in the simulated polar night jet (see section 5.3.3). Since the vertical component of the EP flux is proportional to the poleward eddy heat flux [see Eq. (5.4)], this

underestimation of upward EP fluxes is also likely to have contributed to the cold bias in the northern hemisphere winter stratosphere.

## 5.4 Relationships between ENSO and stratospheric vortex anomalies, and their seasonal dependence

### 5.4.1 Identification of anomalous stratospheric polar vortex months

As discussed in section 5.3.3, there is large interannual variability in the stratosphere mean circulation during fall to spring. To measure the strength of the stratospheric vortex, monthly mean (from November to March) geopotential height anomaly averaged over north of  $70^{\circ}\text{N}$ , and mass-weighted vertically averaged between 3 to 30 hPa, is used as the monthly polar vortex strength index. Such area-averaged polar cap geopotential anomaly has been used in many recent studies (e.g., Garfinkel et al. 2010; Kolstad et al. 2010a; Kolstad and Charlton-Perez 2010b), and is shown to be almost identical to that of the empirical orthogonal function (EOF)-based NAM index, and more effective than zonal wind speed at  $60^{\circ}\text{N}$  when studying the stratosphere–troposphere couplings (Baldwin and Thompson 2009).

The probability distribution function of the vortex strength index is close to Gaussian, but is slightly skewed toward positive anomalies (not shown). Weak and strong vortex months are defined as the months for which the vortex strength index is greater than its wintertime (NDJFM) 90th percentile (+385.8 m) or less than its wintertime 10th percentile ( $-346.5\text{ m}$ ), respectively. The relatively strong amplitude of the weak vortex anomalies has also been noted in Limpasuvan et al. (2004, 2005), as the weak

vortex anomalies produced by planetary wave driving are stronger than those due to the gradual thermal relaxation during strong vortex events.

### 5.4.2 The dependence of the stratospheric vortex anomalies on the phase of ENSO

Fig. 5.5 shows the frequency distribution of the monthly stratospheric vortex strength indices for 123 El Niño winter in comparison with 136 La Niña winters. El Niño and La Niña conditions are defined here when the NDJFM-mean Niño-3 index is more than  $1\sigma$  above and below the time mean, respectively. This figure illustrates that strong positive vortex indices (greater than 300 m) are more frequent during El Niño years than during La Niña years. Conversely, strong negative vortex indices (less than  $-300$  m) are more frequent during La Niña years than during El Niño years.

A higher frequency of weak (strong) stratospheric vortex month for El Niño (La Niña) conditions is also demonstrated in Table 5.1. For example, it is 2–3 times more likely to have a weak vortex during El Niño winters than a strong vortex (i.e., 87 versus 37). Similarly, a strong vortex is also 2–3 times more likely to occur than a weak vortex during La Niña winters (i.e., 103 versus 47). The probability of the occurrence of weak vortex events during El Niña winters ( $\frac{87 \text{ mo}}{123 \text{ yr} \times 5 \text{ mo}} = 0.1414$ ) is significantly larger than that during La Niña winters ( $\frac{47 \text{ mo}}{136 \text{ yr} \times 5 \text{ mo}} = 0.0764$ ), with  $p < 0.0001$  using  $\chi^2$ -test. Likewise, the probability of the occurrence of strong vortex events is also significantly different between El Niño and La Niña winters ( $p < 0.0001$ ). These results indicate that there is indeed an ENSO-stratosphere link, with high level of significance.

### **5.4.3 Seasonal dependence of frequency of occurrence of weak/strong vortex months**

To explore the variation of the frequency of weak and strong vortex months within the winter season, the frequency of occurrence of weak and strong vortex events in each calendar month from November through March is shown in Fig. 5.6. Results based on the ERA-40 reanalysis and CM3 simulation are plotted in black unfilled bars and gray bars, respectively. Fig. 5.6 shows that most of the weak and strong vortex events occur from mid- to late-winter in both observations and models. The frequency peaks in January and February for ERA-40 reanalysis. However, the model simulation shows the tendency for both the strong and weak vortex events to occur later than observed, with the largest frequency in February and March. This model bias towards the late winter probably accounts, at least in part, for the reduced interannual variability in the simulated January mean circulation (see Figs. 5.3c,d).

## **5.5 The individual and combined effects of ENSO and vortex anomalies on the stratospheric stationary waves**

### **5.5.1 Stationary wave response during ENSO winters**

Fig. 5.7 shows the longitude–height cross sections of the wave-1 (left panels) and -2 (right panels) components of geopotential height, as averaged from  $45^{\circ}$  to  $75^{\circ}\text{N}$ , for 123 El Niño winters (upper panels) and 136 La Niña winters (lower panels). To assign equal weights to individual events, the anomalies of individual events have been normalized by the amplitude of the standardized Niño-3 strength index. Thus the composites, as shown in Fig. 5.7, represent a  $1\sigma$  deviation change in the Niño-3

strength index. In Fig. 5.7, and the following Fig. 5.8 and 5.9, the climatological (NDJFM-mean) stationary wave fields are shown in black contours, and the anomalous stationary wave responses are represented using shading.

The composites are averaged during the period of JF(1) when the stationary wave response to ENSO is strongest. In fact, from late autumn to early winter, the stationary wave response (not shown) is relatively very weak, especially for the wave-2 component. The response in the wave-1 is nearly in quadrature with the climatological wave structure. Thus the ENSO responses in late autumn and early winter contribute very little to changes in the amplitude of the stationary wave-1 and -2.

The wave-1 geopotential height anomalies in late winter El Niño events are in phase with the climatological stationary wave-1, and thus enhance the stationary wave-1 (Fig. 5.7a). In contrast, the wave-2 geopotential height anomalies are approximately out of phase with the climatological stationary wave-2, and therefore indicating a general weakening of the stationary wave-2 (Fig. 5.7b).

Similar but opposite signed wave-1 and -2 geopotential height anomalies are shown for the La Niña composites, except the slight westward displacement of the anomaly relative to the El Niño composites (Figs. 5.7c,d). Therefore, weakening and strengthening of the stationary wave-1 and -2 can be deduced for the late winter La Niña events, respectively.

### 5.5.2 Stationary wave precursors one month before the weak/strong vortex-only events

In order to compare the amplitude and structure of the stationary wave response to ENSO winters with the precursory ( $\text{lag} = -1 \text{ mo}$ ) stationary wave pattern during anomalous vortex-only winters, strong/weak vortex-only events are selected for constructing composites in Fig. 5.8. Strong (weak) vortex-only events are the subgroups

of the strong (weak) vortex events when the NDJFM-mean Niño-3 index is between  $-0.2\sigma$  and  $+0.2\sigma$ . In order to examine the precursory patterns of the stratospheric vortex anomalies, a subset of weak/strong vortex months is chosen. When two or more consecutive weak/strong vortex months are identified, only the first of these are included. This procedure also makes the effective sample size, estimated as in Bretherton et al. (1999), closer to the number of sample size in the analysis. There are 42 weak vortex-only and 52 strong vortex-only events based on this criteria (see the 4th row in Table 5.1).

As in Fig. 5.7, the composite shown in Fig. 5.8 represents a  $1\sigma$  deviation change in the vortex strength index. The weak vortex-only events are preceded by an enhancement of both climatological stationary wave-1 and -2 patterns (Figs. 5.8a,b), whereas the strong vortex-only events are preceded by suppressed wave-1 and -2 patterns (Figs. 5.8c,d).

### 5.5.3 Combinations of the ENSO responses and strong/weak vortex precursors

We make the assumption that the stationary wave modulation due to both ENSO and anomalous vortex-only events can be approximately estimated by the linear combination of the effects due to the two individual mechanisms. For the combined El Niño and weak vortex-only events, the stationary wave-1 is significantly enhanced, as the in-phase relationship with the background wave-1 is evident for each of the two individual composites (compare Fig. 5.7a and 5.8a). However, due to the opposite polarity of the anomalous stationary wave-2 (compare Fig. 5.7b and 5.8b), the net effect on the anomalous stationary wave-2 from the El Niño forcing and weak vortex precursor is significantly damped. Similarly, the combined effect of the La Niña and strong vortex-only events is the strong weakening of the background stationary wave-1, and little change of the background stationary wave-2. As such, the above

two types of combination (i.e., El Niño/weak vortex and La Niña/strong vortex) are anticipated to be characterized by the wave-1 structure. Since these two types of combination conform to the statistical relationship between ENSO and the vortex anomalies documented in section 5.4.2, they are referred as the ‘strong combinations’.

Unlike the ‘strong combinations’, the net effect of the other two types of combination does little on wave-1, but weakening/strengthening the wave-2. Since those two types of combination (i.e., La Niña/weak vortex and El Niño/strong vortex) do not conform to the relationship between ENSO and vortex anomalies, they are referred as the ‘weak combinations’.

In this subsection, composite analysis is performed on a monthly basis using the four types of combination as described above.

### Vertical structure

Fig. 5.9 shows the vertical structure of the stationary wave field, as in Fig. 5.8, for the period one month before (lag =  $-1$  mo) the two ‘strong combinations’ (top two rows) and two ‘weak combinations’ (bottom two rows). Results for all wavenumbers are presented on the left panels, with the corresponding zonal wave-1 and -2 components presented on the middle and right panels, respectively.

For the El Niño/weak vortex events, the anomalous ridge and trough in the troposphere (shading in Fig. 5.9a) strongly project onto the wave-1 structure (shading in Fig. 5.9b), and are in phase with the climatological stationary wave-1 pattern (contour in Fig. 5.9b). These height anomalies tilt significantly westward with height, and also enhance the stratospheric climatological stationary wave-1 pattern. However, the anomalous wave-2 structure is in approximate quadrature with the background wave in both the troposphere and stratosphere (Fig. 5.9c).

The stationary wave field for the La Niña/strong vortex events has similar vertical structure, but with opposite sign. In particular, strong wave-1 anomalies are  $180^\circ$

out of phase with the background stationary wave, and weak wave-2 anomalies tilt eastward with height. These results indicate that the precursory stationary wave in the ‘strong combinations’ has a strong wave-1 structure in both troposphere and stratosphere.

In contrast, the stationary wave fields in the ‘weak combinations’ (shading in Figs. 5.9g,j) strongly project onto the wave-2 structure (shading in Figs. 5.9i,l). Unlike the significantly westward tilt with height for the El Niño/weak vortex events, the La Niña/weak vortex events are characterized by smaller westward slope height. [Matthewman et al. \(2009\)](#) has also noted that during the vortex-displacement (wave-1 type) SSW events the vortex tilts westward with height, while for the vortex-splitting (wave-2 type) SSW events the vortex deformation is highly barotropic.

For the El Niño/strong vortex events, although both the wave-1 and -2 structure are 180° out of phase with the climatological structures, the tropospheric amplitude of the anomalous stationary wave-1 is very weak, and is much smaller than its wave-2 counterpart.

## Horizontal structure

In Figs. 5.10–5.11, the horizontal distribution of zonally asymmetric structures of anomalous geopotential height field, along with its zonal wave-1 and -2 components, at 300 and 10 hPa one month before the anomalous vortex months are shown for the four combination types (see shading). To highlight the spatial location of these anomalies relative to the climatological structure, the corresponding climatological situation, same as in Figs. 5.4g–l, is superimposed on Figs. 5.10–5.11 using contours.

At 300 hPa, the extratropical tropospheric precursory pattern for El Niño/weak vortex events (Fig. 5.10d) shows a wavetrain from the Pacific Ocean to North America that is reminiscent of the positive phase of the PNA pattern ([Horel and Wallace 1981](#)). The Aleutian low component of the PNA lies to the northeast of the clima-

tological trough over the Northwestern Pacific. The anomalous wave-1 component of this wave pattern is collocated with the climatological wave-1 pattern in high latitudes (Fig. 5.10e). This leads to the enhancement of the tropospheric forcing of stationary wave-1, which in turn may propagate upward into the stratosphere. This behavior is, indeed, revealed in the predominant wave-1 structure of the height pattern in lower stratosphere (Fig. 5.10b). In particular, the anomalous anticyclone spans half the globe in longitude and the anomalous cyclone covers the other half of the globe, reflecting a displaced polar vortex. This result is consistent with Garfinkel et al. (2010), who suggest that the dominant pathway through which warm ENSO modulates the vortex is the deepened Aleutian low and the increase in the planetary wave-1 driving.

The structure of the height anomaly in the La Niña/strong vortex events is opposite in sign. The destructive interference of the anomalous wave-1 leads to a reduction of the tropospheric forcing of stationary wave-1. As in El Niño/weak vortex events (Fig. 5.10f), wave-2 is mostly in quadrature with climatology (Fig. 5.10l), and contributes very little to changes in the polar vortex.

When comparing the corresponding 300 hPa maps in the La Niña/strong vortex (fourth row in Fig. 5.10) and La Niña/weak vortex events (second row in Fig 5.11), there is a clear eastward phase shift of both wave-1 and -2 patterns in the latter case that leads to approximate quadrature and in-phase relationships with the background wave-1 and -2, respectively. Thus the amplification of the tropospheric wave-2 outweighs the lack of the wave-1 in the La Niña/weak vortex events. Since the constructive interference of tropospheric wave-2 is dominant in the La Niña/weak vortex events, propagation of this signal to the stratosphere leads to a quadruple structure (shading in Fig. 5.11c), with two anomalous highs approximately over Aleutian and Iceland, and splitting anomalous lows over Canada and Siberia. As wave-2 propagates into the stratosphere less efficiently than wave-1, by the Charney-Drazin theory, the zonal wave-2 variation in the stratosphere has smaller amplitudes.

It should be noted that the positive anomaly to the south of Alaska (Fig. 5.11d) is typical of the classic blocking situation over NP (e.g., Dole and Gordon 1983; Renwick and Wallace 1996). The composites of this Pacific blocking pattern are shown to amplify the stationary zonal wave-2 and weaken the wave-1 (Castanheira and Barriopedro 2010). It is also found that the strong upper troposphere ridge around Alaska plays an important role in the wave-2 SSW events in both 2008/09 and 1988/89 winters, which are classified as La Niña condition (Harada et al. 2010). Thus the characteristics of the La Niña/weak vortex composites in our results are qualitatively consistent with the studies cited above. In addition, our results also suggest that whether the vortex weakens or strengthens during the La Niña events may depend on the longitudinal location of the Pacific blocking, although the weak vortex is less likely to be associated with La Niña winters than strong vortex (see Table 5.1).

For the El Niño/strong vortex events, the positive anomaly near the stratospheric polar region is being elongated at 10 mb, although not breaking up into two pieces (Figs. 5.11g). As such, both wave-1 and -2 components are out of phase with the corresponding background wave structures (Figs. 5.11h,i). However, the in-quadrature-phase and out-of-phase relationships with the tropospheric background wave-1 and -2, respectively, are evident at 300 hPa (Figs. 5.11k,h). These features are consistent with the results shown in the longitude-pressure cross sections (Figs. 5.9j–l).

## 5.6 Relationship between wave propagation and zonal-mean meridional circulation

### 5.6.1 EP-flux patterns

Rossby wave propagation may be further visualized by means of EP flux cross sections. Fig. 5.12 shows cross sections of the EP flux and its divergence averaged over the months of four types of combinations. The EP cross sections are shown for the sum of all zonal wavenumbers (left panels), zonal wave-1 (middle panels) and -2 (right panels).

For weak vortex events in both phases of ENSO condition, there is a surplus of upward stationary wave fluxes and strong convergences of the EP flux at the upper stratosphere (Figs. 5.12a,g). Although the cause of the weak vortex in both cases is the upward propagation of the tropospheric Rossby wave, the contribution of these upward wave flux is mainly from the wave-1 component in El Niño condition (compare Fig. 5.12b and 5.12c), while from the wave-2 component in the La Niña condition (compare Fig. 5.12h and 5.12i). This is as expected and consistent with previous results, as shown in Figs. 5.9a–f, that the geopotential height anomaly precursors act to enhance the amplitude of the stationary wave-1 and -2 patterns in the El Niño/weak vortex and La Niña/weak vortex events, respectively.

Conversely, for strong vortex events in both phases of ENSO condition, the downward EP flux anomaly implies anomalously low wave activity (Figs. 5.12d,j). While the contribution of the downward EP flux is primarily from wave-1 in the La Niña/strong vortex events, the contribution from wave-1 is as important as wave-2 in the El Niño/strong vortex case (Figs. 5.12k,i). This result is in line with the above mentioned 180° phase difference between the anomalous stationary wave and background climatological pattern for both the wave-1 and 2 components in the latter case (see Figs. 5.9h,k).

## Vertical propagation entering the stratosphere

The occurrence of strong and weak vortex events has been linked to the upward wave activity entering the stratosphere. It has been shown that time-integrated eddy heat flux several weeks prior is anomalously positive preceding weak vortex events, and anomalously negative preceding strong vortex events (e.g., Christiansen 2001; Polvani and Waugh 2004).

To measure the upward propagation of planetary waves entering the stratosphere, the anomalous vertical component of the EP flux ( $F_z$ ) at 100 hPa averaged over 45°–75°N is calculated, as in Polvani and Waugh (2004). Table 5.2 compares the values of  $F_z$  for wave-1 and -2 in the four combination types for lags of –1 and 0 month.

For both the El Niño/weak vortex and La Niña/strong vortex events, the magnitude of the  $F_z$  due to zonal wave-1 is significantly larger than that due to zonal wave-2 during lags of both –1 and 0 month. In contrast, for the remaining two events in the “weak combinations”, there is evidence of the larger zonal wave-2 component of  $F_z$ . Although the wave-1 component is small, it is not negligible, especially for the El Niño/strong vortex. Only during the lag of 0 month of the La Niña/weak vortex events, the wave-2 component of  $F_z$  is significantly larger than the wave-1 component.

Comparing the amplitude of  $F_z$  between lags of –1 and 0 month,  $F_z$  is generally larger during lag of 0 month than that during lag of –1 month, except for the La Niña/strong vortex events. This relatively strong negative  $F_z$  anomalies during the lag of –1 month might be related to the early development of the westerly anomalies in the La Niña/strong vortex events, as will be shown in section 5.7.1.

## Meridional propagation at upper troposphere

Notable difference among the four combination types is present in the meridional propagation of wave activity ( $F_\phi$ ) near the upper troposphere. Since  $F_\phi$  is proportional to the eddy momentum flux [Eq. (5.3)], the meridional derivative of  $F_\phi$  [i.e.,

$D_M$  in right hand side of Eq. (5.9)] corresponds to the convergence of the eddy momentum flux, and is shown for levels below 200 hPa in the left panels of Fig. 5.12 (shading).

During the El Niño/weak vortex events, the EP flux vectors at the upper troposphere bend strongly poleward, with anomalous convergence (divergence) of  $F_\phi$  to the north (south) of 40°N (see shading in Fig. 5.12a). The strong equatorward refracted EP flux and opposite-signed dipole of  $D_M$  near the upper troposphere are shown in the La Niña/strong vortex events (Fig. 5.12d).

However, during La Niña/weak vortex (Fig. 5.12g), waves refract away from mid-latitudes towards both subtropics and high-latitudes, which results in the tripolar configuration of the  $D_M$  at the upper troposphere. Conversely, waves propagating towards midlatitudes from both subtropics and high-latitudes, and associated opposite-signed tripolar pattern of the  $D_M$  are shown in the El Niño/strong vortex events (Fig. 5.12j).

### The individual effects of ENSO and vortex anomalies on the meridional propagation at upper troposphere

Given the importance of the eddy momentum flux in the maintenance of the upper tropospheric zonal wind anomalies, it is hence of interest to study in more detail the role of the meridional component of the eddy forcing.

The impacts of the stratospheric circulation on the refraction of the vertically propagating waves from the troposphere are discussed in many previous studies (e.g., [Chen and Robinson 1992](#); [Hartmann et al. 2000](#); [Limpasuvan and Hartmann 2000](#)). As shown in [Limpasuvan and Hartmann \(2000\)](#), when the polar vortex is anomalously weak, the index of refraction for planetary waves near the subpolar tropopause is considerably strong, and tends to attract waves toward the polar region according to WKBJ theory ([Andrews et al. 1987](#)). In contrast, when the polar vortex is anom-

lously strong, planetary wave fluxes tend to be refracted equatorward in the upper troposphere/lower stratosphere.

On the other hand, the diagnostic and modeling study by Seager et al. (2003) has illustrated that strengthening of the subtropical jets during El Niño events could modify the meridional potential vorticity gradient of the zonal flow, and the associated refractive characteristics of the atmospheric basic state. These changes result in transient eddies being refracted away from the latitudes when jet is intensified. Opposite situation occurs for La Niña events.

Our main goal in this subsection is to estimate the typical amplitude of the anomalous  $F_\phi$  associated with ENSO and anomalous vortex-only events separately. To do so, composites of  $F_\phi$  at 300 hPa are calculated using the similar approach as described in section 5.5.1 and 5.5.2 for ENSO events and vortex-only events, respectively. Since we are more interested in the responses of  $F_\phi$  during the month of anomalous vortex, composites are computed during the lag of 0 month for weak/strong vortex-only events. As for the ENSO events, composites are constructed for the period of FM(1), when the frequency of the anomalous vortex events peaks, and the ENSO events attain maturity.

In agreement with previous studies cited above, both El Niño and weak vortex-only events correspond to positive  $F_\phi$  (see solid lines in Fig. 5.13). However, the magnitude during the El Niño events is larger south of 50°N, and smaller north of 50°N than during the weak vortex-only events. Symmetrically, La Niña and strong vortex-only events show the reversed structure (see dashed lines Fig. 5.13).

In general, linear additivity of the  $F_\phi$  responses for the combined ENSO and vortex-only events is satisfied. For example, suppose the responses of  $F_\phi$  to El Niño and weak vortex-only events are approximately additive, the sum of these two responses yields broader positive anomalies in both mid- and high- latitudes, as suggested from two solid lines in Fig. 5.13. This is in accordance with the results in

Fig. 5.12a, showing poleward propagation of  $F_\phi$  at 300 hPa during the El Niño/weak vortex events. Similarly, the combined responses of  $F_\phi$  to La Niña and strong vortex-only cases suggest strong equatorward propagation in both mid- and high- latitudes (two dashed lines in Fig. 5.13).

However, for the combined El Niño and strong vortex-only cases, the positive anomaly in the former case and the negative anomaly in the latter case interfere destructively, with net effect being positive south of 50°N, and negative north of 50°N, respectively. Such combination of the response of  $F_\phi$  is also consistent with the results in Fig. 5.12j, showing poleward and equatoward of  $F_\phi$  south and north 50°N, respectively. Similar cancellation between the responses of  $F_\phi$  to La Niña-only and weak vortex-only events in the midlatitudes is also evident in Fig. 5.13.

## 5.6.2 zonal-mean meridional overturning circulation

### Stratospheric residual zonal-mean circulation

Fig. 5.14 illustrates the residual zonal-mean meridional and vertical velocity ( $\tilde{[v]}$ ,  $\tilde{[w]}$ ) for the four combination types during lags of both 0 and +1 months. The quantities of  $\tilde{[v]}$  and  $\tilde{[w]}$  are calculated using Eqs. (5.6)–(5.7). In this subsection, we shall attempt to show the relationship between wave forcings and mean circulation changes [Eqs. (5.1)–(5.2)].

During the lag of 0 month of El Niño/weak vortex events, the anomalous residual circulation (Fig. 5.14a) is directed poleward in the middle and upper stratosphere. The Coriolis acceleration associated with this northward flow primarily balances the negative wave-induced forcing in those regions [see blue contours in Fig. 5.12a; Eq. (5.1)]. Continuity constraint requires residual sinking motion below the region of the EP convergence (Fig. 5.14b), and the associated adiabatic warming is accompanied by warming of the polar vortex. Such stratospheric residual zonal-mean circulation is reversed during the lag of +1 month (Figs. 5.14c,d), as the upward wave activity

weakens and EP-fluxes become divergent during the lag of +1 month (not shown). Analogous arguments of the stratospheric residual circulation also hold for the La Niña/weak vortex events during lags of 0 and +1 month (Figs. 5.14i–l).

The stratospheric residual circulation for the strong vortex events in both phases of ENSO is in the opposite sense. In response to the strong EP divergence during the lag of 0 month, the residual circulation tends to be equatorward with ascent and adiabatic cooling over the pole. A reversal of the stratospheric circulation also appears during the lag of +1 month.

### Tropospheric zonal-mean meridional circulation

To illustrate the relationship between the eddy momentum flux convergence and the zonal mean circulation in the troposphere [Eqs. (5.9)–(5.10)], the standard Eulerian-mean meridional mass streamfunction ( $\Psi_M$ ) is plotted in Fig. 5.15. The mass streamfunction is calculated using Eq. (5.11). Similar approach is used in Limpasuvan et al. (2005) to show the Eulerian-mean meridional and vertical velocity in the troposphere. Unlike the reversal of the residual circulation from lag of 0 month to +1 month (see Fig. 5.14), the tropospheric overturning circulation retains its polarity throughout this period. Thus, the composites are averaged from lag of 0 to +1 month.

For the El Niño/weak vortex events, the tropospheric anomalous circulation consists of a two-cell pattern, with thermally indirect circulation from the subtropics to the midlatitudes and a weak thermally direct circulation at middle-to-high latitudes. Near the tropopause, the anomalous pronounced poleward and equatorward flows are indicated north and south of 40°N, respectively (Fig. 5.15a). This meridional flow configuration nearly coincides with the center of the anomalous  $D_M$  (see shading in Fig. 5.12a). By considering the zonally mean momentum equation [Eq. (5.9)], the term  $D_M$  is primarily balanced by the Coriolis torque associated with the zonal mean meridional flow  $f[v]$ . Hence,  $D_M > 0$  south of 40°N would be coincident with equa-

torward [ $v$ ], and vice versa. In the lower troposphere, Coriolis force acting on the equatorward (poleward) lower branch of the overturning circulation helps maintain the lower-tropospheric easterly (westerly) anomalies against frictional dissipation, as will be shown in section 5.7.1. Opposite directed two-cell pattern of the anomalous tropospheric circulation is evident for the La Niña/strong vortex events (Figs. 5.12b).

Consistent with the tripolar configuration of the  $D_M$  at the upper troposphere, the tropospheric meridional circulation in the two ‘weak combinations’ (Figs. 5.12c,d) is changed to a three-cell pattern, which can be reasoned using analogous arguments above.

## 5.7 Responses of the zonal-mean zonal wind and SLP

### 5.7.1 Zonal-mean zonal wind

Fig. 5.16 shows the composite of the anomalous zonal-mean zonal wind for lags of  $-1, 0, +1$  and  $+2$  month.

#### Downward propagation from upper stratosphere to lower stratosphere

For the El Niño/weak vortex events, the easterly wind anomaly, peaking in the upper stratosphere during the lag of 0 month, is the consequence of the strong upward propagating waves and the attendant convergence of the EP flux in the stratosphere. This weakened zonal flow descends to the middle and lower stratosphere during the lag of  $+1$  and  $+2$  months (Figs. 5.12c,d). There is no clear evidence to suggest whether the high-latitude easterly anomalies in the troposphere originate from the descending signals in the lower stratosphere, or develop simultaneously.

The evolution of the zonal-mean zonal wind during the La Niña/strong vortex events is generally the opposite of the El Niño/weak vortex events, except during the lag of  $-1$  month. The anomalous zonal wind acceleration induced by EP-flux divergence is also most intense during the lag of  $0$  month, and descends down to  $30$  hPa during the lag of  $+2$  month. However, while the easterly anomaly poleward of  $50^{\circ}\text{N}$  occurs during the lag of  $0$  month of El Niño/weak vortex events, the westerly anomaly for the La Niña/strong vortex events begins to appear during the lag of  $-1$  month. This early development of the westerly anomalies for the latter cases agrees with the above mentioned relatively large attenuation of  $F_z$  during the lag of  $-1$  month compared to the lag of  $0$  month (see Table 5.2). This result also suggests slow and fast development for the La Niña/strong vortex and El Niño/weak vortex events, respectively, and is consistent with previous studies ([Limpasuvan et al. 2005](#)). As cited earlier in section 5.4.1, [Limpasuvan et al. \(2005\)](#) attribute the difference to the different driving mechanisms between the strong and weak vortex events. In particular, the slow intensification of the polar vortex is associated with the gradual radiative cooling (thermal relaxation), whereas the fast weakening of the polar vortex is related to the rapid wave driving.

Comparing the zonal-mean zonal wind anomalies between El Niño/weak vortex and La Niña/weak vortex (Fig. 5.16, first and third rows), the wind structure is remarkably similar in the stratosphere. Similarity is also found in the evolution of stratosphere zonal flow between the La Niña/strong vortex and El Niño/strong vortex (Fig. 5.16, second and fourth rows), except that the latter shows a faster decay than the former during the lag of  $+2$  month (Figs. 5.16h,p).

### Tropospheric wind anomalies

Although the wind structure is remarkably similar in the stratosphere between El Niño/weak vortex and La Niña/weak vortex, notable differences are apparent in the

troposphere (Fig. 5.16, first and third rows). The El Niño/weak vortex events are characterized by the meridional profile of the out-of-phase fluctuations in the zonal-mean zonal wind field, with centers of action located near 20° and 60°N and the nodal line nearly collocated with the climatological jet position ( $\sim$ 40°N). This dipole pattern is evident from lag of  $-1$  month throughout lag of  $+2$  month. However, a persistent tripolar pattern is apparent throughout the La Niña/weak vortex events, with positive wind anomalies centered near 45°N and negative anomalies in the subpolar and subtropical latitudes. Similar but opposite signed dipolar and tripolar patterns of the wind anomalies are shown for the La Niña/strong vortex and El Niño/strong vortex events, respectively (Fig. 5.16, second and fourth rows).

Such dipolar (tripolar) pattern of the zonal-mean zonal wind anomalies is in accord with the behavior of dipolar (tripolar) structure of  $D_M$  (Fig. 5.12), and two-cell (three-cell) tropospheric overturning circulation (Fig. 5.14) for the events in ‘strong combinations’ (‘weak combinations’). It has been shown that the upper troposphere is communicated vertically to the surface via the eddy-driven tropospheric overturning circulation (Limpasuvan and Hartmann 2000; Thompson and Wallace 2000). While the upper-tropospheric flow anomaly is maintained by the eddy momentum flux convergence, the lower-tropospheric flow anomaly is maintained by the Coriolis forcing acting on the surface branch of the overturning circulation.

### 5.7.2 Response of surface annular mode anomalies

It has been shown in previous studies that extreme stratospheric events can be followed by long-lasting tropospheric response up to 2 months later (Baldwin and Dunkerton 2001; Thompson et al. 2002). To investigate the surface response, the composite mean anomalies in SLP, averaged from the lag of 0 to  $+2$  month, are presented in Fig. 5.17 for the four combination types.

Response to the El Niño/weak vortex events (Fig. 5.17a) is characterized by a positive center of action over the Arctic region, and an opposing negative center at midlatitudes with prominent features over both the Atlantic and Pacific Oceans. This pattern is more zonally symmetric, and projects on the negative surface NAM/Arctic Oscillation pattern (e.g., [Thompson and Wallace 1998, 2000](#)). The SLP pattern in the NA region from the central North America to Europe resembles the negative NAO. The surface response to La Niña/strong vortex events captures the similar zonally symmetric pattern, but with opposite polarity (Fig. 5.17b).

In contrast, the surface response for the La Niña/weak vortex events is not zonally symmetric. The poleward part of the positive SLP anomaly is still in phase with the weakened strength of the polar vortex, and may represent downward influence from the stratosphere. However, negative anomaly over the NA midlatitudes becomes narrower and is shifted northward, and a positive anomaly is apparent in the lower latitudes. As such, the SLP anomaly over NA is characterized by a tripolar pattern. This tripolar pattern of the SLP anomaly over NA is consistent with the tripolar pattern of zonal-mean zonal wind within the tropospheric level (see Figs. 5.16j–l).

## 5.8 Summary

The possible stratospheric pathway in the teleconnection between ENSO and NAO is examined based on a multi-century pre-industrial integration using a coupled GCM with a more realistic upper atmosphere (CM3). The ENSO/NAO relationship based on this model simulation has been compared with a coupled model with limited resolution in the model stratosphere (CM2.1). The late winter NAO-like dipolar response to ENSO in the CM3 simulation is stronger than that in the CM2.1 simulation, and comparable to the observations.

The CM3 also captures the observed features of both tropospheric and stratospheric climatological stationary waves. As in CM2.1, the ENSO mature phase in the CM3 simulation exhibits a 1-month delay relative to the observations. It is found that ENSO plays an important role in modulating the frequency occurrence of the stratospheric polar vortex anomalies via its impact on the amplitude of the stationary wave-1 and wave-2, especially in late winter.

The analysis incorporates both the strong and weak stratospheric vortex events. The key results in this chapter for the weak stratospheric vortex events are thus the following:

- 1) The El Niño/weak vortex events are preceded by enhancement of climatological stationary wave-1 pattern in both the stratosphere and troposphere, whereas La Niña/weak vortex events preceded by enhancement of stationary wave-2.
- 2) The changes in the amplitude of stationary wave are coincident with the anomalous propagation of the wave from the troposphere into the stratosphere: the increased amplitude of stationary wave indicates enhanced upward propagation of stationary wave, and vice versa. Thus, the contribution of the upward wave flux is mainly from the wave-1 component in the El Niño/weak vortex events, and from the wave-2 component in the La Niña/weak vortex events.
- 3) In the stratosphere level, the EP flux convergence (divergence) leads to the zonal-mean zonal wind deceleration (acceleration). The anomalous easterlies during the weak vortex events descend to the middle and lower stratosphere, with the zonal flow in the tropospheric polar region also marked by the easterly anomalies.
- 4) At the tropopause level, during the El Niño/weak vortex events, the EP fluxes bend strongly poleward, with the largest value of  $F_\phi$  in the midlatitudes. The associated eddy momentum flux is convergence ( $D_M > 0$ ) in the subtropics, and divergence ( $D_M < 0$ ) in the subpolar region. Such pattern of eddy momentum

flux convergence acts to maintain the anomalous westerlies and easterlies south and north of 40°N, respectively, in the upper troposphere. However, during the La Niña/weak vortex events, the meridional wave propagation includes anomalous positive  $F_\phi$  north of 45°N, and anomalous negative  $F_\phi$  south of 45°N. The associated eddy momentum flux convergence is a tripolar pattern, with convergence in the mid-latitude, straddled by the divergence to the south and north. Again, such eddy momentum flux pattern acts to maintain the tripolar pattern of the anomalous zonal-mean zonal wind at the upper troposphere.

- 5) The upper troposphere is communicated vertically to the surface via the eddy-driven two-cell and three-cell tropospheric overturning circulation in the El Niño/weak vortex and La Niña/weak vortex events, respectively. In the lower troposphere, the Coriolis force acting on the lower branch of the overturning circulation maintains the dipolar lower-tropospheric flow anomalies against frictional dissipation in the El Niño/weak vortex events, whereas maintains the tripolar flow anomalies in the La Niño/weak vortex events. Thus the northern lobe of the NAO does appear to be linked to the state of the polar vortex. However, the negative annular mode response only appears during El Niño winters, which is projected on the negative NAM pattern, whereas the SLP anomaly over NA in La Niña/weak vortex events is characterized by a tripolar pattern.

Particular attention has been focused on contrasting the behavior in ‘strong combinations’ (i.e., El Niño/weak vortex and La Niña/strong vortex) against that in ‘weak combinations’ (i.e., La Niña/weak vortex and El Niño/strong vortex). First, the stationary wave modulation in the ‘strong combinations’ has strong impact on the amplitude of the wave-1, but has little effect on the wave-2. Conversely, stationary wave modulation in the ‘weak combinations’ is dominated by the anomalous wave-2 structure. The number of events in the ‘strong combinations’ is significantly larger than the counts in the ‘weak combinations’. This result suggests that weakening or

strengthening of the polar vortex may be, at leading order, due to the stationary wave-1 component, and El Niño and La Niña winters are associated with the weakening and strengthening of the polar vortex, respectively. The relatively small number of events in ‘weak combinations’ due to wave-2 weakens the statistical relationship between the phase of ENSO and the stratospheric vortex anomalies.

Another notable difference between the ‘strong’ and ‘weak’ combinations is their effect on the meridional wave propagation ( $F_\phi$ ) at upper troposphere. For the ‘strong combinations’, the individual effects of ENSO and vortex-only events on the refraction of meridional wave are in the same direction, and thus reinforce each other. However, for the ‘weak combinations’, waves are refracted in the opposite direction due to ENSO and vortex-only events, separately, thus resulting in cancellation between the responses of  $F_\phi$  due to these two separate effects.

The eddy momentum flux in  $F_\phi$  is further decomposed into contributions from the stationary waves and transient waves (i.e.,  $\overline{[v^*u^*]} = [\overline{v^*}\overline{u^*}] + [\overline{v'^*}\overline{u'^*}]$ ), with the stationary waves defined as the zonal asymmetries in the monthly means, and the transient waves defined as the deviations from the monthly means. The results (not shown) suggest that the  $F_\phi$  associated with former is as important as that associated with latter.

It would be worthwhile to study this problem in various longitude sections, instead of in zonal average. It is noted that the upper-tropospheric momentum flux anomalies are largest over the NA sector (see Fig. 6 in [Limpasuvan et al. 2004](#)). In that case, the generalized EP flux ([Plumb 1985](#)) should be a useful diagnostic tool, which should also be more appropriate to study the impact of stratospheric anomalies on regional subtropical jet streams.

Table 5.1: The number of weak and strong vortex events for El Niño, La Niña and ENSO-Neutral winters based on the CM3 simulation. The El Niño and La Niña winters are defined when the NDJFM-mean Niño-3 index is more than  $1\sigma$  above and below the time mean, respectively. The ENSO-Neutral winters are those when the NDJFM-mean Niño-3 index is between  $-0.2\sigma$  and  $+0.2\sigma$ . The weak (strong) vortex month is defined when the monthly mean polar vortex strength index is greater (less) than its wintertime (NDJFM) 90th (10th) percentile, see text in section 5.4.1 for details. The numbers in parentheses represent the subset of weak/strong vortex months. When two or more consecutive weak/strong vortex months are identified, only the first of these are included.

	weak vortex	strong vortex
El Niño	87 (64)	37 (27)
La Niña	47 (37)	103 (76)
ENSO-Neutral	55 (42)	73 (52)

Table 5.2: Vertical component of EP fluxes ( $F_z$ ; units:  $10^3 \text{ kg s}^{-2}$ ) at 100 hPa averaged over  $45^\circ$ – $75^\circ\text{N}$  for zonal wavenumber-1 and -2 (third and fourth column), during lags of  $-1$  and  $0$  month of the four types of combination events. Values in bold type indicate anomalies for wavenumber-1 and -2 are significantly different at the 95% confidence level based on the two-tailed  $t$ -test, with the two-tailed  $p$  values are given in the last column.

	Lag (month)	$F_z (\times 10^3 \text{ kg s}^{-2})$			$p$ -value
		WN 1	WN 2		
El Niño/weak vortex	-1	<b>18.25</b>	<b>0.28</b>	< 0.01	
	0	<b>23.56</b>	<b>2.52</b>	< 0.01	
La Niña/strong vortex	-1	<b>-14.32</b>	<b>-7.98</b>	0.03	
	0	<b>-12.53</b>	<b>-2.91</b>	< 0.01	
La Niña/weak vortex	-1	6.65	14.62	0.32	
	0	<b>-1.15</b>	<b>21.20</b>	0.02	
El Niño/strong vortex	-1	-6.46	-10.20	0.46	
	0	-8.19	-12.61	0.42	

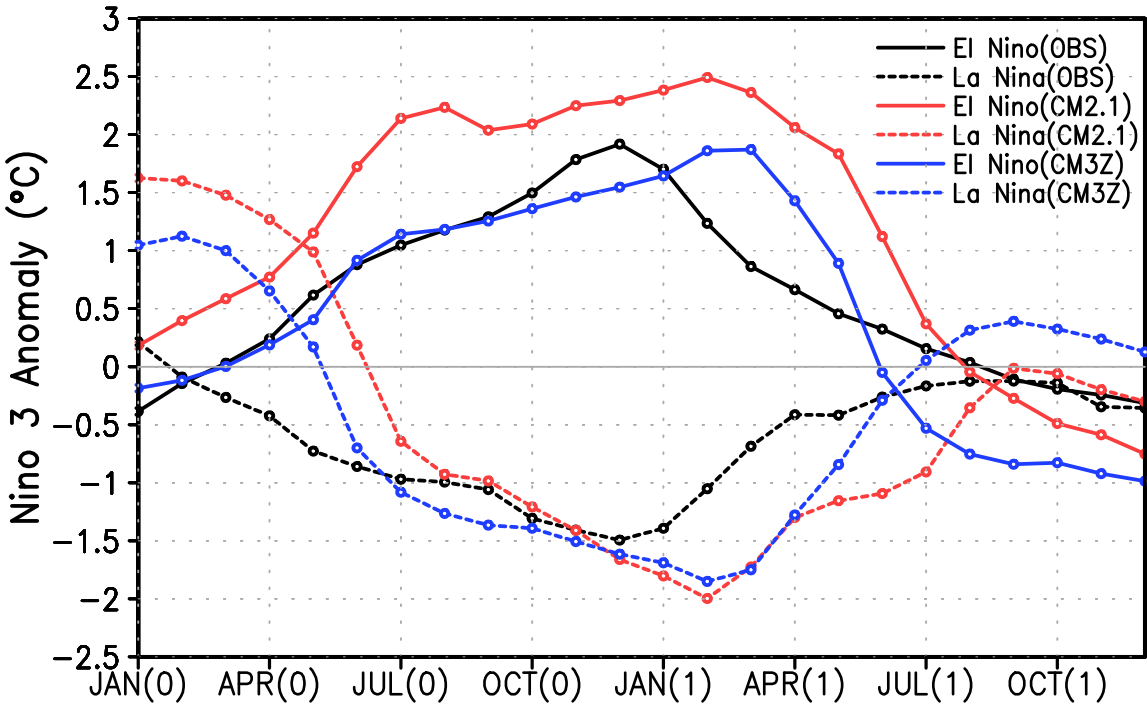


Figure 5.1: Composite monthly evolution of the Niño-3 SSTAs for El Niño (black solid curve) and La Niña (black dashed curve) events in observations, El Niño (red solid curve) and La Niña (red dashed curve) events in the CM2.1 simulation, and El Niño (blue solid curve) and La Niña (blue dashed curve) events in the CM3 simulation. The abscissa represents a 24-month period from January of year(0) to December of year(1). A specific month in this period is identified by a label consisting of the first three letters of that month, followed by the year indicator (0 or 1) in parentheses. For instance, Dec(0) refers to the month of December in year(0).

### SLP [70°–20°W] vs Niño3 (DJF)

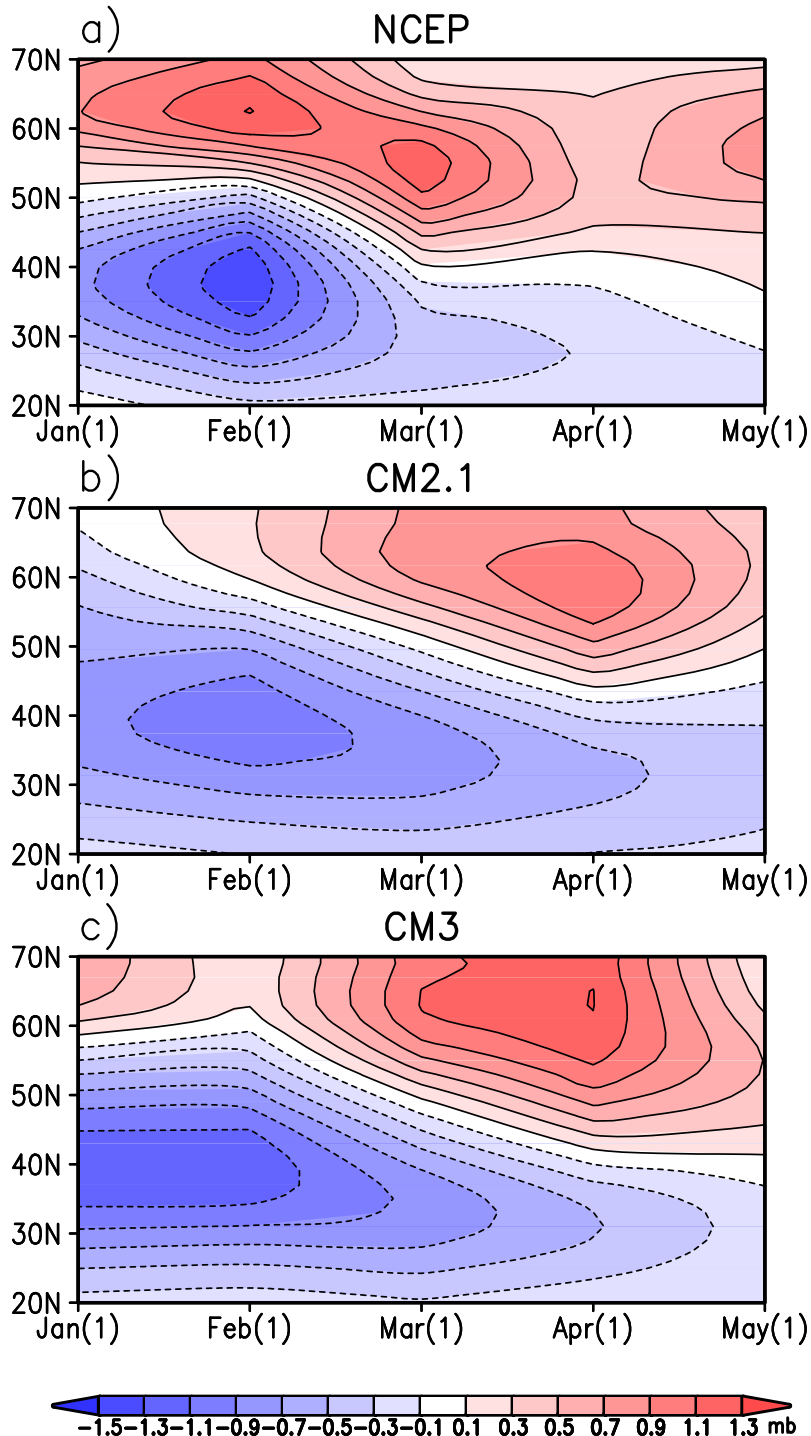


Figure 5.2: Time-latitude variations of the regression coefficients of SLP anomalies versus standardized DJF-mean Niño-3 index, as computed using the (a) NCEP-NCAR reanalysis, (b) CM2.1 simulation and (c) CM3 simulation. Contour interval is 0.2 hPa.

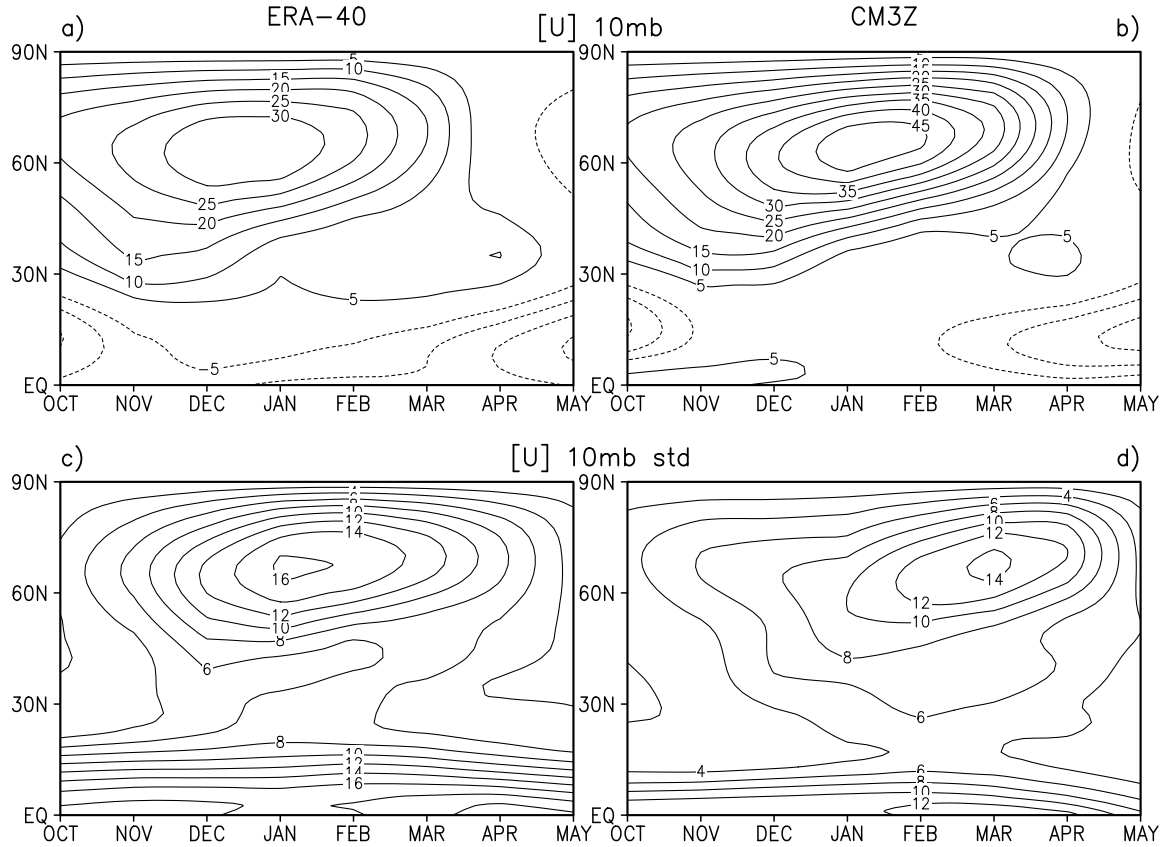


Figure 5.3: Monthly evolution of zonal-mean zonal wind climatology (top panels) and its standard deviation (bottom panels) at 10 hPa for the ERA-40 reanalysis (left panels) and CM3 simulation (right panels). Contour interval is  $5 \text{ m s}^{-1}$  for the zonal-mean zonal wind and  $2 \text{ m s}^{-1}$  for the standard deviation.

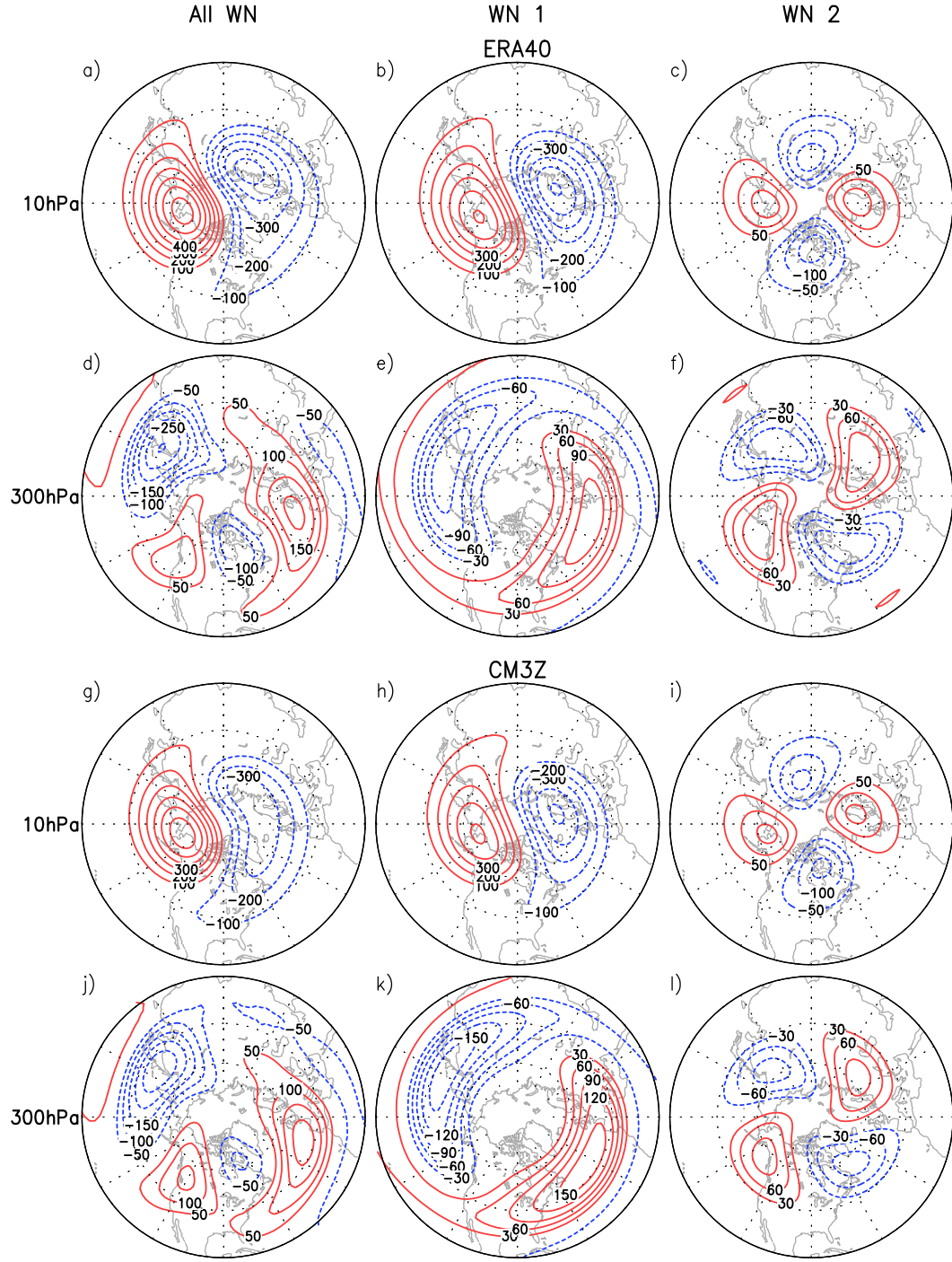


Figure 5.4: Climatological (NDJFM-mean) all-wavenumber (left panels), zonal wavenumber-1 (middle panels) and wavenumber-2 (right panels) of geopotential height fields at 10 hPa (first and third rows) and 300 hPa (second and fourth rows) for the ERA-40 reanalysis (upper half) and CM3 simulation (lower half). Plots in (a), (b), (g) and (h) are contoured every 100 m. Plots in (c), (d), (i) and (j) are contoured every 50 m. Plots in (e), (f), (k) and (l) are contoured every 30 m. In all plots, positive and negative contours are colored red and blue, respectively, and the zero contour is omitted.

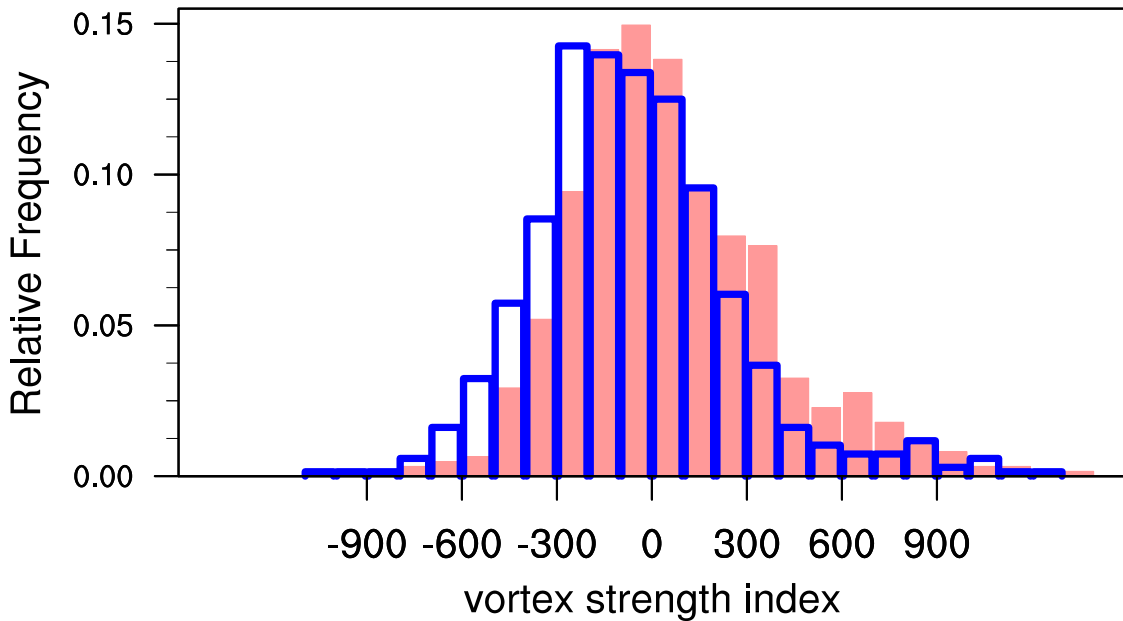


Figure 5.5: Frequency distribution of the monthly (November to March) vortex strength indices for the selected El Niño winters (red-filled columns) and La Niña winters (blue unfilled columns) in the CM3 simulation.

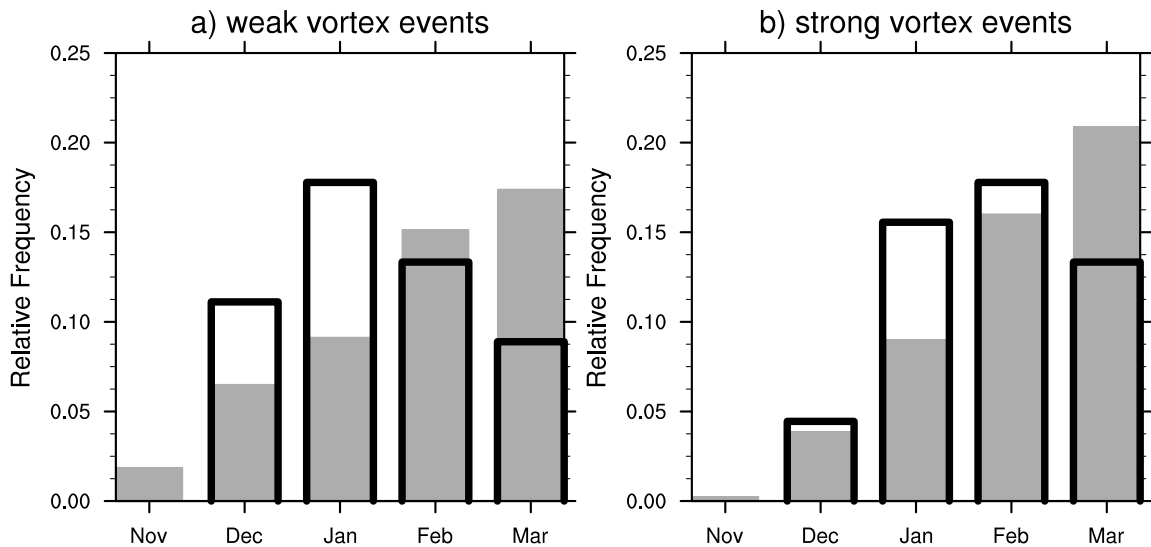


Figure 5.6: Frequency distribution of (a) weak and (b) strong vortex events per year in given month for the ERA-40 reanalysis (black unfilled bars) and CM3 simulation (gray bars).

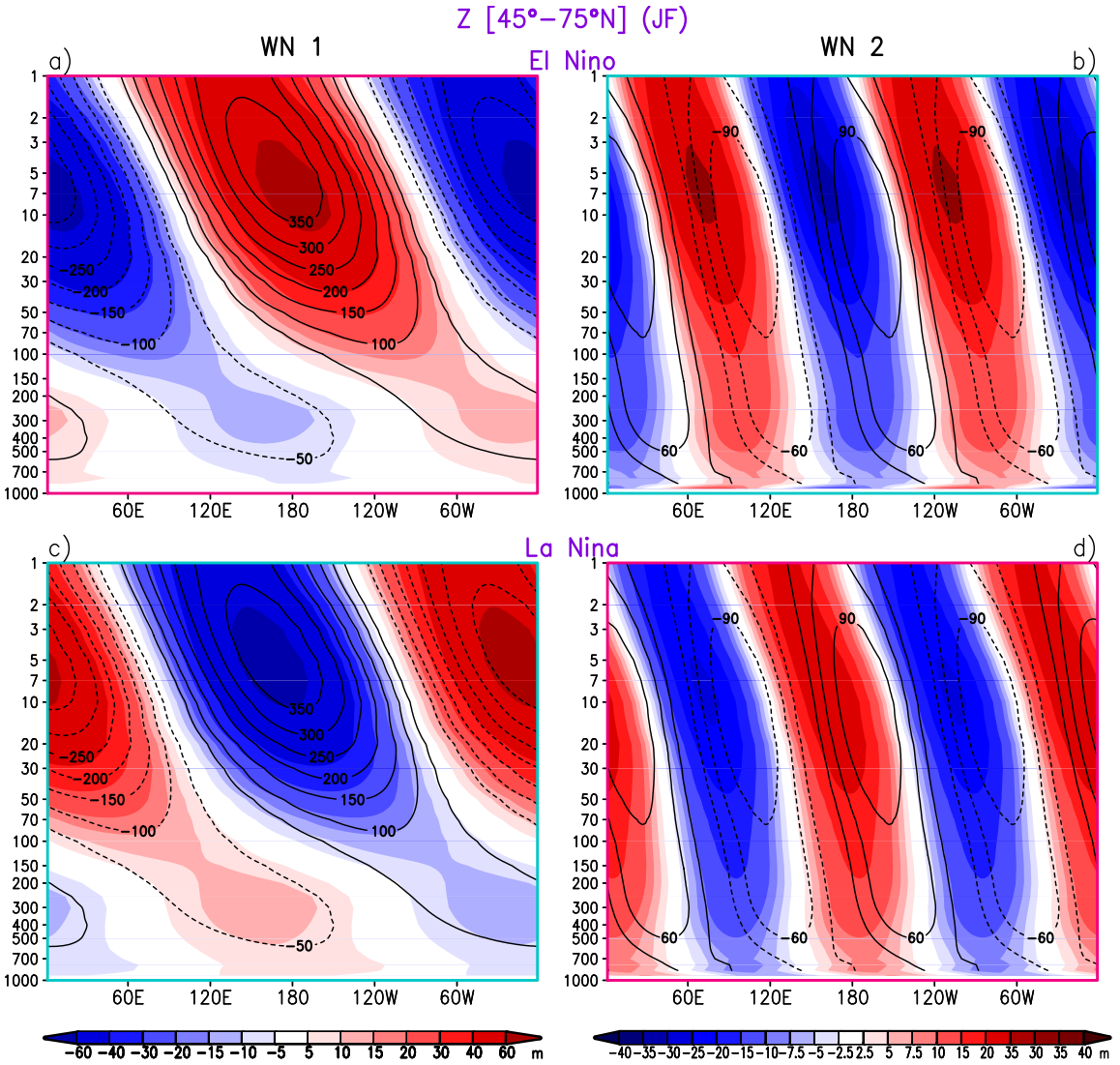


Figure 5.7: Composite longitude–height cross sections of zonal wavenumber-1 (left panels) and wavenumber-2 (right panels) components of geopotential height (m) averaged between 45° and 75°N. Results are shown for climatology (NDJFM-mean, contours) and composite El Niño (upper panels) and La Niña (lower panels) anomalies (shading) based on the CM3 simulation. The composites are computed for the period JF(1). Anomalous stationary wave pattern interferes constructively and destructively with climatological stationary field is framed in red and blue colors, respectively.

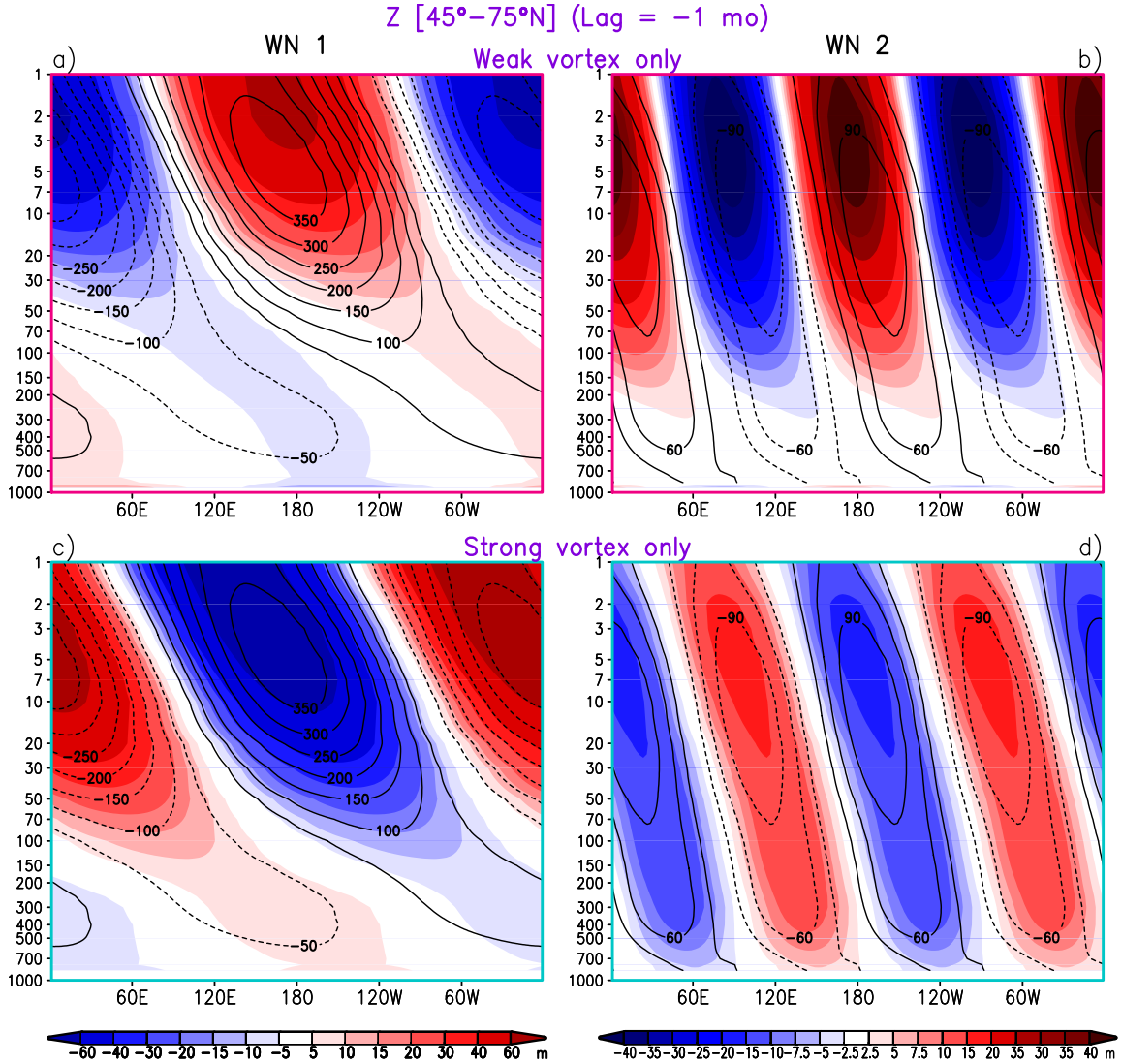


Figure 5.8: As in Fig. 5.7, but for weak (upper panels) and strong vortex (bottom panels) events in the neutral ENSO winters. The composites are computed during the lag of  $-1$  month of the anomalous vortex events.

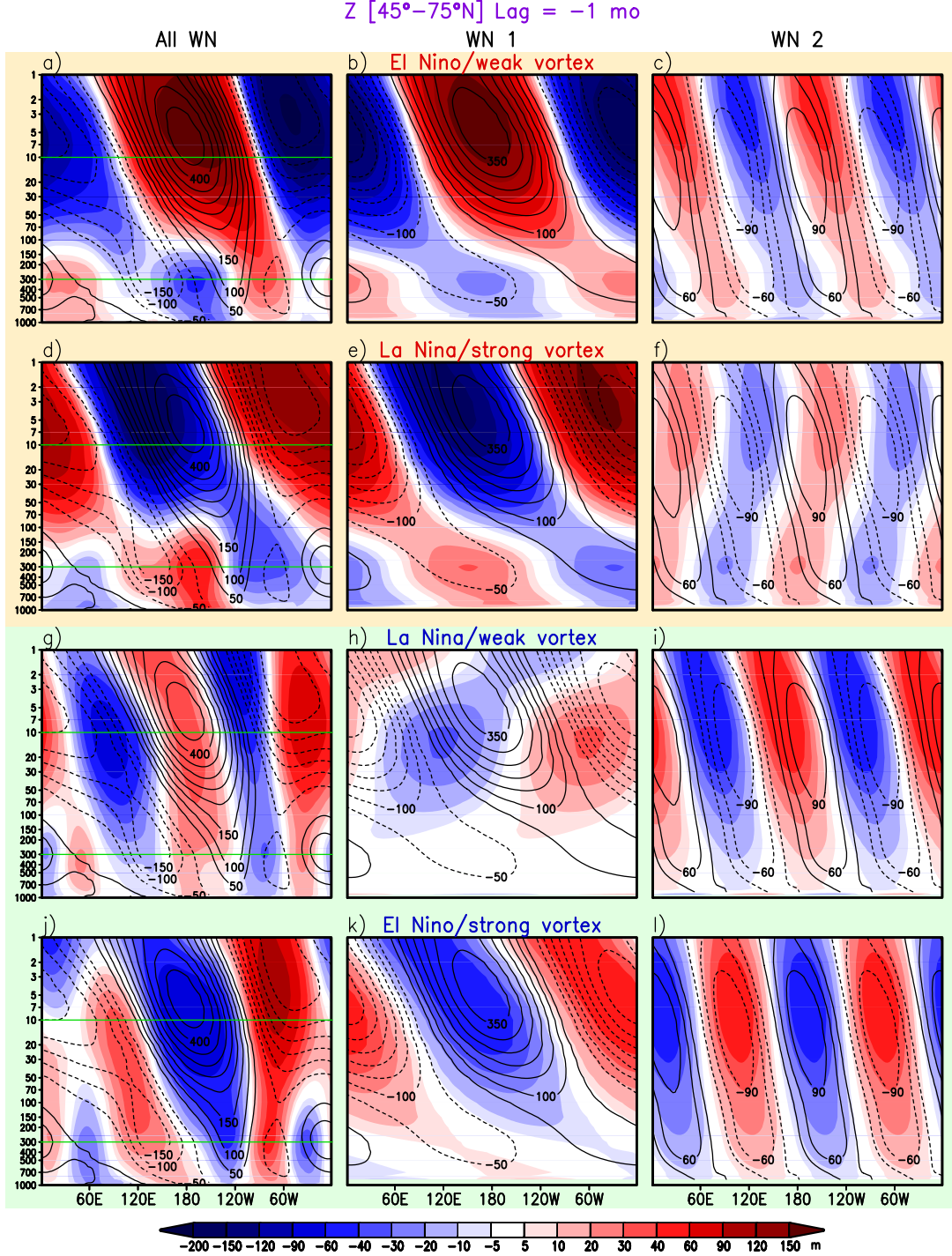


Figure 5.9: As in Fig. 5.8, but for the El Niño/weak vortex (first row), La Niña/strong vortex (second row), La Niña/weak vortex (third row) and El Niño/strong vortex (fourth row) events. Geopotential height anomalies for all zonal wavenumbers are shown on the left panels. Results for the two ‘strong combinations’ (upper half) and two ‘weak combinations’ (lower half) are presented with yellow and green backgrounds, respectively. The 300-hPa and 10-hPa levels where the horizontal distribution of the geopotential height fields are computed (see Figs. 5.10 and 5.11) are marked by thin green horizontal lines.

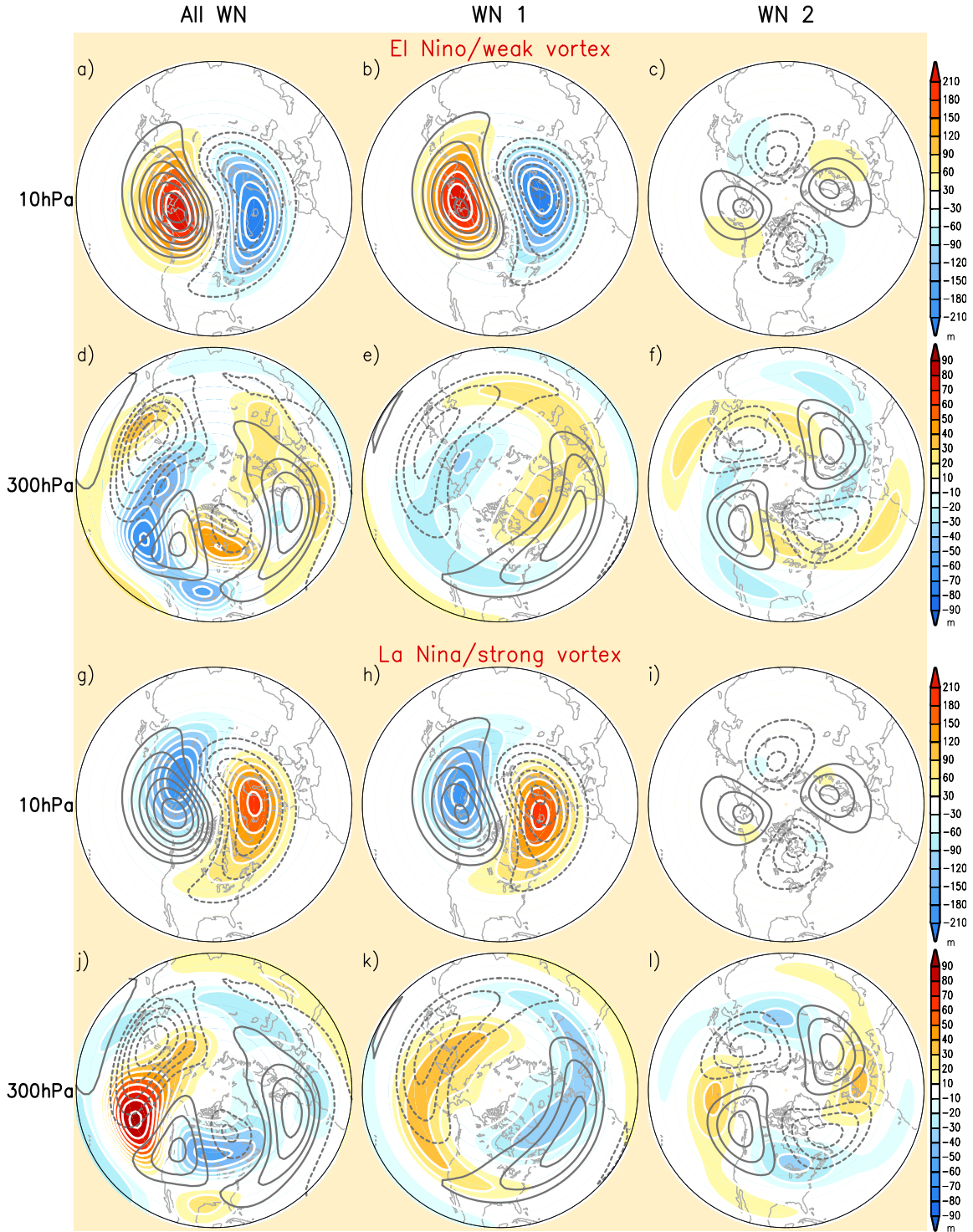


Figure 5.10: Horizontal distributions of the composites all-wavenumber (left panels), zonal wavenumber-1 (middle panels) and wavenumber-2 (right panels) of geopotential height fields at 10 hPa (first and third rows) and 300 hPa (second and fourth rows) for El Niño/weak vortex (upper half) and La Niña/strong vortex (lower half). The composites are computed during the lag of  $-1$  month of the anomalous vortex events.

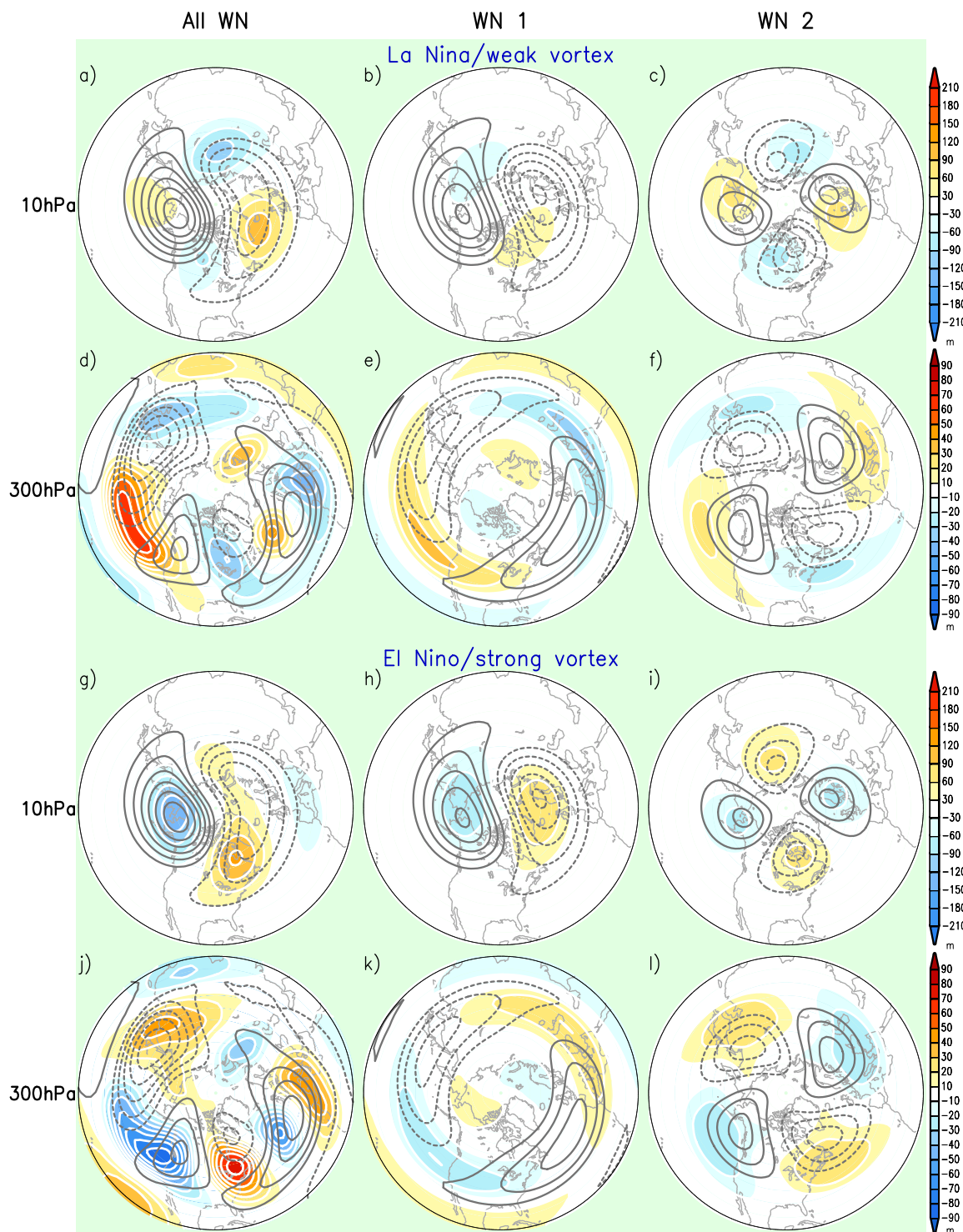


Figure 5.11: As in Fig. 5.10, but for La Niña/weak vortex (upper half) and El Niño/strong vortex (lower half).

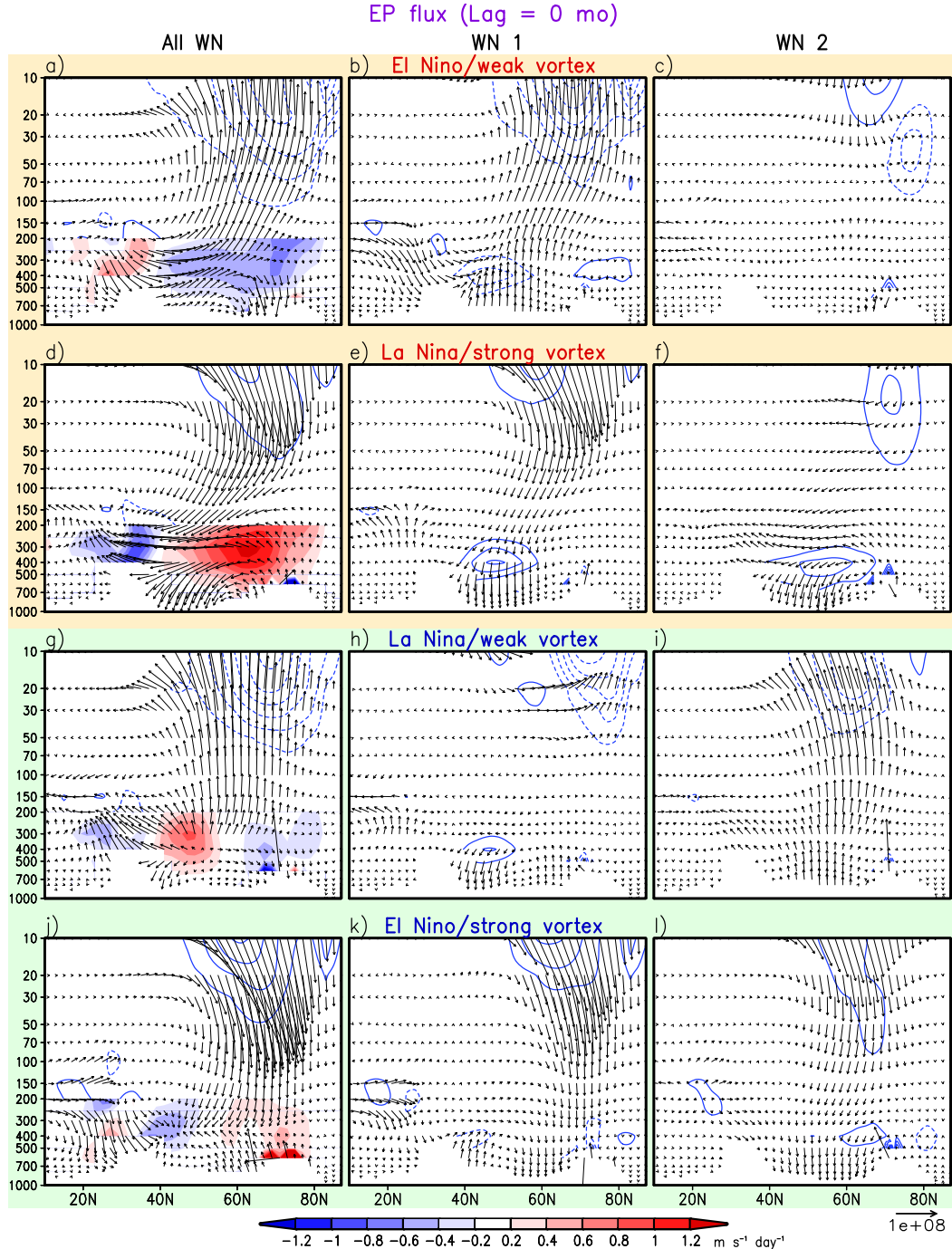


Figure 5.12: Composite latitude–height cross sections of EP flux (divided by the background density; arrows) and its divergence ( $D_F$ ; contours; interval  $0.5 \text{ m s}^{-1} \text{ day}^{-1}$ ) for all zonal wavenumbers (left panels), zonal wavenumber-1 (middle panels) and zonal wavenumber-2 (right panels). Shadings below 200 hPa superimposed on the left panels are the meridional derivative of  $F_\phi$  ( $D_M$ ; see scale at bottom). Composites are averaged during the lag of 0 month of the El Niño/weak vortex (first row), La Niña/strong vortex (second row), La Niña/weak vortex (third row) and El Niño/strong vortex (fourth row) events based on the CM3 simulation.

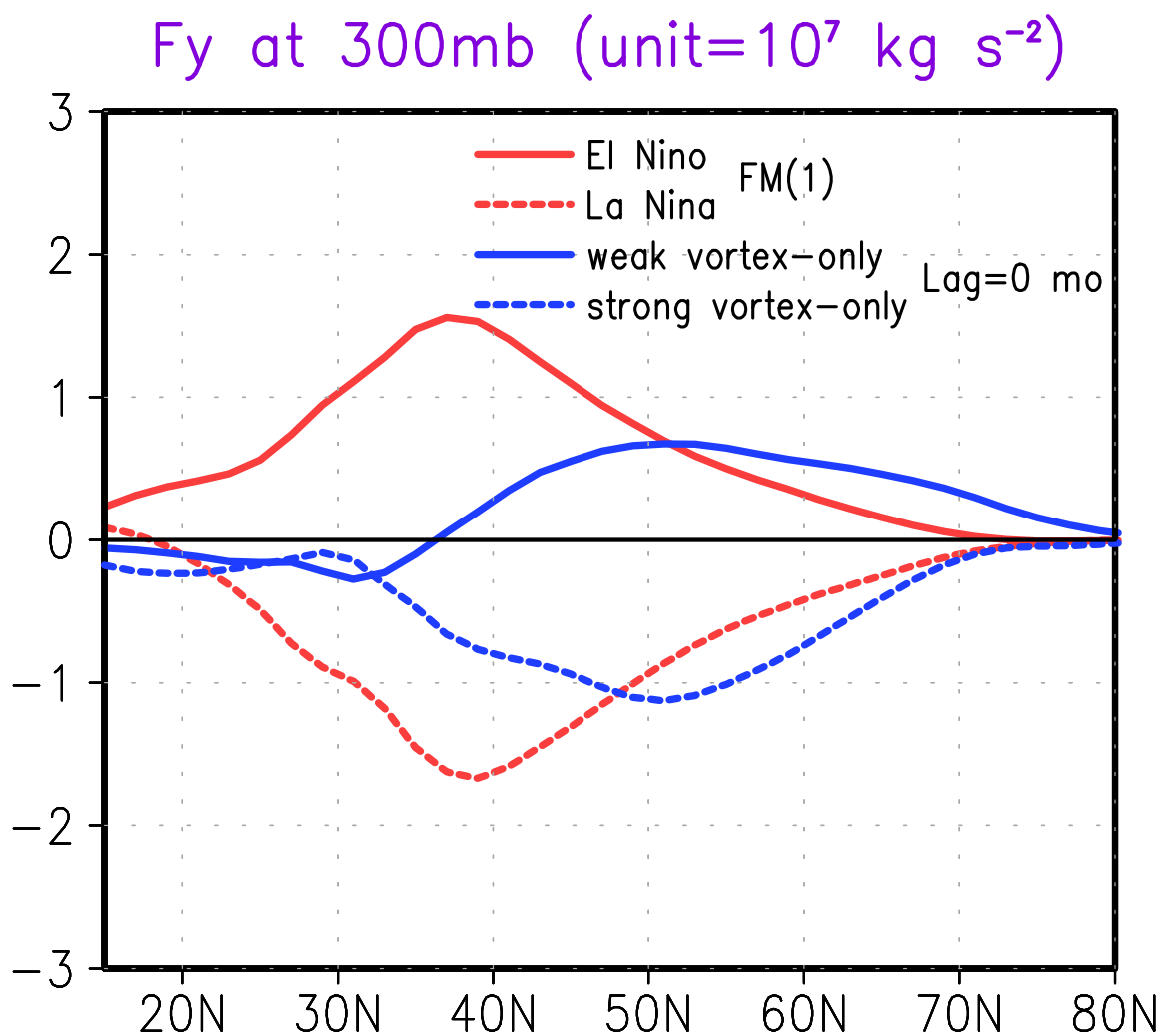


Figure 5.13: Composites of latitudinal profile of meridional component of anomalous EP flux ( $F_\phi$ ) at 300 hPa for El Niño (red solid line), La Niña (red dashed line), weak vortex-only (blue solid line), strong vortex-only (blue dashed line) events. The composite is averaged during the period FM(1) for the ENSO events, and during the lag of 0 month for vortex-only events.

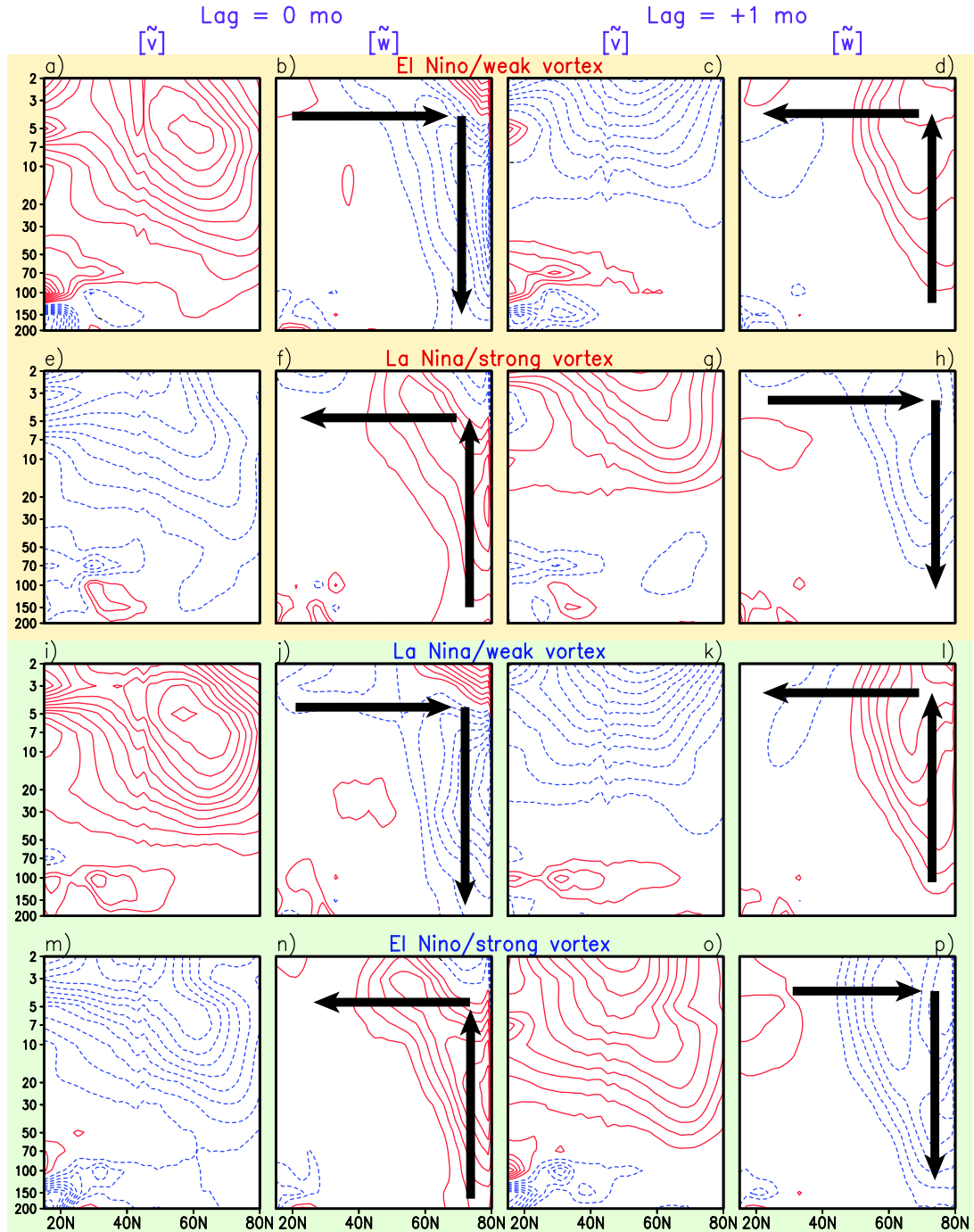


Figure 5.14: Composites of latitude–height cross sections of anomalous residual zonal-mean meridional ( $\tilde{[v]}$ ; first and third columns) and vertical ( $\tilde{[w]}$ ; second and fourth columns) circulation. Composites are averaged during lags of 0 (left two columns) and 1 month (right two columns) for the El Niño/weak vortex (first row), La Niña/strong vortex (second row), La Niña/weak vortex (third row) and El Niño/strong vortex (fourth row) events based on the CM3 simulation. The meridional (vertical) wind is contoured every  $2 \text{ cm s}^{-1}$  ( $10^{-1} \text{ mm s}^{-1}$ ). Vertical (horizontal) bold arrows indicate upward/downward (north/south) motion.

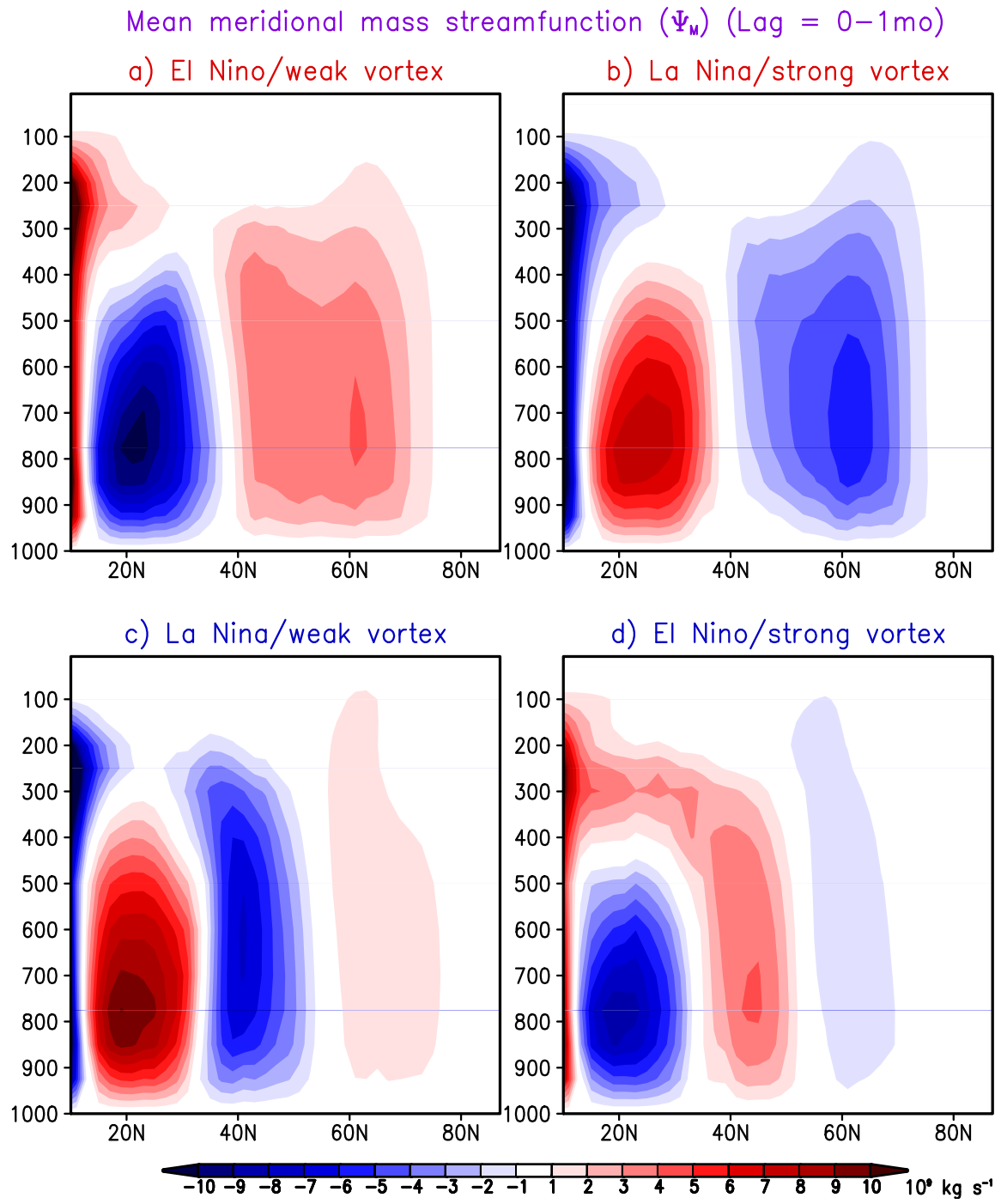


Figure 5.15: Composites of anomalous mean meridional mass streamfunction ( $\Psi_M$ ; units:  $10^9 \text{ kg s}^{-1}$ ) for a) El Niño/weak vortex, b) La Niña/strong vortex, c) La Niña/weak vortex, and d) El Niño/strong vortex. The composites are averaged from the lag of 0 to +1 month.

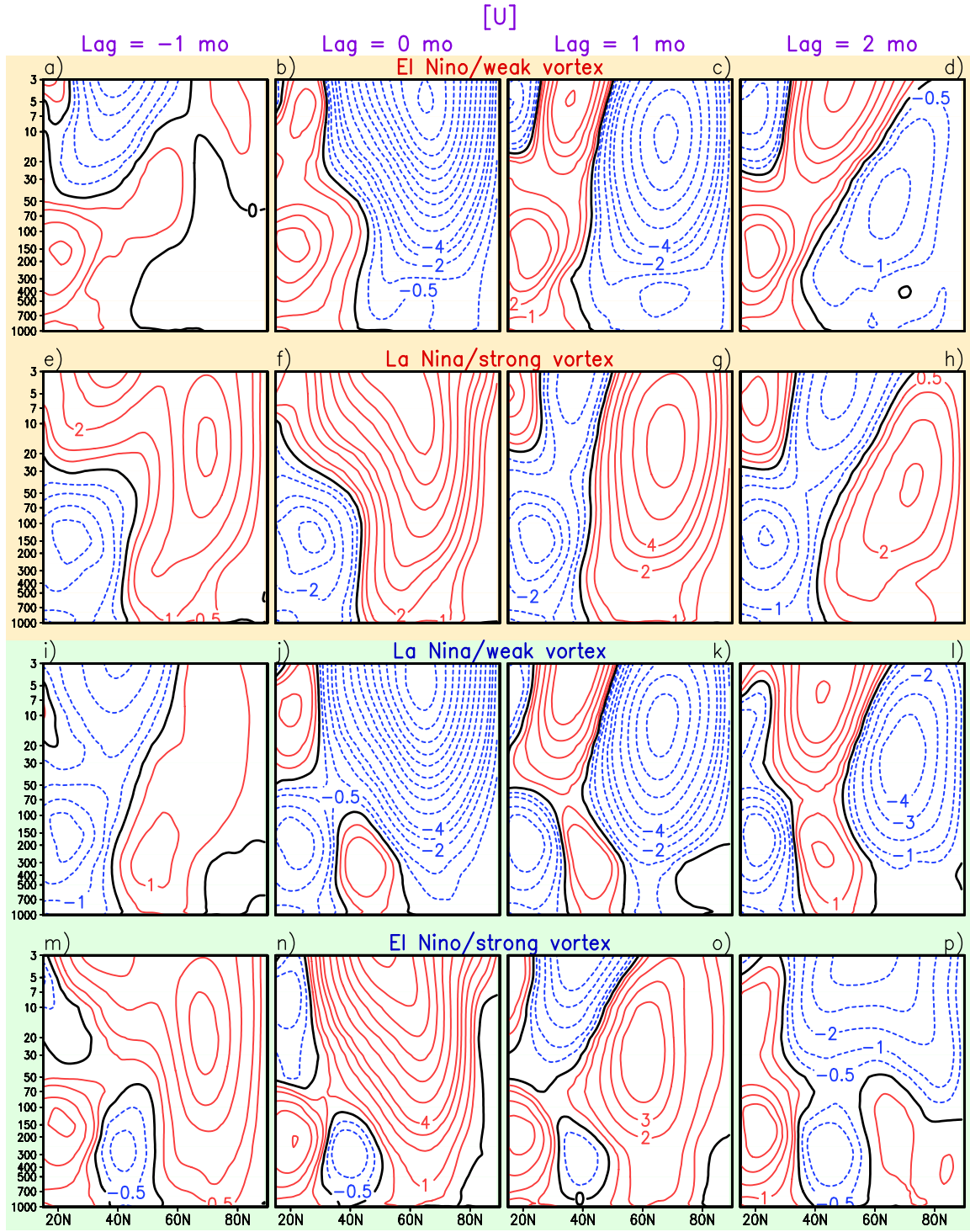


Figure 5.16: Composites of latitude–height cross sections of anomalous zonal-mean zonal wind for the El Niño/weak vortex (first row), La Niña/strong vortex (second row), La Niña/weak vortex (third row) and El Niño/strong vortex (fourth row) events based on CM3 simulation. The composites are averaged for the lags of  $-1$  (first column),  $0$  (second column),  $+1$  (third column), and  $+2$  (fourth column) month. Units:  $\text{m s}^{-1}$ .

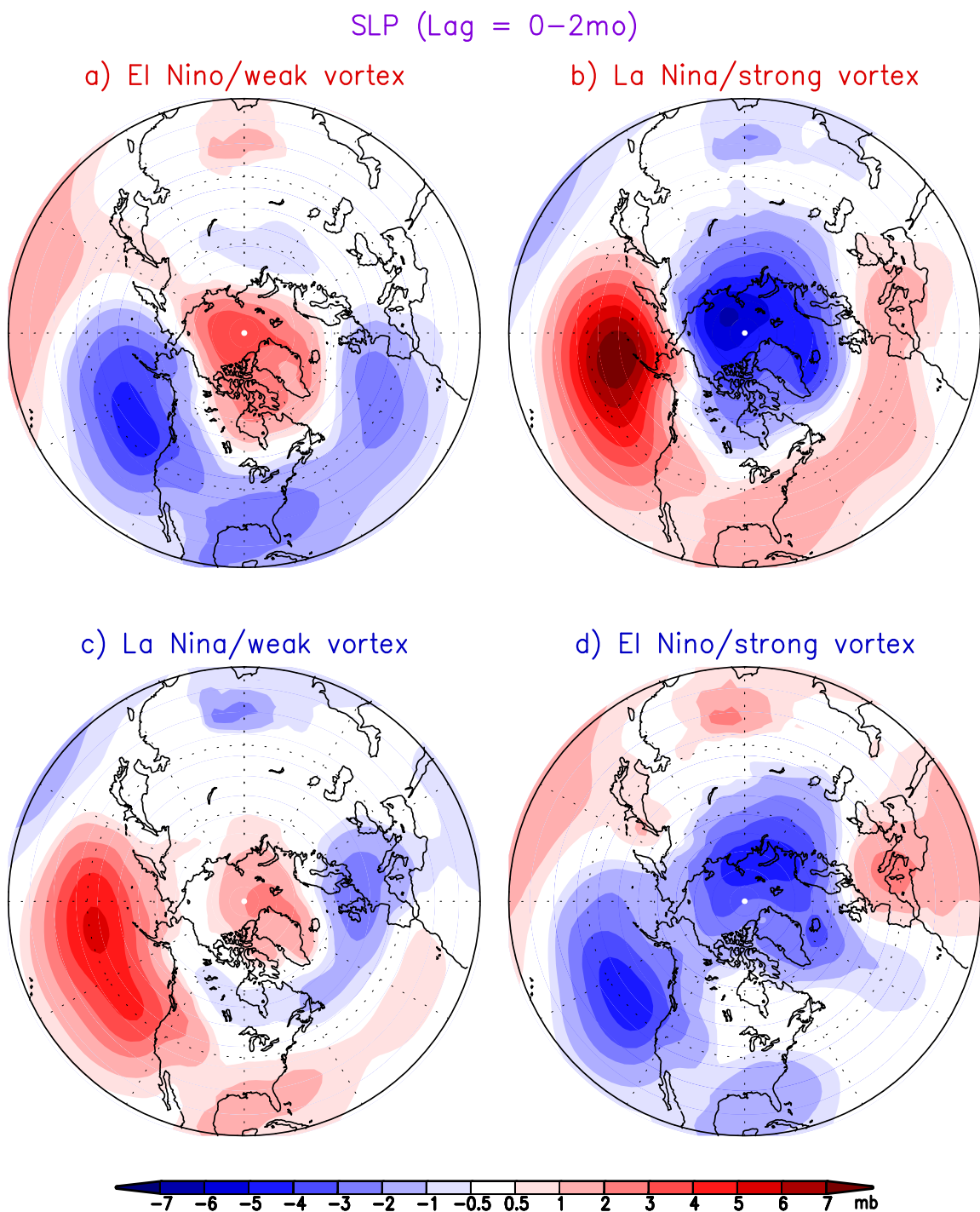


Figure 5.17: Horizontal distributions of composites of SLP for the (a) El Niño/weak vortex, (b) La Niña/strong vortex, (c) La Niña/weak vortex, and (d) El Niño/weak vortex based on the CM3 simulation. The composites are averaged from lag of 0 to +2 month.

# Chapter 6

## Conclusions

### 6.1 Summary

In this thesis, we study the dynamical mechanisms for the teleconnection between ENSO and NAO. The possible pathways in both the troposphere and stratosphere for this teleconnection have been identified, and the questions raised in chapter 1 are addressed.

In chapter 2, by analyzing a 2000-yr pre-industrial control simulation of the GFDL CM2.1 coupled model and comparing it with two reanalysis datasets, we show that the tropospheric teleconnection between ENSO and NAO is strongest in late winter. A strong negative NAO phase is 2–3 times more likely to occur during El Niño events in late winter than a strong positive NAO phase. Similarly, a strong positive NAO phase is 2–3 times more likely to occur than a strong negative NAO phase during late La Niña winters. In addition, the difference between the composite NAO indices for El Niño and La Niña events exceeds  $0.7\sigma$  in both the reanalysis and CM2.1 datasets. This difference is of practical use in seasonal prediction.

The potential role of the high-frequency transient eddies in the above tropospheric teleconnection between ENSO and NAO is diagnosed. During El Niño winters, the in-

tensified transient disturbances along the equatorward-shifted NP storm track extend their influences farther downstream. The negative height tendencies induced by the transient disturbances are found to be more coherent and stronger over the Atlantic sector than the tendencies over the Pacific sector. These negative height tendencies over the Atlantic sector are coincident with the southern lobe of the NAO, and thus favor more occurrences of negative NAO events. The opposite situation prevails in La Niña winters.

During those El Niño winters with relatively strong SST warming in eastern equatorial Pacific, the eastward extension of eddy activity is reinforced by the enhanced near-surface baroclinicity over the subtropical eastern Pacific. This flow environment supports a stronger linkage between the Pacific and Atlantic storm tracks, and is more conducive to a negative NAO phase.

In chapter 3, by analyzing the daily data from the same datasets as in chapter 2, we further demonstrate the role of downstream development of the wave packets in linking the circulation over the Pacific and Atlantic basins. We make use of a one-point lagged regression analysis based on selected persistent episodes. These persistent anomalous episodes are characterized by a strong Pacific subtropical jet stream and an equatorward-shifted Pacific storm track, and are associated with El Niño-related tropical forcing. It is illustrated that in the course of those persistent episodes, the downstream development of the wave packet extends farther eastward into the Atlantic storm track, as compared with the climatological scenario. This downstream extension of the wave packets is reinforced during the persistent flow pattern due to the strengthened phase speed and group velocity, as well as enhanced eddy kinetic energy near the Gulf of Mexico. In such development, the barotropic forcing of the synoptic-scale eddies embedded in the wave packets over the NA is conducive to the formation of the negative phase of the NAO. Furthermore, the more frequent occurrence and longer duration of those episodes during El Niño winters lead to stronger

and more steady transient eddy forcing, as well as farther eastward penetration of the wave packets to the NA sector. These effects contribute to the higher incidence of negative NAO-like anomalies in El Niño winters. Thus, this portion of the work provides additional evidence on the contribution of ENSO-related synoptic-scale eddy activity over the NA to NAO variability.

We also conduct a case study of the winter season 2009/2010, which featured a moderate El Niño and a persistent negative NAO, and was also noted for a series of significant winter storms across the United States. It is illustrated that the frequent and intense surface cyclone development over North America and the western Atlantic throughout that winter is associated with upper-level troughs propagating across North America, which in turn are linked to the downstream evolution of the wave packets originating from the Pacific storm track.

In chapter 4, we design and analyze numerical experiments with AGCM integrations in order to gain better understanding of the atmospheric response to the SST forcing in the tropical Pacific. A set of experiments is conducted using the atmospheric component of CM2.1 (AM2.1), with the ENSO-related SST forcing prescribed only in the tropical Pacific region. The reproduction of the transient eddy forcing over the NA associated with ENSO events confirms the important role of the ENSO-related SSTAs in the tropical Pacific.

In chapter 5, we study the stratospheric pathway using a 800-yr pre-industrial control simulation of a global coupled climate model with a more realistic upper atmosphere (CM3). It is shown that the enhanced stratospheric resolution in the model does yield a stronger late winter ENSO/NAO relationship. In addition, the amplitude of NAO-like dipolar anomaly in the CM3 simulation is about 20% larger than that in the CM2.1 simulation.

We first examine the dynamical linkage between ENSO and the stratospheric variability based on monthly values. The number of months with weak stratospheric

vortex in El Niño winters is notably larger than the counts in La Niña winters. The El Niño/weak vortex events are driven by the increased upward propagation of the tropospheric stationary wave-1 associated with the deepened Aleutian low. In contrast, the La Niña/weak vortex events are driven by the increased upward propagation of the tropospheric stationary wave-2, which may be associated with the NP blocking.

The anomalous easterlies induced by the EP flux convergence north of 60°N propagate downward to the lower stratosphere and upper troposphere during weak vortex events regardless of the phase of ENSO. However, the flow pattern south of 60°N in the upper troposphere is influenced by the pattern of eddy momentum flux convergence at the tropopause level. For the weak vortex events during El Niño winters, the individual effects of El Niño and weak vortex events reinforce each other and both effects leads to poleward wave refraction, which results in convergence of eddy momentum flux in the subtropics, and divergence in the subpolar region. This pattern of eddy momentum flux convergence drives anomalous westerlies and easterlies south and north of 40°N, respectively. In the resulting eddy-driven two-cell tropospheric overturning circulation, the Coriolis force acting on the lower branch of the circulation maintains the dipolar lower-tropospheric flow anomalies against frictional dissipation. In the 2-month period after the onset of the weakened stratospheric vortex anomalies, the SLP anomaly response is similar to the negative NAM pattern in the NH, and resembles negative NAO in the NA region.

In contrast, La Niña events are accompanied by the equatorward refraction of the planetary wave in the upper troposphere, in the opposite sense to the meridional wave propagation occurring in the weak vortex events. The equatorward refraction to the south of 50°N due to La Niña events is larger than the polarward refraction due to weak vortex events. The combined response in the La Niña/weak vortex events is the equatorward and poleward wave propagation south and north of 50°N, respectively,

which leads to a tripolar pattern of the eddy momentum flux convergence. The tripolar pattern of the SLP over NA can be deduced by analogous arguments to those presented in the preceding paragraph.

Conversely, the number of strong vortex months is notably larger during La Niña events than that during El Niño events. The La Niña/strong vortex events are associated with the reduction of tropospheric wave-1 driving, whereas the El Niño/strong vortex events are related to the reduction of both wave-1 and -2 forcing. The positive phase of the NAO is evident in the La Niña/strong vortex events, but no coherent NAO positive anomalies appear in the subtropical NA during the El Niño/strong vortex events.

Finally, we conclude that both the tropospheric and stratospheric pathways are important for the teleconnection between ENSO and NAO. The results from chapter 5 suggest that the northern lobe of the NAO is linked to the state of the stratospheric polar vortex that propagates downward, whose frequency of occurrence in turn is modulated by the phase of ENSO. However, the upper tropospheric eddy momentum flux plays an important role in determining the flow pattern over the region corresponding to the southern lobe of the NAO. This finding is consistent with the evidence on the effects of ENSO-related transient eddy vorticity forcing over the Atlantic sector on the southern lobe of the NAO, as highlighted in chapters 1–4.

## 6.2 Future Work

While this work has revealed some dynamical processes in the ENSO/NAO relationship, there are still many uncertainties that call for further investigation.

In this thesis work, there was considerable difficulty in ascertaining the cause-and-effect relationships between the stationary wave and transient eddy forcing over the NA. To address this issue, additional numerical experiments are required. For

example, storm track models such as those developed by [Branstator \(1995\)](#) may be employed to demonstrate the response of transient eddy fluxes to changes in zonal-mean flow. Moreover, solving the stationary wave model (e.g., [Ting and Yu 1998](#)) forced by eddy fluxes that are obtained from the storm track model will help us to better understand the contribution of the eddy forcing to the maintenance of the low-frequency flow pattern.

The AGCM (such as AM2.1) is a useful tool for understanding the atmospheric response to SST forcing since the model atmosphere responds passively to prescribed SST changes. In order to highlight the important role of the ENSO-related SSTAs in the tropical Pacific, the AGCM experiments are forced with ENSO-related SSTAs prescribed only in the tropical Pacific region. However, remote SST forcings originating from other ocean basins, such as tropical Indian and Atlantic Oceans, could amplify or reduce the circulation response to the ENSO-related SST forcing in the tropical Pacific ([Alexander et al. 2002; Annamalai et al. 2007](#)). In addition, SSTAs in other ocean basins may also modulate the ENSO signal over the NAE region. For instance, it has been suggested that when SSTAs over the tropical North Atlantic and tropical eastern Pacific are both warm, the SLP response is amplified and resembles the negative phase of the NAO (e.g., [Gouirand and Moron 2003; Mathieu et al. 2004](#)). It has also been noted that ENSO-related SSTAs over the Indo-Pacific region can contribute to the long-term trend in NAO (e.g., [Hoerling et al. 2001](#)). A recent study by [Kwon et al. \(2010\)](#) demonstrates that low-frequency variability of SSTAs in the western boundary current regions (i.e., Gulf Stream) may influence the storm track and circulation over the NA during ENSO events. Future study is needed to delineate the modulation of ENSO signal over the NAE region by SSTAs beyond the tropical Pacific. Additional simulations with air-sea coupling being incorporated in other ocean basins are recommended to study the relative importance of the two-way air-sea coupling in those ocean basins.

As mentioned in the introduction, this study focuses on the understanding of the possible link between the natural variability of ENSO and NAO utilizing the pre-industrial control run. Considering the possible effects of anthropogenically induced climate changes on the centers of warming in the tropical Pacific for the El Niño events (Yeh et al. 2008) and on the latitudinal position of storm track (Yin 2005), it is desirable to apply the analysis in this study to the 20<sup>th</sup>/21<sup>st</sup> century simulations.

## Appendix A

### Partial Correlation Coefficient

The partial correlation coefficient  $r_{12.3}$  between two variables,  $A_1$  and  $A_2$ , with the contribution from  $A_3$  being removed from both, is given by

$$r_{12.3} = \frac{r_{12} - r_{13}r_{23}}{\sqrt{(1 - r_{13}^2)(1 - r_{23}^2)}}, \quad (\text{A.1})$$

where the term  $r_{ij}$  represents the linear correlation coefficient between  $A_i$  and  $A_j$ .

# Bibliography

- Adler, R. F., G. J. Huffman, A. Chang, R. Ferraro, and Coauthors, 2003: The version-2 Global Precipitation Climatology Project (GPCP) monthly precipitation analysis (1979–present). *J. Hydrometeor.*, **4**, 1147–1167. [12](#)
- Alexander, M. A., I. Bladé, M. Newman, J. R. Lanzante, N.-C. Lau, and J. D. Scott, 2002: The atmospheric bridge: Influence of ENSO teleconnections on air–sea interaction over the global oceans. *J. Climate*, **15**, 2205–2231. [32](#), [103](#), [164](#)
- Alexander, M. A. and J. D. Scott, 2002: The influence of ENSO on air–sea interaction in the Atlantic. *Geophys. Res. Lett.*, **29**, 1701, doi:10.1029/2001GL014347. [32](#)
- Alexander, M. A. and J. D. Scott, 2008: The role of Ekman ocean heat transport in the Northern Hemisphere response to ENSO. *J. Climate*, **21**, 5688–5707. [32](#)
- Ambasum, M. H. P. and B. J. Hoskins, 2002: The NAO troposphere-stratosphere connection. *J. Climate*, **15**, 1969–1978. [7](#)
- Andrews, D. G., J. R. Holton, and C. B. Leovy, 1987: *Middle Atmosphere Dynamics*. Academic Press, 489 pp. [113](#), [119](#), [131](#)
- Annamalai, H., H. Okajima, and M. Watanabe, 2007: Possible impact of the Indian Ocean SST on the Northern Hemisphere circulation during El Niño. *J. Climate*, **20**, 3164–3189. [103](#), [164](#)

- Baldwin, M. P. and T. J. Dunkerton, 2001: Stratospheric harbingers of anomalous weather regimes. *Science*, **294**, 581–584. [7](#), [33](#), [137](#)
- Baldwin, M. P. and D. O’Sullivan, 1995: Stratospheric effects of ENSO-related tropospheric circulation anomalies. *J. Climate*, **8**, 649–667. [7](#)
- Baldwin, M. P. and D. W. J. Thompson, 2009: A critical comparison of stratosphere-troposphere coupling indices. *Quart. J. Roy. Meteor. Soc.*, **135**, 1661–1672. [120](#)
- Bell, C. J., L. J. Gray, A. J. Charlton-Perez, M. M. Joshi, and A. A. Scaife, 2009: Stratospheric communication of El Niño teleconnections to European winter. *J. Climate*, **22**, 4083–4096. [3](#), [8](#), [19](#)
- Benedict, J. J., S. Lee, and S. B. Feldstein, 2004: Synoptic view of the North Atlantic Oscillation. *J. Atmos. Sci.*, **61**, 121–144. [78](#)
- Bjerknes, J., 1969: Atmospheric teleconnections from the equatorial Pacific. *Mon. Wea. Rev.*, **97**, 163–172. [1](#)
- Black, R. X., 2002: Stratospheric forcing of surface climate in the Arctic Oscillation. *J. Climate*, **15**, 268–277. [7](#)
- Blackmon, M. L., Y.-H. Lee, and J. M. Wallace, 1984a: Horizontal structure of 500-mb height fluctuations with long, intermediate, and short time scales. *J. Atmos. Sci.*, **41**, 961–979. [66](#)
- Blackmon, M. L., Y.-H. Lee, J. M. Wallace, and H.-H. Hsu, 1984b: Time variation of 500-mb height fluctuations with long, intermediate, and short time scales as deduced from lag-correlation statistics. *J. Atmos. Sci.*, **41**, 981–991. [66](#), [70](#)
- Branstator, G., 1987: A striking example of the atmosphere’s leading traveling pattern. *J. Atmos. Sci.*, **44**, 2310–2323. [73](#)

- Branstator, G., 1995: Organization of storm track anomalies by recurring low-frequency circulation anomalies. *J. Atmos. Sci.*, **52**, 207–226. [22, 164](#)
- Branston, A. and R. E. Livezey, 1987: Classification, seasonality and persistence of low-frequency circulation patterns. *Mon. Wea. Rev.*, **115**, 1083–1126. [2](#)
- Bretherton, C. S., M. Widmann, V. P. Dymnikov, J. M. Wallace, and I. Bladé, 1999: The effective number of spatial degrees of freedom of a time-varying field. *J. Climate*, **12**, 1990–2009. [124](#)
- Brönnimann, S., 2007: Impact of El Niño-Southern Oscillation on European climate. *Rev. Geophys.*, **45**, RG3003, doi:10.1029/2006RG000199. [2](#)
- Brönnimann, S., J. Luterbacher, J. Staehelin, T. M. Svendby, G. Hansen, and T. Svenøe, 2004: Extreme climate of the global troposphere and stratosphere 1940–1942 related to El Niño. *Nature*, **431**, 971–974. [2, 8](#)
- Brönnimann, S., E. Xoplaki, C. Casty, A. Pauling, and J. Luterbacher, 2007: ENSO influence on Europe during the last centuries. *Climate Dyn.*, **28**, 181–197. [2](#)
- Butler, A. H. and L. M. Polvani, 2011: El Niño, La Niña, and Stratospheric Sudden Warmings: A re-evaluation in light of the observational record. *Geophys. Res. Lett.*, L13807, doi:10.1029/2011GL048084. [111](#)
- Cagnazzo, C. and E. Manzini, 2009: Impact of the stratosphere on the winter tropospheric teleconnections between ENSO and the North Atlantic and European region. *J. Climate*, **22**, 1223–1238. [8, 33](#)
- Camp, C. D. and K. K. Tung, 2007: Stratospheric polar warming by ENSO in winter: A statistical study. *Geophys. Res. Lett.*, **34**, L04809, doi:10.1029/2006GL028521. [7](#)

- Cassou, C., L. Terray, J. W. Hurrell, and C. Deser, 2004: North Atlantic wintertime climate regimes: Spatial asymmetry, stationarity with time and oceanic forcing. *J. Climate*, **17**, 1055–1068. [34](#)
- Cassou, C., L. Terray, and A. S. Phillips, 2005: Tropical Atlantic influence on European heat waves. *J. Climate*, **18**, 2085–2811. [34](#)
- Castanheira, J. M. and D. Barriopedro, 2010: Dynamical connection between tropospheric blockings and stratospheric polar vortex. *Geophys. Res. Lett.*, **37**, L13809, doi:10.1029/2010GL043819. [128](#)
- Cattiaux, J., R. Vautard, C. Cassou, P. Yiou, V. Masson-Delmotte, and F. Codron, 2010: Winter 2010 in Europe: A cold extreme in a warming climate. *Geophys. Res. Lett.*, **37**, L20704, doi:10.1029/2010GL044613. [74](#)
- Chang, E. K. M., 1993: Downstream development of baroclinic waves as inferred from regression analysis. *J. Atmos. Sci.*, **50**, 2038–2053. [6](#), [67](#), [69](#), [74](#)
- Chang, E. K. M., 1998: Poleward-propagating angular momentum perturbations induced by zonally symmetric heat sources in the tropics. *J. Atmos. Sci.*, **55**, 2229–2248. [5](#), [10](#), [20](#)
- Chang, E. K. M., 1999: Characteristics of wave packets in the upper troposphere. Part II: Seasonal and hemispheric variation. *J. Atmos. Sci.*, **56**, 1729–1747. [6](#)
- Chang, E. K. M., S. Lee, and K. L. Swanson, 2002: Storm track dynamics. *J. Climate*, **15**, 2163–2183. [74](#)
- Chang, E. K. M. and D. B. Yu, 1999: Characteristics of wave packets in the upper troposphere. Part I: Northern Hemisphere winter. *J. Atmos. Sci.*, **56**, 1708–1728. [6](#), [69](#)

- Charney, J. G. and P. G. Drazin, 1961: Propagation of planetary-scale disturbances from the lower into the upper atmosphere. *J. Geophys. Res.*, **66**, 83–109. [119](#)
- Chen, G. and I. M. Held, 2007: Phase speed spectra and the recent poleward shift of southern hemisphere surface westerlies, geophys. *Geophys. Res. Lett.*, **34**, L21805, doi:10.1029/2007GL031200. [7](#)
- Chen, P. and W. A. Robinson, 1992: Propagation of planetary waves between the troposphere and stratosphere. *J. Atmos. Sci.*, **49**, 2533–2545. [7](#), [131](#)
- Cheng, X. and J. M. Wallace, 1993: Cluster analysis of the Northern Hemisphere wintertime 500-hPa height field: spatial patterns. *J. Atmos. Sci.*, **50**, 2674–2696. [59](#)
- Christiansen, B., 2001: Downward propagation of zonal mean zonal wind anomalies from the stratosphere to the troposphere: Model and reanalysis. *J. Geophys. Res.*, **106**, 27307–27322. [130](#)
- Compo, G., J. Whitaker, and P. Sardeshmukh, 2006: Feasibility of a 100-year reanalysis using only surface pressure data. *Bull. Amer. Meteor. Soc.*, **87**, 175–190. [12](#)
- Delworth, T. L., A. J. Broccoli, A. Rosati, R. J. Stouffer, and Coauthors, 2006: GFDL’s CM2 global coupled climate models, Part I: Formulation and simulation characteristics. *J. Climate*, **19**, 643–674. [11](#), [56](#)
- Deser, C. and M. L. Blackmon, 1993: Surface climate variations over the North Atlantic Ocean during winter: 1900–1993. *J. Climate*, **6**, 1743–1753. [32](#)
- Dole, R. M., 1986: Persistent anomalies of the extratropical Northern Hemisphere wintertime circulation: Structure. *Mon. Wea. Rev.*, **114**, 178–207. [55](#)

- Dole, R. M. and N. D. Gordon, 1983: Persistent anomalies of the extratropical Northern Hemisphere wintertime circulation: Geographical distribution and regional persistence characteristics. *Mon. Wea. Rev.*, **111**, 1567–1586. [54](#), [57](#), [59](#), [65](#), [128](#)
- Dong, B.-W., R. T. Sutton, S. P. Jewson, A. O’Neil, and J. M. Slingo, 2000: Predictable winter climate in the North Atlantic sector during the 1997–1999 ENSO cycle. *Geophys. Res. Lett.*, **27**, 985–988. [2](#)
- Donner, L. J., B. L. Wyman, R. S. Hemler, L. W. Horowitz, and Coauthors, 2011: The dynamical core, physical parameterizations, and basic simulation characteristics of the atmospheric component AM3 of the GFDL Global Coupled Model CM3. *J. Climate*, **24**, 3484–3519, doi:10.1175/2011JCLI3955.1. [33](#), [111](#), [112](#), [118](#)
- Duchon, C., 1979: Lanczos filtering in one and two dimensions. *J. Appl. Meteor.*, **18**, 1016–1022. [13](#), [57](#)
- Dunkerton, T., C.-P. F. Hsu, and M. E. McIntyre, 1981: Some Eulerian and Lagrangian diagnostics for a model stratospheric warming. *J. Atmos. Sci.*, **38**, 819–843. [113](#), [116](#)
- Edmon, H. J., B. J. Hoskins, and M. E. McIntyre, 1980: Eliassen-Palm cross sections for the troposphere. *J. Atmos. Sci.*, **37**, 2600–2616. [113](#)
- Feldstein, S. B., 1998: The growth and decay of low-frequency anomalies in a gcm. *J. Atmos. Sci.*, **55**, 415–428. [60](#)
- Feldstein, S. B., 2000: The timescale, power spectra, and climate noise properties of teleconnection patterns. *J. Climate*, **13**, 4430–4440. [34](#), [55](#)
- Fraedrich, K., 1994: An ENSO impact on Europe? A review. *Tellus*, **46**, 541–552. [2](#), [3](#)

- Fraedrich, K. and M. Lutz, 1987: A modified time-longitude diagram applied to 500 mb heights along 50° north and south. *Tellus*, **39A**, 25–32. [69](#)
- Fraedrich, K. and K. Müller, 1992: Climate anomalies in Europe associated with ENSO extremes. *Int. J. Climatol.*, **12**, 25–31. [2](#), [3](#)
- Franzke, C., S. Lee, and S. B. Feldstein, 2004: Is the North Atlantic Oscillation a breaking wave? *J. Atmos. Sci.*, **61**, 145–160. [5](#), [78](#)
- García-Herrera, R., N. Calvo, R. R. Garica, and M. A. Giorgetta, 2006: Propagation of ENSO temperature signals into the middle atmosphere. *J. Geophys. Res.*, **111**, D06 101, doi:10.1029/2005JD006061. [7](#), [33](#)
- Garfinkel, C. I. and D. L. Hartmann, 2008: Effects of the el niño-southern oscillation and the quasi-biennial oscillation on polar temperatures in the stratosphere. [7](#)
- Garfinkel, C. I., D. L. Hartmann, and F. Sassi, 2010: Tropospheric precursors of anomalous northern hemisphere stratospheric polar vortices. *J. Climate*, **23**, 3282–3299, doi:10.1175/2010JCLI3010.1. [120](#), [127](#)
- GFDL Global Atmospheric Model Development Team, 2004: The new GFDL global atmosphere and land model AM2/LM2: Evaluation with prescribed SST simulations. *J. Climate*, **17**, 4641–4673. [11](#)
- Giorgetta, M. A., E. Manzini, R. Roeckner, M. Esch, and L. Bengtsson, 2006: Climatology and forcing of the quasi-biennial oscillation in the MAECHAM5 model. *J. Climate*, **19**, 3882–3901. [113](#)
- Gnanadesikan, A., K. W. Dixon, S. M. Griffies, and Coauthors, 2006: GFDL's CM2 global coupled climate models, Part II: The baseline ocean simulation. *J. Climate*, **19**, 675–697. [12](#), [56](#), [113](#)

Gouirand, I. and V. Moron, 2003: Variability of the impact of El Niño-Southern Oscillation on sea-level pressure anomalies over the North Atlantic in January to March (1874–1996). *Int. J. Climatol.*, **23**, 1549–1566. [3](#), [164](#)

Gouirand, I., V. Moron, and E. Zorita, 2007: Teleconnections between ENSO and North Atlantic in an ECHO-G simulation of the 1000–1990 period. *Geophys. Res. Lett.*, **34**, L06 705, doi:10.1029/2006GL028852. [2](#), [3](#)

Greatbatch, R. J., J. Lu, and K. A. Peterson, 2004: Nonstationary impact of ENSO on Euro-Atlantic winter climate. *Geophys. Res. Lett.*, **31**, L02 208. [2](#)

Griffies, S. M., 2009: Elements of MOM4p1. GFDL Ocean Group Tech. Rep. 6, NOAA/Geophysical Fluid Dynamics Laboratory, 444 pp., Princeton, NJ. [Available online at <http://www.gfdl.noaa.gov/fms/>]. [112](#)

Griffies, S. M., A. Gnanadesikan, K. W. Dixon, and Coauthors, 2005: Formulation of an ocean model for global climate simulations. *Ocean Science*, **1**, 45–70. [113](#)

Griffies, S. M., M. J. Harrison, R. C. Pacanowski, and A. Rosati, 2004: A technical guide to MOM4. GFDL Ocean Group Tech. Rep. 5, NOAA/Geophysical Fluid Dynamics Laboratory, 342 pp., Princeton, NJ. [12](#), [56](#), [112](#)

Hakim, G. J., 2003: Developing wave packets in the North Pacific storm track. *Mon. Wea. Rev.*, **131**, 2824–2837. [67](#)

Hamilton, K., 1988: A detailed examination of the extratropical response to tropical El Niño/Southern Oscillation events. *Int. J. Climatol.*, **8**, 67–86. [3](#)

Hamilton, K., 1993: An examination of observed Southern Oscillation effects in the Northern Hemisphere stratosphere. *J. Atmos. Sci.*, **50**, 3468–3473. [6](#), [7](#)

Harada, Y., A. Goto, H. Hasegawa, N. Fujikawa, H. Naoe, and T. Hirooka, 2010: A major stratospheric sudden warming event in January 2009. *J. Atmos. Sci.*, **67**, 2052–3069, doi:10.1175/2009JAS3320.1. [128](#)

Hartley, D. E., J. T. Villarin, R. X. Black, and C. A. Davis, 1998: A new perspective on the dynamical link between the stratosphere and troposphere. *Nature*, **391**, 471–474. [7](#)

Hartmann, D. L., J. M. Wallace, V. Limpasuvan, D. W. J. Thompson, and J. R. Holton, 2000: Can Ozone depletion and global warming interact to produce rapid climate change? *Proc. Natl. Acad. Sci.*, **97**, 1412–1417. [7](#), [131](#)

Haynes, P. H., M. E. McIntyre, T. G. Shepherd, C. J. Marks, and K. P. Shine, 1991: On the “downward control” of extratropical diabatic circulations by eddy-induced mean zonal forces. *J. Atmos. Sci.*, **48**, 651–680. [7](#)

Held, I. M., S. W. Lyons, and S. Nigam, 1989: Transients and the extratropical response to El Niño. *J. Atmos. Sci.*, **46**, 163–174. [5](#), [22](#)

Held, I. M., M. Ting, and H. Wang, 2002: Northern winter stationary waves: Theory and modeling. *J. Climate*, **15**, 2125–2013. [119](#)

Higgins, R. W. and S. D. Schubert, 1996: Simulations of persistent North Pacific circulation anomalies and interhemispheric teleconnections. *J. Atmos. Sci.*, **53**, 188–207. [59](#)

Higgins, R. W. and S. D. Schubert, 1997: Persistent North Pacific circulation anomalies and the tropical intraseasonal oscillation. *J. Climate*, **10**, 223–244. [59](#)

Hoerling, M. P., J. W. Hurrell, and T. Y. Xu, 2001: Tropical origins for recent North Atlantic climate change. *Science*, **292**, 90–92. [164](#)

Hoerling, M. P., A. Kumar, and M. Zhong, 1997: El Niño, La Niña, and the nonlinearity of their teleconnections. *J. Climate*, **10**, 1769–1786. [21](#)

Hoerling, M. P. and M. Ting, 1994: Organization of extratropical transients during El Niño. *J. Climate*, **7**, 745–766. [5](#), [10](#)

Holton, J. R., 2004: *An Introduction to Dynamic Meteorology*. 4th ed., Academic Press, 535 pp. [75](#)

Holton, J. R. and C. Mass, 1976: Stratospheric vacillation cycles. *J. Atmos. Sci.*, **33**, 2218–2225. [118](#)

Holton, J. R. and H. C. Tan, 1980: The influence of the equatorial quasi-biennial oscillation on the global circulation at 50 mb. *J. Atmos. Sci.*, **37**, 2200–2208. [113](#)

Holton, J. R. and H. C. Tan, 1982: The quasi-biennial oscillation in the Northern Hemisphere lower stratosphere. *J. Meteor. Soc. Japan*, **60**, 140–148. [113](#)

Honda, M., H. Nakamura, J. Ukita, I. Kousaka, and K. Takeuchi, 2001: Interannual seesaw between the Aleutian and Icelandic lows. Part I: Seasonal dependence and life cycle. *J. Climate*, **14**, 1029–1042. [28](#), [31](#), [65](#)

Horel, J. D. and J. M. Wallace, 1981: Planetary-scale atmospheric phenomena associated with the Southern Oscillation. *Mon. Wea. Rev.*, **103**, 813–829. [1](#), [20](#), [126](#)

Hoskins, B. J., I. N. James, and G. H. White, 1983: The shape, propagation and mean-flow interaction of large-scale weather systems. *J. Atmos. Sci.*, **40**, 1595–1612. [13](#), [20](#)

Hoskins, B. J. and P. J. Valdes, 1990: On the existence of storm-tracks. *J. Atmos. Sci.*, **47**, 1854–1864. [21](#), [29](#)

- Hurrell, J. W., 1995: Decadal trends in the North Atlantic Oscillation regional temperatures and precipitation. *Science*, **269**, 676–679. [2](#)
- Hurrell, J. W., 1996: Influence of variations in extratropical wintertime teleconnections on Northern Hemisphere temperatures. *Geophys. Res. Lett.*, **23**, 665–668. [19](#)
- Hurrell, J. W. and H. van Loon, 1997: Decadal variations in climate associated with the North Atlantic Oscillation. *Climate Change*, **36**, 301–326. [2](#)
- Ineson, S. and A. A. Scaife, 2009: The role of the stratosphere in the European climate response to El Niño. *Nat. Geosci.*, **2**, 32–36, doi:10.1038/ngeo381. [2](#), [7](#), [8](#), [33](#)
- James, I., 1994: *Introduction to Circulating Atmospheres*. Cambridge University Press, 422 pp. [77](#)
- James, I. and U. Burkhardt, 2006: A sidelong look at storm tracks. *Atmos. Sci. Lett.*, **7**, 69–74, doi:10.1002/asl.134. [6](#), [59](#)
- Kalnay, E., M. Kanamitsu, R. Kistler, and Coauthors, 1996: The NCEP/NCAR 40-Year Reanalysis Project. *Bull. Amer. Meteor. Soc.*, **77**, 437–471. [12](#), [56](#)
- Kok, C. J. and J. D. Opsteegh, 1985: Possible causes of anomalies in seasonal mean circulation patterns during the 1982/83 El Niño event. *J. Atmos. Sci.*, **42**, 677–694. [5](#)
- Kolstad, E. W., T. Breiteig, and A. A. Scaife, 2010a: The association between stratospheric weak polar vortex events and cold air outbreaks in the Northern Hemisphere. *Quart. J. Roy. Meteor. Soc.*, **136**, 886–893, doi:10.1002/qj.620. [120](#)
- Kolstad, E. W. and A. J. Charlton-Perez, 2010b: Observed and simulated precursors of stratospheric polar vortex anomalies in the Northern Hemisphere. *Climate Dyn.* [120](#)

Kumar, A. and M. P. Hoerling, 1997: Interpretation and implications of the observed inter-El Niño variability. *J. Climate*, **10**, 83–91. [3](#)

Kumar, A. and M. P. Hoerling, 2003: The nature and causes for the delayed atmospheric response to El Niño. *J. Climate*, **16**, 1391–1403. [31](#)

Kushner, P. J. and L. M. Polvani, 2004: Stratosphere-troposphere coupling in a relatively simple AGCM: The role of eddies. *J. Climate*, **17**, 629–639. [7](#)

Kushnir, Y., 1987: Retrograding wintertime low-frequency disturbances over the North Pacific Ocean. *J. Atmos. Sci.*, **44**, 2727–2742. [73](#)

Kushnir, Y., 1994: Interdecadal variations in North Atlantic sea surface temperature and associated atmospheric conditions. *J. Climate*, **7**, 142–157. [32](#)

Kushnir, Y., W. A. Robinson, I. Bladè, N. M. J. Hall, S. Peng, and R. Sutton, 2002: Atmospheric GCM response to extratropical SST anomalies: Synthesis and evaluation. *J. Climate*, **15**, 2233–2256. [5](#), [22](#), [32](#)

Kwon, Y.-O., M. A. Alexander, N. A. Bond, C. Frankignoul, H. Nakamura, B. Qiu, and L. A. Thompson, 2010: Role of the Gulf Stream and Kuroshio–Oyashio systems in large-scale atmosphere–ocean interaction: A review. *J. Climate*, **23**, 3249–3281, doi:10.1175/2010JCLI3343.1. [164](#)

Labitzke, K. G. and H. van Loon, 1999: *The Stratosphere: Phenomena, History, and Relevance*. Springer-Verlag, Berlin, 190 pp. [32](#)

Larkin, N. K. and D. E. Harrison, 2005: Global seasonal temperature and precipitation anomalies during El Niño autumn and winter. *Geophys. Res. Lett.*, **32**, L16705, doi:10.1029/2005GL022860. [3](#)

Lau, N.-C., 1979: The observed structure of tropospheric stationary waves and the local balances of vorticity and heat. *J. Atmos. Sci.*, **36**, 996–1016. [119](#)

Lau, N.-C., 1988: Variability of the observed midlatitude storm tracks in relation to low-frequency changes in the circulation pattern. *J. Atmos. Sci.*, **45**, 2718–2743.

13

Lau, N.-C. and E. O. Holopainen, 1984: Transient eddy forcing of the time-mean flow as identified by quasi-geostrophic tendencies. *J. Atmos. Sci.*, **41**, 313–328. 13, 23

Lau, N.-C., A. Leetmaa, M. J. Nath, and H.-L. Wang, 2005: Influences of ENSO-induced Indo–Western Pacific SST anomalies on extratropical atmospheric variability during the boreal summer. *J. Climate*, **18**, 2922–2942. 5, 10, 20

Lau, N.-C. and M. J. Nath, 1991: Variability of the baroclinic and barotropic transient eddy forcing associated with monthly changes in the midlatitude storm tracks. *J. Atmos. Sci.*, **48**, 2589–2631. 23

Lau, N.-C. and M. J. Nath, 1996: The role of the “atmospheric bridge” in linking tropical Pacific ENSO events to extratropical SST anomalies. *J. Climate*, **9**, 2036–2057. 103

Lau, N.-C. and M. J. Nath, 1999: Observed and GCM-simulated westward-propagating, planetary-scale fluctuations with approximately three-week periods. *Mon. Wea. Rev.*, **127**, 2324–2345. 73

Lau, N.-C. and M. J. Nath, 2001: Impact of ENSO on SST variability in the North Pacific and North Atlantic: Seasonal dependence and role of extratropical sea–air coupling. *J. Climate*, **14**, 2846–2866. 32

Lau, N.-C. and M. J. Nath, 2004: Coupled GCM simulation of atmosphere–ocean variability associated with zonally asymmetric SST changes in the tropical Indian Ocean. *J. Climate*, **17**, 245–265. 36

Lau, N.-C. and M. J. Nath, 2009: A model investigation of the role of air-sea interaction in the climatological evolution and ENSO-related variability of the summer monsoon over the South China Sea and western North Pacific. *J. Climate*, **22**, 4771–4792. [97](#)

Lee, S. and I. Held, 1993: Baroclinic wave packets in models and observations. *J. Atmos. Sci.*, **50**, 1413–1428. [6](#), [69](#), [70](#)

Li, Y. and N.-C. Lau, 2012a: Impact of ENSO on the atmospheric variability over the North Atlantic in late winter – Role of transient eddies. *J. Climate*, in press, doi:10.1175/JCLI-D-11-00037.1. [8](#), [9](#)

Li, Y. and N.-C. Lau, 2012b: Contributions of downstream eddy development to the teleconnection between ENSO and atmospheric circulation over the North Atlantic. *J. Climate*, in revision. [9](#)

Lim, G. H. and J. M. Wallace, 1991: Structure and evolution of baroclinic waves as inferred from regression analysis. *J. Atmos. Sci.*, **48**, 1718–1732. [67](#)

Limpasuvan, V. and D. L. Hartmann, 2000: Wave-maintained annular modes of climate variability. *J. Climate*, **13**, 4414–4429. [131](#), [137](#)

Limpasuvan, V., D. L. Hartmann, D. W. J. Thompson, K. Jeev, and Y. L. Yung, 2005: Stratosphere-troposphere evolution during polar vortex intensification. *J. Geophys. Res.*, **110**, doi:10.1029/2005JD006302. [7](#), [120](#), [134](#), [136](#)

Limpasuvan, V., D. Thompson, and D. Hartmann, 2004: On the life cycle of Northern Hemisphere stratosphere sudden warming. *J. Geophys. Res.*, **13**, 2584–2596. [120](#), [141](#)

Lin, S.-J., 2004: A “vertically Lagrangian” finite-volume dynamical core for global models. *Mon. Wea. Rev.*, **132**, 2293–2307. [12](#), [112](#)

- Manzini, E., M. A. Giorgetta, M. Esch, L. Kornblueh, and E. Roeckner, 2006: The influence of sea surface temperatures on the northern winter stratosphere: Ensemble simulations with the MAECHAM5 model. *J. Climate*, **19**, 3863–3881. [7](#), [33](#)
- Mathieu, P.-P., R. T. Sutton, B. Dong, and M. Collins, 2004: Predictability of winter climate over the North Atlantic European region during ENSO events. *J. Climate*, **17**, 1953–1974. [3](#), [164](#)
- Matsuno, T., 1971: A dynamical model of the stratospheric sudden warmings. *J. Atmos. Sci.*, **28**, 1479–1494. [118](#)
- Matthewman, N. J., J. G. Esler, A. J. Charlton-Perez, and L. M. Polvani, 2009: A new look at stratospheric sudden warmings. Part III: Polar vortex evolution and vertical structure. *J. Climate*, **22**, 1566–1585. [126](#)
- Merkel, U. and M. Latif, 2002: A high resolution AGCM study of the El Niño impact on the North Atlantic/European sector. *Geophys. Res. Lett.*, **29**, 1291, doi:10.1020/2001GL013726. [2](#), [3](#), [19](#)
- Moron, V. and I. Gouirand, 2003: Seasonal modulation of the El Niño-Southern Oscillation relationship with sea level pressure anomalies over the North Atlantic in October–March (1873–1996). *Int. J. Climatol.*, **37**, 143–155. [2](#), [3](#), [16](#)
- Müller, W. A. and E. Roeckner, 2006: ENSO impact on midlatitude circulation patterns in future climate change projections. *Geophys. Res. Lett.*, **33**, L05711, doi:10.1029/2005GL025032. [4](#)
- Nakamura, H., T. Izumi, and T. Sampe, 2002: Interannual and decadal modulations recently observed in the Pacific storm track activity and East Asian winter monsoon. *J. Climate*, **15**, 1855–1874. [57](#)

- Nakamura, H., M. Nakamura, and J. L. Anderson, 1997: The role of high- and low-frequency dynamics in blocking formation. *Mon. Wea. Rev.*, **125**, 2074–2093. [58](#)
- Nakamura, H. and A. Shimpo, 2004: Seasonal variations in the Southern Hemisphere storm tracks and jet streams as revealed in a reanalysis dataset. *J. Climate*, **17**, 1828–1844. [57](#)
- Nakamura, H. and J. M. Wallace, 1990: Observed changes in baroclinic wave activity during the life cycles of low-frequency circulation anomalies. *J. Atmos. Sci.*, **47**, 1100–1116. [57](#), [58](#), [60](#)
- Nigam, S., 2003: Teleconnections. *Encyclopedia of Atmospheric Sciences*, J. R. Holton, J. A. Pyle, and J. A. Curry, Eds., Academic Press, Vol. 6, 2243–2269. [1](#)
- Orlanski, I., 1998: Poleward deflection of storm tracks. *J. Atmos. Sci.*, **55**, 2577–2602. [20](#), [74](#)
- Orlanski, I., 2003: Bifurcation in eddy life cycles: Implications for storm track variability. *J. Atmos. Sci.*, **60**, 993–1023. [77](#)
- Orlanski, I., 2005: A new look at the Pacific storm track variability: Sensitivity to tropical SSTs and to upstream seeding. *J. Atmos. Sci.*, **62**, 1367–1390. [5](#), [10](#), [22](#), [29](#)
- Pawson, W. M., K. Kodera, K. Hamilton, T. G. Shepherd, and Coauthors, 2000: The GCM-reality intercomparison project for SPARC (GRIPS): Scientific issues and initial results. *Bull. Amer. Meteor. Soc.*, **81**, 781–796. [118](#)
- Perlitz, J. and N. Harnik, 2003: Observational evidence of a stratospheric influence on the troposphere by planetary wave reflection. *J. Climate*, **16**, 3011–3026. [7](#)

Perlitz, J. and N. Harnik, 2004: Downward coupling between the stratosphere and troposphere: The relative roles of wave and zonal mean processes. *J. Climate*, **17**, 4902–4909. [7](#)

Petterssen, S. and S. J. Smebye, 1971: On the development of extratropical cyclones. *Quart. J. Roy. Meteor. Soc.*, **97**, 547–482. [75](#)

Plumb, R. A., 1985: On the three-dimensional propagation of stationary waves. *J. Atmos. Sci.*, **42**, 217–229. [141](#)

Polvani, L. M. and D. W. Waugh, 2004: Upward wave activity flux as precursor to extreme stratospheric events and subsequent anomalous weather regimes. *J. Climate*, **17**, 3548–3554. [130](#)

Pozo-Vázquez, D., M. J. Esteban-Parra, F. S. Rodrigo, and Y. Castro-Díez, 2001: The association between ENSO and winter atmospheric circulation and temperature in the North Atlantic region. *J. Climate*, **14**, 3408–3420. [2](#), [3](#), [18](#)

Pozo-Vázquez, D., S. R. Gámiz-Fortis, J. Tovar-Pescador, M. J. Esteban-Parra, and Y. Castro-Díez, 2005: North Atlantic winter SLP anomalies based on the autumn ENSO state. *J. Climate*, **18**, 97–103. [2](#), [3](#), [18](#)

Putman, W. M. and S.-J. Lin, 2007: Finite-volume transport on various cubed-sphere grid. *J. Comput. Phys.*, **227**, 55–78. [112](#)

Renwick, J. A. and J. M. Wallace, 1996: Relationships between North Pacific winter-time blocking, El Niño, and the PNA pattern. *Mon. Wea. Rev.*, **124**, 2071–2076. [65](#), [128](#)

Rivière, G. and I. Orlanski, 2007: Characteristics of the Atlantic storm-track eddy activity and its relation with the North Atlantic Oscillation. *J. Atmos. Sci.*, **64**, 241–266. [5](#), [78](#)

Rogers, J. C., 1984: The association between the North Atlantic Oscillation and the Southern Oscillation in the Northern Hemisphere. *Mon. Wea. Rev.*, **112**, 1999–2015. [2](#)

Sassi, F., K. Kinnison, B. A. Boville, R. R. Garcia, and R. Roble, 2004: Effect of El Niño-Southern Oscillation on the dynamical, thermal, and chemical structure of the middle atmosphere. *J. Geophys. Res.*, **109**, D171108, doi:10.1029/2003JD0044344. [7](#), [33](#)

Seager, R., N. Harnik, Y. Kushnir, W. Robinson, and J. Miller, 2003: Mechanisms of hemispherically symmetric climate variability. *J. Climate*, **16**, 2960–2978. [5](#), [10](#), [20](#), [28](#), [132](#)

Seager, R., Y. Kushnir, J. Nakamura, M. Ting, and N. Naik, 2010a: Northern Hemisphere winter snow anomalies: ENSO, NAO and the winter of 2009/10. *Geophys. Res. Lett.*, **37**, L14703, doi:10.1029/2010GL043830. [20](#), [25](#), [74](#), [99](#)

Seager, R., N. Naik, M. Ting, M. A. Cane, N. Harnik, and Y. Kushnir, 2010b: Adjustment of the atmospheric circulation to tropical Pacific SST anomalies: Variability of transient eddy propagation in the Pacific–North America sector. *Quart. J. Roy. Meteor. Soc.*, **136**, 277–296, doi:10.1002/qj.588. [70](#)

Shindell, D. T., G. A. Schmidt, R. L. Miller, and D. Rind, 2001: Northern Hemisphere winter climate response to greenhouse gas, ozone, solar, and volcanic forcing. *J. Geophys. Res.*, **106**, 7193–7210. [7](#)

Simmons, A. J. and B. J. Hoskins, 1979: The downstream and upstream development of unstable baroclinic waves. *J. Atmos. Sci.*, **36**, 1239–1254. [6](#), [70](#)

Smirnov, N. V., 1948: Table for estimating the goodness of fit of empirical distributions. *Ann. Math. Statist.*, **19**, 279–281. [17](#), [62](#)

- Smith, T. M., R. W. Reynolds, T. C. Peterson, and J. Lawrimore, 2008: Improvements to NOAA's historical merged land-ocean surface temperature analysis (1880–2006). *J. Climate*, **21**, 2283–2296. [13](#), [56](#), [113](#)
- Song, Y. and W. A. Robinson, 2004: Dynamical mechanisms for stratospheric influences on the troposphere. *J. Atmos. Sci.*, **61**, 1711–1725. [7](#)
- Spiegel, M. R., 1988: *Schaum's Outline of Theory and Problems of Statistics*. 2nd ed., McGraw-Hill, 504 pp. [26](#)
- Straus, D. and J. Shukla, 1997: Variations of midlatitude transient dynamics associated with ENSO. *J. Atmos. Sci.*, **54**, 777–790. [5](#), [10](#)
- Straus, D. and J. Shukla, 2002: Does ENSO force the PNA? *J. Climate*, **15**, 2340–2358. [1](#)
- Straus, D. M., S. Corti, and Molteni, 2007: Circulation regimes: Chaotic variability versus SST-forced predictability. *J. Climate*, **20**, 2251–2272. [34](#)
- Strong, C. and G. Magnusdottir, 2008a: How Rossby wave breaking over the Pacific forces the North Atlantic Oscillation. *Geophys. Res. Lett.*, **35**, L10706, doi:10.1029/2008GL033578. [78](#)
- Strong, C. and G. Magnusdottir, 2008b: Tropospheric Rossby wave breaking and the NAO/NAM. *J. Atmos. Sci.*, **65**, 2861–2876. [78](#)
- Taguchi, M. and D. L. Hartmann, 2006: Increased occurrence of stratospheric sudden warmings during El Niño as simulated by WACCM. *J. Climate*, **19**, 324–332. [7](#), [32](#), [111](#)
- Thompson, D. W. J., M. P. Baldwin, and J. M. Wallace, 2002: Stratospheric connection to Northern Hemisphere wintertime weather: Implications for predictions. *J. Climate*, **15**, 1421–1428. [137](#)

Thompson, D. W. J., J. C. Furtado, and T. G. Shepherd, 2006: On the tropospheric response to anomalous stratospheric wave drag and radiative heating. *J. Atmos. Sci.*, **63**, 2616–2629. [7](#)

Thompson, D. W. J. and J. M. Wallace, 1998: The Arctic oscillation signature in the wintertime geopotential height and temperature fields. *Geophys. Res. Lett.*, **25**, 1297–1300. [2, 138](#)

Thompson, D. W. J. and J. M. Wallace, 2000: Annular modes in the extratropical circulation. Part I: Month-to-month variability. *J. Climate*, **13**, 1000–1016. [2, 137, 138](#)

Thompson, D. W. J. and J. M. Wallace, 2001: Regional climate impacts of the Northern Hemisphere annular mode. *Science*, **293**, 85–89. [2](#)

Thorncroft, C. D., B. J. Hoskins, and M. E. McIntyre, 1993: Two paradigms of baroclinic-wave life-cycle behavior. *Quart. J. Roy. Meteor. Soc.*, **17**, 201–355. [78](#)

Ting, M. F. and L. H. Yu, 1998: Steady response to tropical heating in wavy linear and nonlinear baroclinic models. *J. Atmos. Sci.*, **55**, 3565–3582. [164](#)

Toniazzo, T. and A. A. Scaife, 2006: The influence of ENSO on winter North Atlantic climate. *Geophys. Res. Lett.*, **33**, L24704. [2, 3, 19](#)

Trenberth, K. E., 1981: Observed Southern Hemisphere eddy statistics at 500 mb: Frequency and spatial dependence. *J. Atmos. Sci.*, **38**, 2507–2520. [58](#)

Trenberth, K. E., 1986: An assessment of the impact of transient eddies on the zonal flow during a blocking episode using localized Eliassen-Palm flux diagnostics. *J. Atmos. Sci.*, **43**, 2070–2087. [13, 21, 22, 58, 64](#)

Trenberth, K. E., G. W. Branstator, D. Karoly, A. Kumar, N.-C. Lau, and C. Ropelewski, 1998: Progress during TOGA in understanding and modeling global tele-

connections associated with tropical sea surface temperatures. *J. Geophys. Res.*, **103**, 14 291–14 324. 1, 2

Trenberth, K. E. and J. W. Hurrell, 1994: Decadal atmosphere-ocean variations in the Pacific. *Climate Dyn.*, **9**, 303–319. 5

Uppala, S. M., P. W. Källberg, A. J. Simmons, U. Andrae, and Coauthors, 2005: The ERA-40 re-analysis. *Quart. J. Roy. Meteor. Soc.*, **131**, 2961–3012. 113

Vallis, G. K., 2006: *Atmospheric and Oceanic Fluid Dynamics: Fundamentals and Large-Scale Circulation*. Cambridge University Press, Cambridge, U.K., 561 pp. 113

van Loon, H. and K. Labitzke, 1987: The Southern Oscillation. Part V: The anomalies in the lower stratosphere of the Northern Hemisphere in winter and a comparison with the quasi-biennial oscillation. *Mon. Wea. Rev.*, **115**, 357–369. 6

van Loon, H. and J. C. Rogers, 1978: The seesaw in winter temperatures between Greenland and northern Europe. *Mon. Wea. Rev.*, **106**, 296–310. 2

Vautard, R., 1990: Multiple weather regimes over the North Atlantic: Analysis of precursors and successors. *Mon. Wea. Rev.*, **118**, 2057–2081. 34, 54

Walker, G. T. and E. W. Bliss, 1932: World weather. *V. Mem. Roy. Meteor. Soc.*, **4**, 53–84. 2

Wallace, J. M. and D. S. Gutzler, 1981: Teleconnections in the geopotential height field during the Northern Hemisphere winter. *Mon. Wea. Rev.*, **109**, 784–812. 1, 59, 64

Wallace, J. M., G. Lim, and M. L. Blackmon, 1988: Relationship between cyclone tracks, anticyclone tracks, and baroclinic waveguides. *J. Atmos. Sci.*, **45**, 439–462. 59, 67

Whitaker, J. S., G. P. Compo, X. Wei, and T. M. Hamill, 2004: Reanalysis without radiosondes using ensemble data assimilation. *Mon. Wea. Rev.*, **132**, 1190–1200.

12

Wittenberg, A. T., 2009: Are historical records sufficient to constrain ENSO simulations? *Geophys. Res. Lett.*, **36**, L12702, doi:10.1029/2009GL038710. 11

Wittenberg, A. T., A. Rosati, N.-C. Lau, and J. J. Poshay, 2006: GFDL's CM2 global coupled climate models. Part III: Tropical Pacific climate and ENSO. *J. Climate*, **19**, 698–722. 15, 36

Xue, Y., T. M. Smith, and R. W. Reynolds, 2003: Interdecadal changes of 30-yr SST normals during 1871–2000. *J. Climate*, **16**, 1601–1612. 13, 56, 113

Yeh, S.-W., J.-S. Kug, B. Dewitte, M.-H. Kwon, B. Kirtman, and F.-F. Jin, 2008: El Niño in a changing climate. *Nature*, **461**, 511–514. 165

Yin, J. H., 2005: A consistent poleward shift of the storm tracks in simulations of 21st century climate. *Geophys. Res. Lett.*, **32**, L18701, doi:10.1029/2005GL023684.

165

Zhang, Y. and I. M. Held, 1999: A linear stochastic model of a GCM's midlatitude storm tracks. *J. Atmos. Sci.*, **56**, 3416–3435. 5, 10